NOVEL CAD/CAM RAPID PROTOTYPING OF NEXT-GENERATION BIOMEDICAL DEVICES

Anand Doraiswamy

A dissertation submitted to the faculty of the University of North Carolina at Chapel Hill in partial fulfillment of the requirements for the degree of Doctor of Philosophy in the Department of Biomedical Engineering at the School of Medicine.

Chapel Hill
2007

Approved by:

Douglas B. Chrisey

Stephen B. Knisley

Yuan-Shin Lee

Peter L. Mente

Roger J. Narayan

ABSTRACT

ANAND DORAISWAMY: Novel CAD/CAM Rapid Prototyping of Next-generation Biomedical Devices
(Under the direction of Roger J. Narayan)

An aging population with growing healthcare needs demands multifaceted tools for diagnosis and treatment of health conditions. In the near-future, drug-administration devices, implantable devices/sensors, enhanced prosthesis, artificial and unique functional tissue constructs will become increasingly significant. Conventional technologies for mass-produced implants do not adequately take individual patient anatomy into consideration. Development of novel CAD/CAM rapid prototyping techniques may significantly accelerate progress of these devices for next-generation patient-care.

In this dissertation, several novel rapid prototyping techniques have been introduced for next-generation biomedical applications. Two-photon polymerization was developed to microfabricate scaffolds for tissue engineering, microneedles for drug-delivery and ossicular replacement prostheses. Various photoplymers were evaluated for feasibility, mechanical properties, cytotoxicity, and surface properties. Laser direct write using MDW was utilized for developing microstructures of bioceramics such as hydroxyapatite, and viable mammalian osteosarcoma cells. CAD/CAM laser micromachining (CLM) was developed to engineer biointerfaces as surface recognition

regions for differential adherence of cells and growth into tissue-like networks. CLM was also developed for engineering multi-cellular vascular networks. Cytotoxic evaluations and growth studies demonstrated VEGF-induced proliferation of HAAE-1 human aortic endothelial cells with inhibition of HA-VSMC human aortic smooth muscle cells. Finally, piiezoelectric inkjet printing was developed for controlled administration of natural and synthetic adhesives to overcome several problems associated with conventional tissue bonding materials, and greatly improve wound repair in next generation eye repair, fracture fixation, organ fixation, wound closure, tissue engineering, and drug delivery devices.

“To my parents, Leelu & Dorai”

ACKNOWLEDGMENTS

In my journey through graduate school, I have had the unique opportunity to work with a variety of people on various technologies in a range of settings. I have thoroughly enjoyed my discussions and interactions with all. It has been a great learning and rewarding experience and I have many to thank for this.

In 2003, I had completed my Master's degree in materials science and engineering from the University of Arizona under the guidance of Prof. Joseph Simmons and Dr. Pierre Lucas. I would like to thank them for their support during that period. In 2004, I joined the group of Dr. Roger J. Narayan, M.D, Ph.D. at Georgia Institute of Technology to pursue my doctoral research in biomaterials. I would like to express my deepest gratitude to him for being instrumental in guiding and supporting me through my doctoral research. I would also like to thank members of the group including Timothy Patz, Wei Wei, Jamal Lewis, Ravi Aggarwal. Dr. Junping Zhang, and Dr. Chunming Jin for their support.

Later in 2004, I had the opportunity to work at the plasma processing division at US Naval Research Laboratory in Washington, D.C. Here, I had the opportunity to work under the guidance of Prof. Douglas Chrisey (currently at Rensselaer Polytechnic Institute). Prof. Chrisey has been influential throughout my doctoral research, especially during the early stages of work on laser direct writing. I would like to thank him for his continued support.

Working at NRL was a unique experience where I had the opportunity to interact with distinguished scientists. I would like to thank Dr. Rohit Modi and Ray Auyeung for their guidance and direction with the laser direct write setup. Dr. Modi has been of tremendous support in helping me being focused during the initial stages. I would also like to thank Lance Harris, Dr. Syed Qadri, and Dr. Tom Lippert for their contribution to the MDW project.

In 2005, I had the opportunity to work at the nanotechnology division at Laser Zentrum Hannover (LZH) eV. in Germany on developing a unique laser direct write technology. I am very grateful to Aleksandr Ovsianikov and Prof. Boris Chichkov for this exclusive collaboration which allowed pioneering of 2PP for next-generation medical devices. I wish to thank them for the bier and brezls as well. Later in 2005, I moved along with my primary advisor Dr. Roger Narayan to the joint department of biomedical engineering at the University of North Carolina at Chapel Hill. After relocation, new collaborative opportunities arose over the last two years toward developing novel rapid prototyping systems. I wish to thank Dr. Oliver Adunka at the department of Otolaryngology in UNC School of medicine for his collaboration in developing ear replacement prosthesis. I wish to thank Dr. Jan Sumerel from Fujifilm-Dimatix for her inputs and discussions in developing piezoelectric inkjet technology for biomedical applications. I wish to thank Timothy Dunaway and Dr. Jonathan Wilker for providing natural mussel adhesive proteins and valuable inputs to the bioadhesive project. I wish to thank Yi -Jen for his assistance with the Si micromachining study. I am very greatful to Prof. Stephen Kinsley, Prof. Yuan-Shin Lee, and Dr. Peter Mente for their guided inspiration and for serving in my committee. I would like to extend my gratitude to Prof. Banes, Prof. Narayan, and Prof. Nagle for their

motivation and support. I am also grateful to the various staff members at UNC, NCSU, and Georgia Tech and would like to extend a special note of thanks to Nancy McKinney, Sharon Womble, Harriett Brewer, and Linda Simerson who were of great assistance.

I would like to thank Prof. Nancy Monteiro-Riviere for the collaboration and guidance towards performing cytotoxic evaluations of biomaterials. Working briefly at CCTRP was a valuable experience towards learning to perform cytotoxicity studies, transdermal diffusion study, and cryo-sectioning. I would like to extend my gratitude to Al Inman for his patient guidance and Katharine Evaul for her continued assistance. I would like to thank several other labs/members who assisted with the various characterization works: Dr. Wei He and Prof. Ravi Bellamkonda at Georgia Tech. for their assistance with the confocal imaging of neuroblast cells, Wijaya Martanto and Prof. Mark Prausnitz at Georgia Tech. for discussions on microneedle technology, Prasath Mageswaran for his assistance in NCSU tissue mechanics laboratory, Birgit Anderson at NCSU for assisting with the FTIR characterization, Fred Stevie at AIF/NCSU for assistance with XPS, Eva Johannes at NSCORT and Mike Chua & Wendy Salmon at the UNC Michael Hooker facility for their assistance with optical microscopy, and Rene Crombez, Eva Montalvo, & Weidian Shen at Eastern-Michigan University for their assistance with the nanoindentation measurements.

I would like to thank all my friends and family for making this journey satisfying and enjoyable. A special thanks to all my climbing cronies and sherpas who have made mountaineering an imperative part of my life which has allowed me to conclude my doctoral research strikingly similar to a successful summit-climb. None of this would have been possible without the constant motivation and everlasting support from Tejas, Alexandra, Vinu, Anu, Srini, Dorai and Leelu. Thanks once again.

TABLE OF CONTENTS

LIST OF TABLES

Table

LIST OF FIGURES

Figure

ABBREVIATIONS

2D	Two dimensional
2PP	Two-photon polymerization
3D	Three dimensional
A431	Human skin epithelial carcinoma cell-line
AFM	Atomic force microscopy
AOM	Acoustic optical modulator
ArF	Argon-fluoride
B35	Rat neuroblast clonal cell line
C2C12	Mouse myoblast cell line
CAD	Computer-aided design
CAM	Computer-aided machining
CCD	Charge-coupled device
CLM	CAD/CAM laser micromachining
DIC	Differential interference contrast
DOPA	3, 4-dihydroxy-phenylalanine
ECM	Extra-cellular matrix
FDM	Fused deposition modeling
FL	Fluorescence

FTIR	Fourier transform infra-red
H1-H1000	Concentration of heparin from 1-1000 units/ml
HA587	Human soluble elastin
HAAE-1	Human aortic endothelial cell line
HA-VSMC	Human aortic smooth muscle cell line
HEK	Human epidermal keratinocyte
HT1080	Human fibrosarcoma epithelial-like cell line
HTS	Height/topographic scan
LASER	Light amplification by stimulated emission of radiation
LB	Langmuir-blodgett
LFM	Lateral force mode
MDW	Matrix-assisted pulsed laser evaporation direct write
Mefp	Mytilus edulis foot protein
MTT	(3-[4,5-dimethyl-2-thiazol]-2,5-diphenyl-2H-tetrazolium bromide)
ORMOCER	Organically modified ceramics
OVR	Overlay
PEG	Poly-ethylene glycol
PIT	Piezo-electric ink-jet technology
PTFE	Polytetrafluoroethylene

RP	Rapid prototyping
SEM	Scanning electron microscopy
SLA	Stereolithography
SLS	Selective laser sintering
SR499	Ethoxylated (6) trimethylolpropane triacrylate
SR610	PEG (600) diacrylate
TORP	Total ossicular replacement prosthesis
UV	Ultra-violet
V1-V1000	Concentration of VEGF from 1-1000 ng/ml
VEGF	Vascular endothelial growth-factor
WP	Wave-plate
XPS	X-ray photoelectron spectroscopy
XRD	X-ray diffraction

CHAPTER 1

INTRODUCTION

This dissertation establishes novel CAD/CAM rapid prototyping techniques for processing advanced biomaterials for a variety of biomedical applications. The first chapter highlights the various aspects involved in understanding the increasing demands for development of novel technologies for biomedical applications.

1.1 Rapid Prototyping (RP)

Rapid prototyping (RP) is a material processing technology originally developed approximately thirty years ago for the preparation of machine tool prototypes.[1] It is a process planning technology that offers rapid production with design verification, automation, manufacturability, reliability, iterations, visualization, and allowing just in time manufacture. In conventional rapid prototyping, three-dimensional structures are created by selectively joining materials in an additive manner, or subtraction/removal of materials from stock (machining). These technologies include processing solids, liquids, or powders.

Solid-based rapid prototyping techniques involve the cutting and joining or fusing/solidifying or melting of extruded material (in the form of wire, roll, laminates, and pellets).[2] Fused deposition modeling (FDM) is a widely used solid-based rapid prototyping technique where the material is melted and extruded from the head (Figure 1) into thin filaments of liquid, pastes, melts, or reactive materials on a mobile platform, which can operate along X-, Y-, and Z- planes. The filaments fuse together upon cooling with the previously deposited layer. Advantages of the FDM process includes rapid building of bottle-like and hollow parts, costs, non-toxicity, and easy handling. Disadvantages of fused deposition modeling include high operating temperatures that preclude patterning of many biological materials due to thermal denaturation.[3] In addition, materials prepared using this process exhibit very high porosities and poor mechanical properties. Accuracy of the build is very low and it is difficult to build parts with complicated details. The FDM technology is marketed exclusively by Stratasys Inc.[4] and often used to process polycarbonate materials, polyphenylsulfones and waxes.

Liquid-based techniques involve selective solidification of material in the liquid phase. Stereolithography (SLA) is a liquid-based rapid prototyping technique where a photocurable resin is selectively solidified upon exposure to ultraviolet laser radiation. The laser polymerizes the liquid resin layer to generate a layer of solidified material. Subsequent layers are selectively cured and this layer-by-layer buildup process is repeated until the desired three-dimensional (3D) structure is obtained. The structure is then removed from the liquid reservoir, baked, and cleaned. In this technique, the interplay between encoder resolution, table step height, and laser spot size often determine the resolution of structures fabricated. Advantages of this process include good surface finish, easy curing, and relatively

high resolutions of end product. Compensation for shrinkage and changes in polymer properties are some issues associated with the process. High operating temperatures and laser power/wavelengths that damage biological components reduce applicability of this process.[6-7] In addition, breakdown products, diluents, and dispersants used in stereolithography may not be suitable for many medical and biological applications.

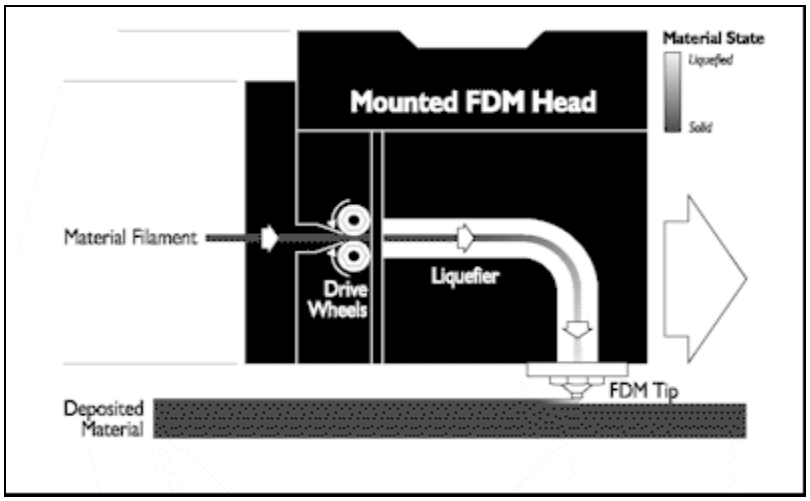

Figure 1: Schematic of the fused deposition modeling (FDM) process.[5]

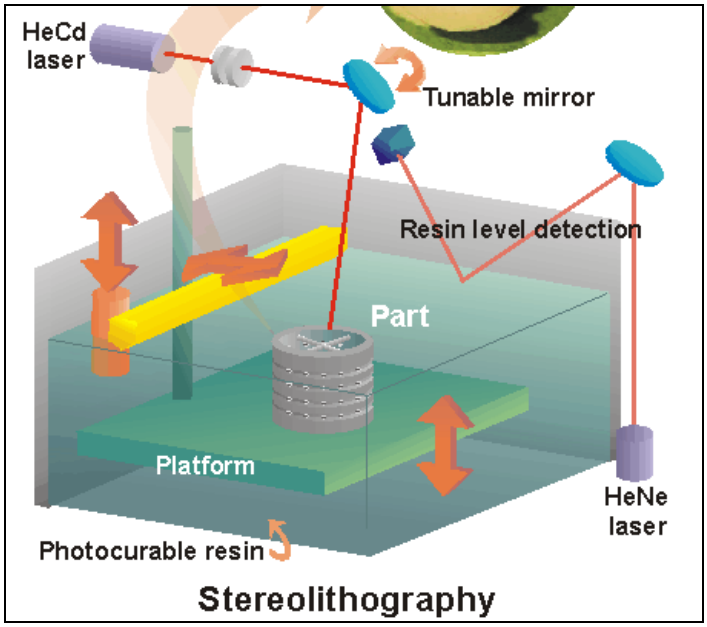

Figure 2: Schematic of the stereolithography (SLA) process.[8]

Powder-based rapid prototyping techniques such as selective laser sintering (SLS) involve selective melting of powders or granules in a powder bed using a high power laser. In SLS prior to laser exposure, the powder is annealed to a temperature close to its transition melting point, such that only a small increase in temperature is required to cause localized melting. A three-dimensional object is formed by moving the height-adjustable table containing the powder bed after processing of each layer (Figure 3). This technique has been utilized to fabricate complex porous ceramic matrices suitable for implantation in a bone defect.[9] Many other materials, including nylon, polystyrene, and titanium, may also be processed using this technique. The technique has the capability to process 3D structures with complex features, including overhangs and undercuts. However, materials processed using selective laser sintering generally exhibit high porosity and surface roughness, which may preclude its use in many medical applications. Although, process parameters such as the laser spot size, laser energy, scan speed, and bed temperature can be controlled to determine the resulting porosity and surface roughness of the final 3D structure.

A comparative summary of standard rapid prototyping methods for biomedical applications have been previously reported by Boland *et al.*[11] Conventional rapid prototyping techniques have serious limitations towards developing and processing materials for growing needs in the biomedical field. High temperature of processing, poor accuracy and resolutions and other limitations preclude the use of conventional approaches for microfabrication of biomaterials. The main goal of this dissertation was to develop novel CAD/CAM processing techniques for microfabrication of biomaterials for various medical applications. In current rapidly growing biomedical fields, efficient and controlled processing of organic and inorganic biological materials can be seen as an imminent requirement.

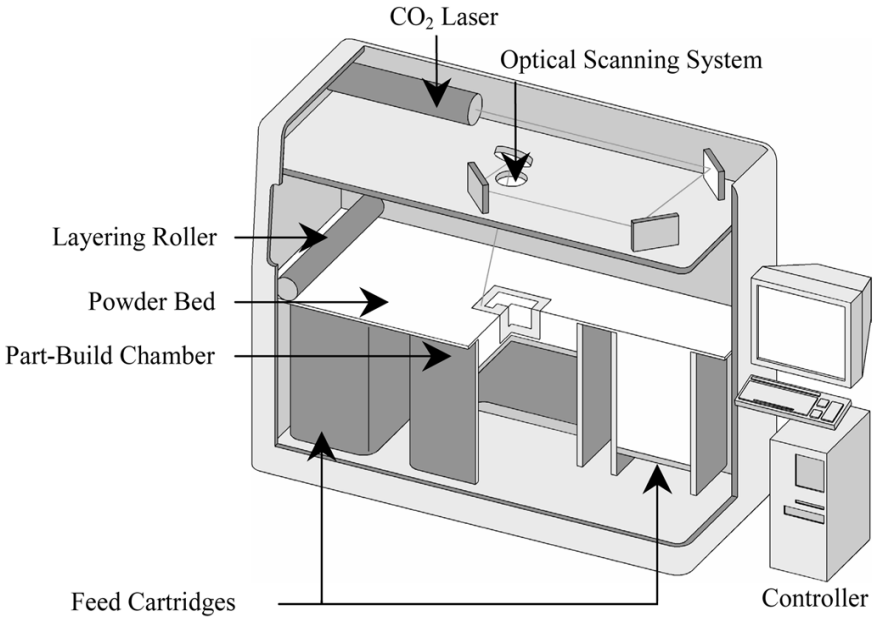

Figure 3: Schematic of the selective laser sintering (SLS) process.[10]

1.2 Laser Based Technology

Free form fabrication of microstructured medical devices presents great growth potential in a growing medical device market. In developing laser based techniques for rapid prototyping, it is critical to establish the structure-property correlation during laser interaction with material. As shown in Figure 4, various possible events (release of photons, charged particles, vapor, absorption, spallation, etc.) occur during laser interaction with a solid.

Absorption of photons causes various thermal and athermal reactions in materials. In *photothermal interactions*, the incident light energy is absorbed and transformed to heat energy. The absorption occurs according to the exponential absorption law: Light intensity at depth x, $I(x) = I_o e^{-ax}$; where 'a' is the absorption coefficient of material. Athermal interactions include *photoelectrical, photochemical,* and *photophysical* effects.[13] *Photoelectrical effects* occur with the emission of electrons and ionized species with sufficient laser energy. Laser lights can also be used to modify the electric fields in the interaction zone. *Photochemical effects* cause alteration of chemical bonds by absorption of photons. Bonds can be formed (*photochemical curing*) or broken (*micromachining and photochemical disruption*). *Photophysical effects* involve the removal of material by direct cleaving of molecular bonds at high laser energy. Processes such as *photoablation, plasma-induced ablation*, and *photodisruption* are *photophysical* effects, where material is removed by breaking molecular bonds, by the formation of ionizing species (plasma), and by mechanical forces, respectively.[14]

Laser-induced effects such as *photothermal ablation, photovaporization, photomelting,* are often used in biomedical applications such as tissue ablation, atherectomy,

disposable medical devices, stents, catheter drilling, retinal attachment, engraving and texturing.[12-13] Lasers have found many medical uses due to their ability to direct high energy radiation of a single wavelength onto a focused location. Use of lasers to process biomaterials may transfer directly into clinical setting. In developing laser-based rapid prototyping tools for biomedical applications, it is vital to understand the laser interaction with biomaterials.

1.3 Two-photon Polymerization (2PP)

Two photon polymerization (2PP) is an additive process that involves both temporal and spatial overlap of photons to induce chemical reactions between starter molecules and monomers within a transparent matrix.[15] Near simultaneous absorption of two photons creates a so-called virtual state for several femtoseconds. This electronic excitation is analogous to electronic excitation by a single photon with a much higher energy. When the two photons are of different wavelengths, the process is referred to as non-degenerate two photon absorption.[16] When the two photons are of identical wavelengths, the process is referred to as degenerate two photon absorption. The two photon absorption process exhibits a non-linear (quadratic) dependence on the incident intensity. Negligible absorption occurs except in the immediate vicinity of the focal volume of the light beam. Hence, high resolution polymerization is achievable using appropriate optics. Photonic crystals, micro-rotors, microcapsules, micro-pillars, mechanical devices (tubes, oscillators, gear wheels, chains) are some of the many structures that have been fabricated by this technique.[17-19]

Amorphous organic-inorganic hybrid materials (organically modified ceramics, or Ormocer®) and other photopolymers can be polymerized using this process with the use of appropriate initiator species. Ormocer® materials are prepared by sol-gel processes from liquid precursors, and contain organically modified silicon alkoxides, metal alkoxides, and organic monomers. Strong covalent bonds form between the ceramic and polymer moieties during the two photon induced polymerization reactions. The inorganic components (e.g., alkoxysilane precursors) crosslink and form inorganic silicon-oxygen-silicon networks through condensation of organically modified silicon alkoxides and controlled hydrolysis. The organic components (e.g., methacrylate groups) crosslink through light-, thermal-, or redox-initiated processes.[21] The crosslinking of both organic and inorganic components creates a three dimensional network, which prevents separation of the material into separate phases and provides Ormocer® material with exceptional chemical and thermal stability. For example, Ormocer® materials exhibit duroplastic behavior on heating; they remain stable to 350 °C in an oxygen atmosphere and 415 °C in a nitrogen atmosphere.[22]

Development of 2PP as a novel rapid prototyping technology is presented in Chapter three. Applications in three-dimensional microstructured medical devices, scaffolds for tissue engineering, microneedles for drug delivery, and ossicular implants are discussed.

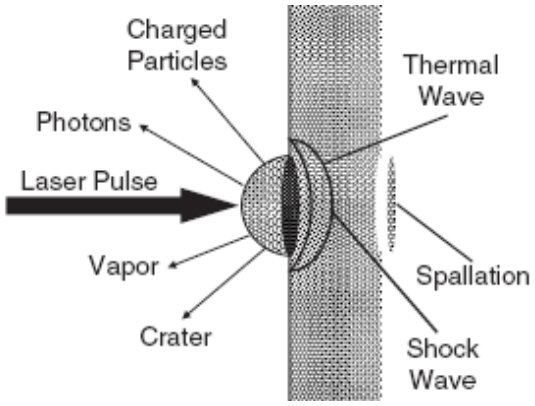

Figure 4: Schematic of possible events during laser interaction with a solid material.[12]

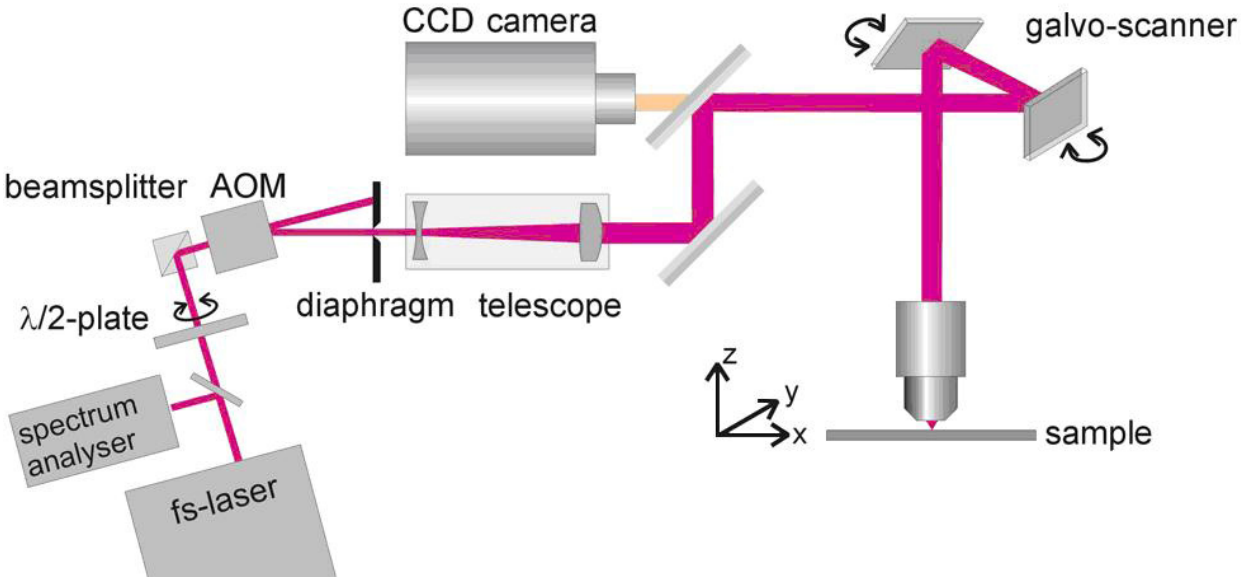

Figure 5: Schematic of the two-photon polymerization system.[18]

1.4 MAPLE Direct Write (MDW)

Two-dimensional patterning of a single cell-type has been demonstrated previously by various surface recognition techniques. In a biomimetic approach Garcia *et al*.[23] demonstrate that the cell adhesion, proliferation, and differentiation can be controlled by functionalizing the surface using RGD peptides. In another approach, laminar flow of the media in capillary systems has been used to create simple patterns of different types of "cells and proteins" within the same substrate.[24] Laborious steps are used to create elastomeric stencils using photoresists that are then used as masks to pattern cells and proteins.[25] Soft photolithographic methods such as microcontact printing, which involve the fabrication of stamps using masking techniques, have been demonstrated to create cell and protein patterns.[26, 27] Rapid patterning techniques were proposed by using dielectrophoretic force to transfer cells from the electrode to a glass substrate, however with relatively low resolutions and accuracy.[28]

Matrix-assisted pulsed laser evaporation direct-write (MDW) was originally developed to satisfy the need for conformal and mesoscopic passive electronic components.[29] As in a typewriter ribbon, the material to be transferred is solvated and evenly coated on the ribbon surface. The incident light is absorbed by the solvent, and the solute material is driven forward to a receiving substrate. The resolution and pattern is controlled by distance between the ribbon and substrate, laser energy-density, spot-size, and translation speed of the stage. This process (Figure 6) has recently been extended to soft and biological materials including a variety of polymers, biomolecules, and viable cells. Using this process various lines of viable cells have been generated into mesoscopic patterns onto a variety of receiving substrates.[30, 31] Such a technique may allow integration of cell into the matrix while the

construct is being created. The development of MDW as a novel rapid prototyping tool for regenerative medicine is presented in detail in Chapter three.

1.5 CAD/CAM Laser Micromachining (CLM)

Laser micromachining of materials have been previously employed as a rapid prototyping technique for developing microfluidic devices with channel features of ~ 10 μm with relative ease.[32] Micromachining of various materials including poly(dimethylsiloxane), GaN, SiC, fused silica, quartz, sapphire, have been studied for developing microchips, intracortical probes[33], microstructure parts[34], hybrid processing[35], and surface modifications[36]. Extending MDW technology to higher laser power allows CAD/CAM laser micromachining capabilities using previous setup (Figure 6). The micropositioning system is integrated with the CAD model (3D geometry) and laser process parameters (laser energy density, laser spot-size, laser pulse frequency, remote trigger) to allow efficient processing capabilities. Laser interaction with a material is unique and thus the processing parameters and integration needs to be developed for each new material.

One possible application for laser micromachining of biomaterials is in tissue engineering. 2D silicon micromachining (by etching) has been previously studied for developing vascular channels.[37] CAD/CAM laser micromachining of biomaterials may allow better control for a 3D geometry in the micron scale. CLM may allow development of differential adherent structures with programmed dimensions and required functionality. The development of CAD/CAM laser micromachining (CLM) for tissue engineering applications is presented in detail in Chapter three.

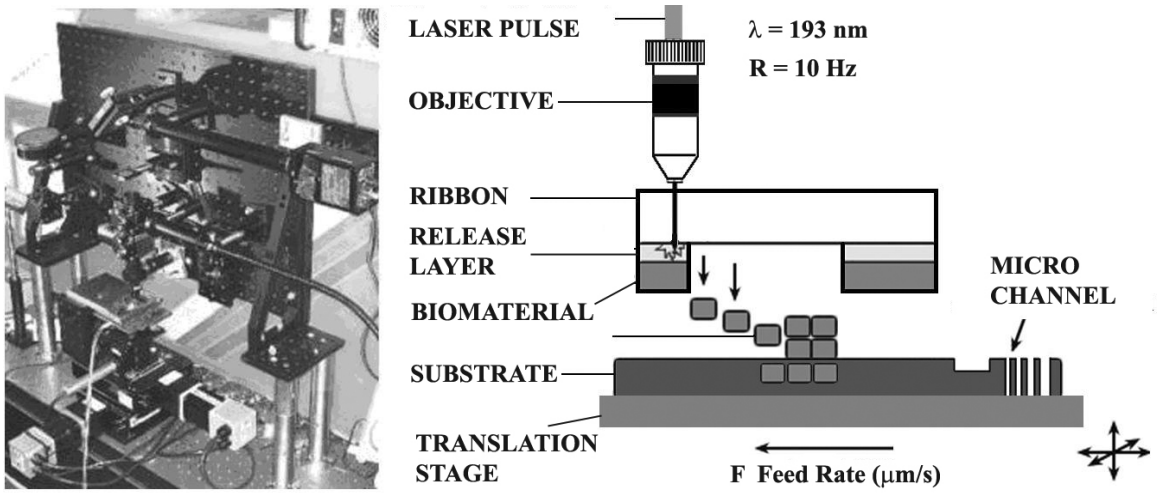

Figure 6: Experimental setup and schematic of the MDW and CLM process.[30]

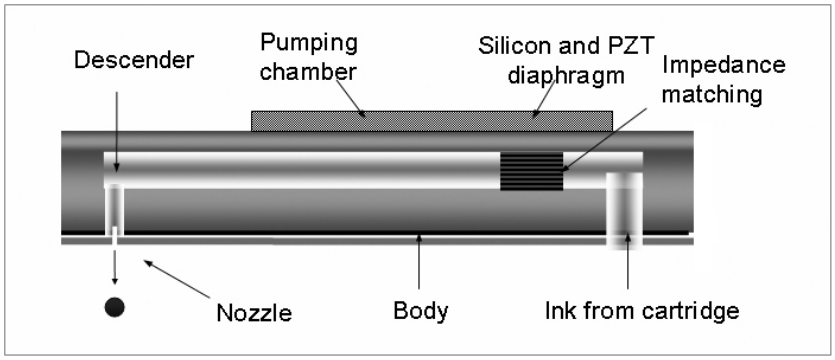

Figure 7: Schematic of the piezoelectric print-head.[45]

1.6 Piezoelectric Ink-jet Technology (PIT)

One possible application for rapid prototyping technology is microscale processing of biomaterials. CAD/CAM rapid prototyping techniques such as ink jet printing may allow for high-throughput production of patterned multiplexed biological materials without the use of masks, stamps, ribbons, or other expensive processing equipment.[38, 39] The general principle of operation involves the creation of a rapidly moving stream of fluid that passes through a small nozzle. Ink-jet technology was initially developed as a thermal non-contact printing process, where drops were created by thermal stimulus.[40, 41] In thermal printing, a resistive element is used to heat the fluid creating a bubble that forces the ink out of the nozzle. A similar process has been utilized for printing proteins and various living cells.[42-44] However, the thermal stimulus does not entirely preclude damage to biological materials.

In athermal ink-jet printing technology, syringe-solenoid and piezoelectric systems have been previously developed.[46] In a solenoid system, a syringe pump is used with a microsolenoid actuator to create controlled fluid flow across an orifice. However, high internal pressures can result in damage to the print-head. In a piezoelectric ink-jet system (Figure 7), piezoelectric crystals are used to create mechanical vibrations to control fluid flow via the nozzle by the application of external voltage. Piezoelectric printers are categorized based on the deformation mode such as squeeze, bend, push and shear modes in the piezoelectric crystal.[47] Ink-jet printers can dispense a wide range of volumes from picoliters to microliters with a firing frequency between 5 – 12 kHz and resolutions greater in tens of micrometers. Resolution of the printed features are dependent on various factors including fluid viscosity, surface tension, fluid-mass velocity, nozzle size, droplet size, and

lateral resolution of the printer head. The development of piezoelectric ink-jet technology as a rapid prototyping tool for biomedical applications is presented in Chapter three.

In a rapidly growing field of biomedical engineering, there is a rising need for novel CAD/CAM rapid prototyping technology. The following sections ahead describe the focus areas in biomedical engineering where novel RP techniques may provide vital, innovative, and enhanced solutions.

1.7 Microneedles for Next-generation Drug Administration

Microneedles provide a unique approach for transdermal drug delivery of DNA- and protein-based pharmacologic agents.[48]. Many of these novel agents cannot be administered orally or transdermally, because they may be metabolized by the liver, intestine, kidneys, or lungs before reaching systemic circulation. These agents may be administered intravenously to avoid diffusional/enzymatic barriers and provide complete and instantaneous absorption. Intravenous administration of pharmacologic agents usually involves the use of hypodermic needles, which provide injection directly into blood vessels, muscles, or subdermal fat.[49] These conventional needles are limited by traditional manufacturing processes to outer diameters of ~ 300 μm and wall thicknesses of 75 μm. In addition, use of hypodermic needles involves pain, trauma at the injection site, medical expertise to administer the injection, and difficulty in providing sustained/controlled delivery of the agent.

One emerging option for delivery of pharmacologic agents involves the use of microneedles. The use of microneedles for drug delivery was proposed in the 1970s; however, these devices have been fabricated using novel microfabrication tools only within the past decade.[50] These devices, which can take the shape of lancets, thorns, or miniaturized hypodermic needles, contain at least one dimension that is less than 500 μm in length. By reducing the needle dimensions, pain to the patient and damage at the injection site may be reduced. In addition, administration of pharmacologic agents via microneedles requires no specialized medical training; the microneedles may be utilized in a similar manner to conventional transdermal patches. The amount and rate of drug delivery can be precisely controlled. For example, hollow microneedles may allow diffusion- or pressure-driven transport of pharmacologic agents through the needle bore to be adjusted over an extended period of time. By reversing the valve direction, pumps used for drug delivery through the microneedle can also be used for fluid extraction.[51, 52]

Microneedles must meet several requirements in order to be effective for drug delivery. Microneedles for drug delivery must penetrate the outermost 15 μm of epidermis, known as the stratum corneum layer, which contains keratinized dead cells and serves as the highest barrier against drug transport through the skin.[53] Microneedle shafts must be greater than 100 μm in length and 300–400 μm in length, since mammalian stratum corneum is flexible and variable in thickness. In addition, microneedles with high aspect ratios and small radii of curvature require lower forces for skin penetration.[54] The microneedles must also not fracture during skin penetration. The ratio between microneedle fracture and skin insertion force is highest for needles exhibiting large wall angles, large wall thicknesses, and small tip radii. Finally, arrays of microneedles provide injection or extraction over a wider area and at

higher rates than solitary needles. Having several needles provides redundancy in case individual needles are obstructed or fractured during insertion.[55] In addition, arrays of needles possess a greater possibility of directly reaching dermal blood vessels for extraction. Microneedle arrays are also less prone to fracture if exposed to shear force, because the shear force is distributed over a wider area.[56]

Several investigators have demonstrated individual microneedles and microneedle arrays using conventional microelectronics fabrication technologies, including chemical isotropic etching, injection molding, reactive ion etching, surface micromachining, bulk micromachining, polysilicon micromolding, and lithography–electroforming–replication (LIGA) techniques.[57-61] These techniques have inherent limitations in terms of fabricating array structures with high microneedle densities or large microneedle wall thicknesses. As a result, conventional microneedle devices have yet to find widespread clinical use.

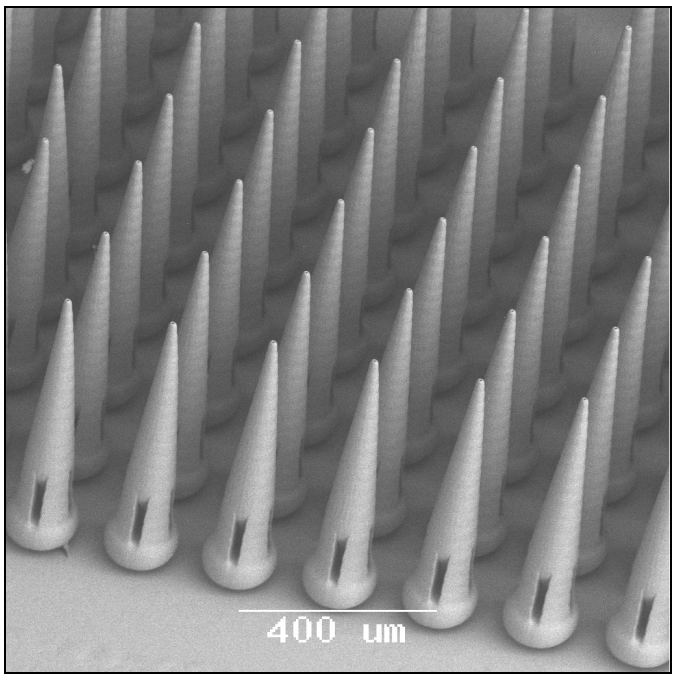

Figure 8: Scanning electron micrograph of an array of polymeric microneedles.[11]

1.8 Ossicular Replacement Prosthesis

In human ear, the malleus, incus, and stapes bones allow transmission of sounds from the tympanic membrane to the inner ear. Diseases of the middle ear may cause discontinuity or fixation of the ossicles, which results in conductive hearing loss. For example, ossicular damage may result from chronic otitis media, cholesteatoma, trauma, neoplasia, or congenital malformation.[62, 63] Fixation of the ossicular chain may result from tympanosclerosis, from malleus head ankylosis, or from otosclerosis. Over the last 40 years, otologists have sought alternatives in materials and designs for ossicular reconstruction prostheses to provide favorable sound transmission and tissue compatibility.[64-66] Middle ear implants must also be able to perform microscale movements between the tympanic membrane and the inner ear. Traditional methods for restoring sound conduction in the middle ear involve the use of the remaining ossicles.[67] A commonly used material in ossicular replacement procedures is the patient's own incus bone. However, autograft materials are not always available in cases of chronic middle ear disease. Additional concerns include high operative times and loss of structural rigidity.

Synthetic materials such as polyethylene, polytetrafluoroethylene (PTFE), and Proplast (PTFE–carbon composite) pistons have been employed in middle ear reconstruction.[68] These materials have shown extrusion, migration, and cytotoxicity. Metals including titanium and gold have also been attempted for prosthesis replacement.[69-74] Titanium prostheses have demonstrated cytocompatibility, sound conduction, and mechanical properties. However, recent studies have shown that cartilage grafts are required to cover the head plate of the prosthesis to prevent prosthesis extrusion through the tympanic membrane. Bioactive materials (such as *Bioglass, Ceravital, hydroxyapatite*) have also been employed

due to low extrusion.[75-80] However, concerns remain with brittleness, difficulty in shaping the prostheses, and mechanical instability.

Novel materials and prostheses that provide improved sound transmission for longer periods of time are demanded by patients and otologic surgeons. These materials must demonstrate appropriate stiffness, cytocompatibility, sound conduction, and ease of handling.[81, 82] Conventional technologies for mass-produced implants do not adequately take individual patient anatomy into consideration. Development of patient-specific implants by novel rapid prototyping technology may allow rapid iterations with better compatibility and lowered costs of development.

1.9 Tissue Engineering and Regenerative Medicine

Tissue substitutes for use in repairing acute injury, chronic disease, or congenital defects may be created in different ways.[83, 84] In autograft tissue transplantation, tissue is relocated from one site to another within the same person. The use of autograft tissue is associated with many problems, including limited availability of tissue. Additionally, surgery at the donor tissue site can cause infection, inflammation, chronic pain, and the need for additional surgery. In allograft tissue transplantation, tissue is transferred from one person to another. Twenty five tissues and organs, including cartilage, cornea, heart, kidney, liver, lung, and pancreas, have been transplanted between different people. However, allograft transplantation is also fraught with many problems, with limited availability being the primary issue. There are currently 80,000 people on organ waiting lists in the United States, and over 10,000 people have died over the last five years waiting for organs.[85] In addition,

the recipient's immune system generates acute vascular rejection and chronic rejection processes that break down transplanted allograft tissue in hours, days, weeks, months, and years after implantation.[86] The immunosuppressive therapy used to counteract the rejection process may itself lead to tumor formation. There is also the risk of infection transmission from allograft organ donor to allograft organ recipient. For example, it has been estimated that the possibility of HIV transmission with allograft bone transplant is one case in 1.6 million.[87] One case of hepatitis B transmission and three cases of hepatitis C transmission have been correlated with allograft transplantation.[88]

The continuing limitations of natural graft therapies and the growing demand for tissue substitutes have led to the growth of a field known as tissue engineering.[89] Tissue engineering or regenerative medicine may be defined as the use of living cells that are manipulated genetically or through their environment with bioresorbable materials as matrix that help guide development to biologically functional tissue substitutes for implantation into the body. Construct technology for tissue engineering is generally approached in either a cell-seeded method using various types of bioresorbable matrix materials or a cell-mediated self-assembly technology.[90] In the first approach, the cell-seeded structures are often placed in bioreactors that provide nutrients and allow cells to multiply within the scaffold, and implanted in the body so that it will resume normal function. Unfortunately, three-dimensional scaffold seeding is very difficult because many cells do not exhibit sufficient multiplication within in vitro bioreactors.

Conventional scaffold technology does not allow penetration of cells into the 3D matrix. Solvent-based direct writing techniques for making organic or cellular films (e.g., ink jetting, Langmuir-Blodgett dip coating, and pin arraying) have recently been used to fabricate

2D and 3D cell-seeded scaffolds for use in tissue engineering. Langmuir-Blodgett (L-B) coatings are capable of creating multilayered cell-seeded films; however, increasing L-B film thickness requires repeating the coating procedure for each additional layer. L-B coatings are also limited in the choice of materials used to create these films. Furthermore, the solvent containing the material of interest may dissolve any underlying layers. These techniques also have limitations in resolution, scale up, speed, and quality.

Selection of bio materials is a critical step in developing 3D tissue constructs. Traditional scaffold materials include natural (*Collagen, extraceullar matrix proteins*) and synthetic degradable organic polymers such as PCL (*poly-caprolactone*), PLA (*poly-lactic acid*), PGA (*poly-glycolic acid*), hydrogels and other non-biodegradable materials. Inorganic materials such as bioceramics (*hydroxyapatite*) are known to be osteoconductive and offer excellent structural integrity with varying bioresorbability, both of which are vital for any tissue construct.[91, 92] Some important considerations of scaffold biomaterials include mechanical properties, structural integrity, ease-of handling/processing, cytotoxicity, shelf-life, and bioresorbability.[93]

In developing novel tissue engineering techniques, it may be significant to have control over cellular penetration, neo-vasculature, concentration gradients of growth factors and various cells, and integration of microstructures/biomaterials. These factors combined with a CAD/CAM feature for the macrostructure may be imperative to provide sufficient leverage and interest over conventional technologies for developing improved tissue constructs.

Table 1. List of key factors when considering a novel tissue engineering approach.[89-94]

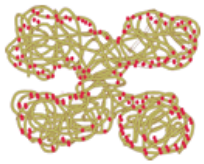	• Extent of distribution and penetration (3D) of cell into scaffold matrix material. • Conventional methods follow a cell-seeded self-assembly and may not allow control over cell-penetration.
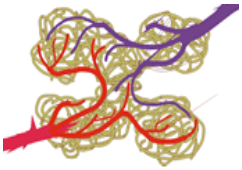	• Vasculature to nourish the cells in the interior of the scaffold. • Variable porosity in the scaffold-matrix material may allow neovascularization.
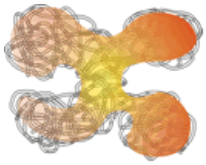	• Concentration gradients of growth factors, e.g. VEGF may be required to facilitate appropriate cellular chemotactic responses and functional differentiations. • Concentration gradients of growth factors may also optimize cell-locomotion and speed-up angiogenesis.
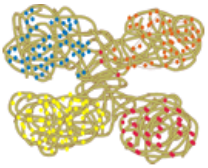	• Incorporation of spatial control over cellular heterogeneity. • Cellular heterogeneity may vary depending on the target tissue (may include endothelial, epithelial, muscle cells, nerve cells, cartilage, tendon, bone cells, etc.).
	• Integration of different (organic/inorganic) materials into one scaffold. • Control over material microstructure may allow mechanical and functional versatility within the construct.

**Images incorporated from.*[94]

Tissue engineering of the cardiovascular system may be one of the most challenging areas in regenerative medicine. In the past few years, several efforts in engineering blood vessel substitutes have been made.[95] Autologous endothelial cells derived from veins have been used on scaffolds derived from polycaprolactone-polylactic acid (PCL-PLA) and polyglycolic acid (PGA) copolymers and implanted in patients with good short-term results.[96] Smooth muscle cells and endothelial cells derived from veins, arteries, omenal fat, and subcutaneous fat have been seeded (monolayer) on tubular polyglycolic acid (PGA) scaffold to develop pulmonary artery conduits.[97] Vascular networks have also been developed under flow conditions by seeding monolayer bovine vascular cells on tubular polymeric grafts.[98, 99] De-cellularized biologic ECM from human fibroblasts have also been employed as scaffold material for development of vascular networks.[100]

A schematic of the human artery is shown in Figure 9. The various concentric layers from the center include *tunica intima, elastin, tunica media, tunica externa, and serosa*. *Tunica intima* contains a thin layer of aortic endothelial cells. *Tunica media* is a thick layer containing aortic smooth muscle cells. *Tunica externa* contains fibrous connective tissue and the external layer of *serosa* contains a thin film of epithelial cells. Thus, it is important to realize that conventional techniques that have employed cell-seeding on a pre-formed polymeric conduit to facilitate growth of vascular networks may not entirely allow control over the various layers and cellular penetration. Novel rapid prototyping techniques with microscale control over the various layers and vasculature geometry may show to be promising in engineering vascular networks.

Tissue engineering of skeletal muscle and neural tissues are also equally challenging and important. In nerve guides or guidance channels, direct axons sprouting from the proximal nerve end provide a conduit from secreted growth factors and reduce scar tissue. Neurons patterned into nerve fascicles or bundles that match with the served nerve stumps can potentially aid in the regeneration of damaged peripheral nerves.[102, 103]

Each tissue and organ in the human body has their own unique geometry which varies in size between individuals undermines the applicability of most conventional fabrication techniques. Conventional techniques have several issues with inadvertent residual solvents, high dependency and sensitivity to manual skills, experiences and procedures, poor consistency and poor repeatability. Additionally, they offer poor flexibility in producing complex macro-architectures. Novel tissue engineering approaches are required to address issues facing conventional techniques and permit scale-up and speed of development of functional three-dimensional networks to replace failed tissue.

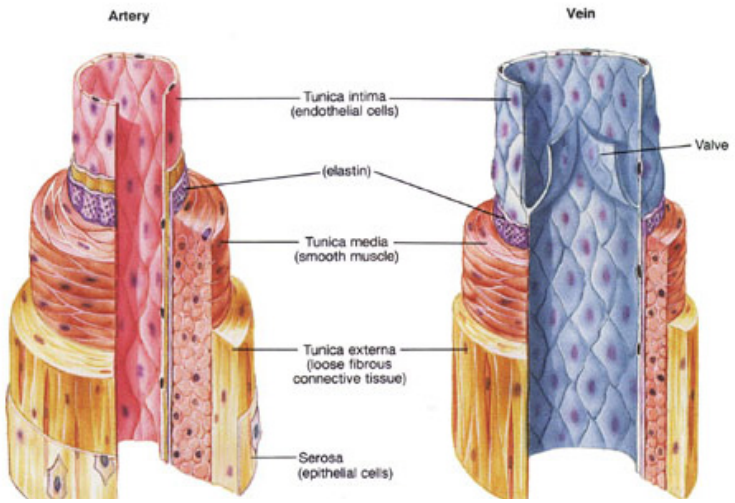

Figure 9: Schematic of the various layers present in a human artery and vein.[101]

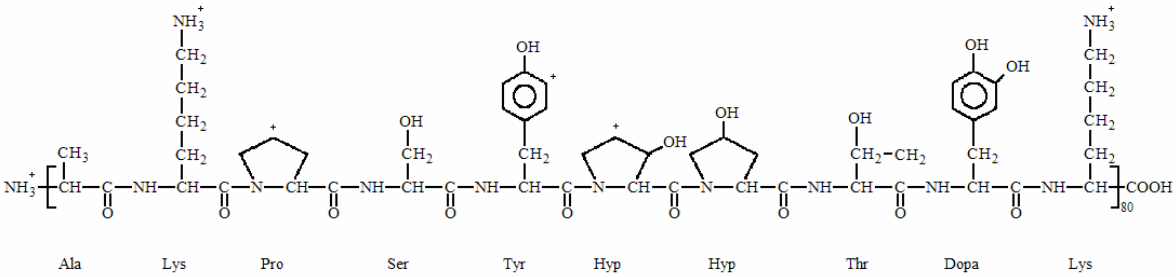

Figure 10. Repeating unit in *Mytilus edulis* foot protein-1.[116]

1.10 Bioadhesives and Wound-Closures

Conventional wound closure techniques include use of sutures, staples, and pins. Closure of soft organs such as kidneys, blood vessels, and tendons remain quite difficult using conventional techniques. An alternative must allow rapid curing and hold tissue together until the defect is healed. In addition, the adhesive must be biodegradable, non-immunogenic, and non-toxic. Tissue sealants derived from cyanoacrylate esters (*Dermabond®, Indermil®, Nexaband®, and Vetbond®*) are often used in repairing Achilles tendons, tooth enamel, corneas, and skin.[104-106] However, these volatile cyanocrylates have demonstrated dose-dependent toxicity, carcinogenic properties and may result in skin allergies and respiratory ailments.[107-109] Formaldehyde, a common constituent of synthetic adhesives, has been associated with nasopharyngeal cancer, leukemia, and sinonasal adenocarcinoma.. Fibrin sealants (*derived from human blood coagulation factors*) have also been considered for use in a variety of surgical and endoscopic applications in soft tissues.[110] However, fibrin adhesive is ineffective for supporting large tensile load and infections may be transmitted from the blood source. Next-generation bioadhesives are currently being developed to preserve the advantages of conventional cyanoacrylate adhesives, while lowering the exposure hazards and illness-associated with these materials.

Marine mussel adhesive protein is a formaldehyde-free natural adhesive that has gained great interest in the scientific community.[111-115] Mussels are sedentary mollusks that inhabit the turbulent environment of the intertidal zone; they attach to underwater surfaces by means of a byssus. This attachment plaque connects the mussel “foot” with the underwater surface, and contains a bundle of 5–50 mm long silky threads. Each thread consists of a

fibrous collagenous core coated with mussel adhesive proteins. Each mussel species has developed unique adhesive proteins.

Mytilus edulis, a blue mussel used in this study produces five unique proteins, which are referred to as *Mytilus edulis* foot protein-1 (Mefp-1) to *Mytilus edulis* foot protein-5 (Mefp-5).[116-119] *Mytilus edulis* foot protein-1, a ~110 kDa material contains roughly 20 % lysine; 15% 3,4-dihydroxyphenylalanine (L-DOPA); and 30-50% hydroxyproline, threonine, and tyrosine. These amino acids form hexapeptide and decapeptide (e.g., (Ala-Lys-Pro-Ser-(Tyr/DOPA)-Hyp-Hyp-Thr-DOPA-Lys)) motifs that that may repeat up to eighty times within the mussel adhesive protein structure. The highly conserved Mefp-1 structure exhibits an open conformation with little secondary structure.

Mussel adhesive proteins provide high strength adhesion to a wide variety of metals and polymers in aqueous environments, and may be an ideal replacement for synthetic adhesives in several technological applications. DOPA (*3,4-dihydroxyphenlylalanine*) is a common constituent of the *Mytilus edulis* and is distributed with the mussel proteins along the mussel plaque and bysall threads.[120] DOPA is also thought to drive the adhesion of the mussel plaque to the interfacem by a metal-mediated catechol complexation process.[121-123] The phenolic hydroxyl groups in DOPA can form strong hydrogen bonds with a variety of substrates and chelate with metal ions. These interactions allow Mefp-1 to adsorb to several classes of materials, including pure metals, metal oxides, polymers, and glasses.[124] In addition, the DOPA group can be oxidized by dissolved oxygen, chemical oxidizing reagents, alkaline environments (>8.5), or enzymes (e.g., catechol oxidase) to form orthoquinones. Orthoquinone groups have shown to react with lysine residues in neighboring Mefp chains to increase Mefp crosslinking. The resulting water-insoluble, three-dimensional

networks exhibit extremely high cohesive strength, water impermeability, and multilayer morphologies.[125]

Unfortunately, mussel adhesive proteins can only be obtained from mussels in very small quantities; 10,000 mussels are needed to extract just one gram of protein. As a result, isolation of mussel adhesive proteins are prohibitively expensive.[111-115] Recombinant proteins, synthetic polypeptides, and modified polymeric systems have been developed that reproduce the properties of natural mussel adhesive proteins.[126-128] Another approach may involve the use of novel techniques to process naturally derived mussel adhesive protein in an efficient and economical manner.

In a rapidly growing field of biomedical engineering there is an imminent need for novel CAD/CAM rapid prototyping technology that offer higher degrees of freedom than conventional technology. This dissertation details the development of novel CAD/CAM rapid prototyping technologies for various biomedical applications. Ahead, chapter two presents the materials and methods used in developing these technologies. Chapter three presents the results and discussion from the various research and development steps involved. The final chapter presents a summary of the developments and steps for future directions.

CHAPTER 2

MATERIALS AND METHODS

2.1 2PP – TWO-PHOTON POLYMERIZATION

The various materials and methodologies used in the development of two-photon polymerization (2PP) for biomedical applications are described ahead.

2.1.1 Photopolymers

Three different classes of low-shrinkage UV-sensitive photopolymers were used in this study. *Ormocomp® or Ormocer®* (Fraunhofer-Institut für Silicatforschung, Wurzburg, Germany) is a polymer-ceramic hybrid material with refractive index of 1.520 at 589 nm.[129] SR610 or 'PEG (600) diacrylate' (*Sartomer, Exton, PA, USA*) is a water-soluble monomer with refractive index of 1.468.[130] SR499 or 'ethoxylated(6) trimethylolpropane triacrylate' (*Sartomer, Exton, PA, USA*) is a trifunctional oligoether acrylate monomer with heat and abrasion resistance properties. 1.8% Irgacure® 369 (*Ciba Specialty Chemicals, Basel, Switzerland*) was used as the photoinitiator for the photopolymers.

2.1.2 CAD/CAM Microfabrication Setup

Figure 11 contains a schematic of the 2PP rapid prototyping setup. Titanium: sapphire oscillator (80fs, 94 MHz) was used as the laser source for two-photon polymerization. The laser was analyzed using a spectrum analyzer and tuned to operate at wavelength of 780 nm and power of approximately 450 mW. An acousto-optical-modulator (AOM) was used as a shutter to control the on-off state during fabrication. The λ/2 wave-plate (WP) was used in combination with the polarization-sensitive beam-splitter to control the average power of the input beam. The beam shape was expanded using a telescope lens setup and a high NA objective was used to tightly focus the beam within the liquid resin. A CCD camera was used to observe the two-photon polymerization process. A CAD module, a galvoscanner (*ScanLab AG, Munich, Germany*) and a micropositioning system (*Physik Instrumente GmbH, Karlsruhe, Germany*) was used to integrate the three-dimensional microfabrication process.

Polymerization of the liquid resin occurred along the trace of the laser focus. Post-fabrication, the non-irradiated resin was washed away using a 1:1 solution of 4-methyl-two-penthanone and isopropanol. Three-dimensional structures of Lego®-like scaffolds, microneedles and ossicular replacement prostheses (similar to TORP prosthesis (*Kurz Medical Inc., Dusslingen, Germany*)) were developed. Microneedles for transdermal administration were fabricated on laser perforated glass substrates with holes aligned to the microneedle channels. The prototypes were UV sterilized prior to characterization.

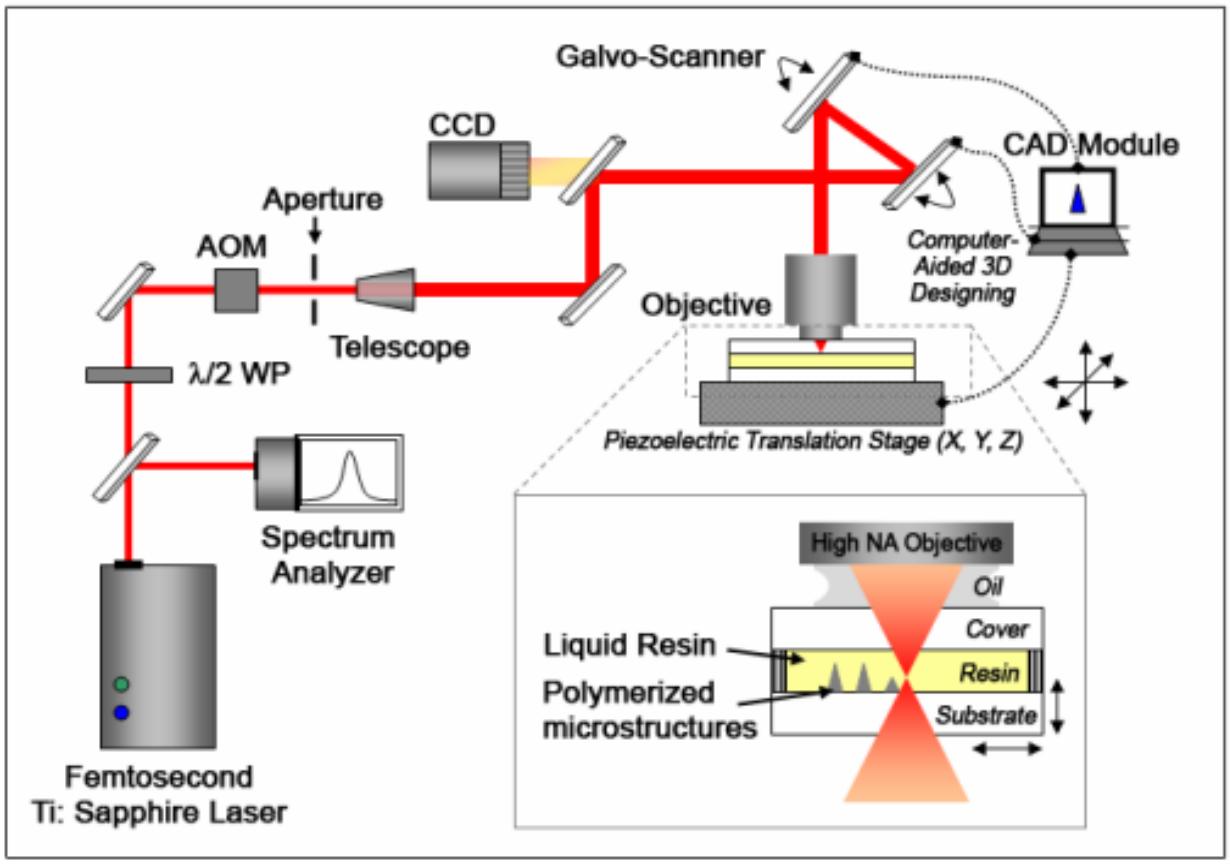

Figure 11. Schematic of the 2PP setup for microfabrication of medical devices.

2.1.3 Microscopy

A Nikon TE2000U (*Nikon, Melville, NY, USA*) inverted microscope equipped with an OrcaER camera was used to record DIC/fluorescence micrographs from the sectioned skin samples containing amino (PEG) quantum dots and fluorescein-biotin. Fluorescent-stained viable cells were examined with an LSM 510 confocal microscope (*Carl Zeiss Inc., Oberkochen, Germany*).

Scanning electron microscopy (SEM) was performed at the Analytical Instrumentation Facility (*NCSU-AIF, Raleigh, NC, USA*) using a *Hitachi S-3200 SEM* operating at 5 kV. Surface morphologies of the thin-film photopolymer substrates were examined using an Atomic Force Microscope operated in the tapping mode. The AFM images were recorded in the lateral force measurement mode and height mode (z-range of 25 nm) with an x-y scan range of 25 μm.

2.1.4 Nanoindentation Study

A Nano-Indenter XP instrument (*MTS Systems, Oak Ridge, TN, USA*) was used to carry out indentation tests in order to measure the elastic modulus (E) and the hardness (H) of the materials. Based on the maximum load applied, the indentation depth, and the slope of the unloading curve, the hardness and elastic modulus values under different maximum load values were calculated. Thin-film samples of the three photopolymers were prepared by sandwiching the polymers between two glass coverslips followed by UV curing for 30 minutes. Prior to indentation tests, one coverslip was carefully removed using X-Acto knife

to expose the film. Indentation tests were performed by the Nano-Indenter XP with a diamond Berkovich tip at nine sites in a clean area on the surface of each sample, which made a three-by-three matrix with 200 μm spacing. The indentation test consisted of ten maximum load cycles in each site, starting from 25 μN and up to 12.6 mN, doubling the load after each cycle. Each cycle consisted of five punches to the maximum load followed by immediate withdrawing, and then indented to the maximum load followed by 180 seconds holding before unloading. The same protocol was used to test the surface of the ear-prosthesis.

2.1.5 Cell-growth and Fluorescent Staining

Cell growth and viability studies were performed using B35 neuroblast-like cells for tissue engineering scaffolds and HT1080 epithelial-like cells for microneedle devices. B35 rat neuroblast clonal cells and HT1080 human fibrosarcoma epithelial-like cells were obtained from American Type Culture Collection (*Manassas, VA, USA*). They were sub-cultured in a culture medium, which contained Dulbecco's Modified Eagle Medium supplemented with 10% heat inactivated fetal bovine serum and 2 mM L-glutamine. The cells in media were stored in a 37 °C, 95% air, 5% CO_2 culture incubator, and re-suspended when the cultures reached 70% confluence. One milliliter of non-diluted extra-cellular matrix was spin-coated at 220 g for 5 minutes, and was then allowed to cross-link. The cells were then incubated on sterile polystyrene Petri dishes, which contained extra-cellular matrix, ECM® (*American Type Culture Collection, Manassas, VA, USA*) at one end and the Ormocer® structures at the other end.

Fluorescent and live/dead cell staining kits (*Biovision Inc., Mountain View, CA, USA*) were used to image the cells. The live/dead cell staining solution was pipetted over the extra-cellular matrix, and the solution was allowed to incubate for 15 minutes. Live-dye^{TM} stained living nuclei a green color, and propidium iodide caused dead cells to fluoresce a red color. The stained cells were viewed with an inverted optical microscope and a digital still camera with an epi-fluorescence attachment. For cytoskeletal staining, cells were first incubated in 0.2% Triton X-100 (*Sigma–Aldrich Company, St. Louis, MO, USA)* for 1 min at room temperature. The cells were then washed three times with phosphate buffered solution (PBS). Cells were then incubated with phalloidin (*Invitrogen Corporation, Eugene, OR, USA*) in PBS (diluted 1:150) for 20 min at room temperature. DAPI develops fluorescent complexes through intercalation and binding processes with adenine–thymine and adenine–uracil base pairs in double-stranded DNA. After washing three times with PBS, cells were incubated in a 10 mM solution of 40-6-diamidino-2-phenylindole (*Invitrogen Corp., Eugene, OR, USA*) for 5 minutes at room temperature. After incubation with the nuclear stain, the samples were washed twice with PBS and mounted on glass microscope slides with Fluoromount-G (*Southern Biotechnology Associates Inc., Birmingham, AL, USA*).

2.1.6 HEK Cytotoxicity Study

Thin-films of Ormocer®, SR610 and SR499 photopolymers and accompanying glass coverslips (as controls) were tested in triplicate for human epidermal keratinocyte (HEK) cytocompatibility. The polymers and controls were placed in plastic Petri dishes and exposed on both surfaces to UVB to sterilize. They were briefly rinsed in cell culture medium (KGM-

2) and placed in 6-well plates with 2 ml of medium per well. Each plate contained one polymer type and control (n=3 wells glass control coverslips; n=3 wells polymer). HEK (100,000) were seeded in each well in 2 ml of medium. The medium was changed after 24 hrs and the cells grown for an additional 48 hrs. The controls and the polymers were transferred to new 6-well plates and cell viability was determined by the MTT (3-[4,5-dimethyl-2-thiazol]-2,5-diphenyl-2H-tetrazolium bromide) assay. MTT medium (2 mL; 0.5 mg per ml KGM-2) was placed on the HEK for 3 hrs. The tetrazolium metabolized within the mitochondria of viable cells was extracted with isopropanol, the extracted solution in each well pipetted into a new 96-well plate (in duplicate), and absorbance determined spectrophotometrically at 550 nm in a microplate reader (*Multiskan RC, Labsystems, Helsinki, Finland*).

2.1.7 Microneedles Study

5X5 square arrays of 25 identical 500µm spaced needles were fabricated on glass cover slips by two photon polymerization of Ormocer® hybrid materials. A CAD program was used to modify the geometry of the microneedles to be fabricated. The fabrication time for a single microneedle was approximately two minutes. The average length of the microneedle design was 800µm with a base diameter of 150-300 µm. Ormocer® hollow microneedles of various aspect ratios such as 3:1, 3.5:1 and 4:1 were developed. Microneedles with off-center displacement of 0 µm, 1.4 µm, and 20.4 µm were also fabricated to study the processing and mechanical properties.

An ELF 3200 (*Bose Corporation, Minnetonka, MN*, *USA*) was used to study fracture and penetration of the microneedles. In these studies, 50 g and 500 g load cells were driven at 0.008 mm/s displacement rate against pork tissue (*Nahunta Pork, NC, USA*) and *Teflon*® polytetrafluoroethylene (*E.I. DuPont de Nemours Company, DE, USA*) surfaces. A live video capture device was used to monitor microneedle penetration behavior.

400 μm thick skin areas were removed from the back of pig as described in *Chang & Riviere*[131] for the transdermal administration studies. The pigs used in this study were in accordance with animal care and guidelines approved by North Carolina State University (*Raleigh, NC, USA*). Microneedles fabricated on perforated glass substrates were used to transdermally administer quantum dots and fluorescein-conjugated biotin on porcine skin. The perforated glass substrate was sealed with plastic tubing and connected to a clamped 10 μL 26G glass syringe (*Hamilton Co., Reno, NV, USA*). 2 μL of fluorescein-conjugated biotin (*Pierce Biotechnology, Rockford, IL, USA*) was carefully injected via the microneedles into porcine full-thickness skin patches. 2 μL of fluorescein-conjugated biotin was topically applied on skin surface to serve as control. Post-administration, the skin samples were frozen at –20 °C with time-delays of 5 minutes, 20 minutes and 60 minutes. In a separate trial, 2 μL of 8 μM Qdot® 655 ITK™ amino (PEG) quantum dots (*Quantum Dot Corporation/ Invitrogen, Hayward, CA, USA*) with emission maxima at 655 nm was carefully injected via the microneedles into porcine full-thickness skin patches. As previously, 2 μL of amino (PEG) quantum dot solution was topically applied on skin surface to serve as control. The skin samples were frozen at 5 minutes and 60 minutes at –20 °C. The skin samples were sectioned at 20 μm on a cryostat and the samples were stored at –20 °C prior to imaging.

2.1.8 Implantation of Ossicular Replacement Prosthesis

Ossicular replacement prostheses (similar to TORP prosthesis (*Kurz Medical Inc., Dusslingen, Germany*)) were developed using 2PP. Implantation of Ormocer® ossicular replacement prostheses were performed into the right ear of a commercially obtained un-frozen human head. Optical micrographs were recorded at the various stages of the procedure. First, the chorda tympani was partly removed. This was followed by the removal of the incus and the head of the stapes using surgical tools. The Ormocer® prosthesis was carefully lined against the posterior canal wall. Finally, the implant was positioned in situ with the tympanomeatal flap raised anteriorly.

2.2 MDW – MAPLE DIRECT WRITE

The various materials and methodologies used in the study of matrix-assisted pulsed laser evaporation direct-write (MDW) are described ahead.

2.2.1 UV Absorbing Polymer

An intermediate UV-absorbing (193 nm) release layer was developed using triazene polymer.[132] The structure of triazene polymer (TP) is shown in Figure 12.

2.2.2 Bioceramics

Hydroxyapatite ($Ca_{10}(PO_4)_6(OH)_2$) of 500 nm average particle size and zirconia (ZrO_2) of 0.33 to 2.19 particle size powders (*Alfa Aesar, MA, USA*) were used for the study. The bioceramic powders were ground using a mortar and pestle and solvated in 50:50 glycerol:water matrices to create slurries for spin coating on quartz ribbons.

2.2.3 Biologics

MG63 osteosarcoma cells (*American Type Culture Collection Manassas,, VA, USA*) were used for the bioceramic study. They were sub-cultured in a Eagle's minimum essential medium (EMEM) media containing 2 mM L-glutamine, 1.5 g/L sodium bicarbonate, 0.1 mM non-essential amino acids, 1.0 mM sodium pyruvate, 10% heat-inactivated fetal bovine

serum, and 1% antibiotic syrup. B35 neuroblast clonal cells (*American Type Culture Collection, Manassas, VA, USA*) were used for the MDW study using triazene polymer. The cells were sub-cultured in a Dulbecco's modified Eagle's medium (DMEM) media, 10% heat-inactivated fetal bovine serum, and 1% antibiotic syrup. Sub-confluent cells are trypsinized and split 1:5 to maintain division of the cell line and avoid differentiation. The cells were stored in a 37^{o} C, 5% CO_2 culture incubator. Extracellular matrix (ECM®) (*American Type Culture Collection, Manassas, VA, USA*) solutions were used to coat the ribbons and the substrates for the MDW experiments.

2.2.4 MDW Microfabrication

In MDW microfabrication and biomaterial patterning, an ArF pulsed excimer laser (λ=193 nm, R=10 Hz) was used as the source light. The laser was focused onto a receiving plane using optics coated with UV reflective material. The biomaterial used for patterning was spin-coated on a quartz disc "ribbon", which was placed directly above a receiving substrate which was held using a vacuum chuck (Figure 13). The gap between the ribbon and substrate was controlled using a stage z-translation. The CAD/CAM program for the translation movement was synchronized with the laser parameters to generate the desired pattern. The translation movements were achieved using Aerotech U500 (*Aerotech, Pittsburgh, PA, USA*) powered x-y translation stages. The transfer process was observed using an inverted lens camera focused on the ribbon plane. The fluence (laser energy density) was systematically varied to determine the threshold level for the biomaterial. All experiments were performed in air and at room temperature.

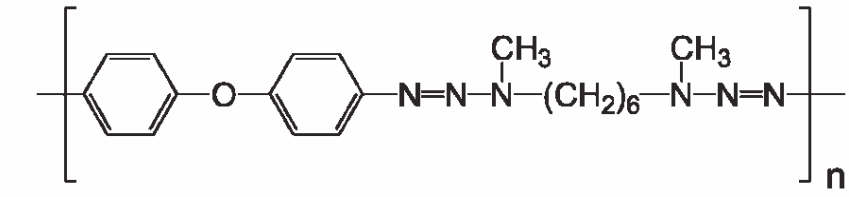

Figure 12. Structure of triazene polymer used as a release layer.

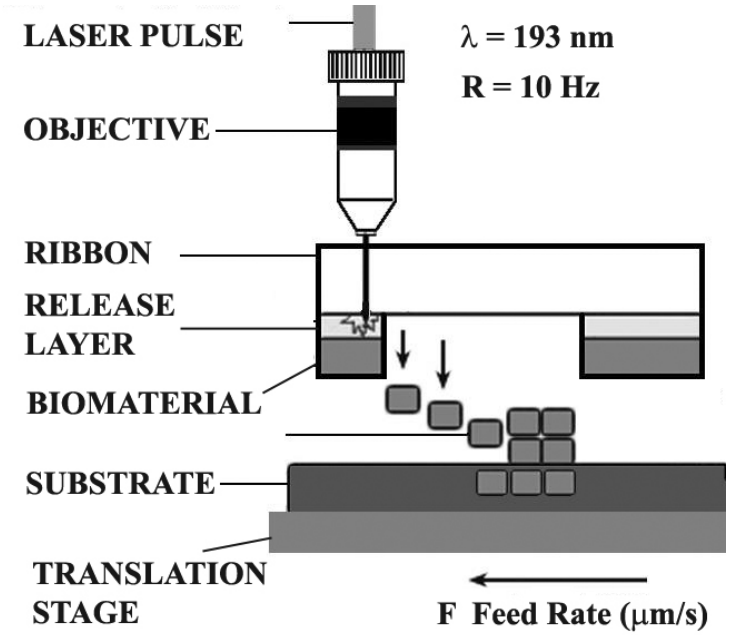

Figure 13. Schematic of the MDW process.

"Ribbons" were prepared by spin-coating the triazene polymer (TP) on clean one inch quartz discs to thicknesses of 60 nm, 70 nm, 80 nm, 90 nm, 110 nm and 140 nm. Ribbon and receiving substrates were then spin coated with ECM® at 1000 rpm for ten seconds. Sub-confluent B35 rat neuroblast-like cells were trypsinized, and centrifuged at 220 g for three minutes. The concentrated cell pellet was reconstituted to obtain approximately 10^7 cells/ml. 250 μl of this solution was pipetted onto the ribbon and incubated for 10 minutes to allow attachment to ECM layer. Post transfer, the ribbon and the substrate were stored in separate Petri dishes containing pre-warmed media. The cells on the substrates were observed for viability and proliferation at time intervals of 0-3 h, 3-6 h, 6-12 h, 12-24 h, 24-48 h.

MDW of bioceramics-osteosarcoma cells were performed without the TP layer. ECM solution was slowly warmed from –20 °C to 0-4 °C in order to avoid rapid polymerization and 500 μL was spin-coated was spin coated on sterilized one inch quartz ribbons and glass substrates for ten seconds at 1000 rpm. The ribbons and substrates were incubated to allow cross-linking of the matrix proteins. Hydroxyapatite and zirconia slurries (concentrations of sixty weight percent and seventy weight percent) were then spin coated at 1000 rpm for ten seconds onto these ribbons.

As previously, sub-confluent MG63 osteosarcoma cells were reconstituted to approximately 10^7 cells/mL and 250 μL pipetted onto the ribbons. The minimum laser energy for MDW transfer was determined by systematically increasing the laser fluence and simultaneously observing the ablation using the digital camera. After MDW transfer, the ribbon and the substrate were stored in separate Petri dishes containing pre-warmed EMEM (EBSS) media.

2.2.5 Microscopy

The ribbon and substrates were stored in separate Petri dishes containing pre-warmed media, after transfer. The cells on the substrates were observed for viability and proliferation at various time points such as 0-3 h, 3-6 h, 6-12 h, 12-24 h, 24-48 h using an inverted Olympus X71 microscope with epi-fluorescence attachment. A live/dead stain (*Biovision Research Products, CA, USA)* was used to examine the cells. The propidium iodide within the staining solution caused non-viable cells to fluoresce red and the Live-dye^{TM} caused the viable cells to fluoresce green. Optical microscopy was also used to examine the feature sizes in the patterns generated.

Hitachi S800 scanning electron microscope (*Hitachi High Technologies, Tokyo, Japan*) was used to examine the microstructure of the MDW-transferred bioceramic patterns. X-ray diffraction was performed to determine the composition, phase, and crystallinity of the transferred material.

2.3 CLM – CAD/CAM LASER MICROMACHINING

The various materials and methodologies used in the study of CAD/CAM laser micromachining are described ahead.

2.3.1 Materials and Biologics

Polished Si (111) wafers were used for the preliminary ablation studies. 1-2% agarose gel was prepared by hydrating 0.5 g of electrophoresis-grade agarose powder (*Sigma Aldrich, MO, USA*).

C2C12 mouse myoblast cells, A431 human skin epithelial carcinoma cells, and B35 neuroblast clonal cells (*American Type Culture Collection, Manassas, VA, USA*) were grown in tissue culture flasks, trypsinized, centrifuged, and re-suspended in 90% Dulbecco's Modified Eagle's Medium (DMEM) supplemented with 10% fetal bovine serum and 1% penicillin–streptomycin–glutamine). HAAE-1 human aortic endothelial cells and HA-VSMC human aortic smooth muscle cells were obtained from the Wistar Special Collection (*American Type Culture Collection, Manassas, VA, USA*). These two cell-lines were used for the vascular network development. All cells were sub-cultured and incubated at 37 °C, 5% CO_2. Matrigel® *(Becton-Dickinson, NJ, USA)*, HA587 human soluble elastin *(Elastin, products, MI, USA)*, vascular endothelial growth factor (VEGF) and heparin (Sigma-Aldrich, MO, USA) were used in the UV-sterilized matrix to study the effect on the growth and proliferation of the cells.

2.3.2 CLM Microfabrication

The setup for CLM microfabrication was similar to the MDW setup. Figure 14 contains the schematic of the CLM setup. An ArF pulsed excimer laser operating at 193 nm was used as a source light. Fused silica biconvex lenses L_1 and L_2 were used in a telescopic to lower the primary spot size of the laser. Apertures A_1 and A_2 were used to further reduce the laser spot size and allow alignment. UV-dielectric mirrors M_1 and M_2 were used to reflect the laser light at 45° incident angle. A 10x UV-objective (O) was used to focus the laser beam to spot-size of up to 5 μm. A CCD camera was aligned with the mirrors and objective to monitor the micromachining process.

The micropositioning module was developed to convert the CAD geometry and synchronize the x-y-z translation movement with the laser parameters. As laser interaction with each material is unique, the ablation characteristic for every new material was studied as a function of laser energy, spot-size, and repetition. This allowed calibration of the system for a unique material.

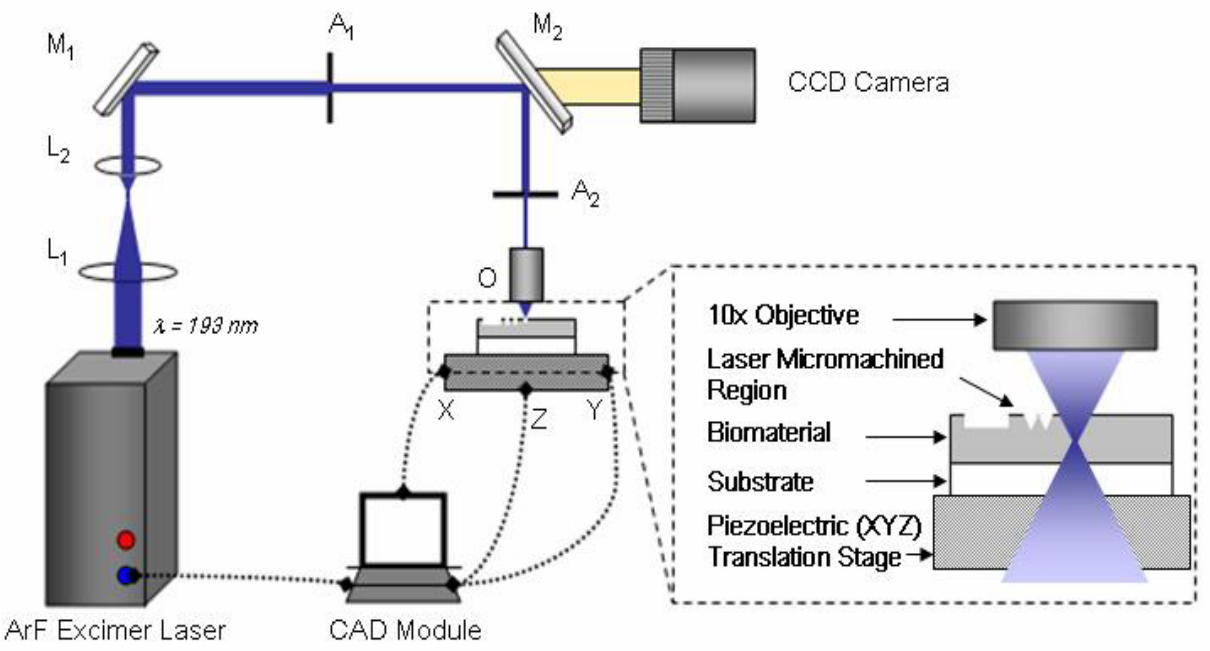

Figure 14. Schematic of the CLM process and setup.

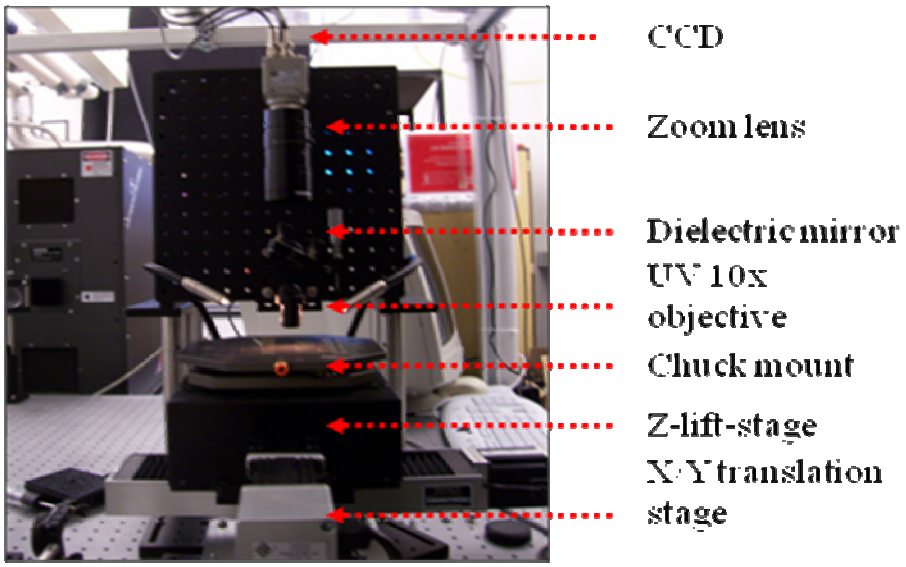

Figure 15. Image of the CLM Setup with key parts labeled.

2.3.3 Cytotoxicity Study

In order to assess the effect of VEGF and heparin on cell-viability, HAAE-1 and HA-VSMC cells were seeded in 24-well culture plates (~ 5000 cells/well) containing VEGF (1, 10, 100, 1000 ng/ml) and heparin (1, 10, 100, 1000 units/ml) separately using plain media as controls with n=4. At 24 hours, the cells were exposed to media (control) and assayed for MTT. The cells were incubated in MTT (3-[4,5-dimethyl-2-thiazol]-2,5-diphenyl-2H-tetrazolium bromide) medium (0.5 mg/ml) for 4 h, the tetrazolium metabolized within the mitochondria extracted, and absorbance quantified. The absorbance was determined spectrophotometrically at 550 nm (*Multiskan RC Labsystems, Helsinki, Finland*).

2.3.4 Development of Tissue Networks

Once the laser ablation characteristics were established, various CAD/CAM patterns were developed. Channels 60 to 400 μm wide and one cm long were developed for the neuroblast, myoblast and epithelial cell study. Each channel was provided with a reservoir to allow easy flow of scaffold material and growth factor/proteins. Non-diluted extracellular matrix solution was micro-pipetted into the channels and allowed to polymerize into a thin film in the channel. The growth and proliferation of the cells within the channels were studied.

In order to allow development of multi-layered vascular networks, a reservoir-ring type design was developed (Figure 16). Each ring (representing each layer) was connected to an independent reservoir to allow selective flow of nutrients/growth-factors. The

micromachined hydrogels were filled with growth factors established from the cytotoxicity/MTT analysis to allow controlled proliferation and growth of cells within the layers. The growth of cells within the network was monitored. The full-grown tissue network after delamination from hydrogel substrate was re-suspended in fresh media.

2.3.5 Microscopy

The growth and proliferation of the cells in micromachined scaffolds were observed with a Meiji 5500 inverted optical microscope (*Meiji Techno, Santa Clara, CA, USA*) and a digital still camera with an epi-fluorescence attachment. A live/dead cell staining kit (*Invitrogen, CA, USA*) was used to stain the cells (dead cells red and live nuclei green).

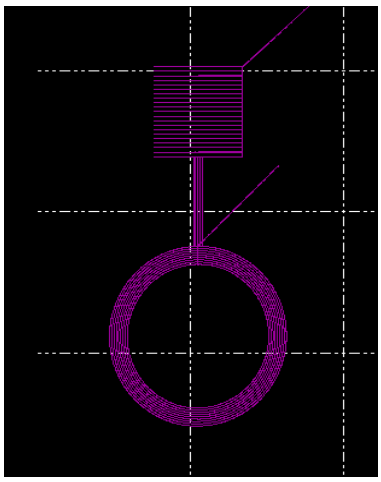

Figure 16. Reservoir-ring design for each layer of vascular network.

2.4 PIT - PIEZOELECTRIC INK-JET TECHNOLOGY

The various materials and methodologies used in the study of piezoelectric ink-jet technology are described ahead.

2.4.1 Materials

Rhodamine-conjugated streptavidin and fluorescein-conjugated biotin (*Pierce Chemicals, IL, USA*) were solvated in phosphate buffer saline solution to a 1.6 μM solution. 1% of polysorbate 20 surfactant (*Fisher Science, NJ, USA*) was added to isolate the water-soluble protein.

Mussel proteins (Mefp-1 and Mefp-2) were extracted from marine mussel *Mytilus edulis* as described previously.[133] *Mytilus edulis* mussel proteins (80% Mefp-1 and 20% Mefp-2) solvated in water with a DOPA concentration of 0.16 mM was obtained from Wilker lab (*Purdue University, West Lafayette, IN, USA*). In order to study iron-induced cross-linking, $FeCl_3$ solution was prepared in series dilution to obtain ratios of 1:1 Fe:DOPA, 10:1 Fe:DOPA, and 100:1 Fe:DOPA. Cell-tak™ cell and tissue adhesive containing polyphelolic proteins derived from *Mytilus edulis* mussels were obtained from BD Biosciences (Franklin lakes, NJ, USA). N-butyl cyanoacrylate (Vetbond® Tissue Adhesive) was obtained from 3M (*St. Paul, MN, USA*). 2-octyl cyanoacrylate (Nexaband® Liquid Topical Tissue Adhesive) was obtained from Abbott Laboratories (*North Chicago, IL, USA*). Ethyl cyanoacrylate (Loctite® Quick Set Adhesive) was obtained from Ted Pella (*Redding, CA, USA*). PEG synthetic hydrogel adhesive CoSeal® surgical sealant was obtained from

Baxter Healthcare *(Fremont, CA, USA*) and contained two synthetic polyethylene glycols (PEGs) buffer solutions that readily formed a hydrogel upon mixing.

2.4.2 PIT Micropatterning

The CAD/CAM piezoelectric ink-jet printer (FujiFilm-Dimatix, SantaClara, CA) was based on a cartridge print-head system: fluid was injected into the fluid module and then the fluid module was attached to the jetting module to form a sealed cartridge. The ink jet print-head itself was a silicon die that consists of 16 individually addressable jets, which were spaced 254 μm apart. The effective nozzle diameter was 21.5 μm, which provided droplets that were approximately 10 pL in volume.

The printer was used to dispense picoliter quantities of adhesive solutions in a predefined pattern onto a variety of substrates (Si (111), borosilicate glass, dermatomed pig-skin and KCl) at 25 °C and 40% relative humidity. The viscosities of solutions were measured prior to jetting, using a Brookfield viscometer (*Brookfield Engineering, Middleboro, MA, USA*). All solutions (except Loctite® monomer) were within jetting viscosity range (5-15 Cps).The waveform pulse shape (amplitude, slew rate and duration), frequency and voltage were optimized for all the bioadhesive solutions independently (sample wave-form shown in Figure 19). The mussel protein solution was ink-jetted at voltages (10, 20, 30, and 40 V) to study the effect of voltage on protein-structure. The droplet flight (distance traveled) from the nozzle was recorded using an ultra-fast camera. The images were recorded at various time-intervals and various voltages.

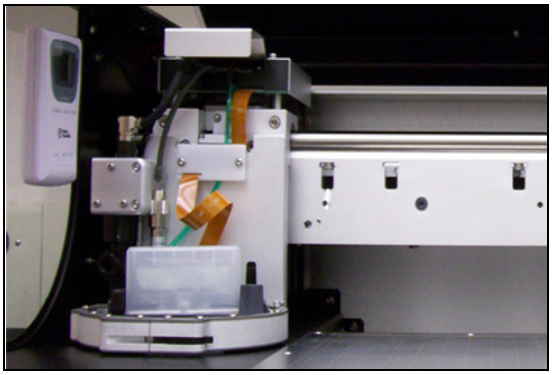

Figure 17. Image of the piezoelectric printer and cartridge.

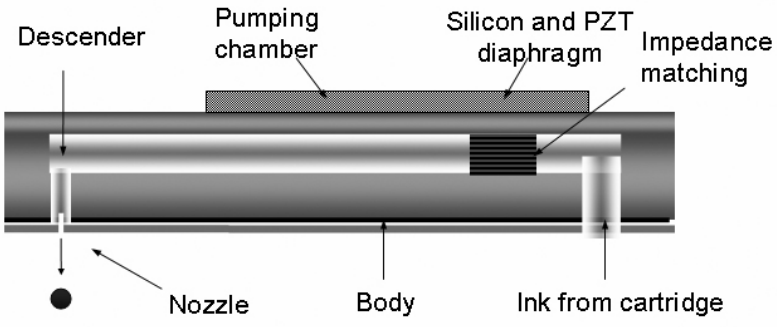

Figure 18. Schematic of a piezoelectric print-head.

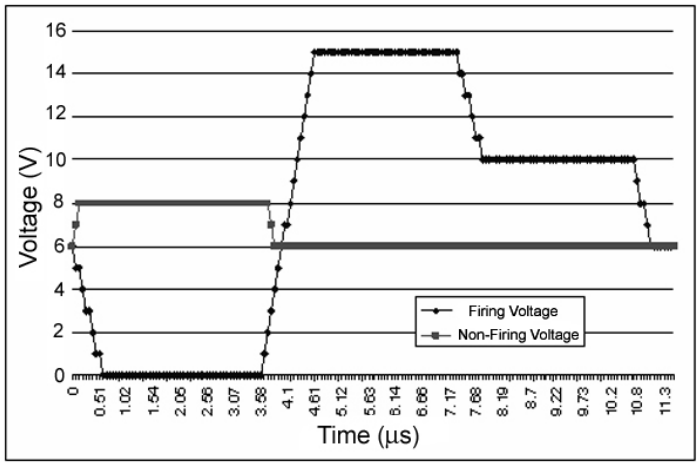

Figure 19. A sample jetting wave-form for 15V peak supply.

The adhesive and protein solutions were also patterned into a 1 cm^2 area (with 10 μL constant volume) on Si (111) substrates for optical/AFM/XPS/contact-angle measurements, on full-thickness porcine skin for adhesion testing, and on KCl/AgCl for FTIR measurements. Vetbond® and Nexaband® tissue adhesives were ink-jetted in their monomer liquid form. Loctite® quick set adhesive composed of ethyl cyanoacrylate was not compatible with the ink-jet system due to the high viscosity and quick-setting properties of the monomer. The Loctite® resin was drop-cast into thin-film samples and used as a control for comparative study.

In order to study iron-induced cross-linking, mussel protein solution (containing 80% Mefp-1, 20% Mefp-2 and 0.16 mM DOPA) was ink-jetted, followed by a layer of $FeCl_3$ solution (at varying concentrations to reach 1:1, 10:1, 100:1 Fe: DOPA respectively) using the same pattern. Drop-cast samples of the protein solution were prepared for the FTIR study. For CoSeal® micropatterning, the liquid component consisted of dilute HCl solution and a sodium phosphate/sodium carbonate solution in two syringes. The liquid solutions and PEG powder components from the syringe assembly were carefully removed and transferred to sterile vials. The PEG powder component (part I) was dissolved in the sodium carbonate/sodium phosphate solution and transferred to an ink-jet cartridge. Part II of the solution was transferred into a separate cartridge to allow subsequent jetting of the additional layer to control the formation of CoSeal® hydrogel.

2.4.3 Spectroscopy Study

A drop-cast sample of the bioadhesives and protein solutions were prepared to compare the absorption peaks to the ink jet deposited material. Fourier transform infrared spectroscopy (FTIR) was performed using a Mattson 5000 series (*Madison Instruments, WI, USA*) spectrometer with 4 cm^{-1} resolution. The absorption spectra (4000-500 cm^{-1}) were recorded for the ink-jetted and drop-cast materials.

X-ray photoelectron spectroscopy (XPS) data was acquired using a Riber dual Mg/Al anode source Auger and photoelectron separation at 12kV/14mA beam energy, 1mm spot size, 0.3 - 4.0 eV resolution and solid angle at 6% of 2(pi).

2.4.4 Mechanical and Surface Testing

Adhesion studies were performed on full-thickness porcine skin and Al substrates using an Instron 8501 uniaxial tensile test system (*Instron, Norwold, MA*, *USA*). The load at failure and mode of failure was assessed. The tests were carried out six times for each sample, and a statistical analysis was performed using Student's t-test. Contact-angle studies were performed using a goniometer, a syringe, an aligned digital zoom camera and an illumination source. Distilled water was used as the liquid source against protein-coated Si substrates.

A Nano-Indenter XP instrument (*MTS Systems, Oak Ridge, TN, USA*) was used to carry out indentation tests using Continuous Stiffness Measurement (CSM) technique in order to measure the elastic modulus (E) and the hardness (H) of the materials. In addition to

measuring the indentation depth under the increasing load, a lock-in amplifier was used to measure the differentiation of loading force over the vertical displacement at the vibrating frequency during the indenting. It eliminates the need of unloading to obtain the slope of the unloading curve at the turning point to calculate the elastic modulus and hardness, thus measuring the modulus and hardness continuously instead of at a discrete set of loads and depths. The tests were performed at four different sites with a spacing of 1000 μm at a depth up to 500 nm on the surface of Vetbond® and Loctite® adhesives. For the CoSeal® sample, a total of five tests were performed at the scattered sites on the surface with spacing from 100 μm to 6 mm at a depth up to 750 nm.

2.4.5 HAAE-1 Cytotoxicity Study

Cytotoxic analysis of bioadhesives was performed using HAAE-1 human aortic endothelial cells (*American Type Culture Collection, Manassas, VA, USA*). HAAE-1 cells were seeded in 24-well culture plates (~ 5000 cells/well) containing equal amounts of ink-jetted bioadhesives (n=4). Cells growing on empty wells with plain media were used as controls. At 24 hours, the cells were exposed to media (control) and assayed for MTT. The cells were incubated in MTT (3-[4,5-dimethyl-2-thiazol]-2,5-diphenyl-2H-tetrazolium bromide) medium (0.5 mg/ml) for 4 h, the tetrazolium metabolized within the mitochondria extracted, and absorbance quantified. The absorbance was determined spectrophotometrically at 550 nm (*Multiskan RC Labsystems, Helsinki, Finland*).

2.4.6 Microscopy

Optical/fluorescent microscopy of the micropatterned substrates were performed using a Leica DLMB upright microscope (*Leica Microsystems, IL, USA*). Optical imaging of the deposited adhesives was performed using an Olympus upright microscope (*Olympus Inc., Center Valley, PA*, *USA*). Scanning electron microscopy (SEM) was performed at the Analytical Instrumentation Facility (*NCSU-AIF, Raleigh, NC, USA*) using a Hitachi S-3200 SEM operating at 5KV. Atomic force microscopy (AFM) was performed using an *N-scriptor* system (*Nanoink, IL, USA*) with a scanning head providing a maximum scan range of 80 x 80 μm^2. The imaging was performed at 2 Hz in the contact mode using silicon nitride cantilevers (spring constant: 0.06 Nm^{-1}) with integrated pyramidal tips. Linear and 3-D profiles of the surface scans were obtained using Nanorule data analysis.

CHAPTER 3

RESULTS AND DISCUSSIONS

3.1 2PP – TWO-PHOTON POLYMERIZATION

The two photon absorption process has a quadratic dependence on laser intensity, which allows high absorption at tightly focused area within the liquid resin. Negligible absorption occurs except in the immediate vicinity of the focal volume of the light beam. This phenomenon allows microscale polymerization in three-dimensional space, unlike stereolithography (a layer by layer approach). All three photopolymers (Ormocer®, SR610, and SR499) were compatible with the two-photon polymerization process. Two-photon polymerization was used to develop CAD/CAM micromedical devices such as Lego-like scaffolds, microneedles for transdermal drug-delivery and ossicular replacement prosthesis. Figure 20 contains a scanning electron micrograph of a 6x5 array of off-centered Ormocer® microneedles with approximate base diameters of 290 μm and length of 650 μm.

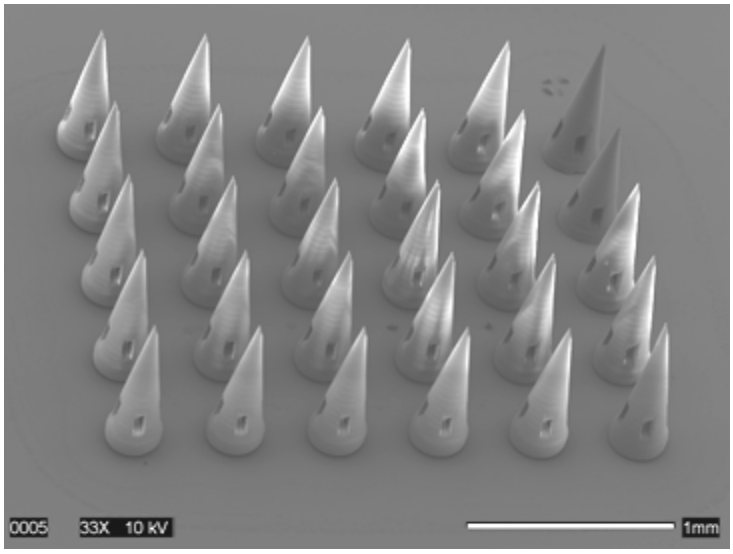

Figure 20. Scanning electron micrograph of a 6x5 array of off-centered Ormocer® microneedles fabricated by two-photon polymerization. *Scale bar equals 1 mm.*

3.1.1 Nanoindentation Study

Studying the mechanical properties of the photopolymers was important in order to establish their applicability in medical usage. Figure 21 contains the measured elastic modulus E and hardness H of the three samples (Ormocer®, SR499, and SR610). Significant viscocreep deformation as well as viscoelastic recovery was observed. The hardness and elastic modulus values started from high values at shallow depths, decreased dramatically with the increasing depth, and then stabilized at a value. The higher hardness and elastic modulus values at the surface were attributed to the ultraviolet curing process. There was a significant difference in mean hardness and modulus values between all three materials. Ormocer® showed highest values with mean hardness of approximately 90 MPa and mean modulus of approximately 2100 MPa at 2 μm indentation depths. SR499 or ethoxylated(6) trimethylolpropane triacrylate showed lowest values with mean hardness of approximately 7.5 MPa and mean modulus of approximately 50 MPa. SR610 or PEG (600) diacrylate showed mean hardness of approximately 30 MPa and mean modulus of approximately 607 MPa. The high hardness and modulus values in Ormocer® may be attributed to the presence of organically modified silicon alkoxides and the strong covalent bonds between the ceramic and polymer components that form during the two photon polymerization process. The mechanical properties may be further modified be varying the amount of organic network units, inorganic network units and fillers.

Figure 22 contains atomic force micrographs (lateral force measurements, LFM and height scan, HTS) of the surface of the polymerized materials (Ormocer®, SR610, and SR499). The surface of Ormocer® showed to be significantly smoother and more uniform

than the other two polymers. The RMS roughness of the surface of Ormocer®, SR610, and SR499 were measured to be 0.651 nm, 1.25 nm, and 4.19 nm, respectively.

The optical, chemical, and mechanical properties of Ormocer® demonstrate a large degree of variability. Ormocer® materials are optically transparent over the 400–1600 nm wavelength range.[134] These materials demonstrate low optical losses in the near infrared range, with losses less than 0.06 dB/cm at 830 nm, and less than 0.6 dB/cm at 1550 nm. The refractive index of Ormocer® materials may be adjusted in the 1.47-1.56 range. Many materials prepared by sol–gel processing exhibit high (>20%) volume shrinkage during solvent removal, curing, and network densifying, which can lead to significant cracks, mechanical stresses, and other defects. Ormocer® materials exhibit far less shrinkage (~2%) than other sol-gel materials due to the stability of the inorganic Si–O–Si network and the inclusion of fillers.[135] The density, Young's modulus, thermal expansion coefficient, gas permeability, refractive index, and other properties of Ormocer® materials exhibit values between those of ceramics and those of polymers.[136, 137] For example, the densities of Ormocer® materials (1.1- 1.6 g/cm^3) are below the densities of oxide materials, but above the densities of organic polymers. In addition, Ormocer® materials demonstrate a high degree of flexural strength. Ormocer® materials demonstrate high adhesive strength to a variety of substrate materials, including metallized silicon wafers, inorganic glasses, and polymers.[138] Ormocer®- based matrix components (Definite™) and Ormocer®- based light-curable dental composites (Admira™) have been commercially available for use in restorative dentistry since 1988. In addition, carboxy-modified Ormocer® materials have been used as matrix materials in light-curable glass ionomer cements.[139]

X-ray diffraction was used to confirm that Ormocer® surfaces created using two photon induced polymerization exhibit an amorphous structure. The X-ray diffraction pattern, shown in Figure 23, also suggests that there is no separation between the inorganic and organic phases in the polymerized Ormocer® material.

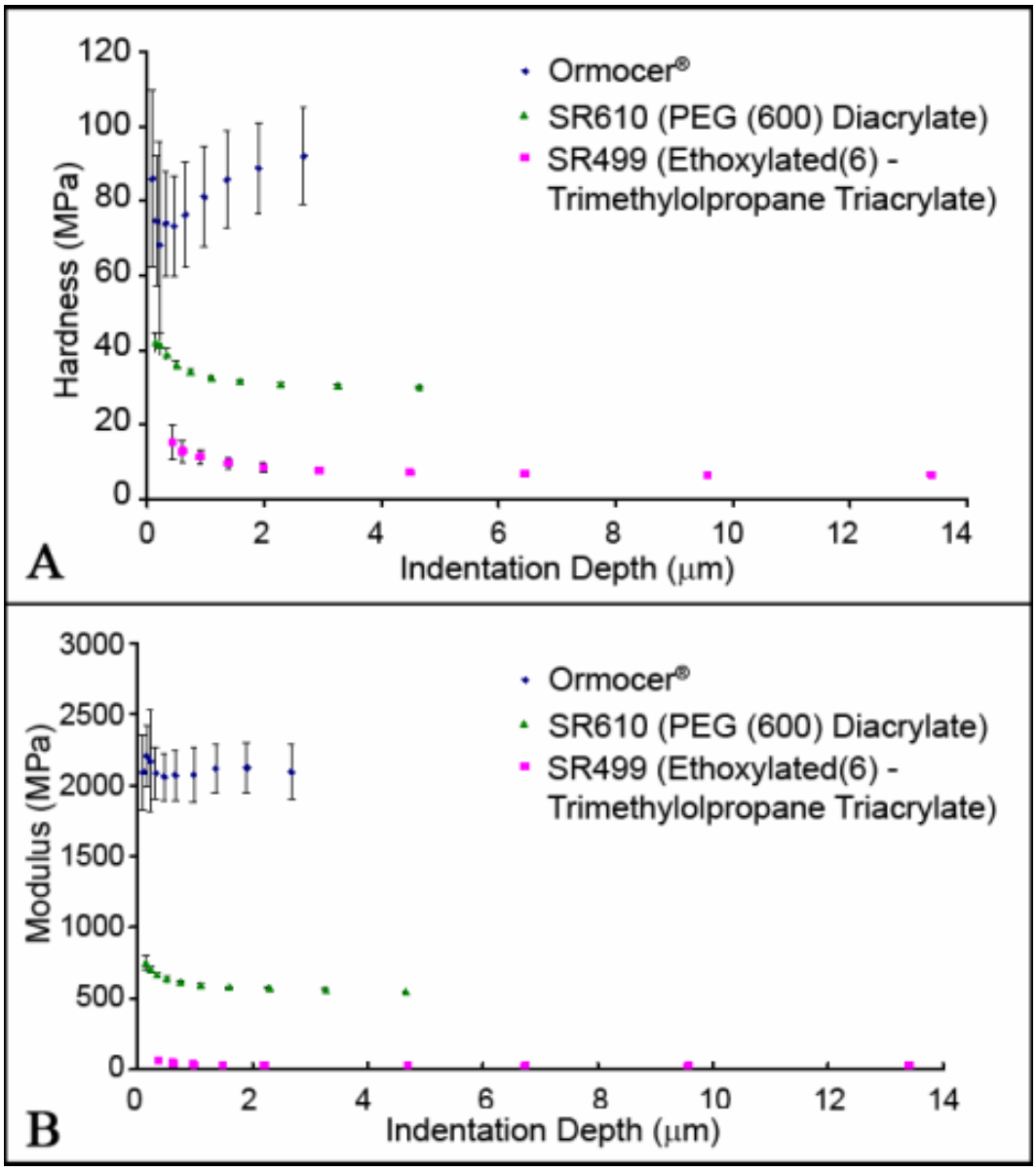

Figure 21. Nanoindentation results of the photopolymers. A. Graph of hardness (MPa) vs. indentation depth (mm) of the photopolymers. B. Graph of modulus (MPa) vs. indentation depth (mm) of the photopolymers. Symbols "◆", "▲", and "■" represent values for Ormocer®, SR610 (PEG(600) diacrylate), and SR499 (Ethoxylated(6) trimethylolpropane triacrylate), respectively. Bars in graph A and graph B indicate standard deviation of mean hardness and modulus values, respectively.

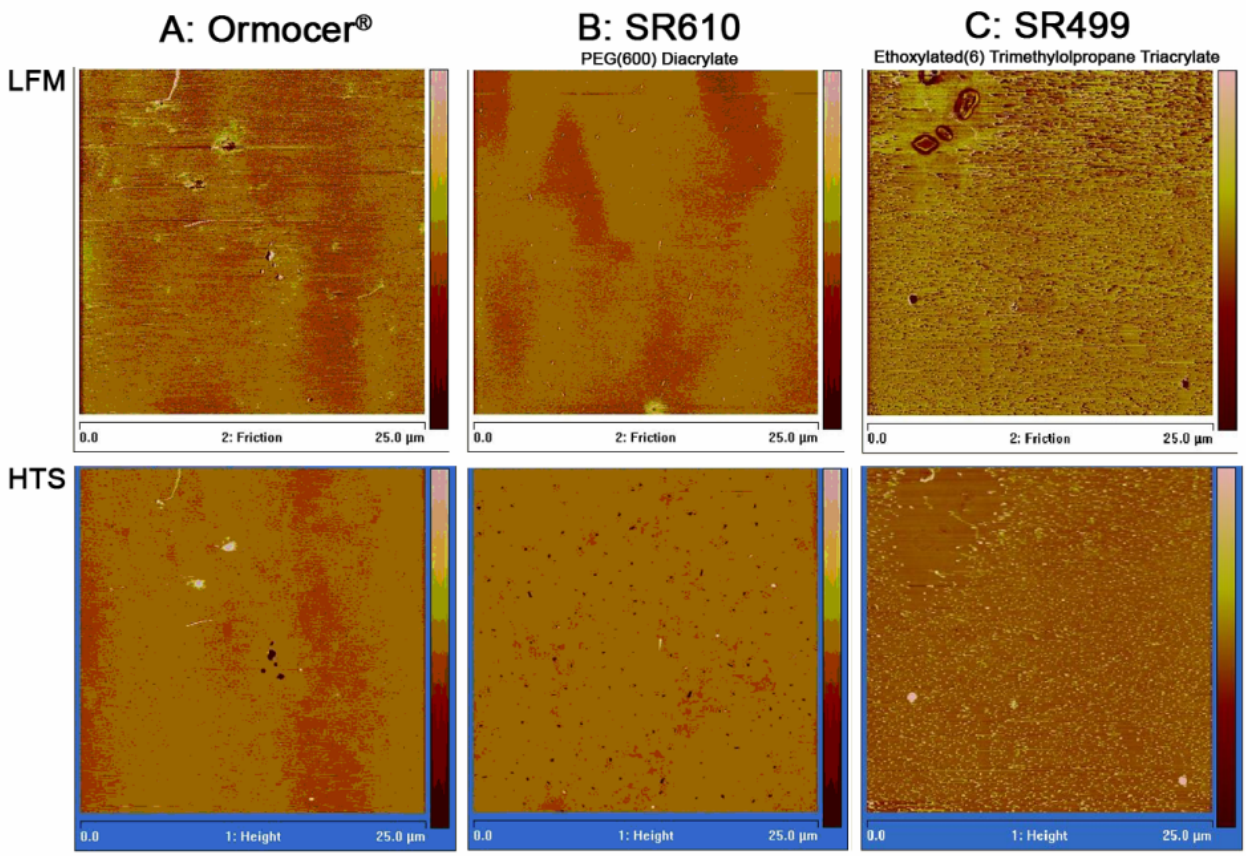

Figure 22. Atomic force micrographs of the surface of **A**: Ormocer®, **B**: SR610 (PEG(600) diacrylate), and **C**: SR499 (Ethoxylated(6) trimethylolpropane triacrylate) recorded in tapping mode. **Top row contains LFM** (lateral force measurement) scan and **bottom row contains HTS** (height scan with z-range of 25 nm) of the three photopolymers for a range of 25 µm x 25 µm.

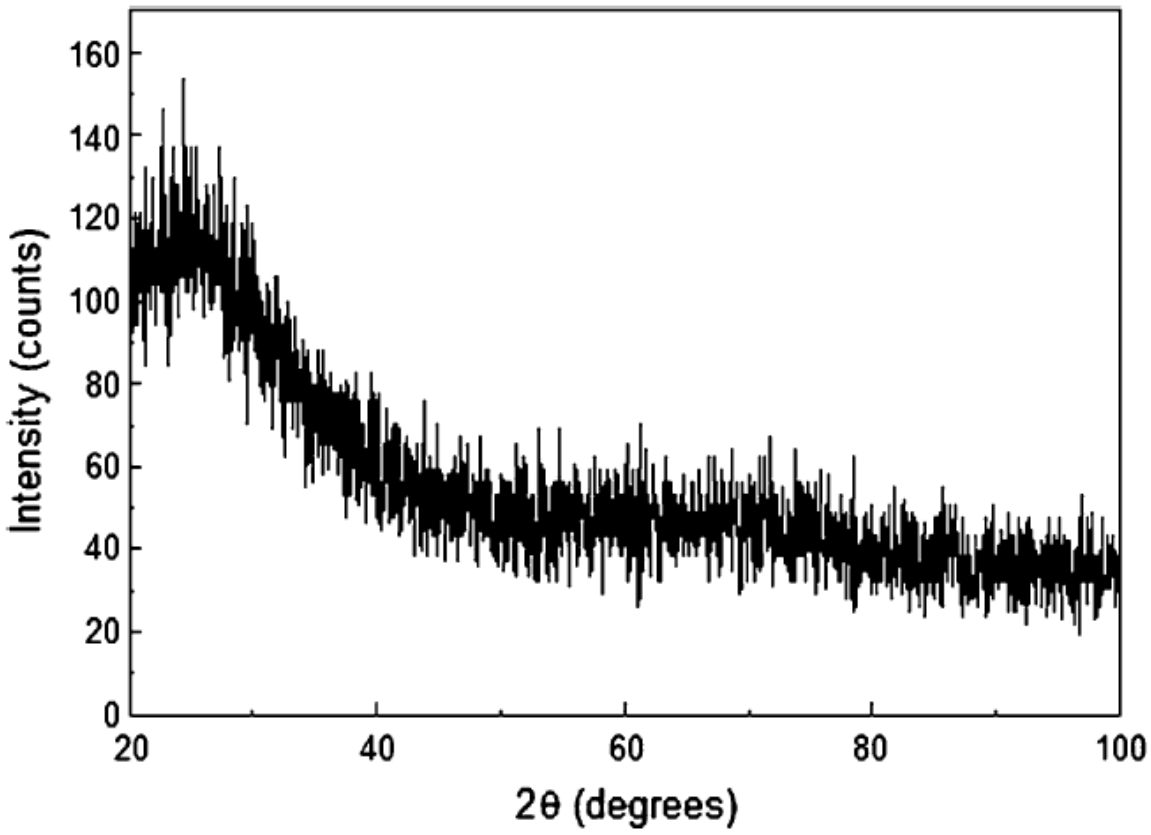

Figure 23. X-ray diffraction pattern of two-photon polymerized Ormocer® surface.

3.1.2 HEK Cytotoxicity

With the exception of SR610, which fragmented during the first medium rinse, the polymers were stable in cell culture medium. After 24 hours, the SR 610 fragments remained intact, while SR 499 detached from the coverslip. Cell growth on all controls and the Ormocer® polymer ranged from 65% to 80% confluency as determined with an inverted microscope. While the Ormocer® substrates (Figure 24A) and the controls (Figure 24D) supported human epidermal keratinocyte (HEK) growth, little growth was observed on the SR610 (Figure 24B) and SR499 (Figure 24C) substrates. Figure 25 contains the MTT viability for the HEK of the three polymers and the controls. The polymers SR610 and SR499 demonstrated to be a very poor substrate for HEK growth with only 14% and 27% viability, and was statistically significant at ($p<0.05$), relative to controls. On the other hand, HEK growth on Ormocer® substrates was similar to controls and not significantly different ($p<0.05$). Previous biological studies, including the ISO 10933-5 cytotoxicity (elution) assay, have shown that Ormocer® materials are nontoxic and biologically inert.[140, 141]

Ormocer® in comparison with SR499 and SR610 showed significantly superior mechanical strengths, surface properties and HEK cytocompatibility (Refer Table 2). Thus, Ormocer® was chosen for subsequent fabrication of Lego®-like scaffolds, microneedles and ossicular replacement prostheses using the two-photon polymerization technique.

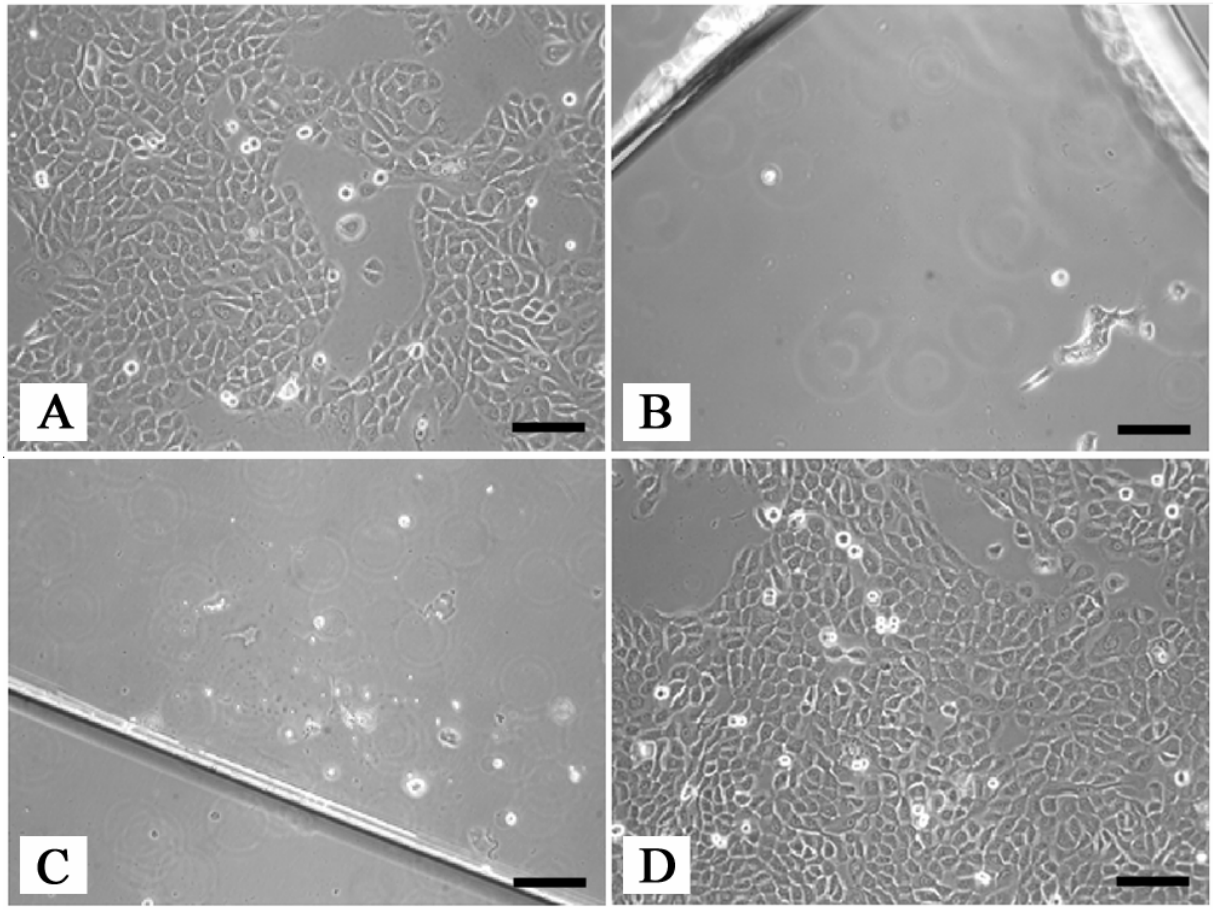

Figure 24. Light micrograph of human epidermal keratinocytes on **A**: Ormocer®, **B**: SR610 (PEG(600) diacrylate), **C**: SR499 (Ethoxylated(6) trimethylolpropane triacrylate), and **D**: control. *Scale bar equals 50 μm.*

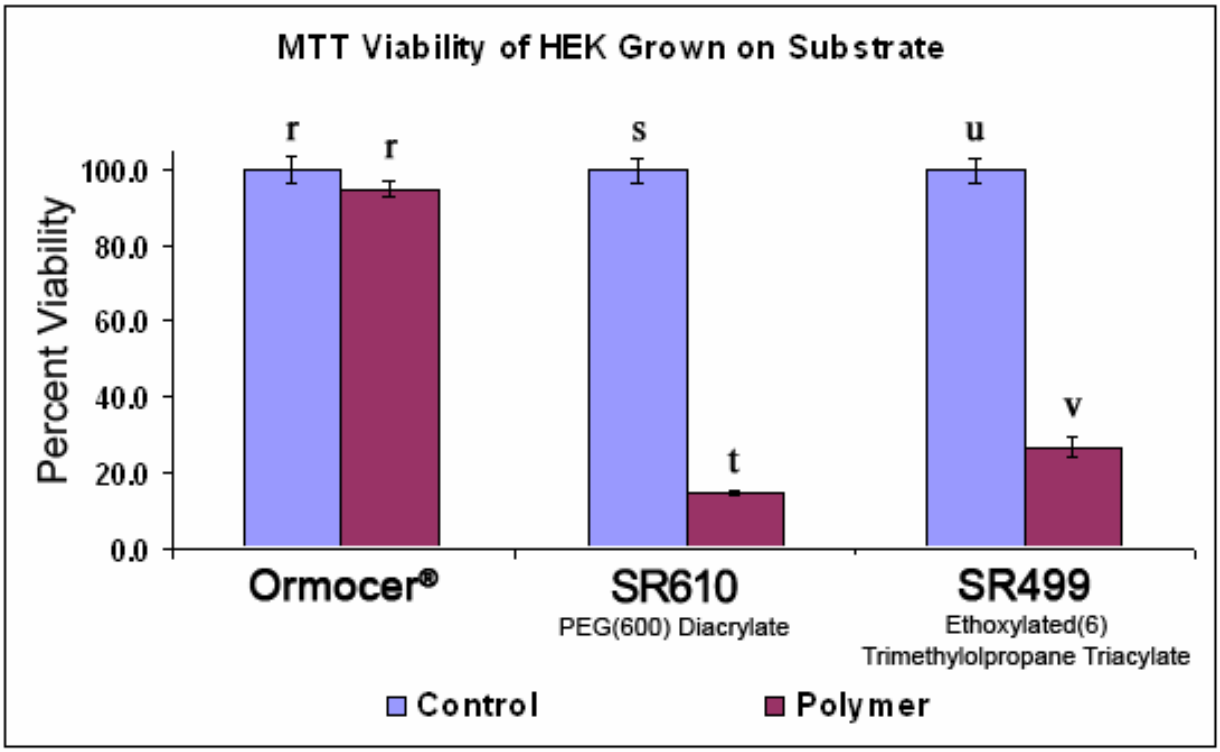

Figure 25. MTT viability of human epidermal keratinocytes on Ormocer®, SR610 (PEG(600) diacrylate), and SR499 (Ethoxylated(6) trimethylolpropane triacrylate) substrates relative to paired controls. *Bars indicate standard deviation of mean viability. (s and t), (u and v) are significantly different ($p<0.05$).*

Table 2. Comparison of properties of different classes of two-photon polymerizable materials. **HEK viability is relative to controls.*

Notation	Monomer	Hardness (MPa)	Modulus (MPa)	RMS Roughness (nm)	HEK Viability (%)*
Ormocer®	Methyl-methacrylate and alkoxy-silane groups	90	2100	0.65	95
SR610	PEG(600) diacrylate	30	607	1.25	14
SR499	Ethoxylated(6) trimethylolpropane triacrylate	7.5	50	4.19	27

3.1.3 Microfabrication of Lego®-like Scaffolds

Two-photon polymerization was used to develop Lego®-like interlocking scaffolds for tissue engineering, which contain arrays of cylindrical pillar structures on both sides of a flat Ormocer® chip. These structures could be used either as free-standing scaffolds or stackable blocks for layer-by-layer replication of heterogeneous tissues. Figure 26 contains a CAD image and an optical micrograph of a free standing Lego®-like scaffold fabricated by two photon induced polymerization. The pillars were 75 μm in diameter and 20 μm in height, and can be observed in and out of focus on either side of the Ormocer® substrate.

Figure 27 contains optical and fluorescence micrographs of live/dead-stained B35 neuroblast-like cells encapsulating the pillars, 48 h after inoculation. Figure 28 contains fluorescent micrographs of B35 neuroblast-like cells on Ormocer® Lego®-like structures at several magnifications. The cytoskeleton is denoted by a green color, and the nuclei are denoted by a blue color. Live/dead assays were performed to determine the viability of epithelial-like and neuroblast-like cells. The optical fluorescence micrographs of live/dead assay-stained B35 neuroblast-like cells on Ormocer® surfaces are shown in Figure 29. 100% of the B35 neuroblast-like cells and HT1080 epithelial-like cells remained viable 48 h after inoculation on the Ormocer® substrates. The growth profiles of the cells are shown in Figure 30. The number of live epithelial-like and neuroblast-like cells was found to gradually increase over time. No significant difference was noted between the growth rates for cells on the polystyrene, Ormocer® or extracellular matrix substrates at 96 h, when the cells were nearing confluency on the substrates. These results suggest that polymerized Ormocer® surfaces do not significantly impair cell viability or growth rates.

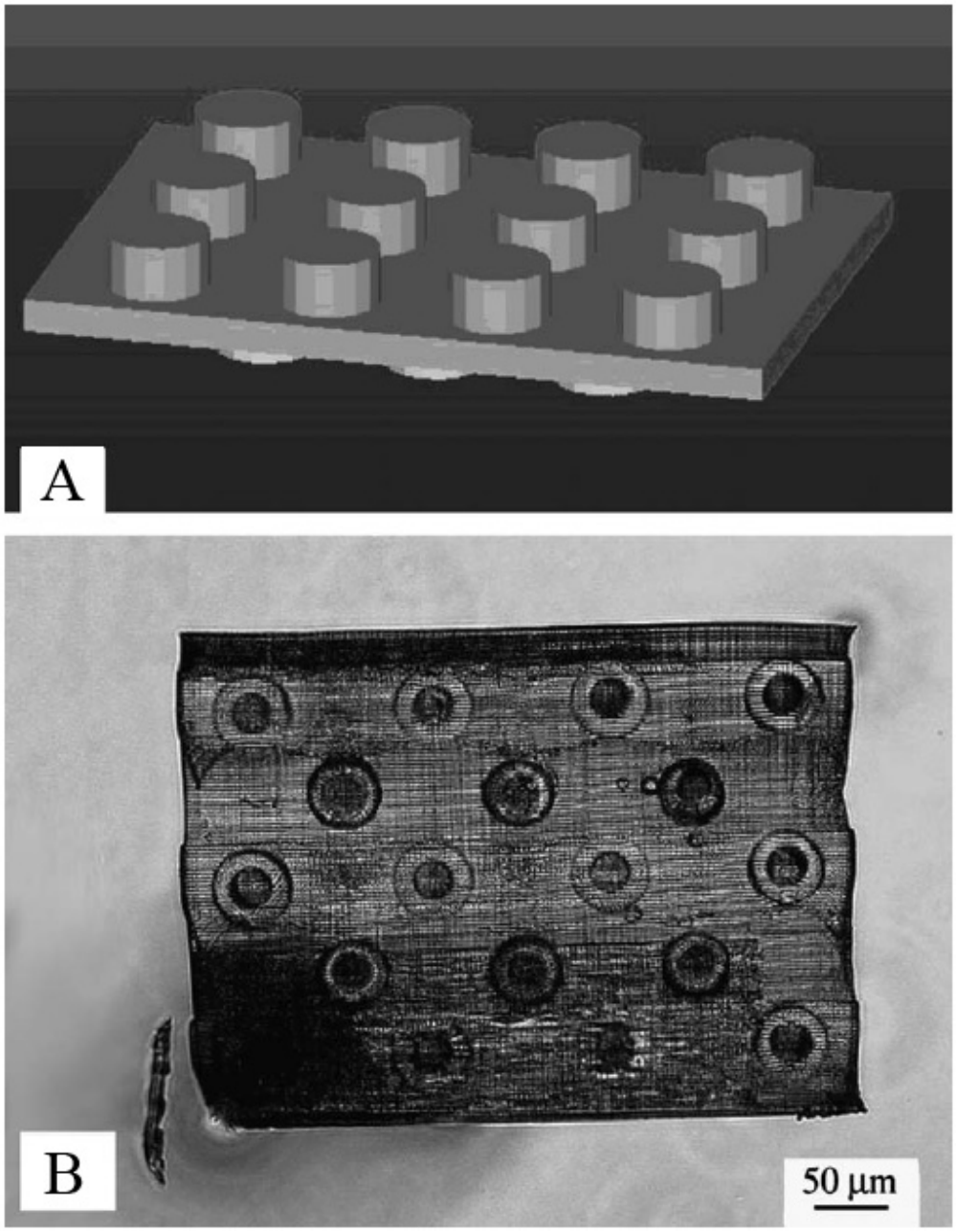

Figure 26. A: CAD image and **B:** optical micrograph of Ormocer® Lego®-like structure microfabricated by 2PP. *Scale bar equals 50 µm.*

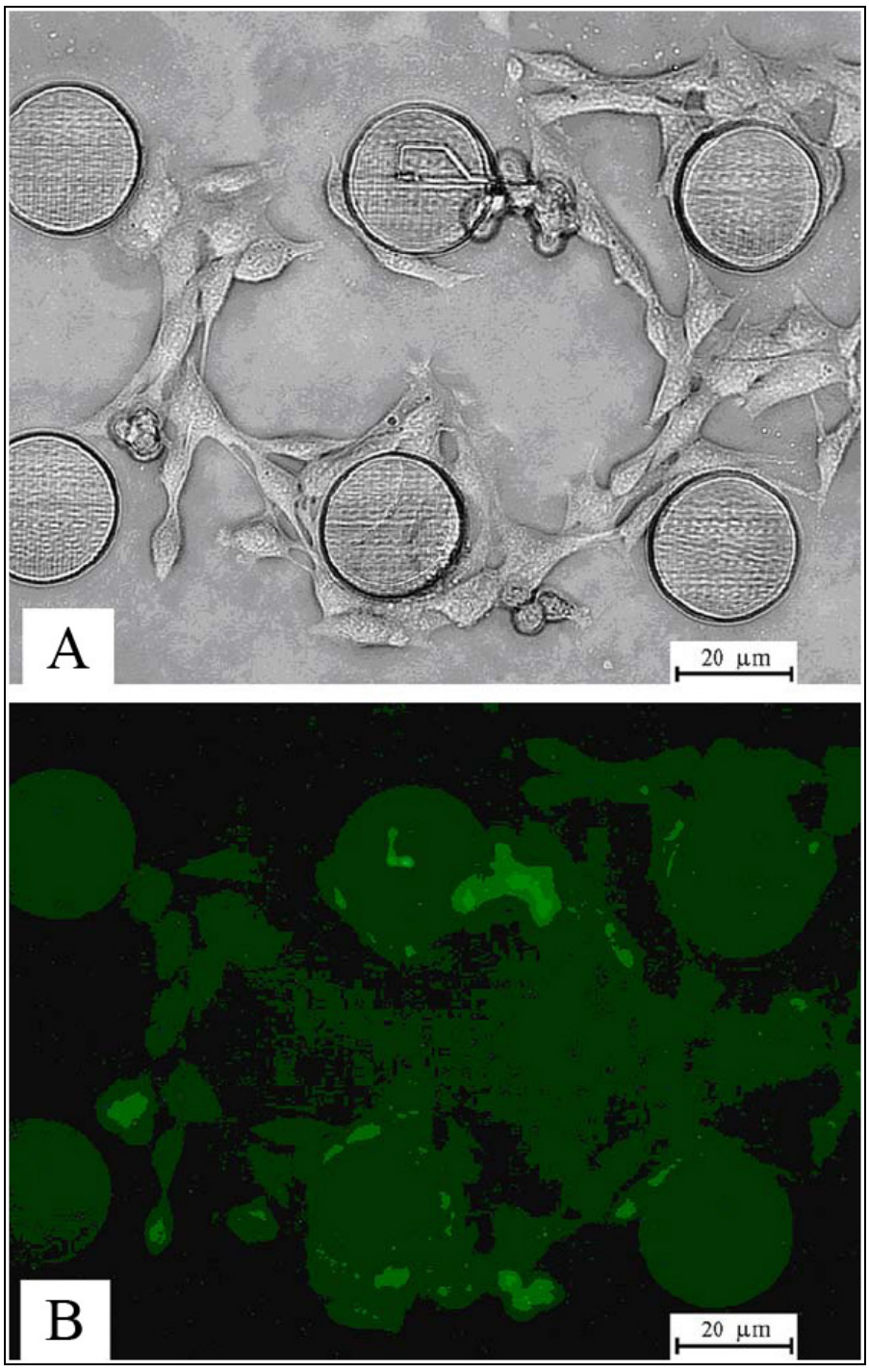

Figure 27. Optical/fluorescent micrograph of B35 neuroblast-like cells on 75 µm Lego®-like structures, 48 h after seeding. *Scale bar equals 20 µm.*

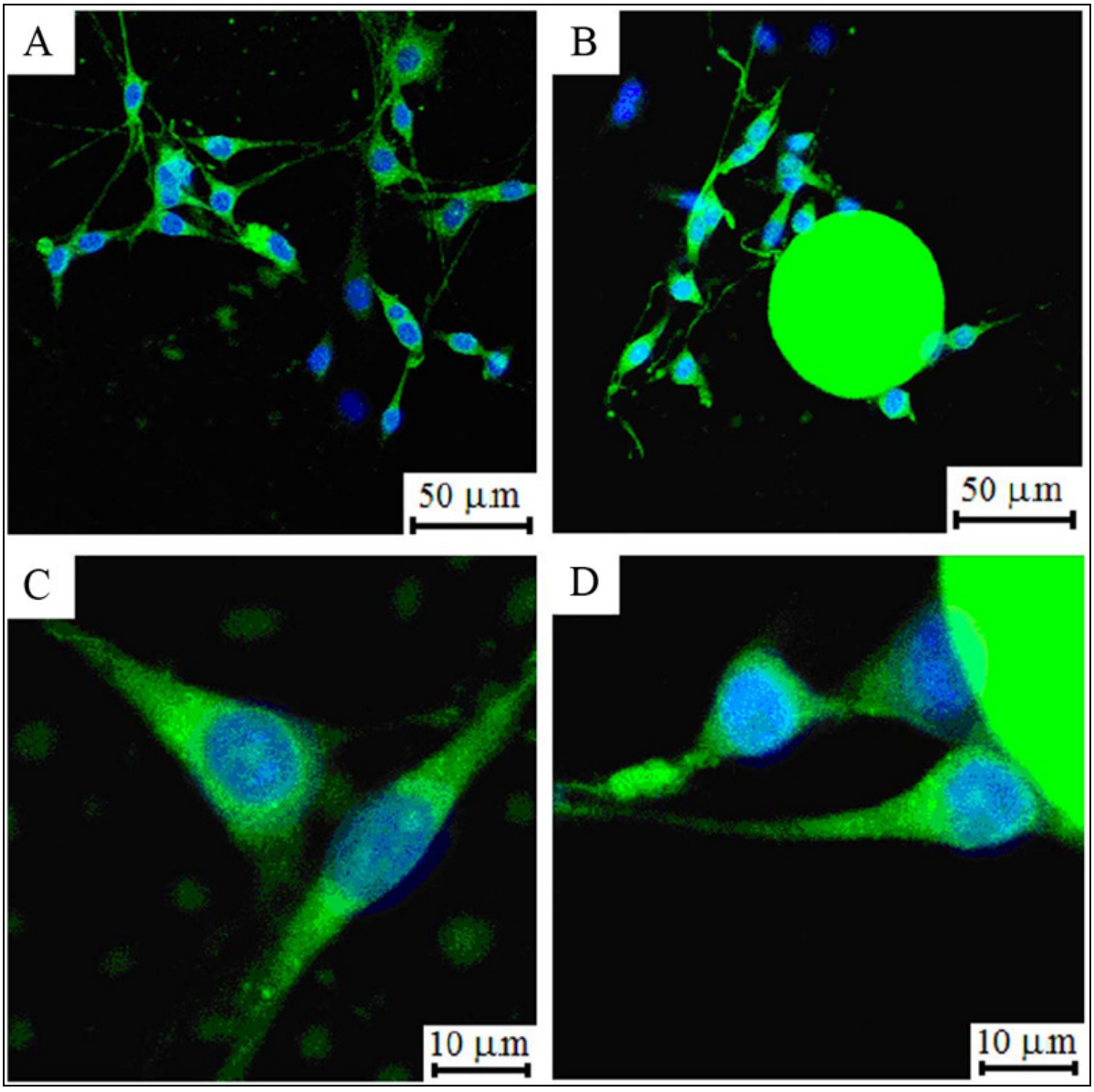

Figure 28. Fluorescent micrographs at several magnifications of B35 neuroblast-like cells on Lego®-like Ormocer® structures 48 h after seeding. *Scale bar equals 50 µm for A, B and 10 µm for C, D.*

.

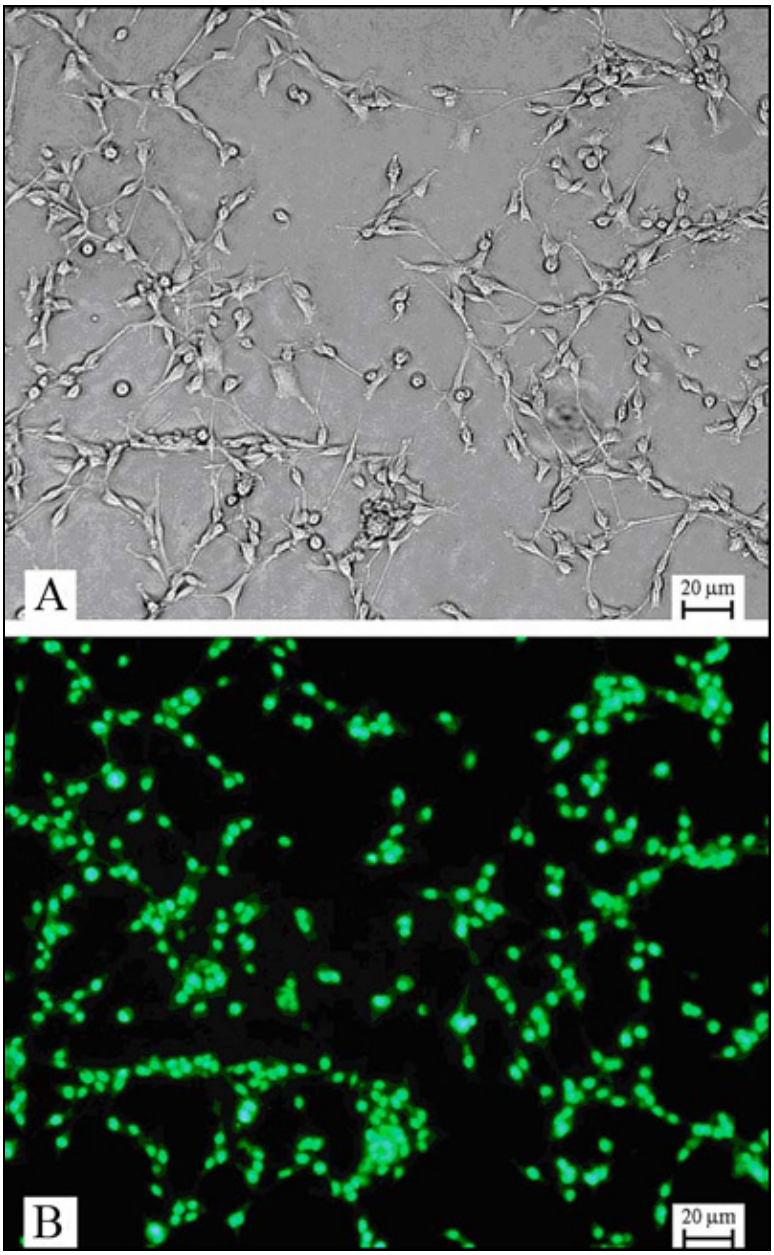

Figure 29. A) Optical micrograph and **B)** fluorescence micrograph of live/dead assay-stained B35 neuroblast-like cells on an Ormocer® surface, 48 hours after inoculation.
Scale bar equals 20 µm.

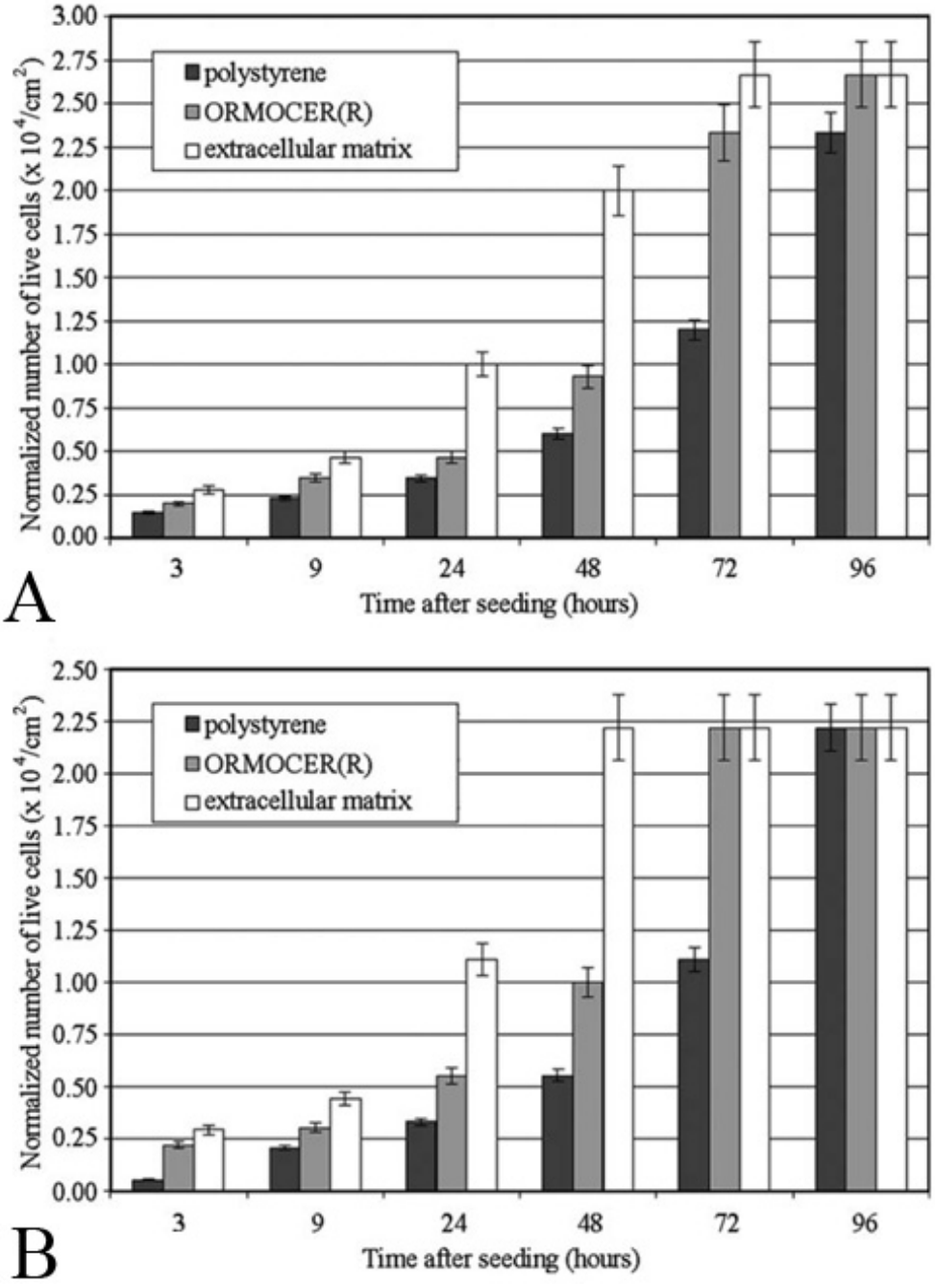

Figure 30. Growth profile of **A:** HT1080 human epithelial cells and **B:** B35 neuroblast-like cells on Ormocer® surfaces. *Values expressed as mean ± standard deviation.*

3.1.4 Microneedles Validation Study

Ormocer® microneedle arrays were fabricated by two-photon polymerization in various geometries. Firstly, CAD images of the various designs were developed using AutoCAD® software. Figure 31 contains a few CAD images used for fabrication of microneedles with varying tip-sharpness. Tip sharpness was changed by adjusting the position of the channel relative to the central symmetry axis in the original design, as illustrated in Figure 32. These designs were developed to allow less than 5% tolerance and after compensating for polymer shrinkage. Figure 33A contains an Ormocer® off-centered microneedle with a base diameter of 150 μm, off-center displacement of 1.4 μm and a length of 550 μm. Figure 33B contains a 3x3 microneedle array that have off-center displacement of 20.4 μm, base diameter of 150 μm and needle lengths of 550 μm.

Scanning electron micrograph of Ormocer® hollow microneedles with 0 μm off-center displacement and aspect ratios of 3:1, 3.5:1 and 4:1 is shown in Figure 34. The microneedle tapers linearly from the base to the tip and a ripple-like feature can be observed on the walls of the needles. This can be attributed to the layer by layer fabrication approach, and can be eliminated by increasing the number of the layers and reducing the distance between them. The aspect ratios were changed by changing the diameter of the base in the original design. However, the inner-channel diameter for flow remained constant for all the samples. The four openings visible at the base of the needle were connected to the channel. These designs were incorporated to allow rapid and efficient removal of the non-cross-linked polymer from the channel, since one end of the needle would be blocked by the substrate. Figure 35 contains image of microneedles developed with saw-toothed walls. Figure 36 compares the size of microneedle arrays with a conventional hypodermic needle.

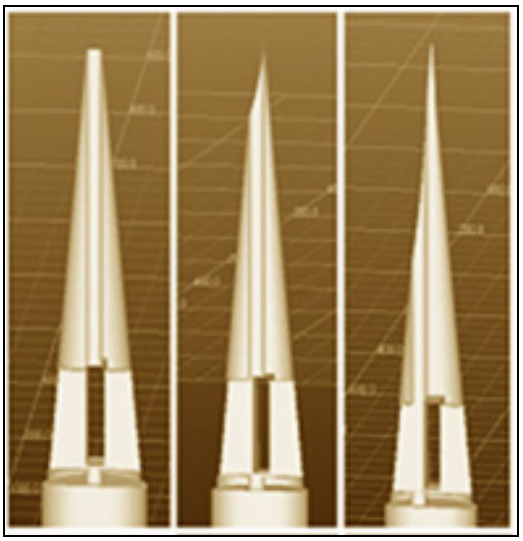

Figure 31. Computer aided design (CAD) of microneedles with varying geometry of tip-sharpness and location of pore from centre.

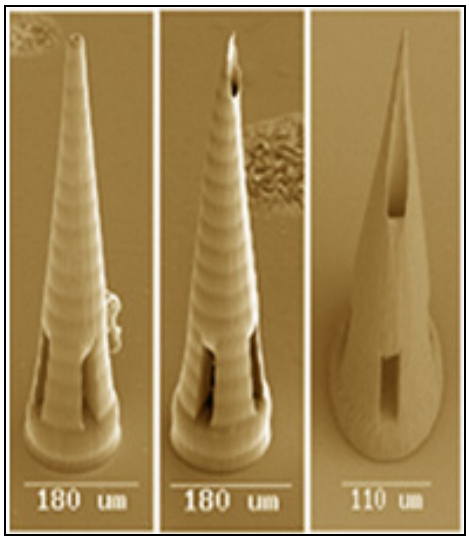

Figure 32. Scanning electron micrograph of Ormocer® microneedle with centre displacement of 0 μm, 1.4 μm, and 20.4 μm (left to right).

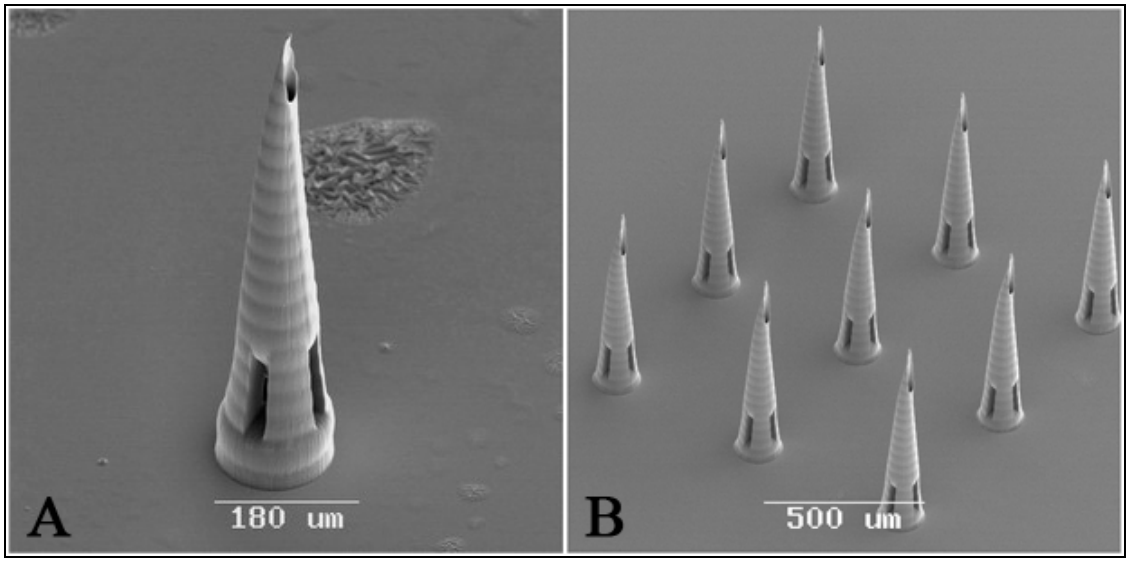

Figure 33. Scanning electron micrograph of **A)** a single 1.4 μm off-centered microneedle and **B)** 3x3 array of 1.4 μm off-centered microneedles fabricated by 2PP process.

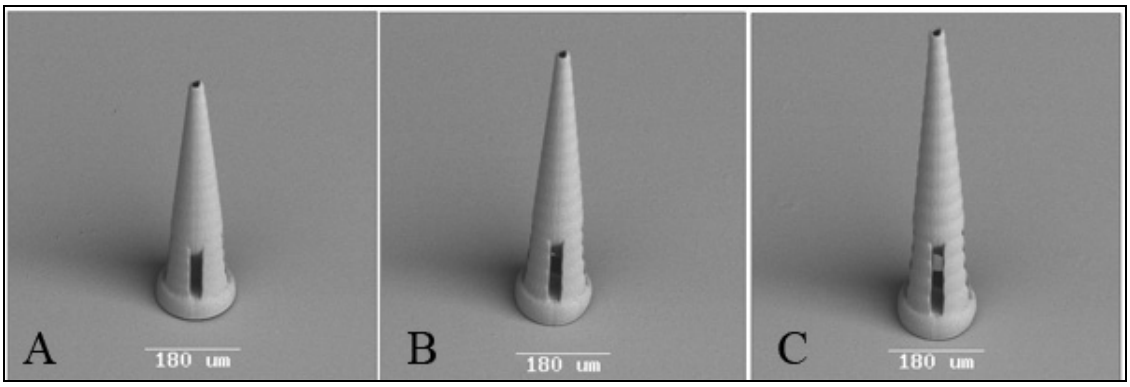

Figure 34. Scanning electron micrograph of Ormocer® hollow microneedles (0 μm off-center displacement) with various aspect ratios such as 3:1, 3.5:1 and 4:1.
Scale bar equals 50 μm.

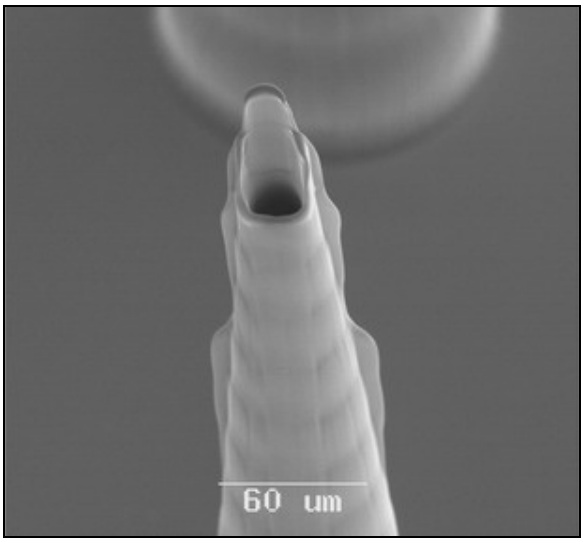

Figure 35. Scanning electron micrograph of microneedles with saw-toothed walls.

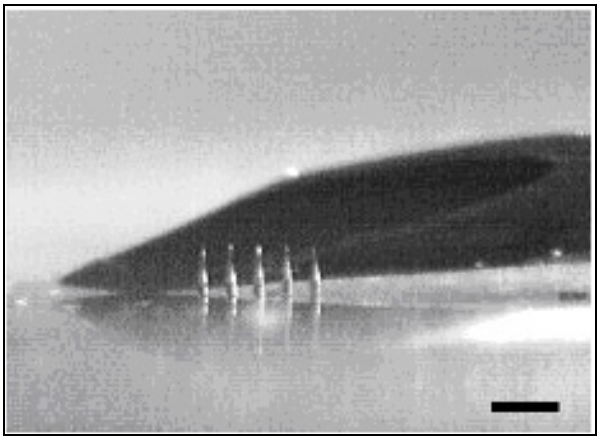

Figure 36. Optical micrograph of Ormocer® microneedle arrays compared with a hypodermic needle. *Scale bar equals approximately 600 μm.*

In developing microneedles, it was desirable to fabricate needles that required least loading during penetration of the skin. Flexibility of 2PP allows rapid iterations in fabrication of microneedles with complex geometries. In order to determine the effect of the needle tip sharpness, different needle arrays were tested against porcine fat and full-thickness skin. Porcine fat provided a uniform surface for testing compared with highly non-uniform skin. Figure 37 contains an optical micrograph of an off-centered microneedle on full-thickness skin with the various layers labeled. Depending on the load and control over z-axis, the microneedle developed may penetrate well into the dermis layers.

Figure 38 contains load-displacement curves for microneedle arrays where the center of the channel was displaced by values indicated. The slopes on the curve may be divided into three regions, exhibiting different trends. The initial displacement occurred when the needles come in contact with the tissue and exerts pressure on it. Subsequently, the middle region contains information on the actual needle penetration through the sample. The initial 'dip' the curve indicated the region where the load threshold on the surface of the tissue was reached. Here, the tissue was pierced by a few microneedles simultaneously. The value of the load at this point would represent the minimum load required to pierce the tissue surface. The final displacement in the curve indicated the contact with the cover slip containing microneedles.

The microneedle with the 20.4 μm off-center location has the sharpest tip and the lowest value of penetration-threshold (*load required to puncture*) among the off-center geometries. Owing to the presence of methacrylate groups in the cross-linked Ormocer®, the structure stays somewhat elastic. During the test the tip bends even further, resulting in increased penetration resistance and therefore the larger values of load threshold for

penetrations. Similar load vs. displacement curves acquired for microneedles with different aspect ratios indicated a minor difference in the load values for different needles, but there was no statistical significance in the difference. The tests against polytetrafluoroethylene surfaces however suggested dependence in failure. In general, the larger the base of the microneedle, the higher the load it can endure before breaking or bending. Majority of the microneedles bend, and eventually tip off the glass when tested against polytetrafluoroethylene. The microneedles with larger base diameters break instead of bending at higher loads, which again confirms their greater mechanical stability. An alternative possibility in improving the mechanical property may be in introducing a microneedle post-bake processing step allowing the epoxy groups contained in the polymer to crosslink. Depending on the post-bake duration, the structures may become less elastic, and eventually brittle.

Fracture and penetration study of microneedles with saw-toothed walls showed no significant differences in load response. A separate trial on piezoelectric actuation (in x, y, and z) over 80 μm range to mimic mosquito fascicle movement also showed no significant difference in load response when compared to no piezoelectric actuation. In previous studies, hollow Ormocer® microneedles with large wall thicknesses fabricated by 2PP have shown a non-linear stress–strain response.[142] These results suggest that 2PP may be employed to create medical microdevices with a larger range of sizes, shapes, and materials than conventional polymer, silicon, stainless steel, or titanium microfabrication techniques.

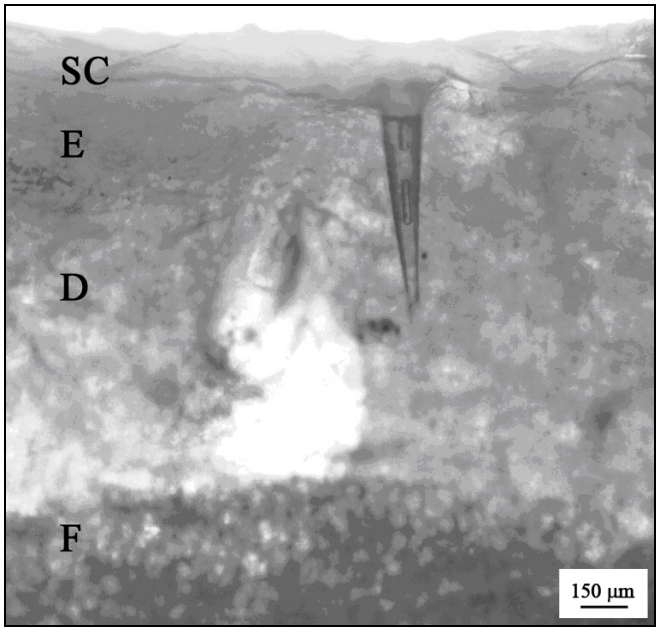

Figure 37. Optical micrograph of an off-centered microneedle on full-thickness porcine skin. The stratum corneum **(SC)**, epidermis **(E)**, and dermis **(D)**, and fat **(F)** layers of the full-thickness skin are indicated. *Scale bar equals 150 µm.*

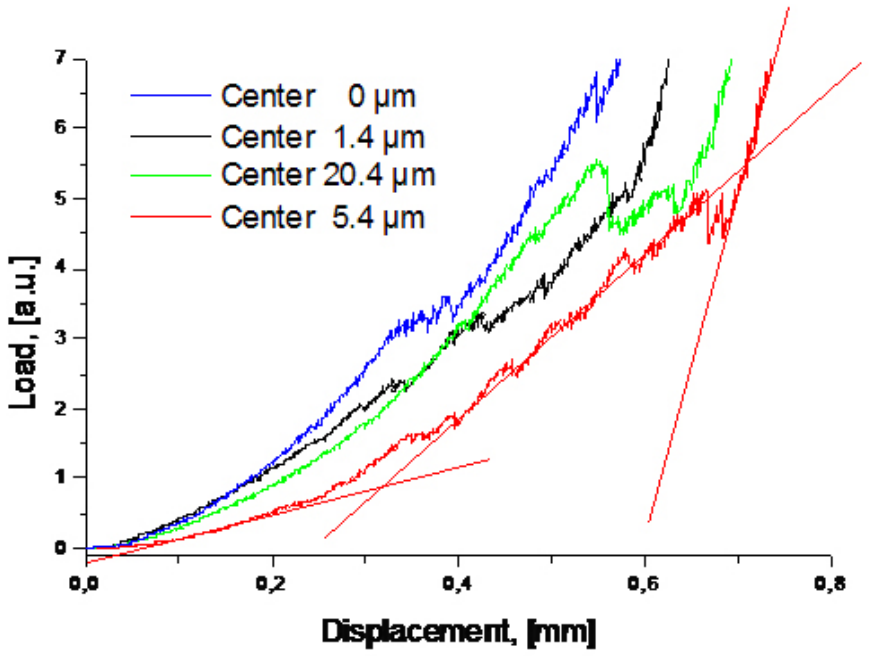

Figure 38. Load vs. Displacement results for microneedle arrays with varying tip sharpness.

Controlled administration of fluorescein-conjugated biotin (a water-soluble B-complex vitamin) into the dermal and hypodermal regions of skin was achieved using off-centered microneedles. Figure 39 contains DIC-fluorescence micrographs of biotin-administered skin sections (frozen at various times). The images containing the microneedle perforations showed penetration into the epidermal/dermal junction. At 60 minutes, the control of topically applied biotin showed no dispersion beyond the stratum corneum layer. However, administration of biotin via microneedles showed penetration well into the dermal layers of skin at 60 minutes. At 0-5 minutes, the biotin was localized in the perforation created by the microneedles. At 20 minutes, the diffusion of biotin into the dermal/epidermal junction was evident. At 60 minutes, the entire dosage of biotin diffused deep into the dermal/hypodermal region of the skin.

Controlled administration of 8 μM Qdot® 655 ITK™ amino (PEG) quantum dot solution into dermal layers was also achieved using off-centered microneedles. Figure 40 contains DIC-fluorescence micrographs of QD-administered skin sections *(frozen at various times)*. As with biotin at 60 minutes, the control of topically administered QD PEG-amine showed no dispersion beyond the stratum corneum layer. Previous studies by Ryman-Rasmussen *et al.*[143] have shown that topical administration of QD PEG-amine leads to localization in the dermal layer by 8 h. Administration of QD PEG-amine by microneedles showed no dispersion at 0-5 minutes. However, at 60 minutes, extensive dispersion of QD PEG-amine was observed within the epidermal and dermal layers of skin. In comparison with topical administration, the passive diffusion/delivery to dermal layers is much more rapid using microneedles. These microneedles may also allow control over rate of dispersion and diffusion of pharmacologic agents into dermal layers by variation in the penetration depths.

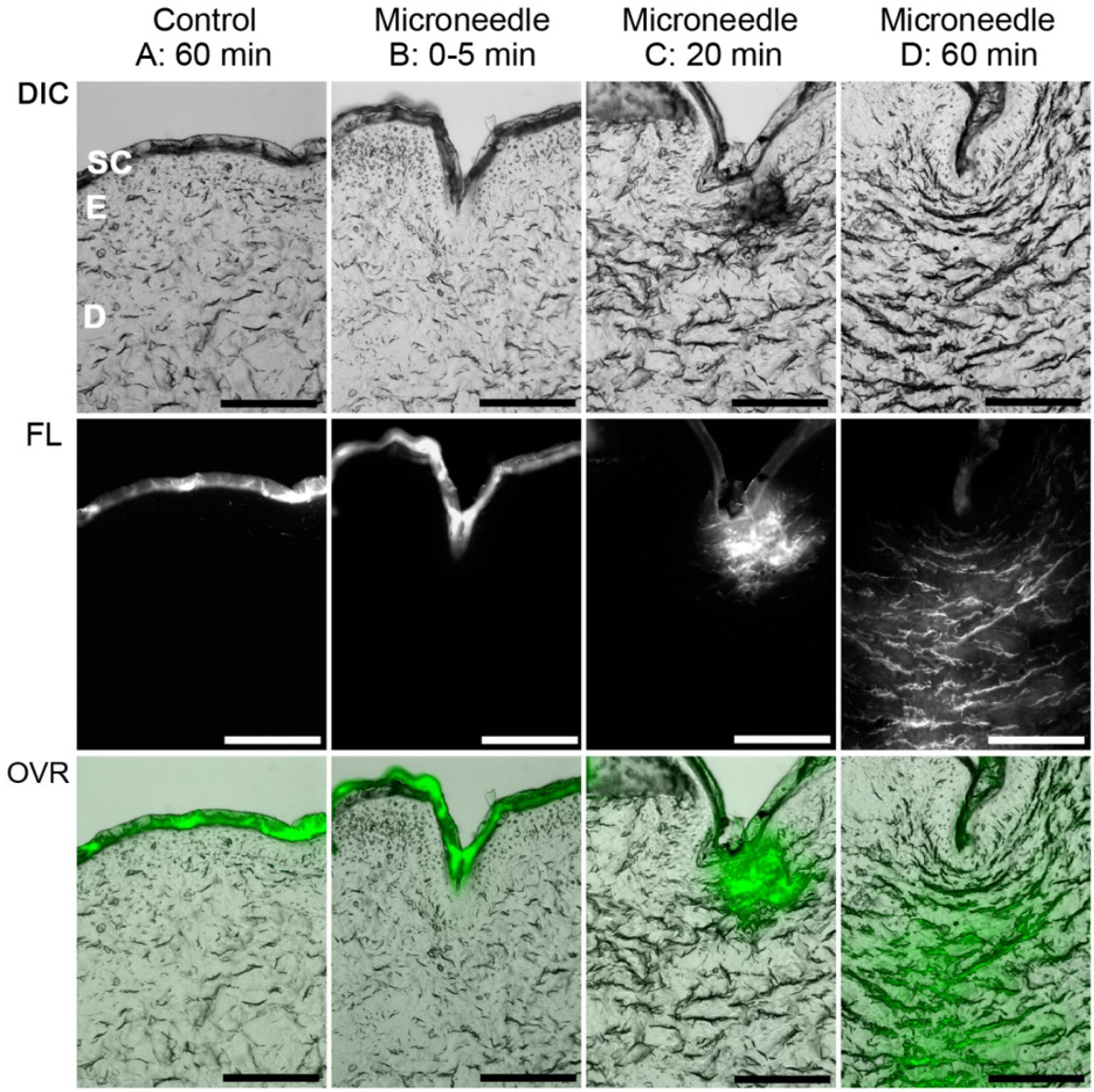

Figure 39. DIC-fluorescence optical microscopy of skin after administration of fluorescein-conjugated biotin using Ormocer® microneedles. Time of treatment with microneedle (5 min, 20 min, and 60 min) is noted on top of each column and may be compared with control at 60 min (without microneedle). **Top row: DIC** single-channel allows clear view of the various skin layers. The stratum corneum (SC), epidermis (E), and dermis (D) layers are indicated. **Middle row: fluorescence scans (FL)** of fluorescein-biotin emission. **Bottom row: DIC-fluorescence overlay (OVR)** with the fluorescence channel (Green) shows distribution of biotin within the skin layers. *Scale bar equals 100 μm.*

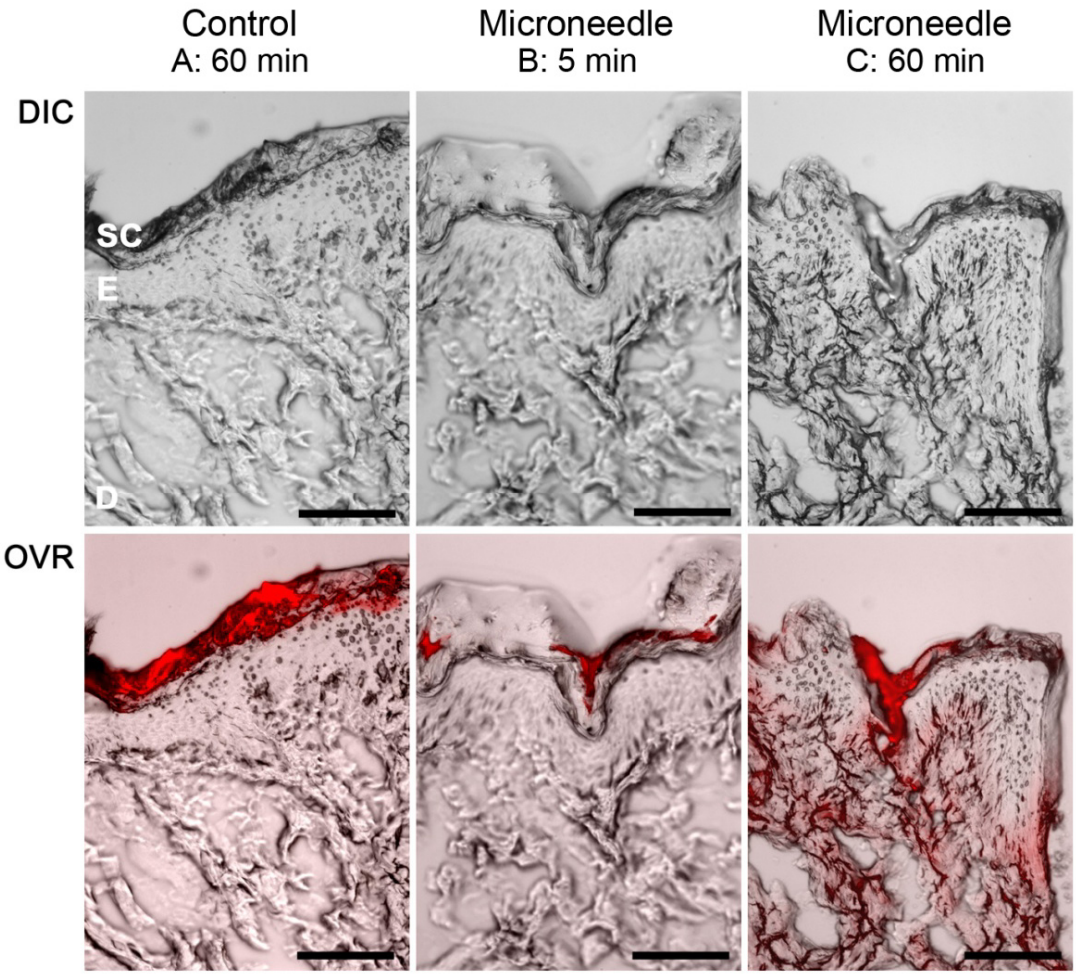

Figure 40. DIC-fluorescence optical microscopy of skin after administration of PEG-amine (NH_2)-coated quantum dot (QD 655) using Ormocer® microneedles. Time of treatment with microneedle (5 min and 60 min) is noted on top of each column and may be compared with control at 60 min (without microneedle). **Top row: DIC** single-channel allows clear view of the various skin layers. The stratum corneum (SC), epidermis (E), and dermis (D) layers are indicated. **Bottom row: DIC-fluorescence overlay (OVR)** with the QD-fluorescence channel (Red) shows distribution of QD within the skin layers. *Scale bar equals 100 μm.*

Microneedle arrays developed using conventional microelectronics fabrication techniques have inherent limitations that preclude the development of complex geometries and large microneedle wall thicknesses.[144-148] CAD/CAM rapid prototyping may allow fabrication of complex geometries with rapid iterations. Novel microneedles developed in this fashion may be integrated with MEMS devices to allow control over amount and rate of pharmacologic administration. The control over the geometry of the microneedle enables its application for both drug delivery and blood drawing.

3.1.5 Ossicular Replacement Prosthesis

Ormocer® ossicular replacement prostheses were fabricated by two-photon polymerization process. The design used in this study was similar to that of a commercially available TORP prosthesis (*Kurz Medical Inc., Dusslingen, Germany*). Figure 41 contains a CAD and optical image of the TORP-shaped Ormocer® ossicular prostheses. The prostheses stand 4.3 mm tall, 300-400 μm wide at shaft, 2.6 mm wide and 400-500 μm thick at the disk-shaped headplate. The disk-shaped headplate of the prosthesis was designed to be placed under the tympanic membrane. The shaft of the prosthesis was designed to connect the footplate of the stapes with the undersurface of the tympanic membrane in order to enable sound conduction. The headplate also contained five microneedle-like structures protruding at 400 μm with 160 μm base width. These structures were introduced to improve cellular adhesion, reduce device migration, and decrease the likelihood of perforation of the tympanic membrane. Figure 42 contains optical micrographs of Ormocer® TORP fabricated by 2PP using two different head-plate designs.

Nanoindentation tests performed on the surface of the headplate of the ossicular prosthesis were compared with thin-film Ormocer® material (Figure 43). As the load increased, the measured values of Hardness (H) and Modulus (E) of the Ormocer® thin-film were found to be significantly higher than the headplate surface. Both values were consistently higher by a factor of four in the thin-film material. Figure 44 contains atomic force micrographs of the Ormocer® headplate surface. A wavy-surface can be observed over a scan range of 70 μm using topographic and LFM mode.

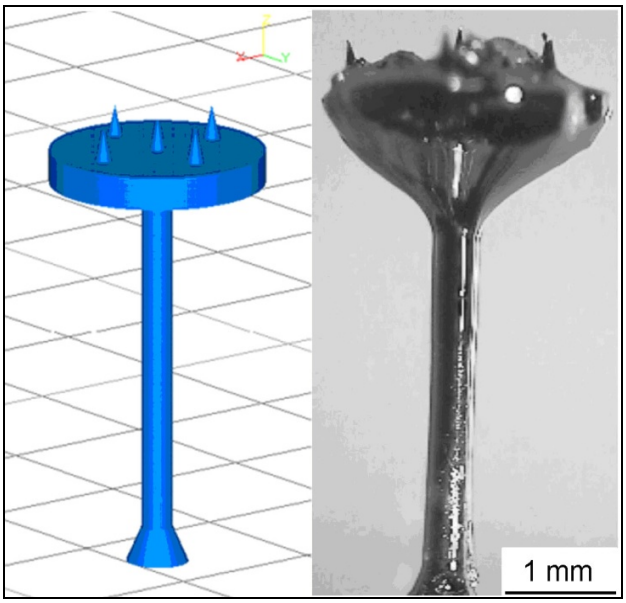

Figure 41. CAD images and optical micrograph of TORP-shaped ossicular replacement prosthesis. *Scale bar equals 1 mm.*

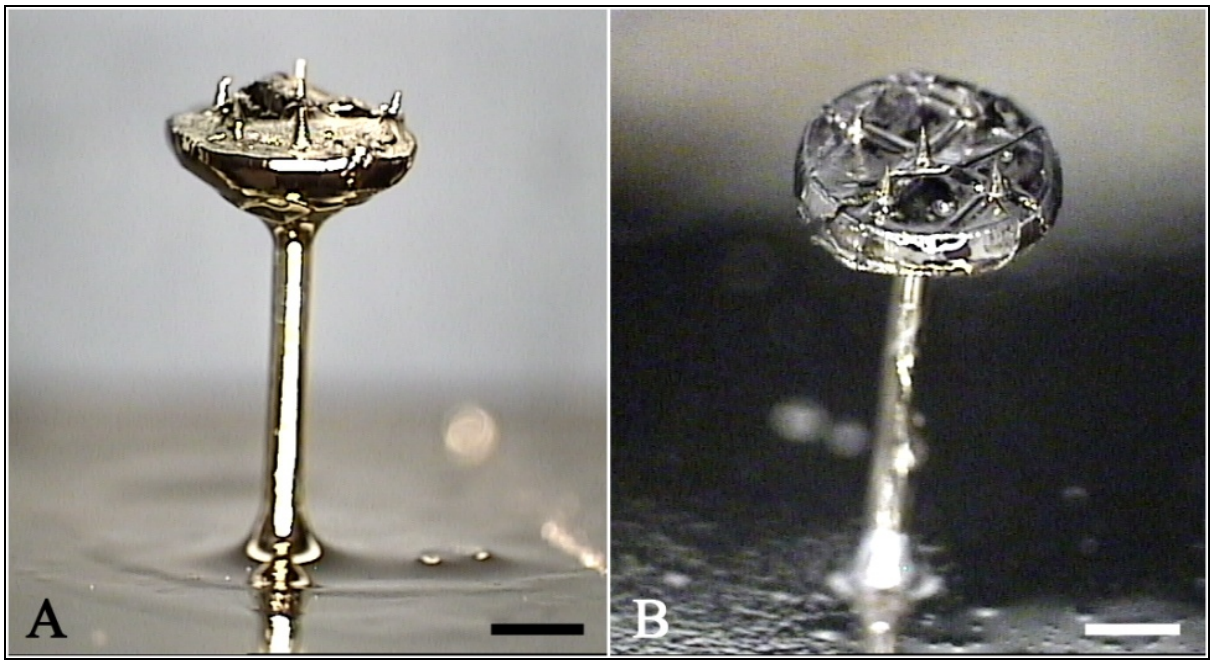

Figure 42. Optical micrographs of total ossicular replacement prosthesis fabricated by two-photon polymerization. Scale bar equals 1 mm.

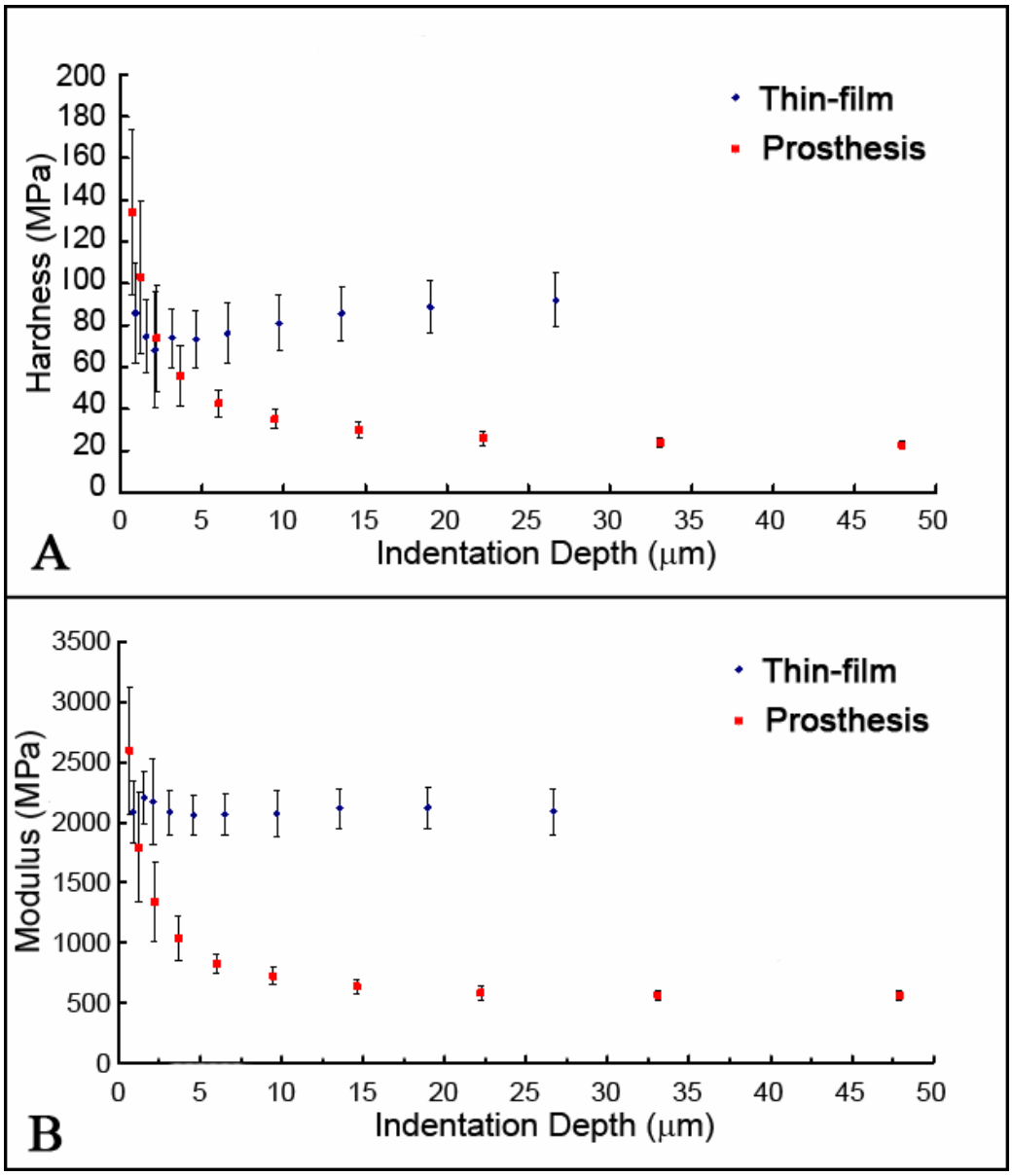

Figure 43. Nanoindentation results of Ormocer® thin-film and ear-prosthesis. **A:** Graph of hardness (MPa) vs. indentation depth (mm) and **B:** graph of modulus (MPa) vs. indentation depth (mm). Symbols "◆" and "■" represent values for Ormocer® thin-film and Ormocer® prosthesis, respectively. *Bars in graph A and graph B indicate standard deviation of mean hardness and modulus values, respectively.*

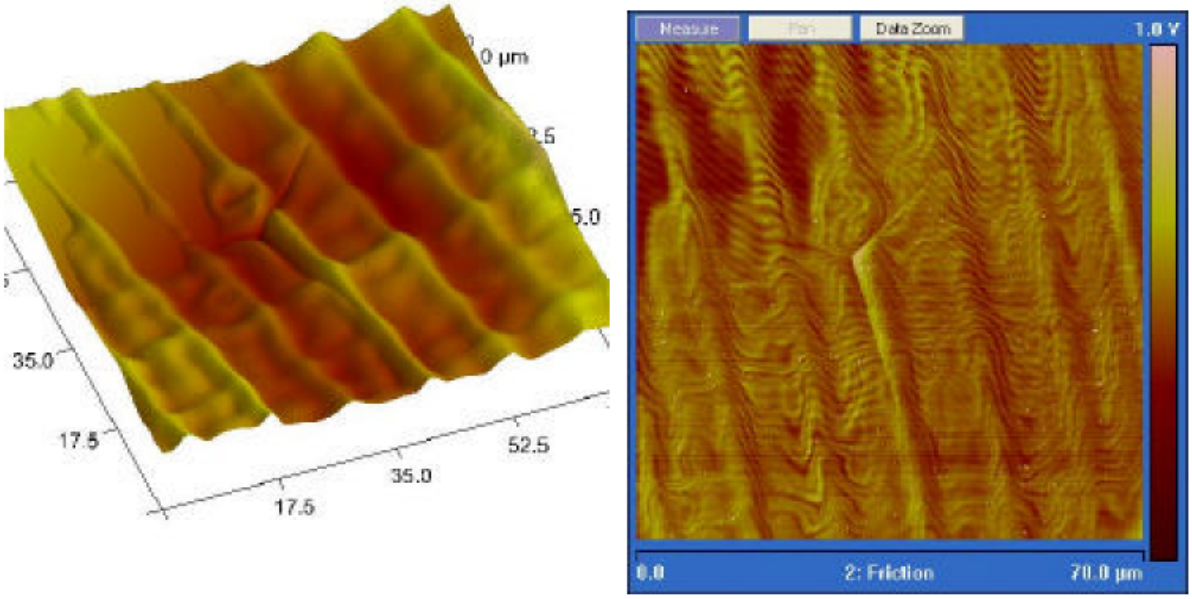

Figure 44. AFM topographic scan and LFM image of Ormocer® ossicular prosthesis surface.

A total ossicular replacement prosthesis fabricated using 2PP may be developed for patient-specific geometries in order: (a) sustain small angles between the stapes and the prosthesis, which is associated with piston-like movement; (b) position the prosthesis on the center of the footplate to minimize rotation; (c) suitably align the prosthesis with respect to the surrounding middle ear structures.[149] The Ormocer® ossicular replacement prosthesis demonstrated greater flexibility than commercially available TORP prostheses. In addition, the shaft–disk interface was more flexible and moldable than that observed in conventional titanium implants. Certain components of the ossicular replacement prosthesis may benefit from increased flexibility. For example, bending of the disk-shaped headplate with respect to the shaft may provide more stable fixation of the implant with respect to the tympanic membrane.[150] The implantation process through the right external auditory canal is shown in Figure 45. A tympanomeatal flap was raised before and was flapped back prior to the procedure. The prosthesis was positioned on the footplate of the stapes below the tympanic membrane to provide sound conduction, as found in natural middle ear. The prosthesis was handled without fracture during the entire procedure.

Ormocer® ossicular replacement prosthesis has shown good mechanical properties, cytocompatibility, ease of forming and ease of handling. As mentioned earlier, conventional mass-produced implants do not sufficiently take individual patient anatomy into account. CAD/CAM rapid prototyping by 2PP may permit development of patient-specific geometries to allow unique fit with surrounding middle ear configurations and minimize prosthesis rotation and migration. Imaging (computed tomography or magnetic resonance imaging) and analysis software may be employed to generate implants with appropriate design, structure, and material properties for a particular patient.

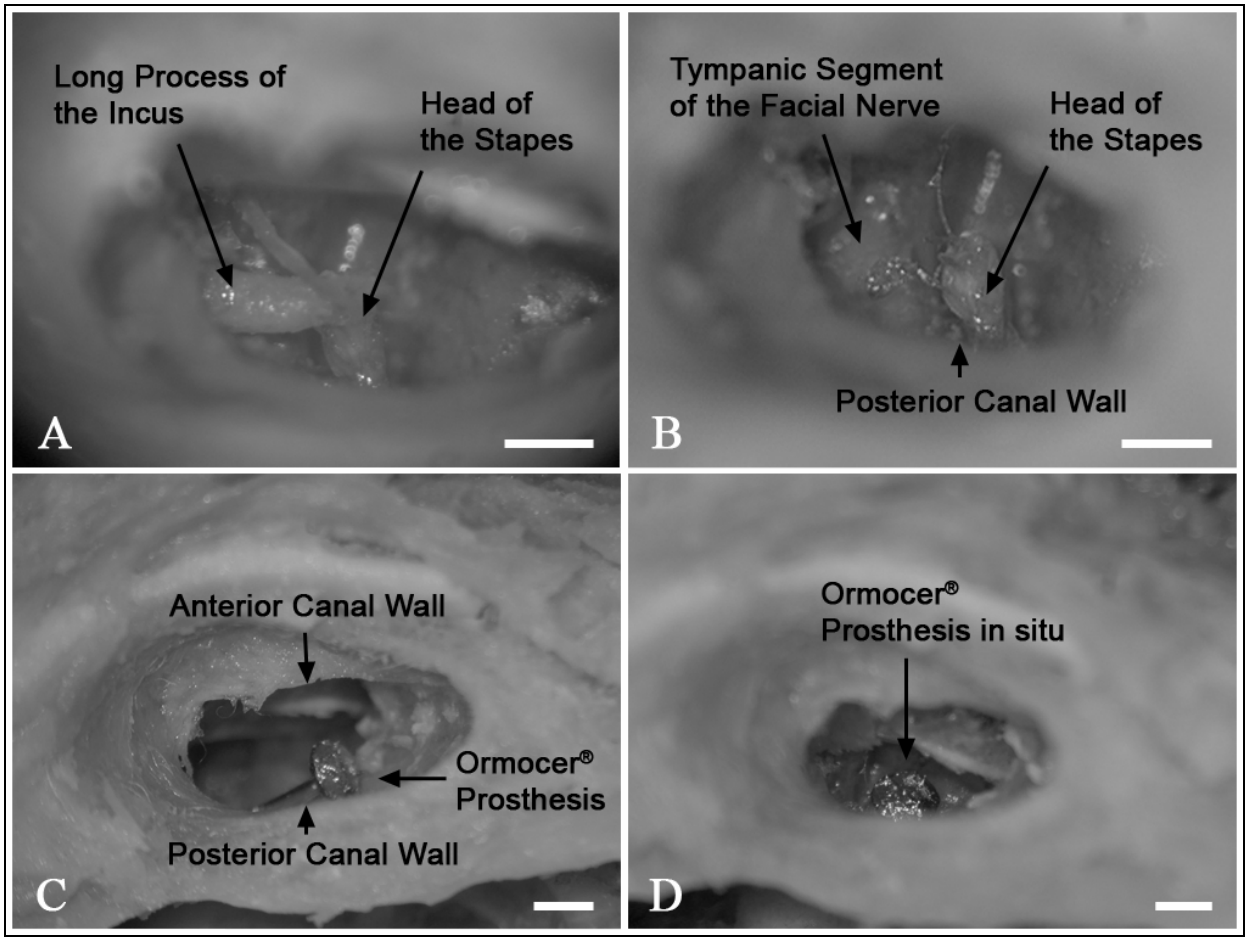

Figure 45. Implantation of Ormocer® ossicular replacement prosthesis into a commercially obtained un-frozen human head (right ear). **A)** View onto the incudo-stapedial joint. The chorda tympani has been partly removed. **B)** View onto the head of the stapes after the incus has been removed. **C)** View through external ear canal onto the eardrum. Ormocer® prosthesis lies against the posterior canal wall. **D)** Implant in situ with tympanomeatal flap raised anteriorly. *Scale bar equals 2 mm.*

3.2 MDW – MAPLE DIRECT WRITE

In a conventional approach, matrix-assisted pulsed laser evaporation direct write or MDW utilizes a UV source light to evaporate the solvent to drive the solute or suspended particles forward to a receiving substrate.[151] In depositing sensitive materials such as biomolecules and viable cells, the absorption coefficient of the solvent might not be entirely preclude absorption by the biomolecules. To by pass this, an intermediate absorbing layer was developed. Decomposing non-toxic polymers with high absorption coefficient near the UV-spectrum are thought to be promising. The ablation characteristics for various polymers have been studied earlier[152] to determine the appropriate polymer for the required absorption coefficient and threshold fluence.

3.2.1 Cell Micropatterning using TP Release Layer

Triazene polymer (TP) has an effective absorption coefficient of the triazene polymer is calculated to be 49800±2900 cm^{-1} at a threshold fluence of 27±2 mJ/cm^2 at 308 nm. At 248 nm the threshold absorption coefficient is at a fluence range of 16 to 32 mJ/cm^2. [153] The increase in transmission ratio with increasing wavelengths suggests lower transmission at 193 nm wavelength. The thermal ablation of the polymer at UV results in release of N_2 with a relevant bond energy in N=N of approximately 1.7 eV. The ablation parameters were calculated by the equation: $d(F) = 1/\alpha_{eff} \ln (F/F_{th})$; where d(F) is the ablation rate (fluence/pulse), α_{eff} is the effective absorption , and F_{th} the threshold ablation rate.

As a preliminary step in the study, the cytoompatibility of the triazene polymer material was investigated. Various cells including MG63 osteosarcoma, B35 neuroblast-like cells-like, and C2C12 myoblast-like cells were studied for adhesion, viability and growth on the triazene polymer substrate. Results demonstrated good adhesion and growth in comparison with polystyrene surface as control. *Live-dead* assays showed 100% viability in triazene surfaces. In the subsequent step, triazene coated ribbons were used for micropatterning viable cells onto substrates coated with ECM®.

In order to study MDW micropatterning of B35 neuroblast-like cells, a capture device was setup and the process monitored for various laser *fluence*. The threshold *fluence* F_{th} for the process was found to be approximately 0.025 J/cm^2. Various cell-patterns were generated using different input designs. Figure 46 contains optical micrographs of the ribbon used in micropatterning B35 neuroblast-like cells with and without the triazene polymer release layer. The arrows shown in Figure 46A indicate laser ablated region of the TP release layer (similar to circular laser spot-size). The cells were transferred to the substrate from the ribbon in a well defined pattern by controlled ablation of the TP layer. The remaining cells on the TP layer were observed to grow around the ablated regions.

Figure 47 contains micrographs of live/dead stained cells in the TP layer on the ribbon. The laser spot size was reduced for subsequent rows (from top right) as seen in Figure 47A. Figure 47B contains fluorescent image of the *live/dead* stained B35 neuroblast-like cells on the TP layer on ribbon. Green fluorescing viable cells can be observed. in the non-ablated regions and in ablated areas where the overlap is poor due to smaller laser spot size. The laser-ablated TP region was found to be approximately the size of an individual B35 neuroblast-like cell. Such control over individual cells may prove to be beneficial.

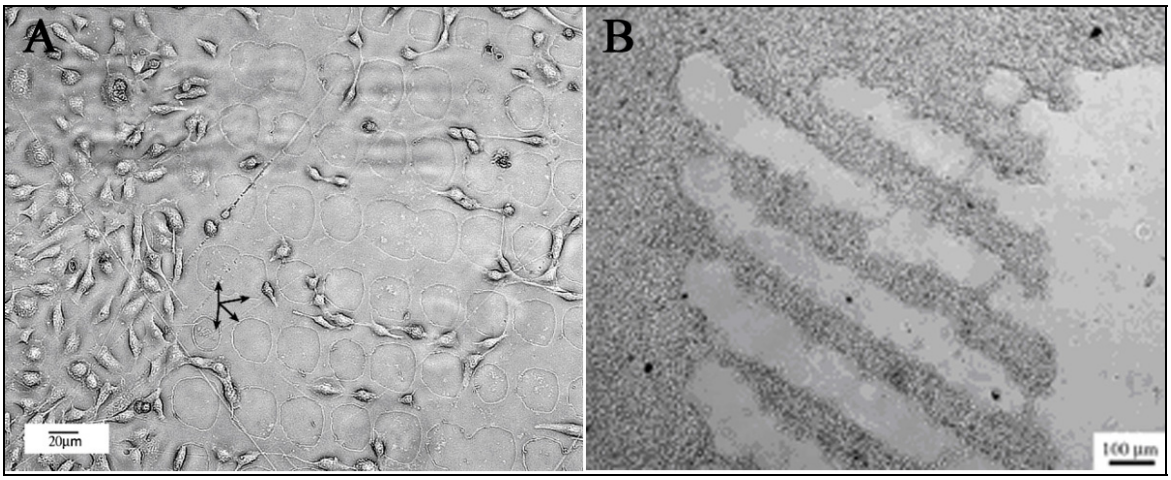

Figure 46. Optical micrographs of the ribbon used for MDW micropatterning of B35 neuroblast-like cells **A)** with triazene polymer release layer *(scale bar equals 20 µm)* and **B)** without any release layer *(scale bar equals 100 µm)*. Arrows indicate circular ablated regions of the polymer. *Images were recorded at 48 h post micropatterning*.

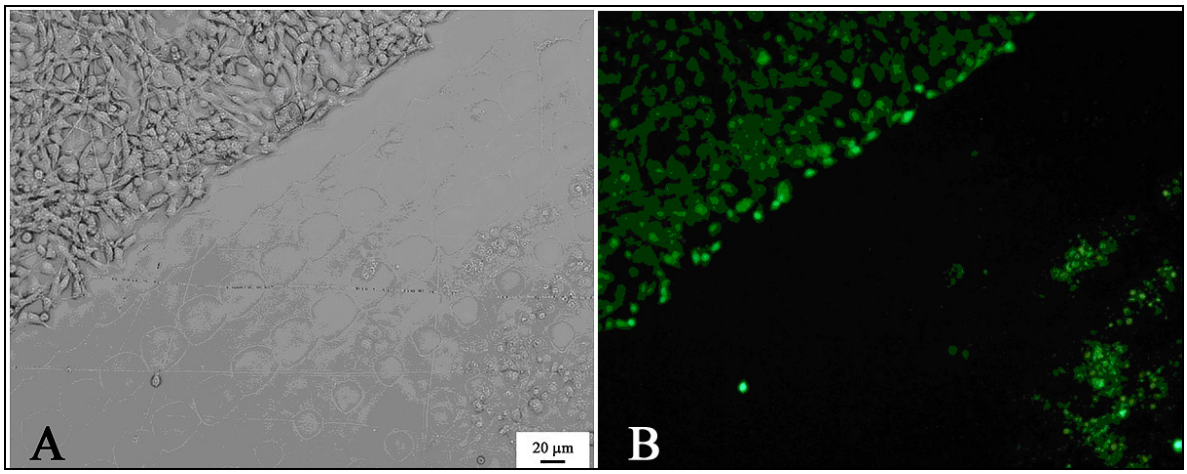

Figure 47. A) Optical and **B)** fluorescent live/dead micrographs of the ribbon with triazene-polymer release layer for MDW micropatterning of B35 neuroblast-like cells. *Images were recorded 48 h post micropatterning*. *Scale bar equals 20 µm.*

Figure 48A contains an optical micrograph of B35 neuroblast-like cells micropatterned into a box-like design. The boundaries were fairly well-defined, considering cell locomotion post micropatterning. In another pattern (Figure 48B), line width of approximately 100 μm was achieved. Figure 49 contains optical micrographs of B35 neuroblast-like cells at 6 h and 48 h post micropatterning. At 3-6 h the substrate contains few neuroblasts cells at the initial stage of growth with short axons. At 24-48 h, there is a significantly higher cell-density with longer axonal extensions, suggesting viability and proliferation post patterning. The optical micrographs at selective time points were compared to determine the growth rate based on the average number of cells per unit area. The growth rate of the B35 neuroblast-like cells micropatterned via MDW using the triazene absorbing layer was statistically similar to the growth rate of as-seeded cells. No preferential growth was observed.

Confocal images of stained nuclei and cytoskeleton of MDW cells were also compared at various time intervals. Figure 50contains confocal images at 24 h and 48 h post micropatterning. At 12-24 h the nuclei of the micropatterned cells appear intact and the development of axons cannot be clearly determined. The cells at 24-48 h post micropatterning show preservation of nuclei and some well developed axonal extensions. The current approach using triazene polymer as a release layer demonstrates successful micropatternings at threshold fluence of approximately 0.025 J/cm^2, while previous efforts were achieved at higher fluence of 0.07 to 0.1 J/cm^2. This is particularly significant in the micropatterning of viable cells and soft biomolecules. These results demonstrate that the MDW technique is competent in creating micropatterns of viable cells at low laser fluence.

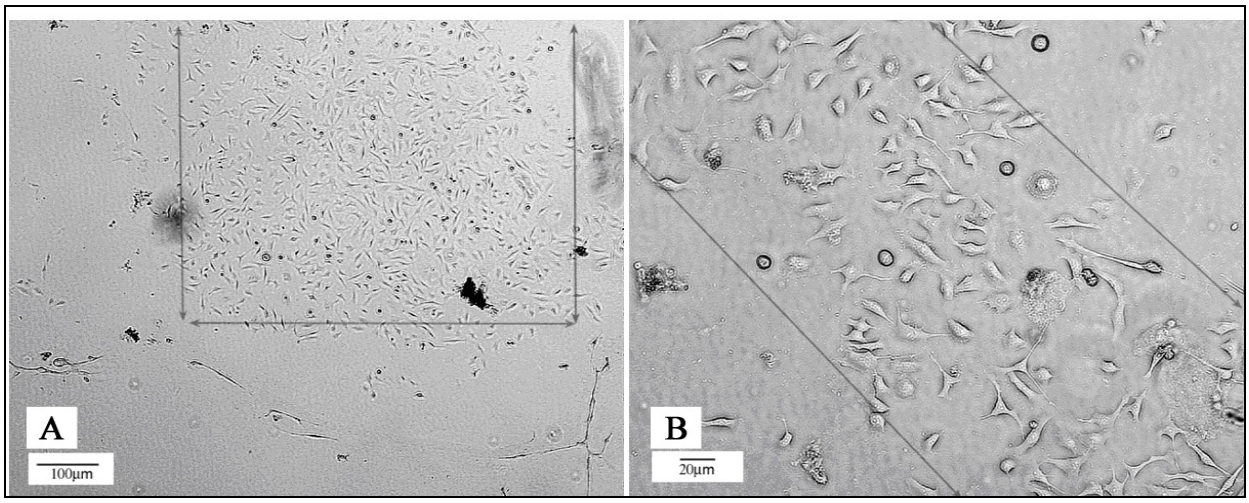

Figure 48. Optical micrograph of B35 neuroblast-like cells micropatterned into **A)** box-like design (*scale bar equals 100 µm) and* **B)** line pattern (*scale bar equals 20 µm). Arrows are drawn to guide the eye.*

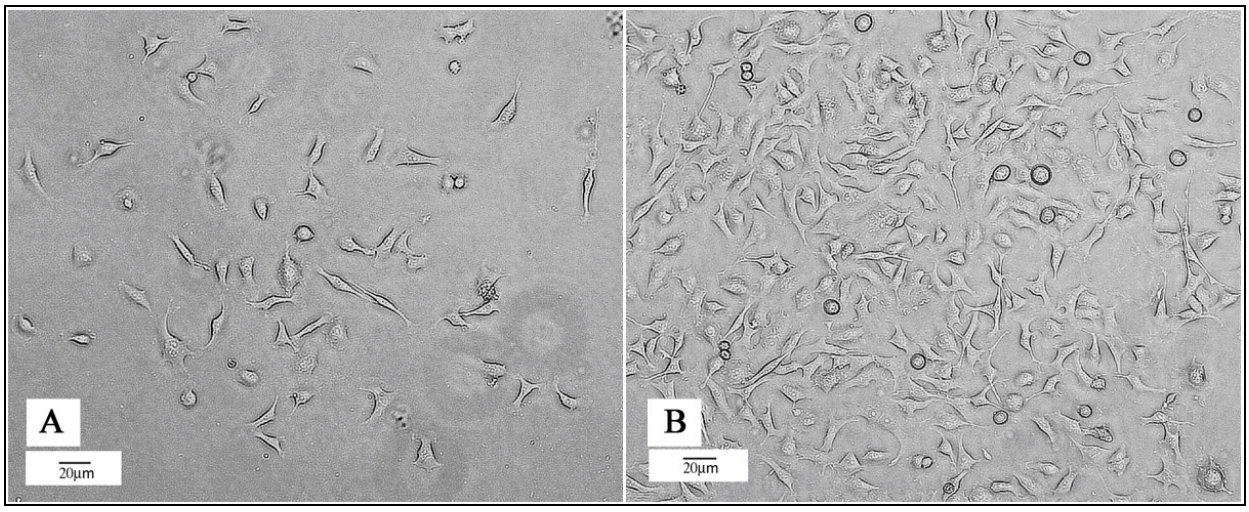

Figure 49. Optical micrograph of B35 neuroblast-like cells at **A)** 6 h and **B)** 48 h post micropatterning. *Scale bar equals 20 µm.*

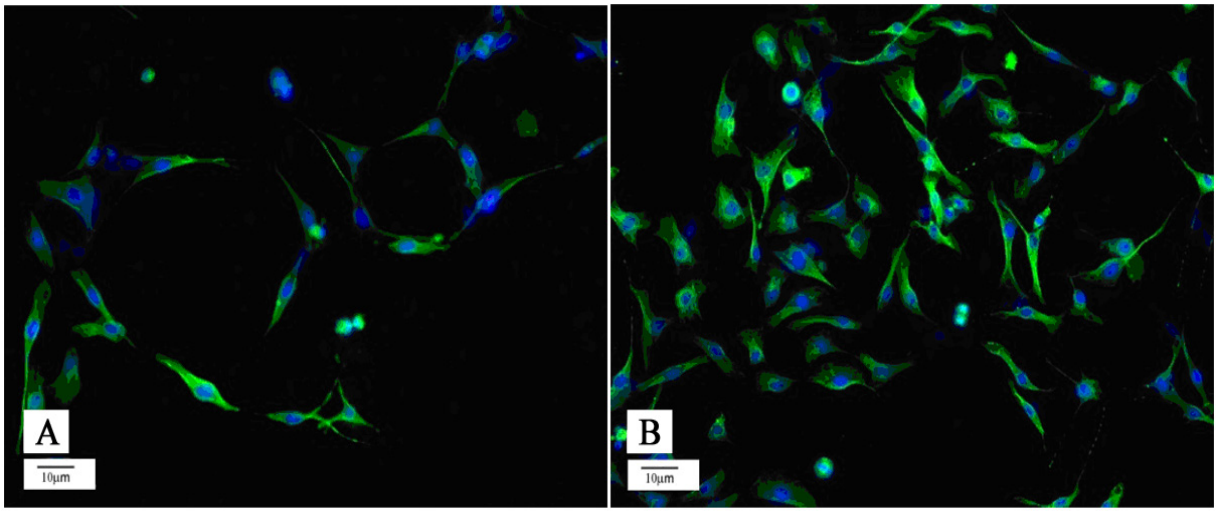

Figure 50. Confocal micrograph of B35 neuroblast-like cells shows viable nucleus and cytoskeleton at **A)** 24 h and **B)** 48 h post micropatterning. *Scale bar equals 10 µm.*

3.2.2 Microfabrication of Bioceramics

The MDW process was also employed to develop microstructures of bioceramics such as hydroxyapatite, zirconia, and viable mammalian osteosarcoma cells. Figure 51 contains optical micrograph of the ribbon and substrates employed in developing micropatterns of hydroxyapatite. Ablated regions lacking the HA coating can be observed in the ribbon (Figure 51A). Discrete points, lines, and squares can be observed in the substrate (Figure 51C-D). These mesoscopic patterns maintain the dimensions and boundaries seen in the ribbon. The MDW process also maintained the composition and phase of the target material. Figure 52, an X-ray diffraction pattern of hydroxyapatite after laser interaction reveals the (200), (111), (002), (102), (210), (211), (112), (300), (202), (310), (222), (320), (213), (004), and (304) peaks of crystalline hydroxyapatite (Figure 53).[154, 155]

Scanning electron micrographs (Figure 54) reveal the microstructure of hydroxyapatite. A porous mesh-like network is observed at various magnifications. The porosity of MDW-transferred hydroxyapatite may be tailored to in vivo application by controlling the size of the ceramic powder, the amount of solvent used to prepare the ribbon, and the choice of solvent used to prepare the ribbon. Figure 55 contains optical micrograph of hydroxyapatite line micropatterned by MDW on borosilicate glass substrate. Label “A” indicates the hydroxyapatite thin film, “B” indicates the borosilicate glass substrate. “C” and “D” indicate micrometer-sized particles, which result from splashing of material during the MDW process. From the scanning electron micrograph (Figure 56) several features can be observed. Region “A” indicates the location of the porous hydroxyapatite thin film, “B” indicates the location of the borosilicate glass substrate, and “C” indicates the location of

micrometer-sized particles, which result from splashing of material during the MDW process.

Figure 57 contains optical images of zirconia micropatterns developed by MDW. A square-edged pattern of zirconia was developed, with a relatively well-defined boundary. Scanning electron micrographs (Figure 58) reveal discrete pebble-like particles with size-distribution of 0.3 to 2 μm. Splashing near the boundary was also observed, and this occurs during the transfer process and may be eliminated using a micromachining technique.

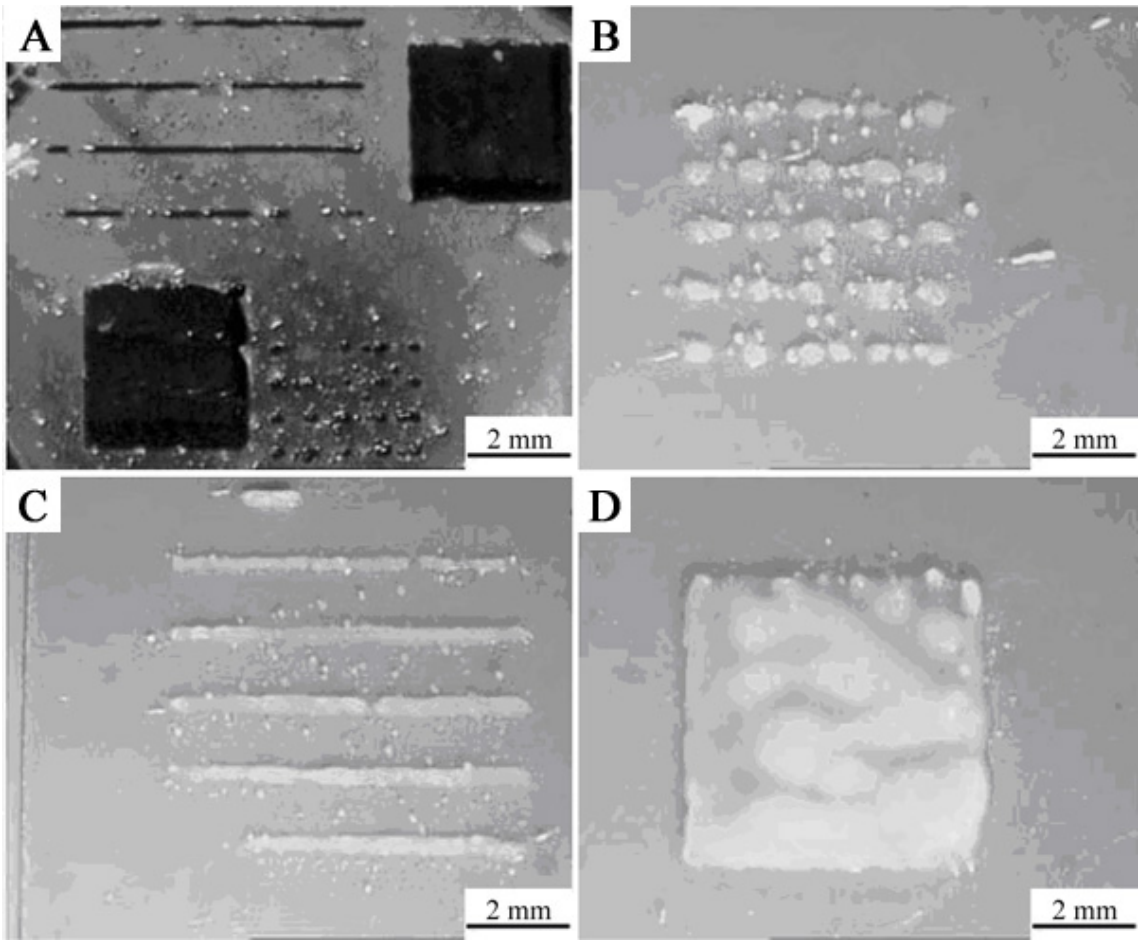

Figure 51. (A) Optical micrograph of MDW ribbon coated with hydroxyapatite. Ablated regions can be observed. **(B-D)** Optical micrographs of hydroxyapatite patterns on borosilicate glass substrates.

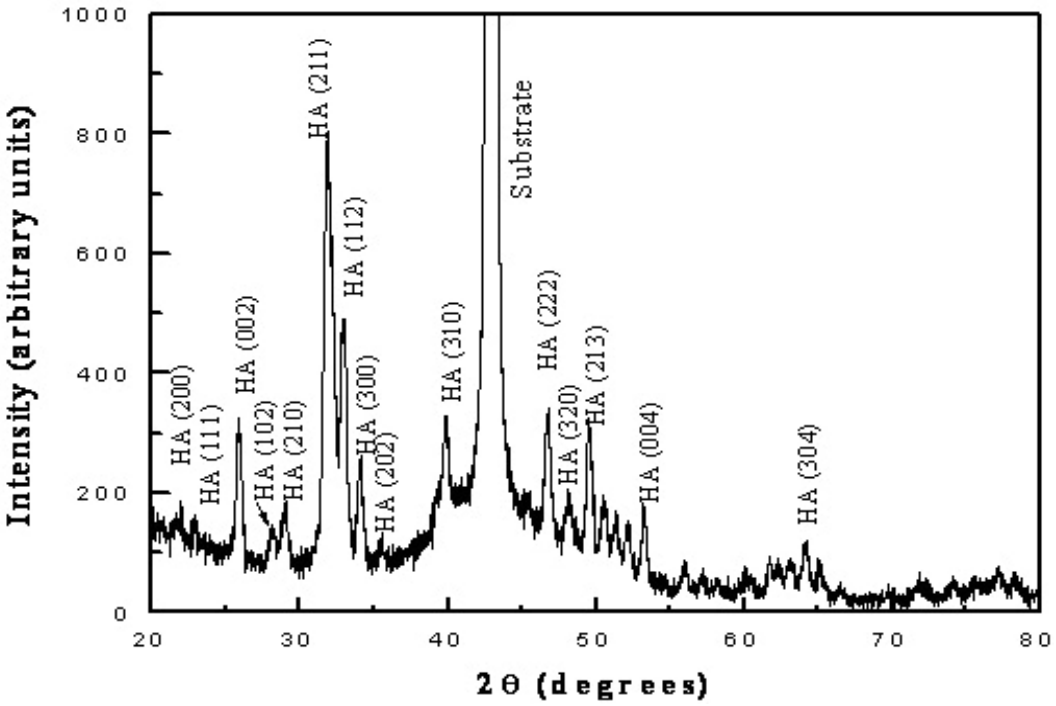

Figure 52. X-ray diffraction of hydroxyapatite after MDW processing. Various peaks that correspond to crystalline hydroxyapatite are labeled.

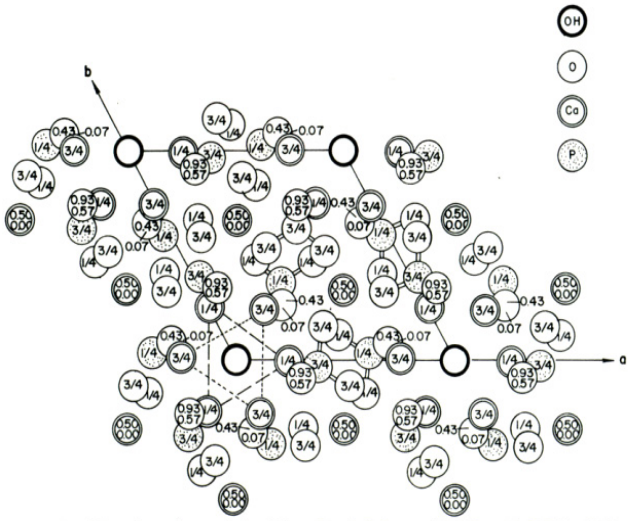

Figure 53. Representative diagram of the structure of crystalline hydroxyapatite with various peaks.[21]

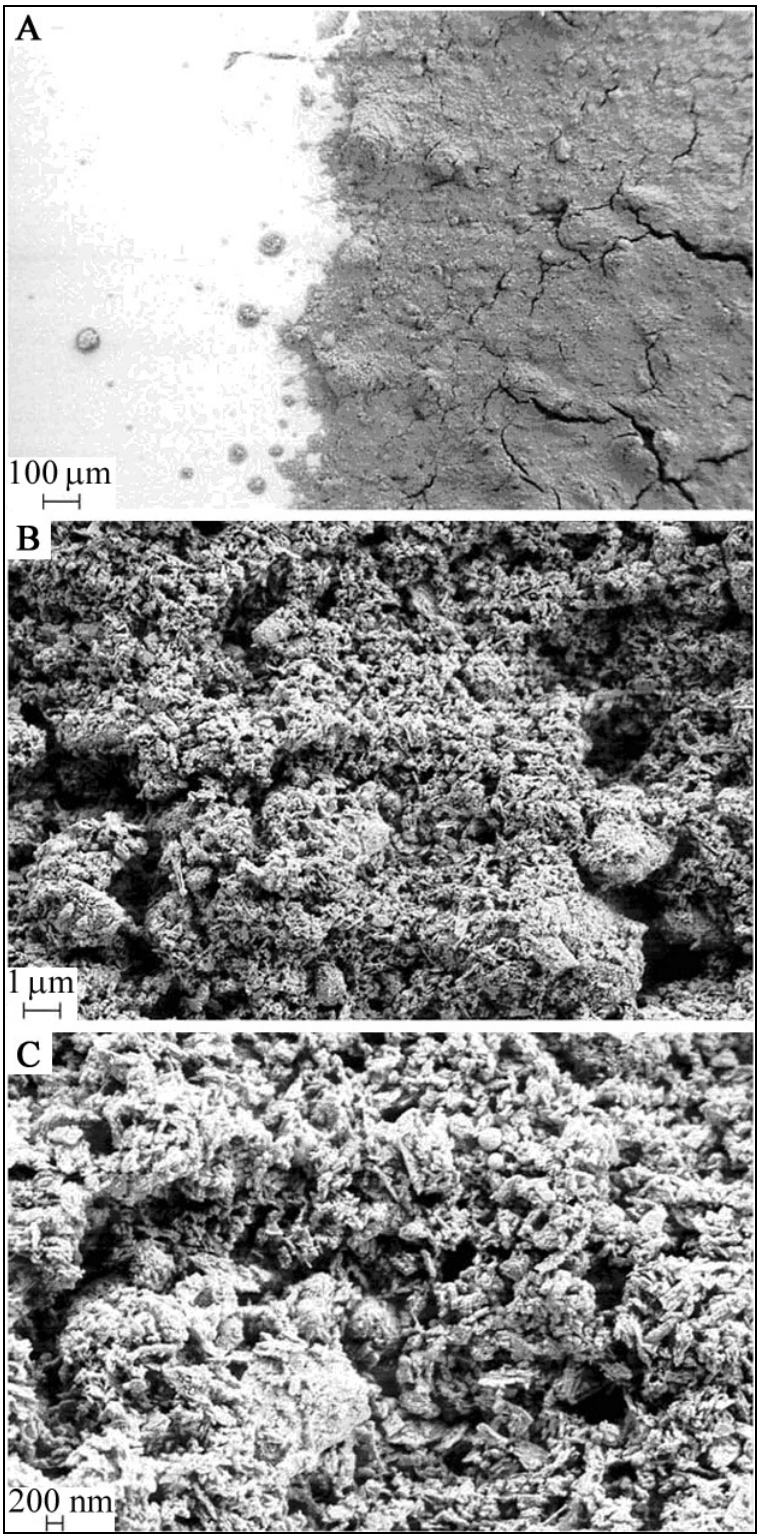

Figure 54. Scanning electron micrographs of hydroxyapatite micropatterned by MDW, at several magnifications.

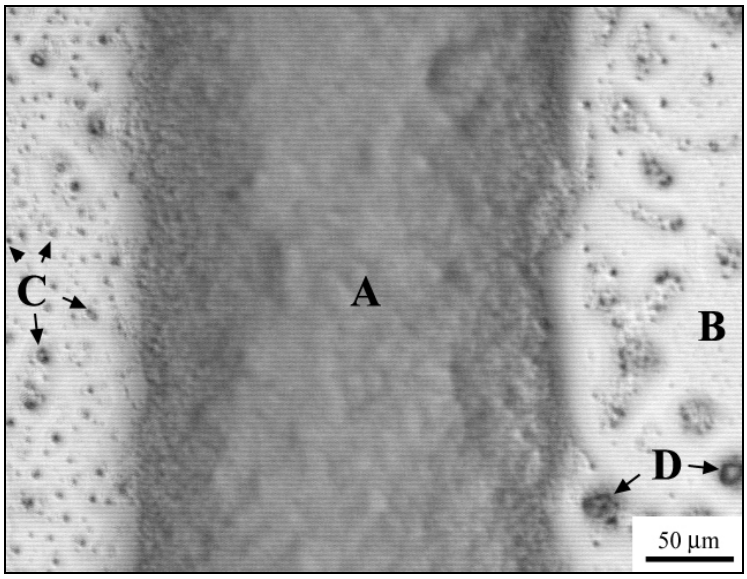

Figure 55. Optical micrograph of hydroxyapatite line micropatterned by MDW on borosilicate glass substrate. "A" indicates the hydroxyapatite thin film, "B" indicates the borosilicate glass substrate. "C" and "D" indicate micrometer-sized particles. *Scale bar equals 50 µm.*

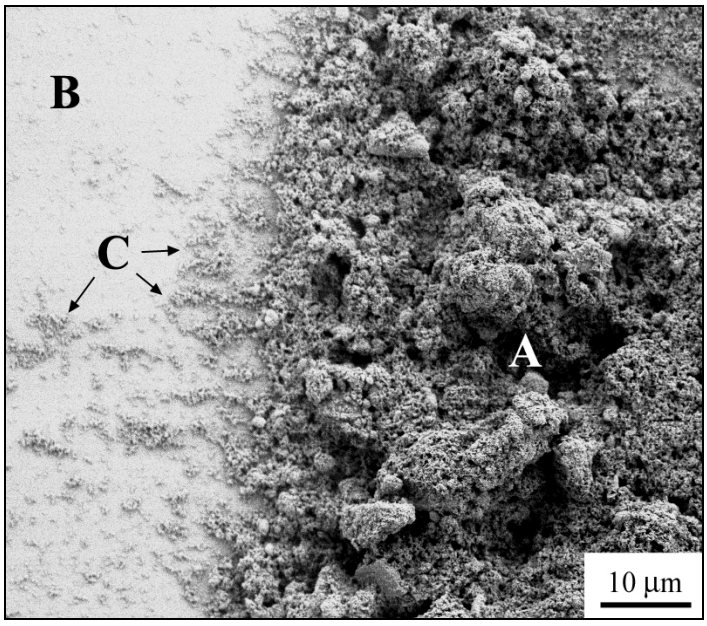

Figure 56. Scanning electron micrograph of hydroxyapatite. "A" indicates the location of the porous hydroxyapatite thin film, "B" indicates the location of the borosilicate glass substrate, and "C" indicates splashing of material during the MDW process. *Scale bar equals 10 µm.*

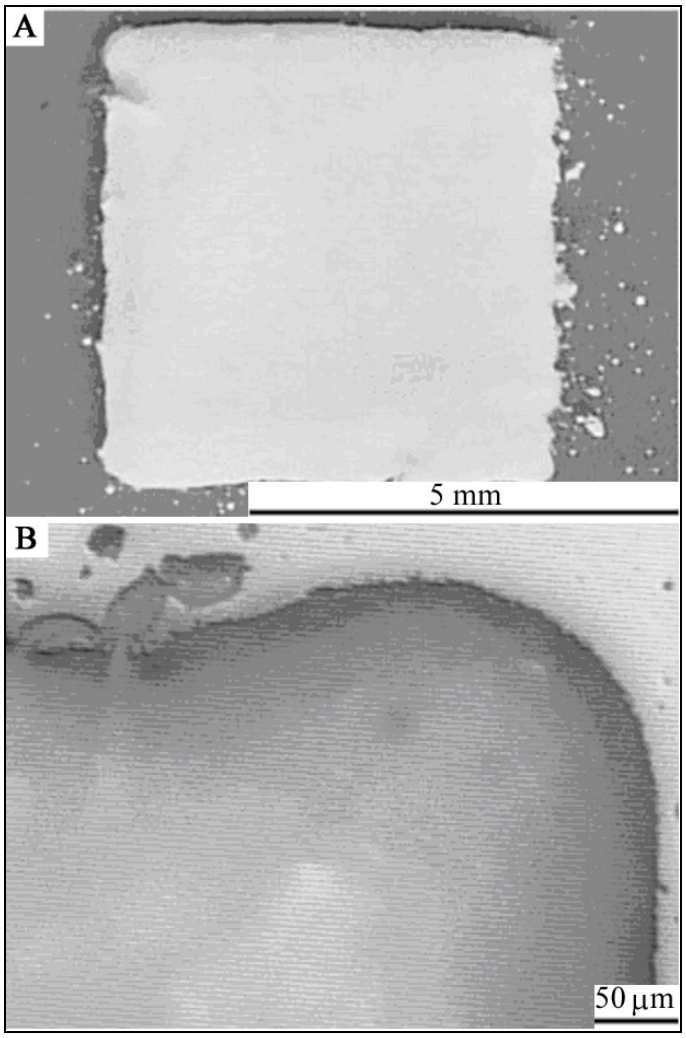

Figure 57. Optical micrographs of zirconia micropatterned by MDW.

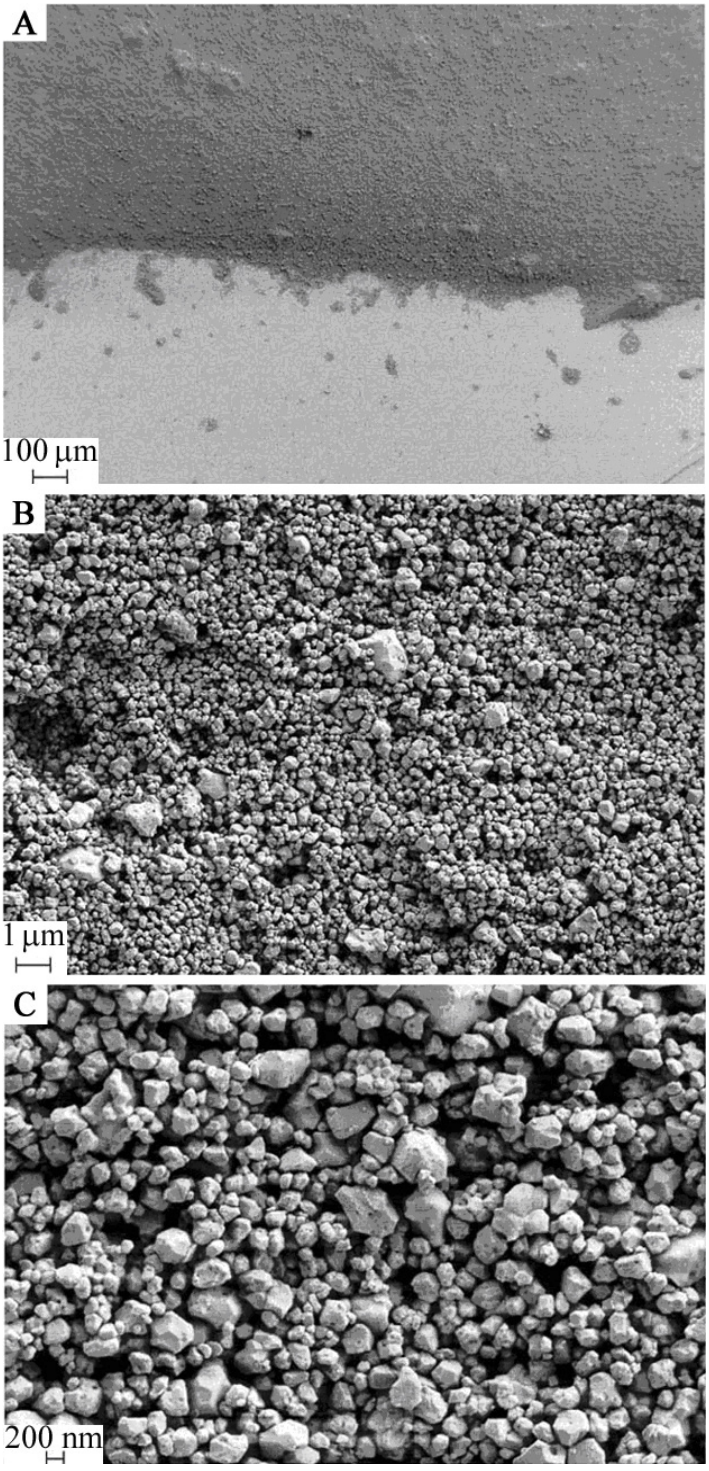

Figure 58. Scanning electron micrographs of zirconia micropatterned by MDW, at several magnifications.

3.2.3 Microfabrication of Osteoblast-bioceramic composite

Hydroxyapatite [$Ca_{10}(PO4)_6(OH)_2$] is a bioactive ceramic that forms chemical bonds with bony tissues. Recent studies have shown that osteoblast cells attach, proliferate, and differentiate on hydroxyapatite surfaces.[156, 157] These cells secrete osteoid (proteoglycans, glycoproteins, type I collagen), enzymes (osteocalcin and alkaline phosphatase), and growth factors (interleukin-1) that mediate in vivo bone growth. Hydroxyapatite also exhibits controlled in vivo degradation rates, which are dependent on phase, surface area, crystallinity, and ionic substitution.[158, 159] In addition, hydroxyapatite acts as a source for calcium, phosphorus, sodium, and magnesium ions necessary for in vivo bone growth. Scaffolds using zirconia, an inert ceramic that exhibits a stable oxide surface, high hardness, high corrosion resistance, and high wear resistance were also developed.[160]

Reproducible control over microstructure and surface characteristics may provide unique biological functionalities at the tissue/implant interface. For example, osteoblast proliferation, osteoblast differentiation, angiogenesis, and other processes can be modulated by surface roughness.[161] *Boyan et al.*[162] have shown that MG63 cells respond to increasing surface roughness with increased differentiation and decreased proliferation. Several markers and mediators of cell activity, including alkaline phosphatase, osteocalcin, TGF-β_1, and prostaglandin E_2, are produced in greater amounts on rougher surfaces. In addition, MG63 cells exhibit enhanced responsiveness to hormones (e.g., 1,25-$(OH)_2D_3$) on rougher surfaces. In addition, *Brauker et al.*[163] have shown that materials with pores with sizes between 0.8 μm-8 μm exhibit increased amounts of cell penetration and neovascularization (blood vessel formation). The interaction among several MDW process parameters, including the laser

fluence, laser spot size, ceramic powder size, ribbon-substrate length, amount of solvent used to prepare the ribbon, and choice of solvent used to prepare the ribbon, may provide additional opportunities to create unique surface morphologies and improved tissue/implant interfaces.[164]

Figure 59 contains optical micrographs of the ribbon and substrate used in the MDW co-deposition of MG63 osteosarcoma cells and hydroxyapatite. Ablated regions within the square-design used for the process can be observed on the ribbon. Figure 60 contains optical micrographs of the substrate containing the MG63 cells and hydroxyapatite particles. The osteosarcoma cells exhibits cytoplasmic extensions in the presence of the hydroxyapatite matrix. Optical micrographs at 3 hours and 96 hours post deposition show increased growth and proliferation of the cells. The cell-density increased significantly and the cells appear to bond with the hydroxyapatite matrix. Figure 61 compares the growth profile of MG63 osteosarcoma under there different conditions: 1) as-seeded without MDW process, 2) deposited by MDW process, and 3) co-deposited with HA by MDW process. The growth profile of the cells in the three cases was found to be statistically identical. No preferential growth was found during the various time intervals (3, 6, 12, 24, 48, 72, and 96 h).

Figure 62 contains the *live/dead* fluorescent images of the osteosarcoma cells 48 hours after deposition by MDW. Viable MG63 cells from an MDW square-pattern can be observed in Figure 62 A-B. The osteosarcoma cells exhibit growth and proliferation after deposition. Results from *live/dead* analysis suggested that nearly 100% of the cells remained viable after the process. Figure 63 contains the *live/dead* stained images of osteosarcoma cells 72 hours after co-deposition with HA. Arrow indicate confluent osteoblast-like cell surrounded by hydroxyapatite matrix.

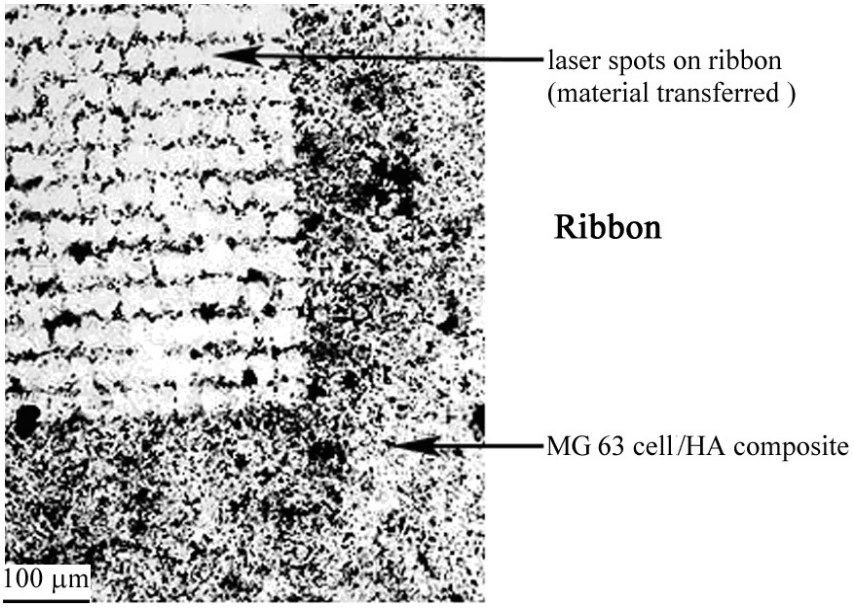

Figure 59. Optical micrograph of the ribbon used for MDW co-deposition of MG63-osteosarcoma cells and hydroxyapatite. Ablated regions can be clearly observed. *Scale bar equals 100 µm.*

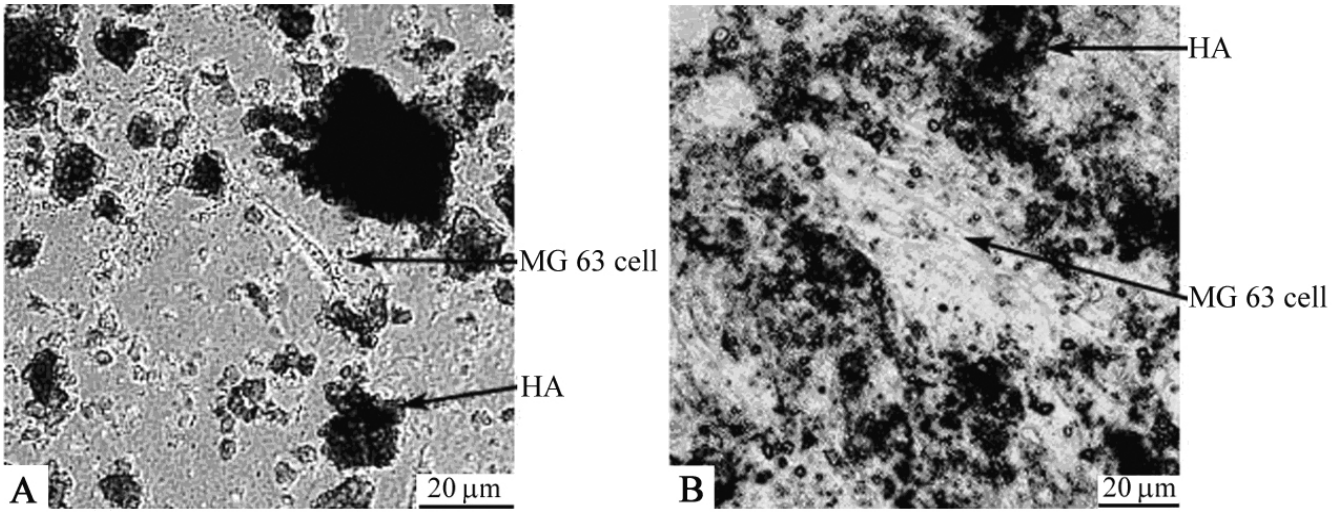

Figure 60. Optical micrograph of the substrate containing MG63-osteosarcoma cells and hydroxyapatite co-deposited by MDW. Images were taken **(A)** 3 hours and **(B)** 96 hours post deposition. *Scale bar equals 20 µm.*

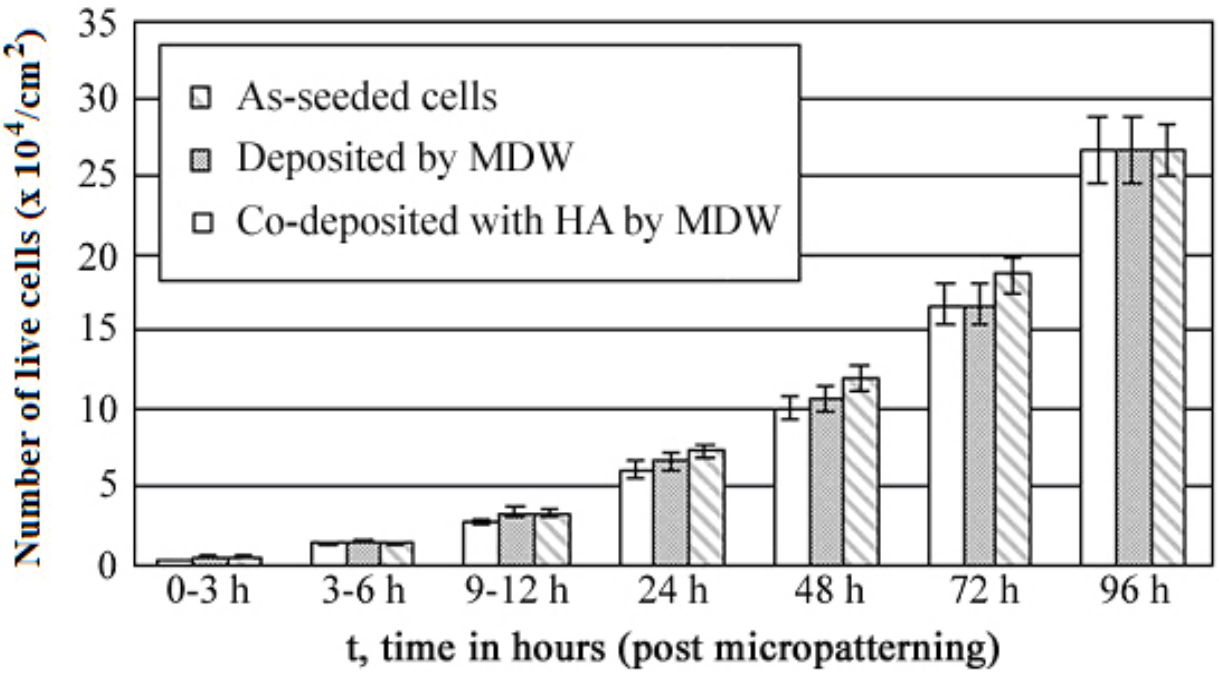

Figure 61. Growth profile of MG63 osteosarcoma cells: (1) as-seeded condition, 2) deposited by MDW process, and 3) co-deposited with HA by MDW process. *Values are expressed as mean ± standard deviation.*

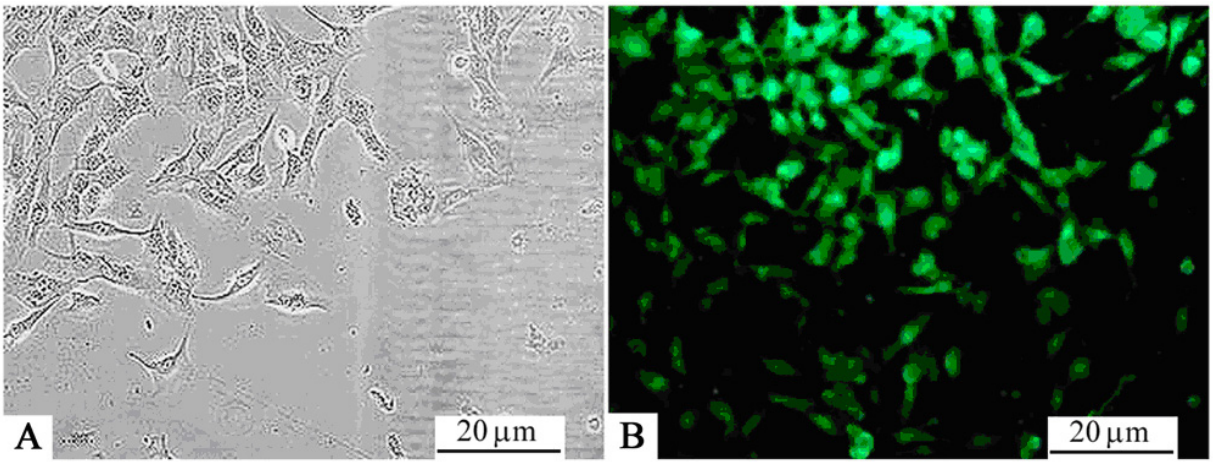

Figure 62. *Live/dead* stained **A)** optical and **B)** fluorescent micrographs of MG63 osteosarcoma cells 48 h after MDW deposition. *Scale bar equals 20 µm.*

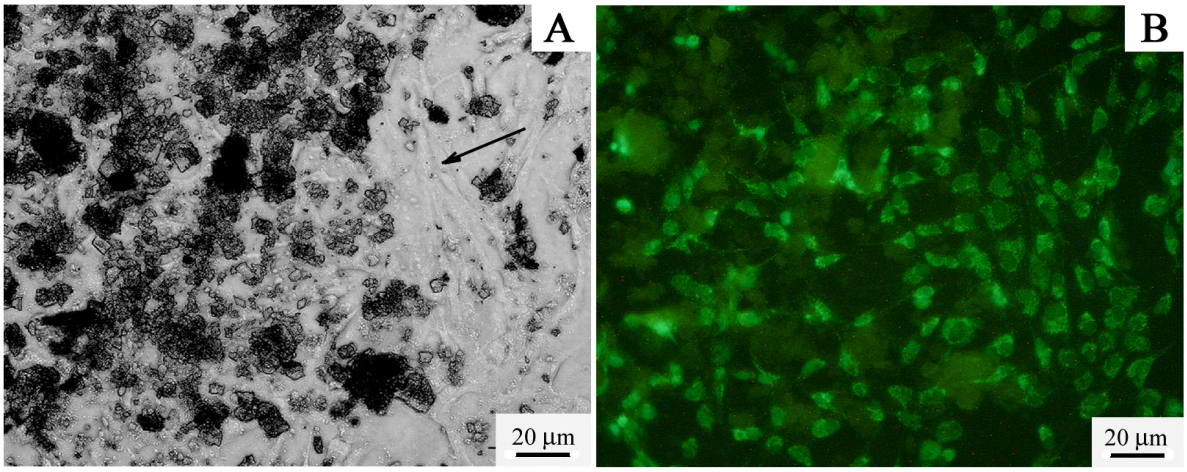

Figure 63. *Live/dead* stained **A)** optical and **B)** fluorescent micrographs of MG63 osteosarcoma cells 72 h after MDW co-deposition with HA. *Scale bar equals 20 µm.*

Previous studies on MDW have also successfully demonstrated micropatterning of several cell types, including C2C12 myoblast-like cells and B35 neuroblast-like cells. Cells have shown ~ 100% viability.[165, 166] Cytotoxicity and mutagenicity studies have confirmed lack of evidence of DNA strand breakage in cells.[167-169] MDW is a versatile technique for creating multilayer, heterogeneous structures that may be developed as tissue scaffolds. The ability to microfabricate cell-ceramic composites offers structural integrity in using two-dimensional layers to build mechanically robust three dimensional heterogeneous constructs.

CAD/CAM co-deposition of osteosarcoma cells and hydroxyapatite may exploit advantage of osteoconductive properties of bioactive ceramics. These findings on depositing mesoscopic patterns of cells, ceramics, and extracellular matrix composites that possess controlled microstructures may allow the development of novel dental and orthopaedic tissue substitutes. Based on the functionality and structural requirements, this concept can also be extended to integrate a variety of cell-lines with most organic/inorganic materials. Integration of viable cells and biomaterials prior to tissue fabrication may allow significant advantages including adequate cell penetration and control over cell-density through the scaffold.

3.3 CLM – CAD/CAM Laser Micromachining

CAD/CAM laser micromachining provides a direct-write approach similar to MDW for microfabrication of biomaterials. Unlike MDW, CLM utilizes a high laser power to selectively ablate biomaterials. Microstructures and biointerfaces developed by CLM may be utilized as surface recognition regions for differential adherence and selective cellular growth to tissue networks. In this section, the development of CLM as a rapid prototyping tool for biomedical applications is described.

3.3.1 Silicon Micromachining

CAD/CAM laser micromachining was developed for controlled direct-write microfabrication of biomaterials. As described earlier, laser interaction with materials depend on the various properties of the material and source light. At the early stage of development, polished silicon substrates were chosen to allow understanding of the laser interaction with material. Silicon substrates are the 'gold-standard' in the microelectronic arena. Microscale integration of biological agents to silicon substrates may also allow advancement in the bio-sensor/electronics field.

CLM of silicon was studied in a systematic approach of varying a single process parameter while keeping the rest constant. In the first step, the aperture was varied to allow control over the laser-spot size. Simple line/channel patterns (with repetition of two) were developed for each aperture. The laser output energy from the tube was kept constant at 186mJ±6mJ using the voltage control at 25V. Figure 64 contains optical micrographs of

ablated regions of Si after CLM processing at various apertures (1-7). The cross-sectional view (Figure 64B) illustrates the depth of ablation. An increase in aperture size causes an increase in depth of ablation. The ablation was noted to be U-shaped for each aperture. The laser spot has a Gaussian spread of energy-density and wavelength, with the peaks approximately in the center of the spot. The Gaussian spread would produce a non-linear ablation at the site of interaction, with peak interactions in the middle, which may explain the U-shaped cut. From the top-view (Figure 64B), it can be observed that an increase in aperture size also causes an increase in the width of ablation (*dark regions*). Additionally, splashing/sputtering of debris around the ablated channels was significantly higher for larger apertures. Evidently, larger apertures would allow more photons to interact with the material. An increase in laser-material interactions would develop deeper, wider ablations with more splashing. Figure 65 contains a graph illustrating the ablation width and depth of Si (111) during CLM with increasing apertures. A linear increase in depth of ablation was noted by a linear increase in width, for increasing aperture sizes.

In the next step, the laser energy density was systematically varied to allow control over intensity of photons in material interaction. Simple line/channel patterns (with repetition of two) were developed for each trial. The aperture controlling the spot-size was kept constant. Figure 66 contains optical micrographs of ablated regions of Si after CLM processing at various energies (controlled by voltage setting). The approximate energy output corresponding to a given voltage setting was as follows: 21V-60 mJ, 22V-96 mJ, 23V-135 mJ, 24V-162 mJ, 25V-186 mJ, 26V-213 mJ, and 27V-225mJ. The tolerance on all energy levels was less than 5%. The cross-sectional view (Figure 66A) illustrates the depth of ablation and the top-view of CLM processed silicon (Figure 66B) illustrates the width of

ablation for a systematic increase in laser energy density. As previously, splashing/sputtering of debris around the ablated channels was significantly higher for larger energy density. Evidently, larger energy densities allow more photons to interact with the material leading to the ablation results observed. Figure 67 contains a graph illustrating the ablation width and depth of Si (111) during CLM with increasing laser energy density.

Finally, CLM was investigated for line/channel patterns with increasing repetitions (1x, 2x, 4x, 8x, 16x) to confirm linearity in laser-material interactions. The laser output energy from the tube was kept constant at 186mJ±6mJ using the voltage control at 25V. The aperture controlling the spot-size was also kept constant. Figure 68 contains optical micrographs of ablated regions of Si after CLM processing using various repetitions (increased exponentially). The depth of ablation increases dramatically to sharper trenches and from a U-shaped cut to a V-shaped cut (Figure 68A). A repetitive ablation would allow an additive Gaussian shift each time the material is ablated. Over additional interactions, the central peak region of the laser spot would have a larger increase in number of photons than that of the periphery, which would explain the non-linear transformation. The width of the channels (Figure 68B) appears to be constant for all the repetition trials. This was anticipated as the aperture size or energy density was not varied. Splashing/sputtering of debris around the ablated channels was significantly higher owing to increased laser interaction within the localized region. Figure 69 contains a graph illustrating the ablation width and depth of Si (111) during CLM with increased interaction times by varying repetitions. As estimated, there was no significant change on the width of ablation. The depth of ablation increased exponentially with an exponential increase in repetition times. Thus, the increase in depth of ablation was found to be linear with increasing interaction times/repetitions.

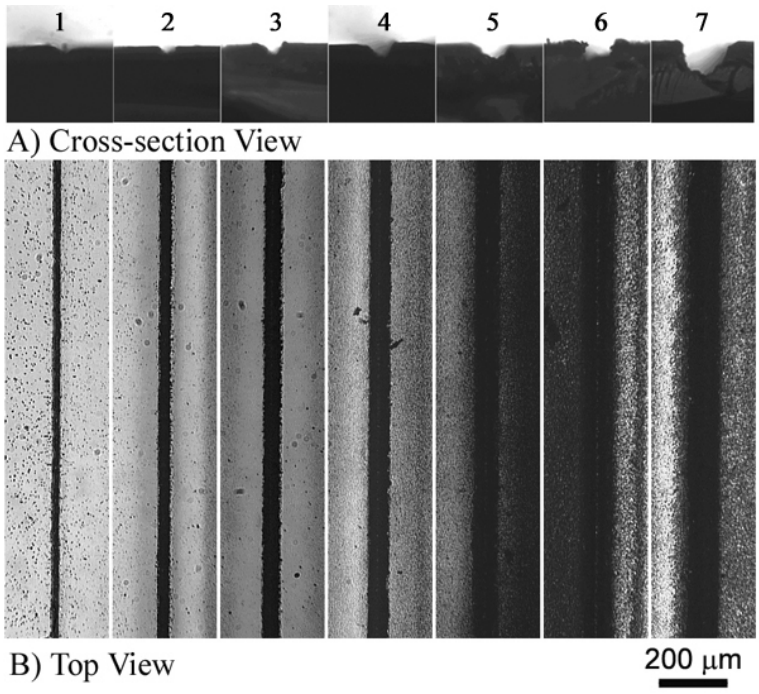

Figure 64. Optical micrograph of Si (111) in **A)** cross-sectional view and **B)** top-view after CLM as a function of aperture. *Scale bar equals 200 µm.*

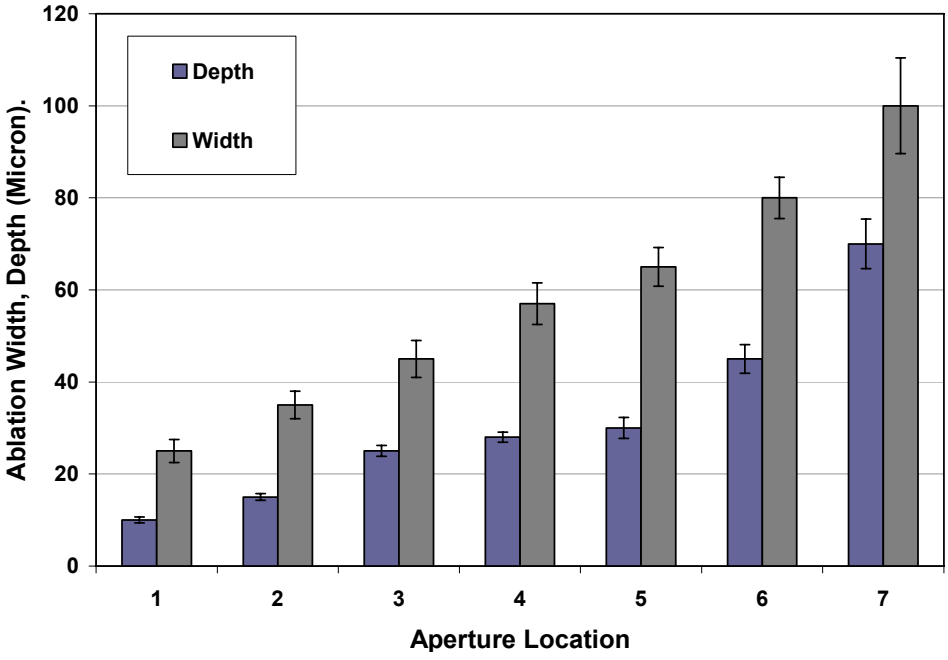

Figure 65. Graph of ablation width and depth on Si (111) as a function of aperture and laser spot size. *Data is expressed as mean ± standard deviation.* (*P<0.05)*

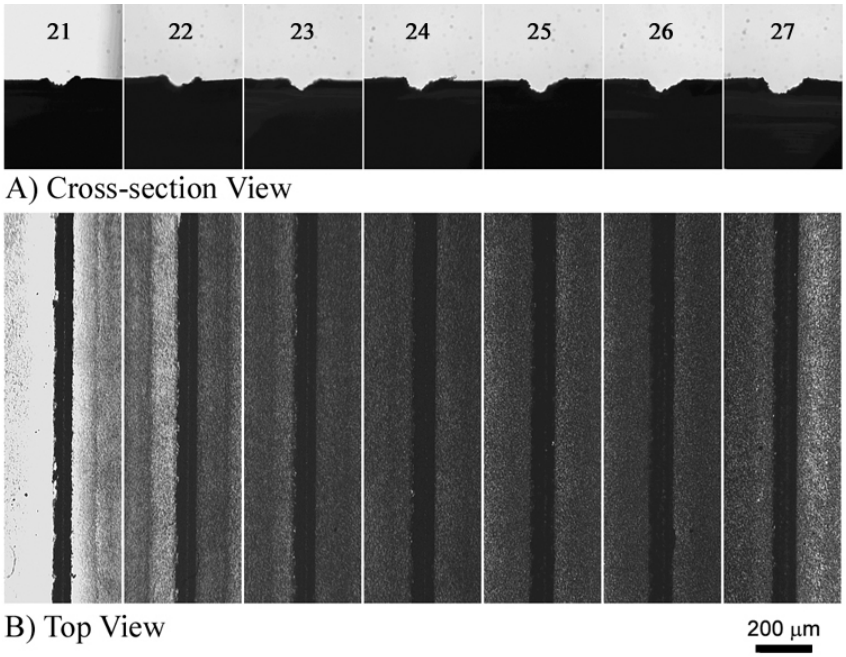

Figure 66. Optical micrograph of Si (111) in **A)** cross-sectional view and **B)** top-view after CLM as a function of laser energy *(shown for control voltage)*. *Scale bar equals 200 µm*

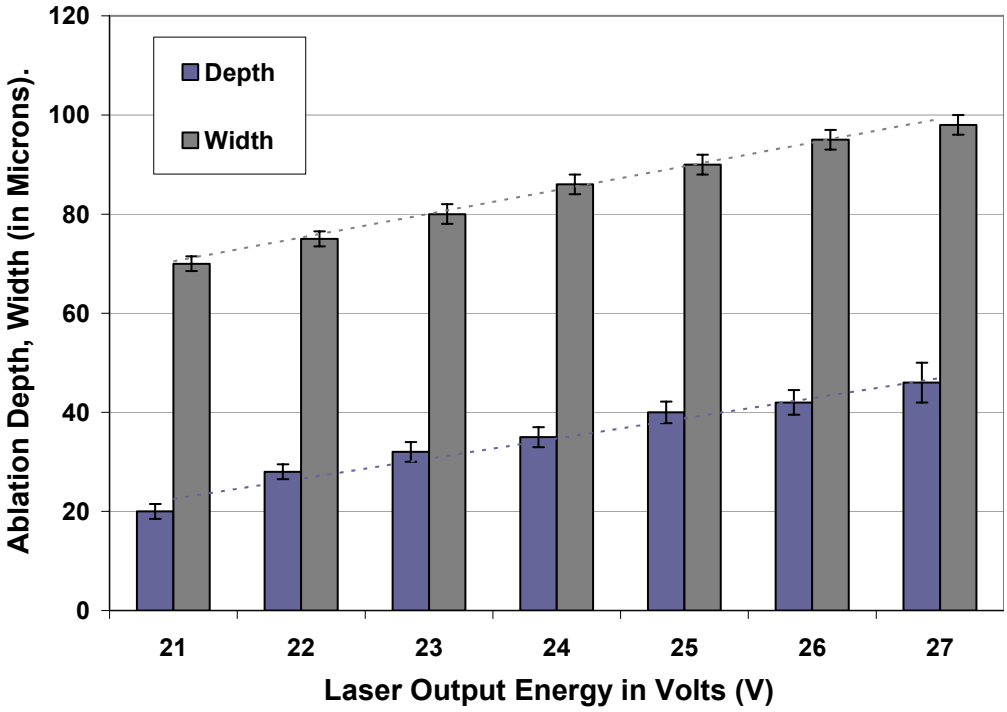

Figure 67. Graph of ablation width and depth on Si (111) as a function of laser energy (control in Volts) at constant aperture and repetition. *Data is expressed as mean ± standard deviation.* (*P<0.05)*

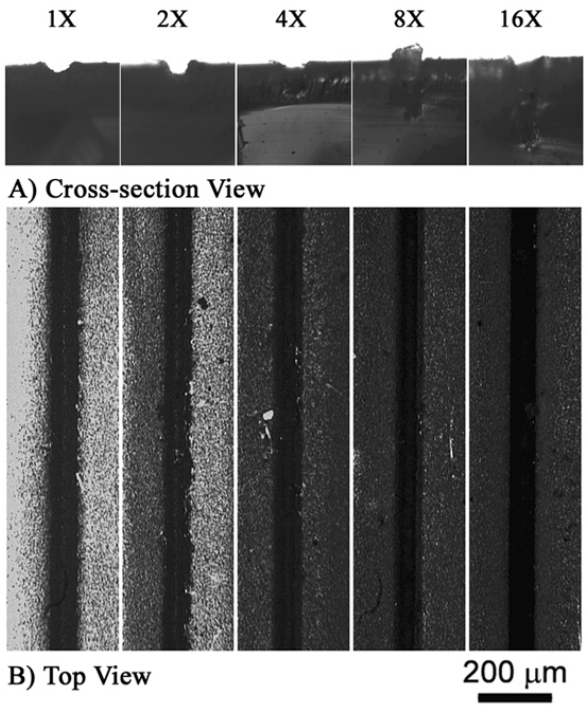

Figure 68. Optical micrograph of Si (111) in **A)** cross-sectional view and **B)** top-view after CLM as a function of pattern repetition or overlap. *Scale bar equals 200 µm.*

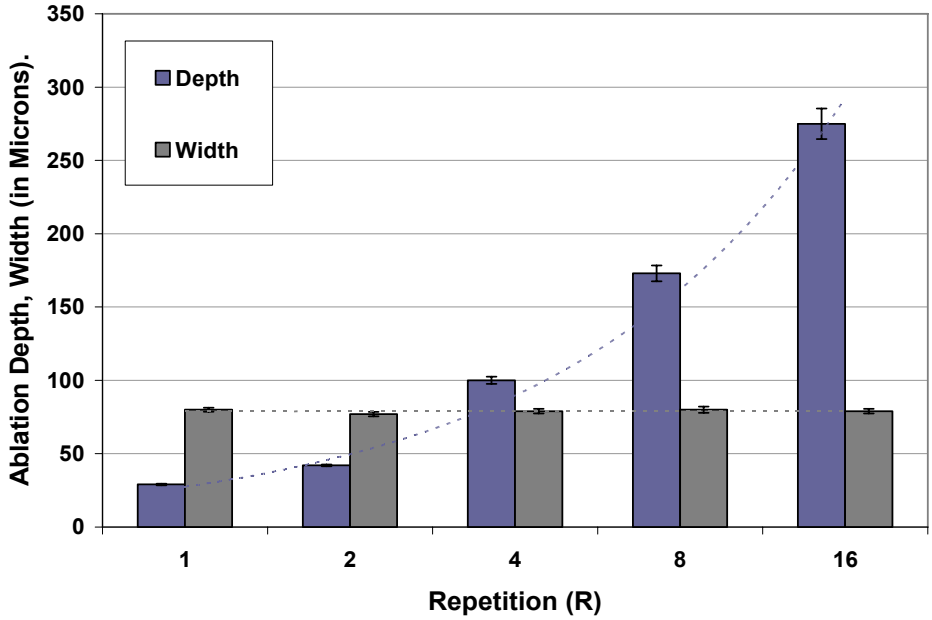

Figure 69. Graph of ablation width and depth on Si (111) as a function of repetition (1x, 2x, 4x, 8x, and 16x) at constant aperture size. *Data is expressed as mean ± standard deviation. ($P<0.05$)*

Figure 70 contains a scanning electron micrograph of CLM processed Si (111) in a 20x20 dot-array pattern. The energy density and aperture was systematically lowered to investigate minimum ablation feature that may be obtained from the CLM setup. Figure 71 contains additional SEM images. Ablations width of approximately 5 μm was observed (Figure 71A) which was also near the theoretical limit for the 10x UV objective. Control over spot-size may be achieved by the aperture shape. An elliptical ablation (~ 40x20 μm) may also be obtained (Figure 71B).

CLM of silicon was also used to develop various groove-like patterns to observe the growth and orientation of human aortic vascular smooth muscle cells (HA-VSMC). Figure 72 contains optical micrographs at 48 h for HA-VSMC on silicon. The cells grow in the non-ablated regions within the micromachined grooves and form contact points with the two ends. Figure 72B illustrates the perpendicular alignment with the cells stretching out on both ends. Figure 72C illustrates random orientation of cells in plain silicon substrate.

CLM processing of silicon was used to understand laser interaction of material. It also allowed means to investigate and integrate the various process parameters. CLM may allow controlled alignment of cells and integration possibilities for bioelectronic applications. Differential growth was observed in the non-ablated regions. However, CLM of silicon may not be an ideal candidate of interfaces to develop tissue constructs owing to a various reasons including ablation splashing and microparticles that may influence cell-growth, hydrophobic nature allowing non-preferential growth of cells, rigidity, non-biodegradable, and time required for processing. Hence, a hydrophilic material that may address these concerns was pursued as an interface for developing tissue networks.

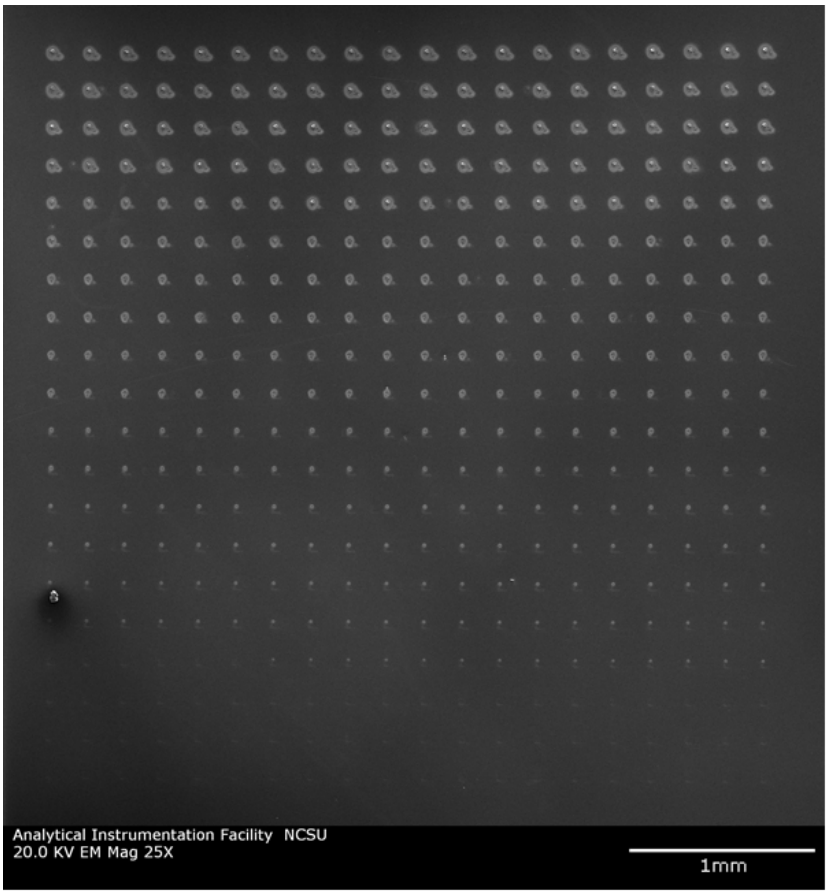

Figure 70. Scanning electron micrograph of a 20x20 micromachined dot array in Si (111) developed by controlled aperture and laser energy density. *Scale bar equals 1 mm.*

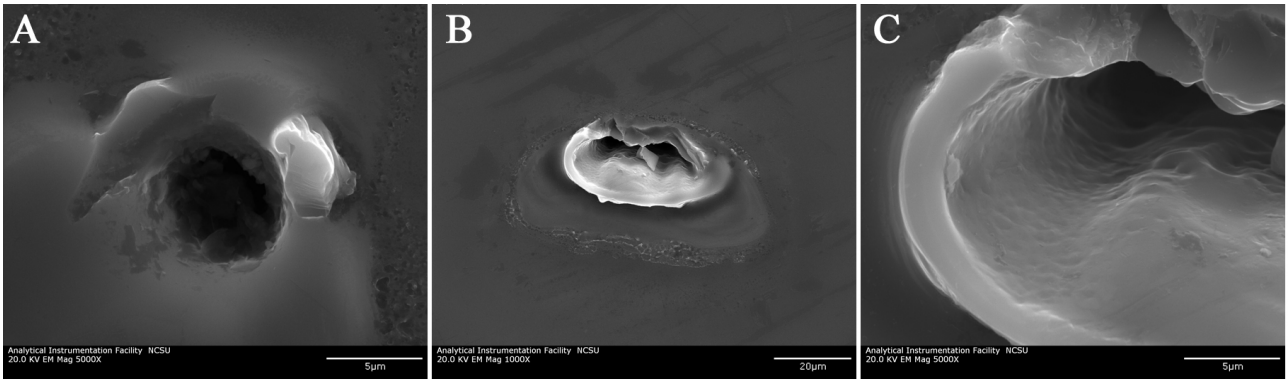

Figure 71. Scanning electron micrograph of CLM processed Si (111). **A)** 5 mm circular ablation, and **B and C)** various magnification of an elliptical ablation.

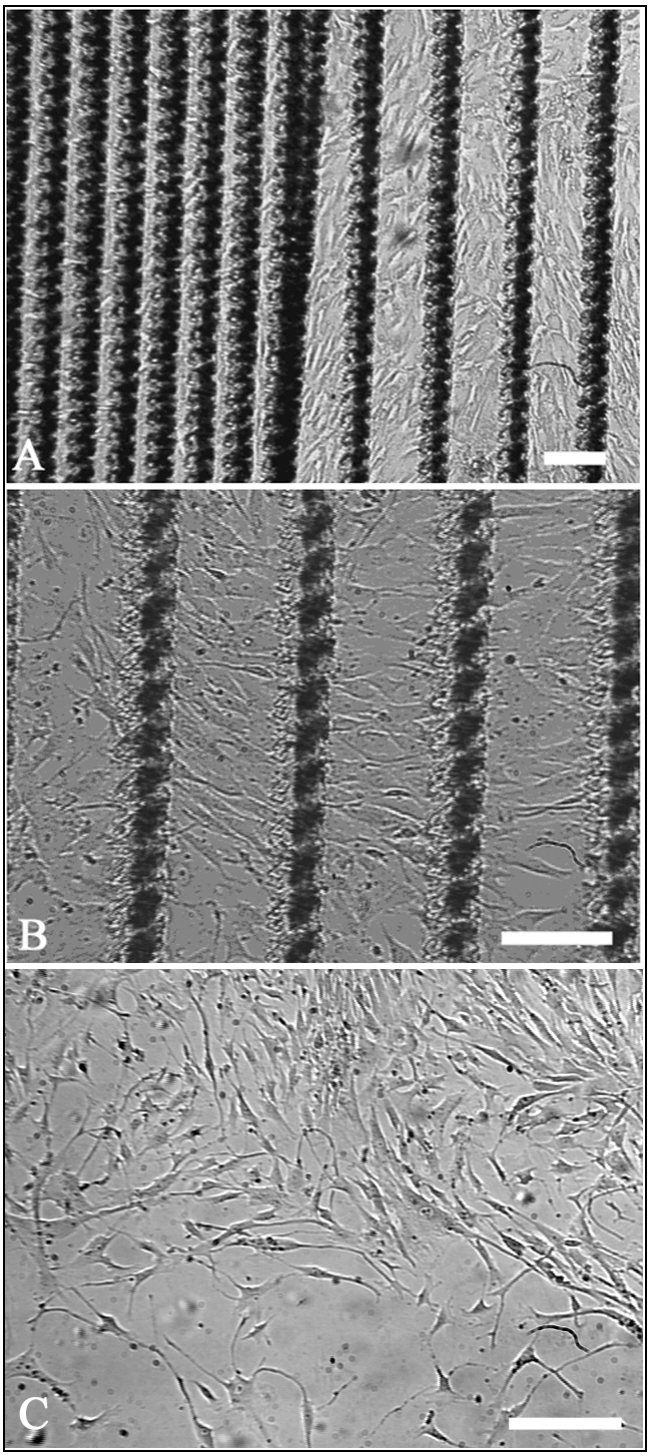

Figure 72. HA-VSMC (human aortic – vascular smooth muscle cells) on **A & B)** laser micromachined Si grooves at different magnifications and on **C)** plain silicon surface as control. Images were recorded 48 h post seeding. *Scale bar equals 100 μm.*

3.3.2 Hydrogel Micromachining

Hydrogels such as agarose gel were thought to be promising candidates as biointerfaces for development of tissue constructs. Owing to the hydrophilic nature of the material, most cell-types would not adhere to the surface. Microfabrication of such materials with growth factors may allow development of differential adherent surfaces to develop novel tissue constructs.

The ablation characteristics of agarose during laser micromachining were examined as a function of laser energy density and as a function of aperture (or laser spot size). 1% agarose gels were micromachined using a constant laser spot size (D) of ~250 μm, repetition rate (R) of 10 Hz, and constant feed rate (F) of 500 μm/s, which allowed for approximately 20% overlap of spots. Figure 73 contains images of cross-sectional and top-view of agarose gel which were prepared by CLM at several energy densities. The laser energy density values of 1.0 -2.2 J/cm^2 in 0.2 J/cm^2 increments were used. Figure 74 contains a corresponding graph illustrating the mean ablation width and depth of the gel at various laser energy densities. This data suggested that the ablation depth increased linearlyas the laser energy density was increased. The ablation width remained relatively constant and did not show a significant increase in the 1-2 J/cm^2 energy density range ($p<0.05$). However, a sharp non-linear increase was observed at higher laser energy density values (e.g., 2.2 J/cm^2), which may be attributed to non-linear laser-biomaterial interaction.

Figure 75 contains an optical micrograph of laser-micromachined agarose channels that were prepared using varying apertures (or laser spot sizes). Approximate spot-sizes of the aperture settings were as follows: Labels 1: 150 μm, 2: 600 μm, and 3: 1000 μm. Figure

76 shows a graph illustrating the mean ablation width and depth of agarose hydrogel for various aperture sizes. The ablation width increased with aperture size, which was noted to be within standard deviations of the laser spot size. The ablation depth also increased linearly with laser spot size. The standard deviation increased with the aperture size. Figure 76 also demonstrated that it was possible to obtain magnitude of difference in ablation dimensions (from approximately 200 μm to 1100 μm) by varying aperture size and laser intensity.

As described earlier, laser spot size (D) may be varied by changing the size of the aperture on the laser path to the objective. For each spot size D, the feed rate F was calculated by F = (0.2).D.R μm/s, which allowed for 20 % overlap. The feed-rate of the translation axes is an important parameter that determines the extent of overlap between subsequent laser pulses at a given laser spot size and repetition rate. The overlap defines the roughness of the undercut (rough schematic shown in Figure 77). For laser micromachining of agarose gels, minimal roughness was obtained at approximately 20% overlap. Greater than 50% overlap resulted in deep trenches toward the channel center, and less than 10% overlap resulted in small ripple structures along the channel. An understanding of the ablation characteristics of agarose and other scaffold materials is critical for obtaining appropriate geometries for CAD/CAM microfabrication of tissues.

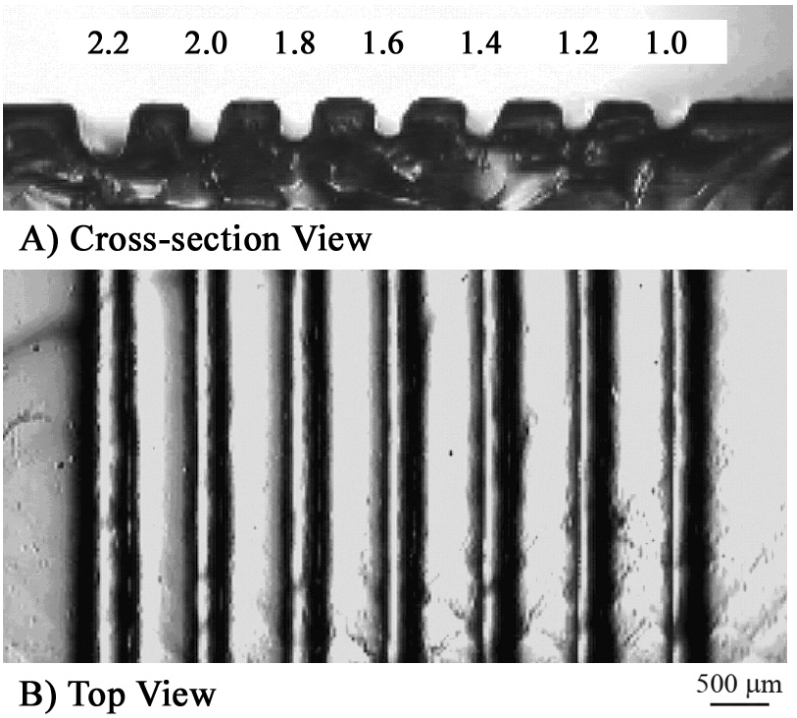

Figure 73. Optical micrograph of 1% agarose hydrogel in **A)** cross-sectional view and **B)** top-view after CLM as a function of *laser fluence (indicated on top row above each channel). Scale bar equals 500 µm.*

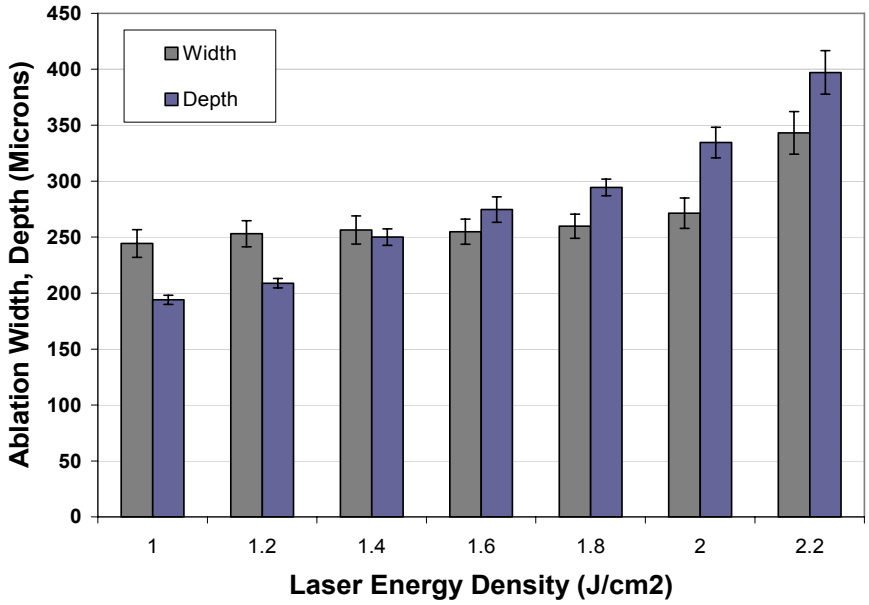

Figure 74. Graph of ablation width and depth of 1% agarose gel as a function of laser energy density at constant aperture and repetition. *Data is expressed as mean ± standard deviation. ($P<0.05$)*

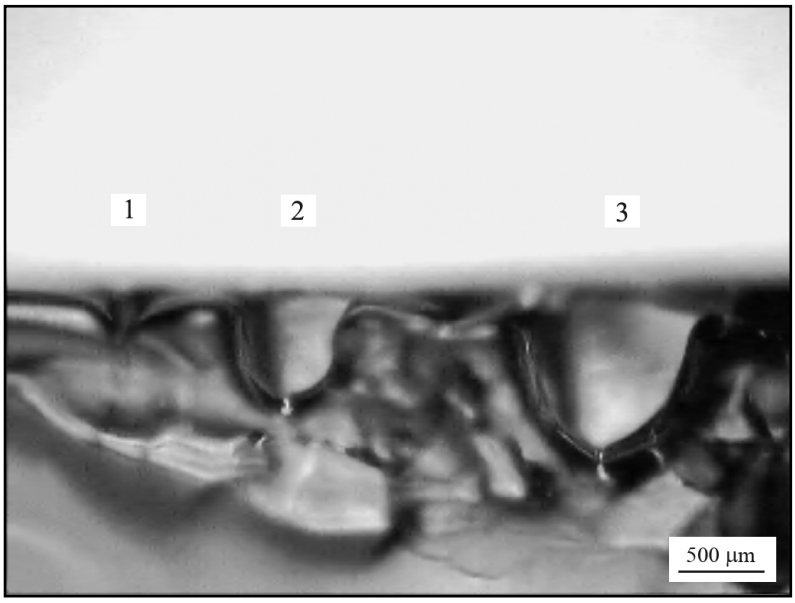

Figure 75. Optical micrograph of 1% agarose hydrogel in cross-sectional view after CLM as a function of aperture. *Scale bar equals 500 µm.*

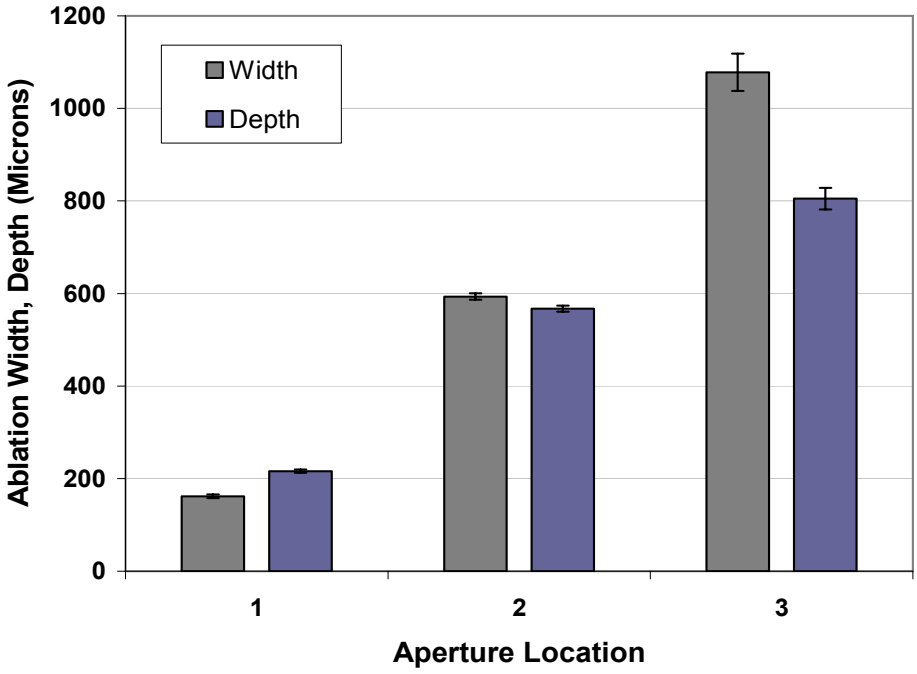

Figure 76. Graph of ablation width and depth of 1% agarose gel as a function of aperture (and laser spot size). *Data is expressed as mean ± standard deviation.* (*P<0.05)*

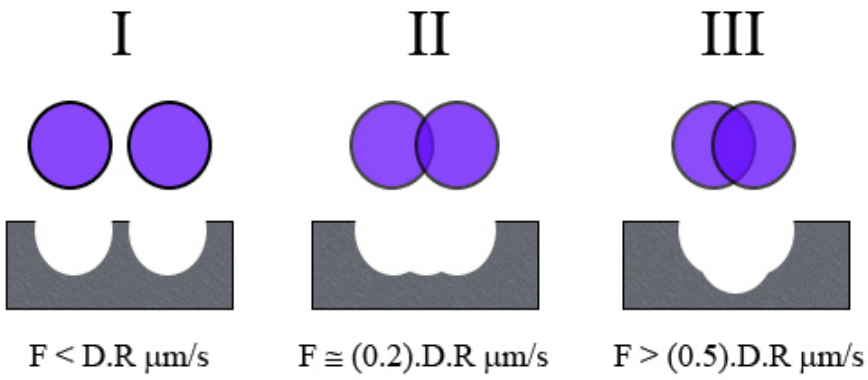

Figure 77. Schematic showing the relationship between feed-rate (F), diameter of spot-size (D) and repetition rate (R) in various overlap scenarios.

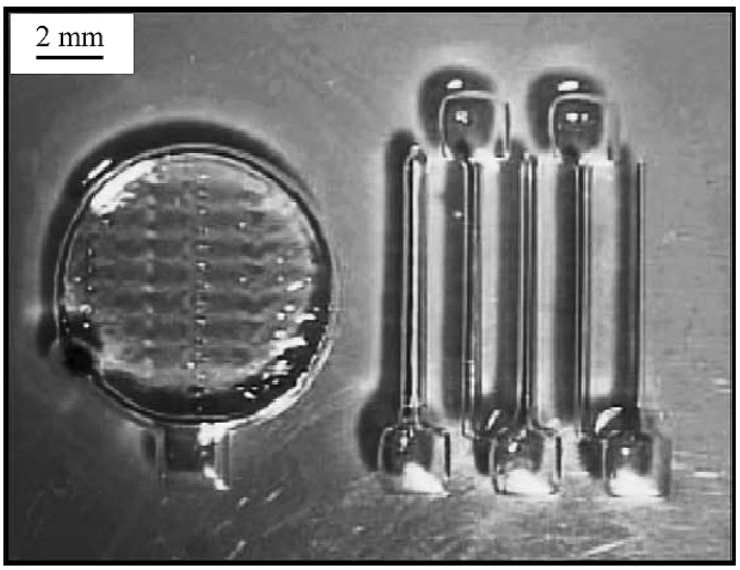

Figure 78. Optical micrograph of 1% agarose channels with reservoirs developed by CLM. *Scale bar equals 2 mm.*

3.3.3 CLM Development of Cellular Networks

An understanding of ablation characteristics of agarose hydrogel was critical in developing CAD/CAM patterns. Process control was achieved by utilizing the ablation characteristics for the material and integrating with the CAD module and laser/stage-translation parameters. In order to investigate differential adherence of cells and development of CAD/CAM tissue networks, various designs were sought. Channels with varying widths were thought to provide insight into preferential adherence and alignment. Each channel and circle design was provided with a reservoir to allow flow of growth factors and other required agents to facilitate cell growth. Figure 78 contains an optical micrograph of the CLM processed agarose hydrogels in channel/lines and circular patterns (widths of 60 – 400 μm). Additional images of microfabricated designs using CLM are shown in Figure 79 and 80.

Microfabricated channels may be employed as biointerfaces or surface recognition regions for differential adherence and selective cellular growth to engineer cell-ECM networks. Extracellular matrix (ECM) proteins are known to induce cellular adhesion, growth and proliferation.[170] Application of ECM within these microchannels may allow controlled alignment of cells. Reservoirs were fabricated adjacent to the channel, and were used to micropipette ECM® proteins into the channels. The undercut of the channel allowed uniform flow of extracellular matrix liquid within the channel. These microfabricated growth-factor filled channels were developed in 6-well plates for cell-growth studies using B35 rat neuroblast-like cells, A431 human epithelial carcinoma cells and C2C12 mouse myoblast-like cells.

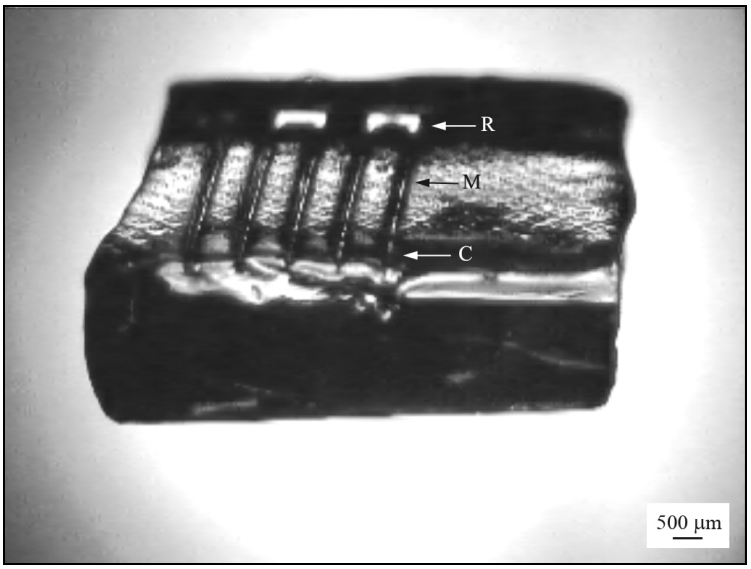

Figure 79. Optical micrograph of a 3D perspective view of micromachined agarose channels (M) and (C) with reservoirs (R). *Scale bar equals 500 µm.*

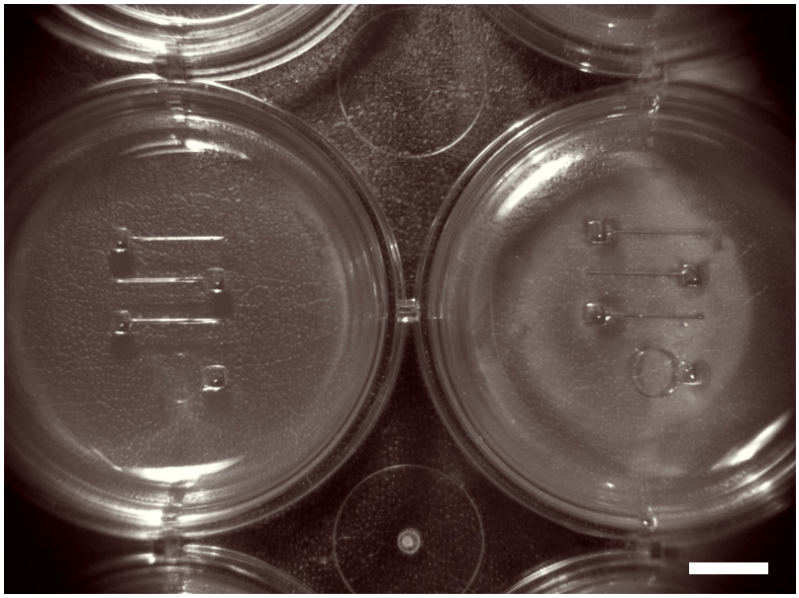

Figure 80. Optical micrograph of CLM processed agarose channels with reservoirs on 6-well plates. *Scale bar equals 1 cm.*

Figure 81 contains the initial coverage, migration, proliferation and growth of B35 neuroblast-like cells in ECM® growth-factor filled 60 μm agarose channels. Upon the initial addition, less than 20% of the cells contacted the ECM. This ensured that the adhered cells would form non-confluent surfaces within the channels and their interactions with neighboring cells could be easily observed. The cells later migrated with increasing coverage across the channel length over time. With continued growth and proliferation the cells in channels aligned parallel to the channel length to form the most packed alignment within the channel. This phenomenon was particularly evident in C2C12 myoblast-like cells where channel width was lower than 150 μm. Previous studies have shown that cells will physically respond to micron-sized features; specifically, cells will align themselves to the groove and become elongated in the direction of the groove.[171, 172]

Figure 81 (a) shows the cells in a trypsinized state and Figure 81 (b) shows the initial coverage of approximately 20%. At longer time-intervals, the cells near the wall were observed to orient themselves along the length of the channel. At 48-72 hours the cells were observed to be multinucleated with a significant change in phenotype, indicating matrix induced differentiation. Figures 82 A and B contains optical micrographs of 60 μm and 150 μm channel with confluent B35 neuroblast-like cells. The images recorded at 72 hours post seeding, show supplemental growth with a high cell-density. There was also an increase in the average number of nuclei over time, suggesting differentiation of some neuroblast-like cells to multinucleated neuron-like cells. Figure 83 contains *live/dead* micrographs of a 60 μm channel with B35 neuroblast-like cells. Green fluorescing nuclei in these live-dead stained cells showed viability of the cell with no damage to the nucleus.

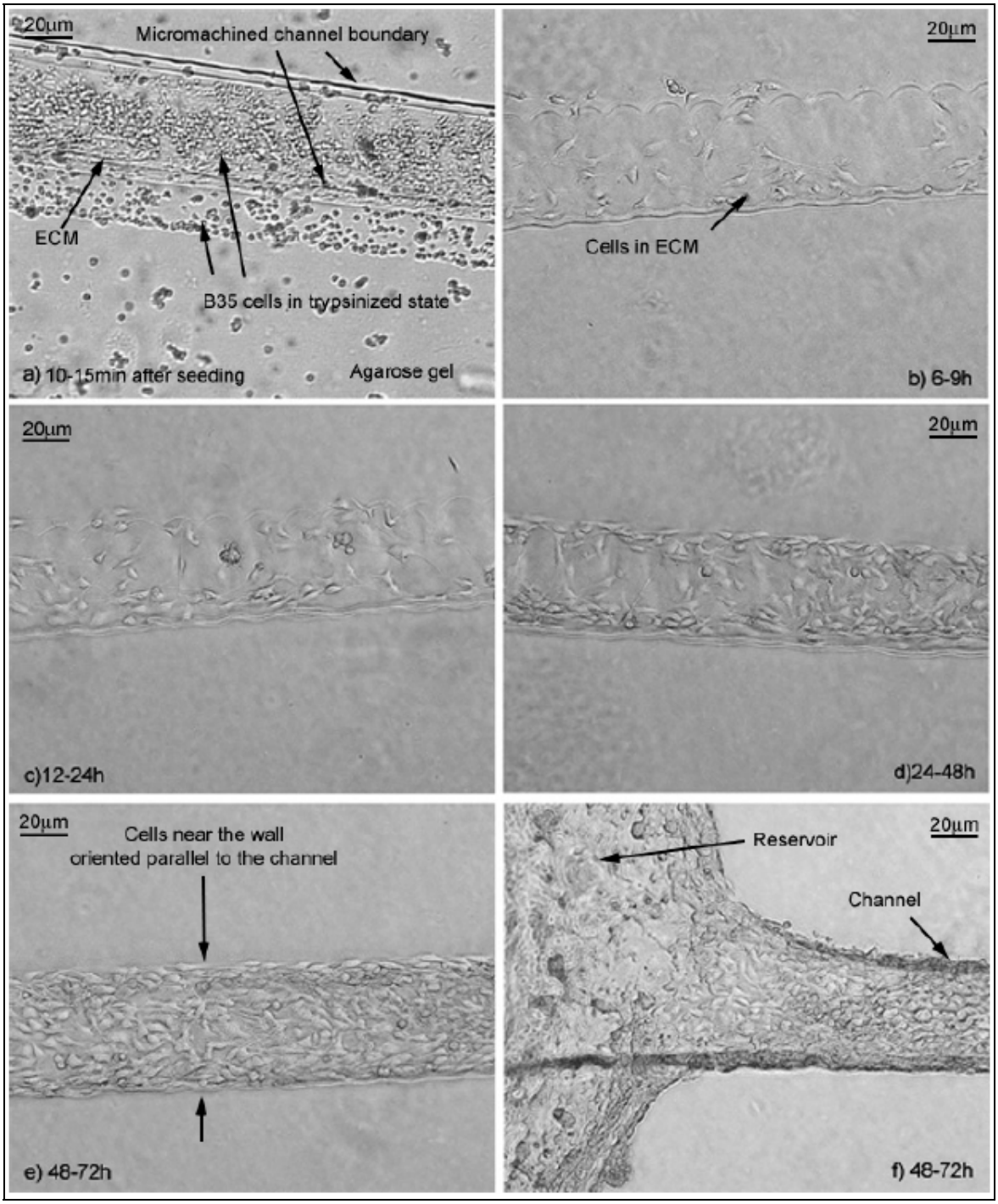

Figure 81. Optical micrograph of growth and proliferation of B35 neuroblast-like cells on ECM filled micromachined channels. Images recorded at **a)** 10-15 min, **b)** 6-9 h, **c)** 12-24 h, **d)** 24-48 h, **e)** 48-72 h, and **f)** 48-72 h near the reservoir end.
Scale bar equals 20 μm.

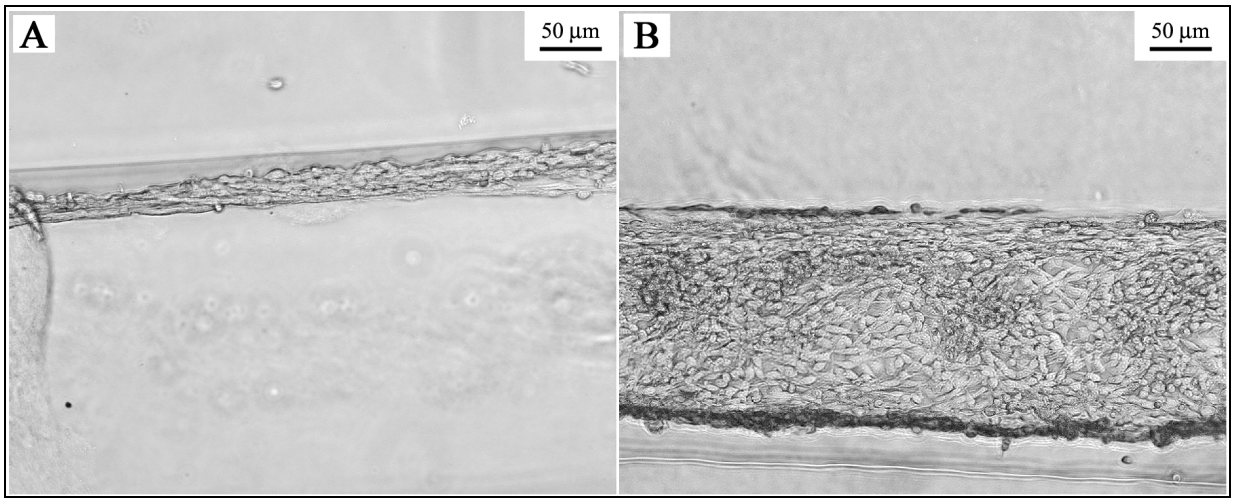

Figure 82. Optical micrographs of confluent B35 neuroblast-like cells in channels of width a) 60 µm and b) 150 µm; recorded 72 hours post seeding. *Scale bar equals 50 µm.*

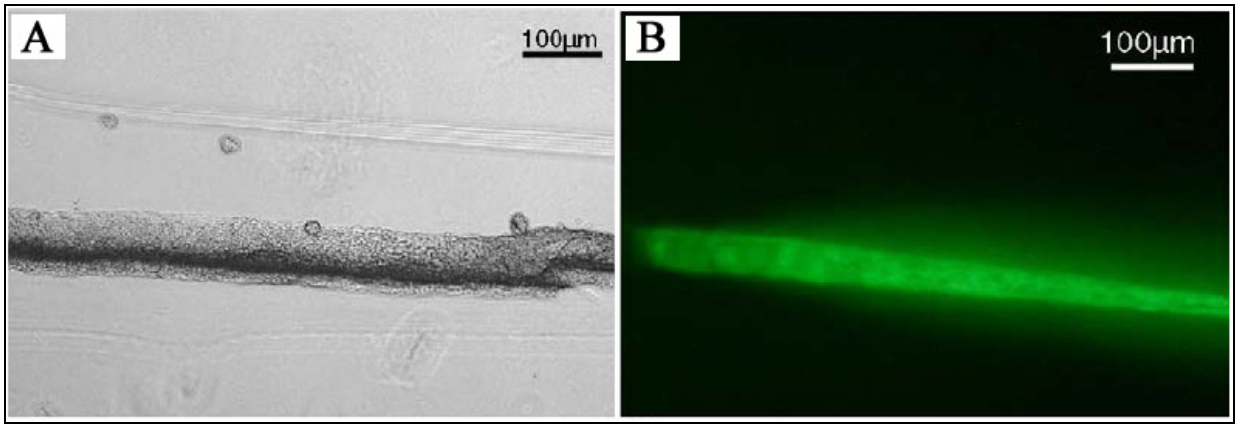

Figure 83. A) Optical light and **B)** fluorescent micrograph of a 60 µm channel containing B35 rat neuroblast-like cells stained with *live/dead* assay. *Scale bar equals 20 µm.*

Figure 84 contains *live/dead* micrographs of a 100 μm channel with C2C12 mouse myoblast-like cells (*adapted from Patz et al*.[39]). The images recorded at 24 hours after seeding, demonstrate cells aligned parallel to the channel length. Green fluorescing nuclei in these live-dead stained cells indicated viability of the cell with no damage to the nucleus. The width of the C2C12 myoblast-like cell-network was observed uniform through the length. Figure 85 contains *live/dead* micrographs of a 60 μm channel with A431 human skin carcinoma cells. These squamous cells are flat and irregular, and renew basally. From Figure 85A a higher cell density near the upper end can be observed. This may be attributed to basal renewal of these cells. The green fluorescing nuclei in these cells observed from Figure 85B demonstrated good viability with no signs of apoptosis.

Further at 96 hours and longer, B35 neuroblast-like cell-matrix network began to delaminate from the agarose gel substrate. For the 1 cm long 100 mm channel, the aspect ratio for the fully grown network is approximately 100:1. This aspect ratio is preserved even after delamination. Figure 86 contains a fluorescent micrograph of a free-standing 100 μm wide cell-matrix-protein network suspended in growth media. This cellular network was obtained after 96 hours by delaminating from the microfabricated agarose channels. The micrograph also shows the neuron-like network curled up at one end with regions slightly out of focus. Also, the alignment and packing of cells within the microfabricated channels may evidently dependent on the shape, growth rate, signaling, and locomotion of cell.

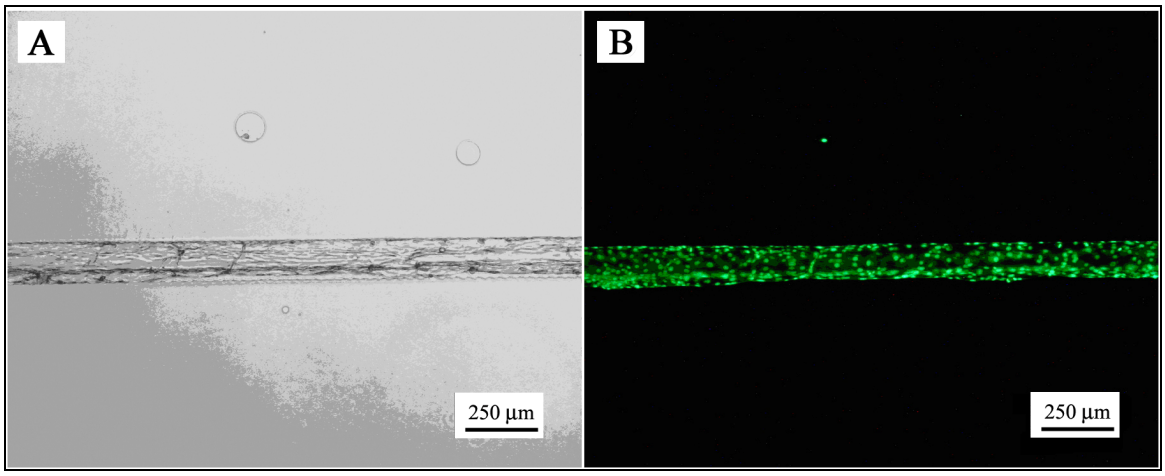

Figure 84. A) Optical light and **B)** fluorescent micrograph of a 100 µm channel containing C2C12 mouse myoblast-like cells stained with *live/dead* assay.[39] Images recorded 24 hours post seeding. *Scale bar equals 250 µm.*

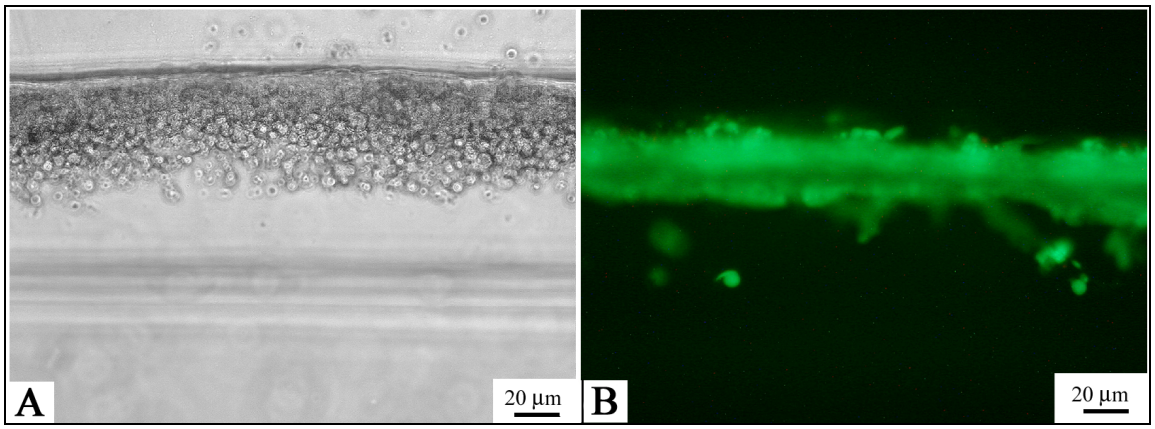

Figure 85. A) Optical light and **B)** fluorescent micrograph of a 60 µm channel containing A431 human skin epithelial carcinoma cells stained with *live/dead* assay. Images recorded 24 hours post seeding. *Scale bar equals 20 µm.*

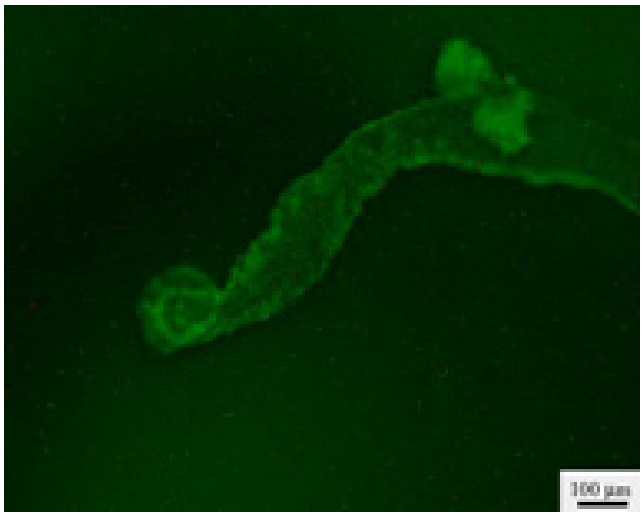

Figure 86. Optical fluorescence micrograph of a free-standing 100 μm wide neuron-like network suspended in a growth media. Image was recorded after delamination from micromachined channel. *Scale bar equals 100 μm.*

3.3.4 VEGF/Heparin-promoted CLM Development of Vascular Networks

From the last section, the CLM process was successfully validated for microfabrication of a variety of cellular networks. Development of CLM for multi-cellular tissue networks using selective growth factors may prove to be further valuable to the field of regenerative medicine.

Figure 87 contains a schematic of the various layers in human arteries and veins. [173] As seen earlier, the artery contains various layers of different thicknesses. The inner sheet is *tunica intima* containing a thin layer of aortic endothelial cells. The subsequent layer contains a thin sheet of *human elastin*. This is followed by a thick layer of *tunica media* containing aortic smooth muscle cells. Subsequent layers of *tunica externa* contain connective tissue and epithelial cells. In order to allow development of multi-layered vascular networks, various designs were sought. Concentric circular rings with varying thicknesses connected to independent reservoirs were thought to be promising. Such a design may allow microfluidic flow of selective growth factors into each ring (representing each layer). As demonstrated earlier, CLM may allow microscale control over thickness and depth.

Figure 88 contains optical and scanning electron micrograph of a two-circle ring with a 2x2 mm reservoir micromachined on Si (111) for validation. The outer ring was 4 mm in diameter and the inner ring was 3.5 mm in diameter. The ring thickness for both was approximately 250 μm. Figure 88B shows the channel from the reservoir connecting to the two rings without overlap to allow controlled microfluidic flow. The micropositioning feed-rate and laser parameters were fine-tuned to obtain ablations within 5% tolerance of the original design. Figure 89 contains images from the various stages of CLM development.

Figure 89A shows the initial design validation from the translation stage after CAD input. Figure 89B shows validation of design from CLM of Si (111). Figure 89C shows development of a similar design on agarose hydrogel. Figure 89D shows confluent aortic cell-growth on the CLM microfabricated design filled with Matrigel® growth factors.

These results were used to develop two/three layered ring networks in agarose gels with the inner layer containing human aortic endothelial cells, the middle layer containing human elastin, and the outer layer containing human aortic vascular smooth muscle cells. In order to develop a differential adherent surface for the two aortic cells (*human aortic endothelial cells and human aortic smooth muscle cells*) various growth factors were sought. There are various angiogenic factors that are responsible for neovascularization and growth/proliferation/inhibition of vascular cells. Some of these factors include fibroblast growth factors (FGF), platelet-derived endothelial cell growth factor (PDGF), transforming growth factors (TGF α &,β), angiogens, TNF-α , IL-8, VEGF, heparin and many other still researched.[174-176] Among them, vascular endothelial growth factor (VEGF) is widely noted for its role on the stimulated growth and proliferation of aortic endothelial cells. Transplantation results with heart cells have shown increased VEGF expression.[177] Other studies have shown heparin as a non-selective agent inhibiting growth of aortic smooth muscle cells.[178, 179] Weatherford *et al.*[180] have shown VEGF-promoted proliferation of endothelial cells and inhibition of smooth muscle cells. Exploiting these phenomena in a microfabricated interface may allow great potential for development of tissue constructs.

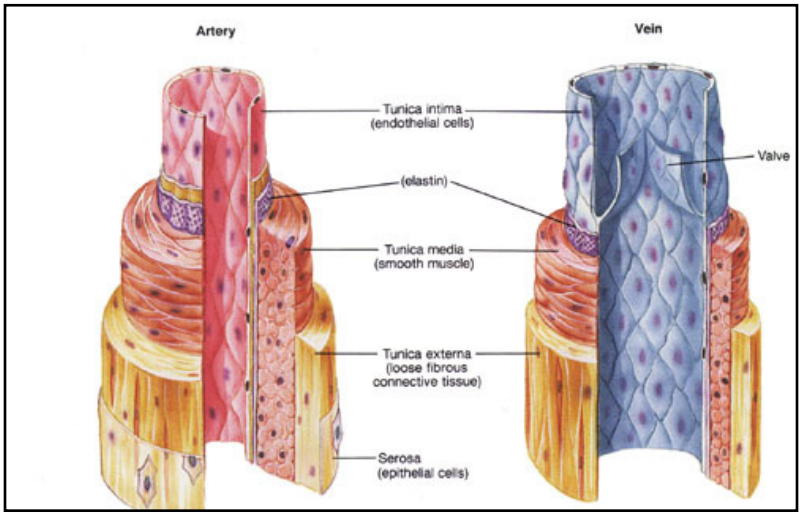

Figure 87. Schematic of the various layers present in a human vasculature.[173]

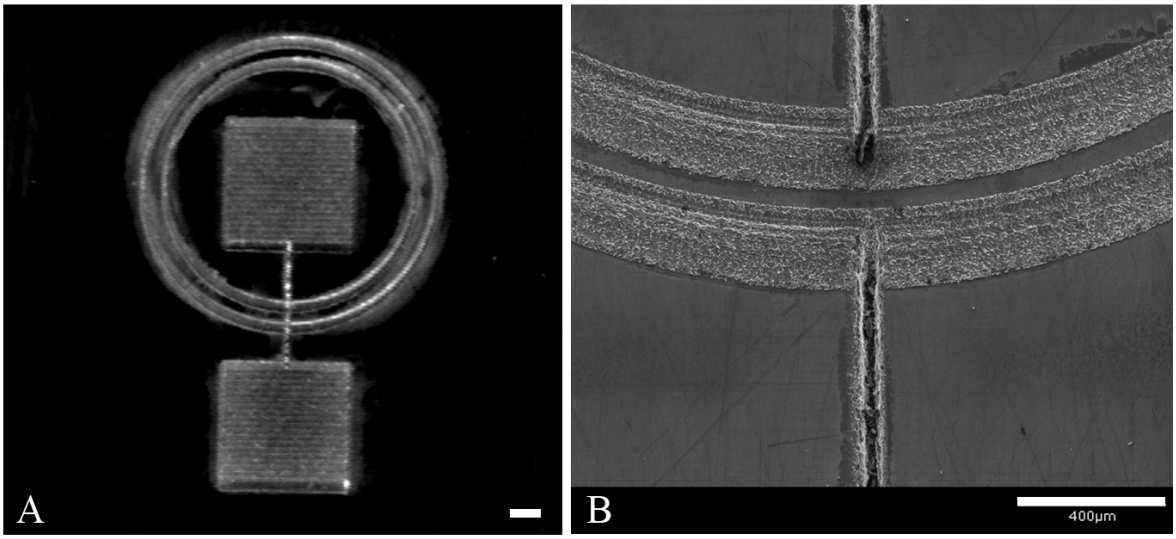

Figure 88. A) Optical micrograph of a two-circle ring design and B) scanning electron micrograph at the channel/ring interface. *Scale bar equals 400 µm.*

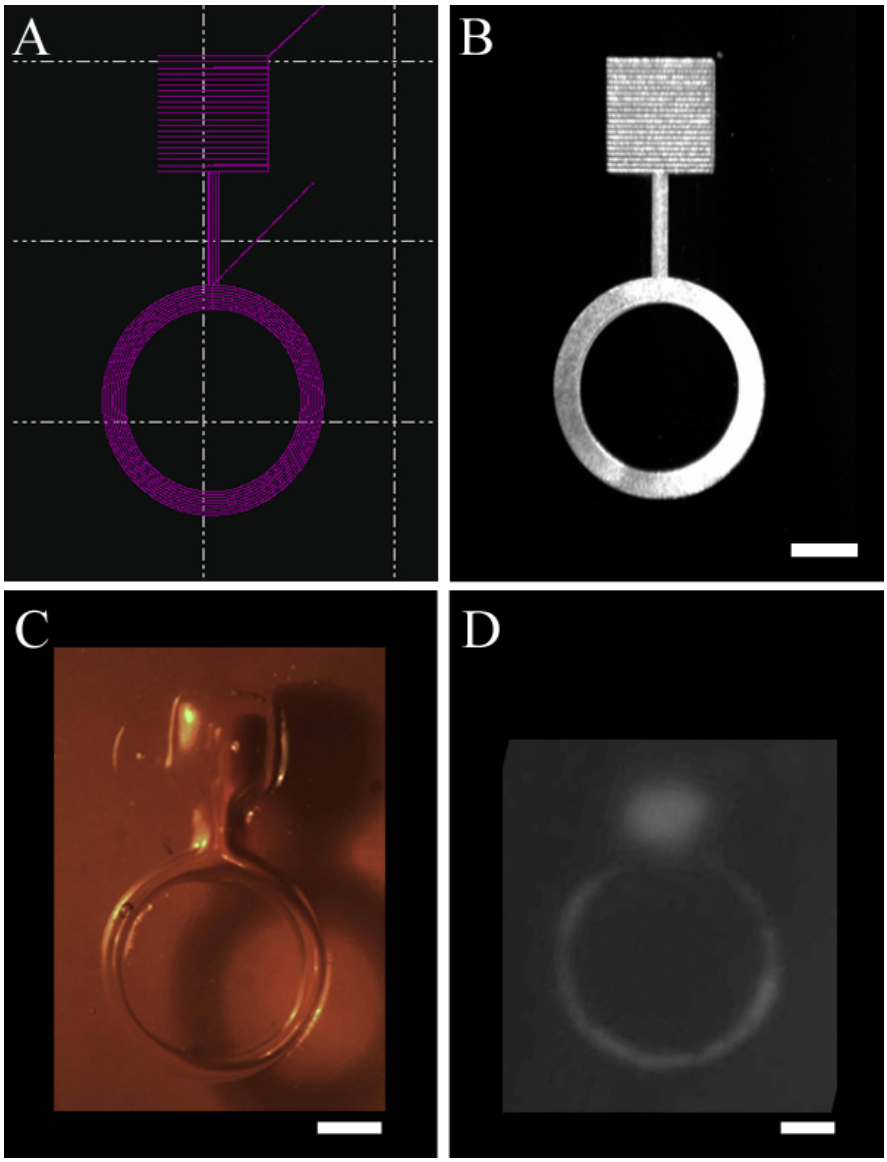

Figure 89. The various stages of CLM development from a CAD design input to microfabricated cellular network output. Image of **A)** CAD design, **B)** CLM of Si (111), **C)** CLM of agarose gel, and **D)** HAAE-1 human aortic endothelial cells on CLM microfabricated agarose/matrix-protein gel. *Scale bar equals ~ 1 mm.*

Vascular endothelial growth factor (VEGF) and heparin were selected to develop differential adherent interfaces for the two types of aortic cells. VEGF in concentrations of 1, 10, 100, 1000 ng/ml and heparin in 1, 10, 100, 1000 units/ml were used to study the cytocompatibility and growth/proliferation of HAAE-1 human aortic endothelial cells and HA-VSMC human aortic smooth muscle cells. The MTT viability data is first analyzed between various concentrations for each cell-type. The viability is then analyzed between the two cell-types at each concentration.

Figure 90 contains graph illustrating the viability of cells with increasing amounts of VEGF (1 to 1000 ng/ml). MTT viability assay suggested that increasing amounts of VEGF reduces viability of HAAE-1 and HA-VSMC cells, in comparison with regular media. Viability of both cells were significantly higher at V1 (VEGF: 1 ng/ml) than at V10 (VEGF: 10 ng/ml), V100 (VEGF: 100 ng/ml) or V1000 (VEGF: 1000 ng/ml) ($p<0.05$). There was no significant difference observed in the viability of the cells for V10, V100 or V1000. When comparing the two cell-types, the viability of HAAE-1 was significantly higher than that of HA-VSMC at all VEGF concentrations. This suggested VEGF-induced proliferation of HAAE-1 human aortic endothelial cells with inhibition of HA-VSMC human aortic smooth muscle cells. The difference in mean viability between the two cells was found to be highest at concentration of V10 (VEGF: 1ng/ml).

Figure 91 contains graph illustrating the viability of cells with increasing amounts of heparin (1 to 1000 units/ml). As previously, MTT viability assay suggested that increasing amounts of heparin reduces viability of HAAE-1 and HA-VSMC cells, in comparison with regular media. Increasing concentrations of heparin typically reduced the viability of both cells. Specifically, viability of both cells were significantly higher at H1 (heparin: 1 unit/ml)

than H10 (heparin: 10 unit/ml), H100 (heparin: 100 unit/ml) and H1000 (heparin: 1000 unit/ml). There was no significant difference for viability of cells between H10 and H100. However viability at H10 and H100 was significantly higher than H1000, for both cell-types. When comparing the two cell-types, the viability of HAAE-1 was significantly higher than that of HA-VSMC at H1, H10 and H100 concentrations. There was no significant difference in viability between the two cell types at H1000. As previously, these results also suggested heparin-induced selective proliferation of HAAE-1 human aortic endothelial cells with inhibition of HA-VSMC human aortic smooth muscle cells. The difference in mean viability between the two cells was found to be highest at concentration of H100 (heparin: 100 units/ml).

These findings were used to develop differential interfaces to allow controlled growth and proliferation of HAAE-1 with inhibition of HA-VASMC in microfabricated regions. VEGF concentration at 10 ng/ml and heparin at 100 units/ml were integrated with Matrigel® polymer matrix to allow development of scaffolds within the microfabricated rings/channels. Figure 92 contains MTT viability analysis of HA-VSMC and HAAE-1 in Matrigel® and Matrigel® with 10 ng/ml of VEGF and 100 units/ml of heparin normalized with media. Viability of HA-VSMC reduced significantly and viability of HAAE-1 increased significantly with addition of V10/H100 to Matrigel® matrix. Evidently, the viability between the cells was significantly larger with addition of V10/H100 to Matrigel®. Figure 93 contains optical micrographs of the two cell-types under V10/H100 conditions. These results confirmed earlier finding of VEGF- and heparin-induced proliferation of HAAE-1 human aortic endothelial cells with inhibition of HA-VSMC human aortic smooth muscle cells.

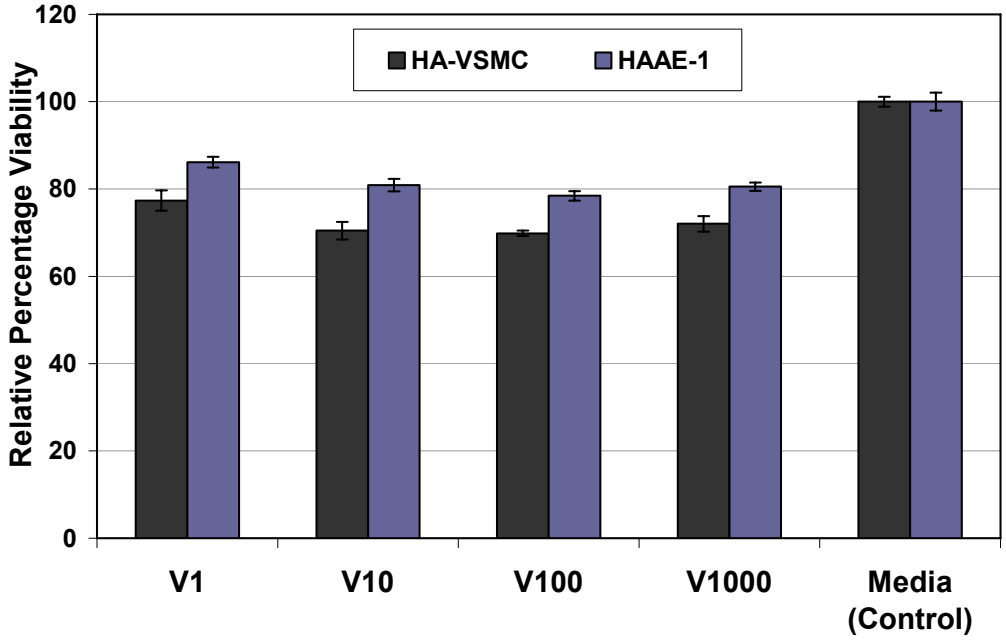

Figure 90. MTT cell viability of HA-VSMC and HAAE-1 for varying amounts of vascular endothelial growth factor (VEGF: 1-1000 ng/ml) normalized with media. *Data represented as mean ± standard deviation. ($p<0.05$)*

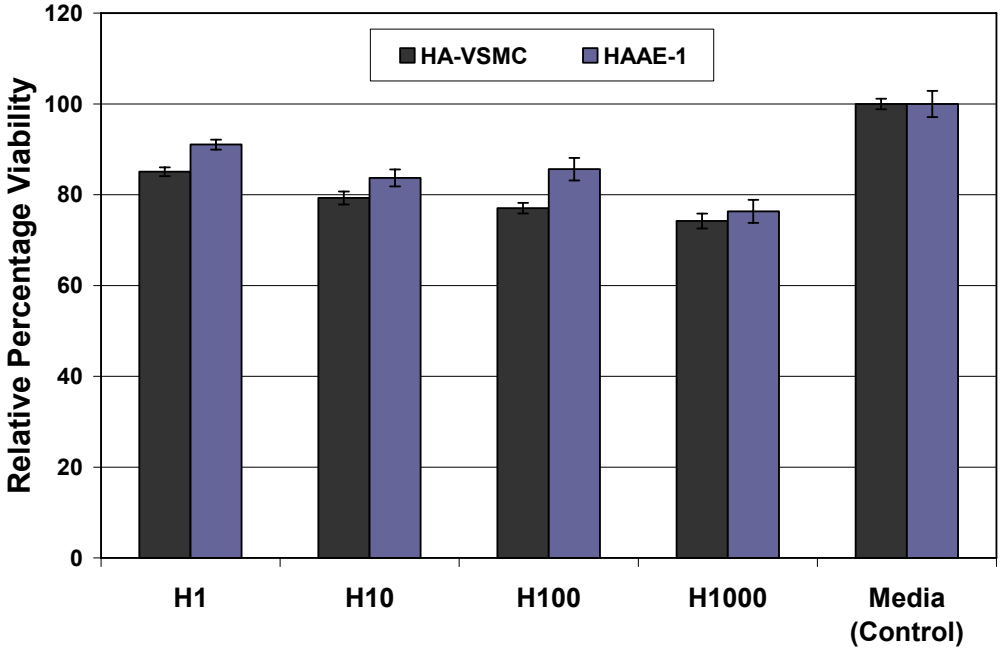

Figure 91. MTT cell viability of HA-VSMC and HAAE-1 for varying amounts of heparin (1-1000 units/ml) normalized with media. *Data represented as mean ± standard deviation. ($p<0.05$)*

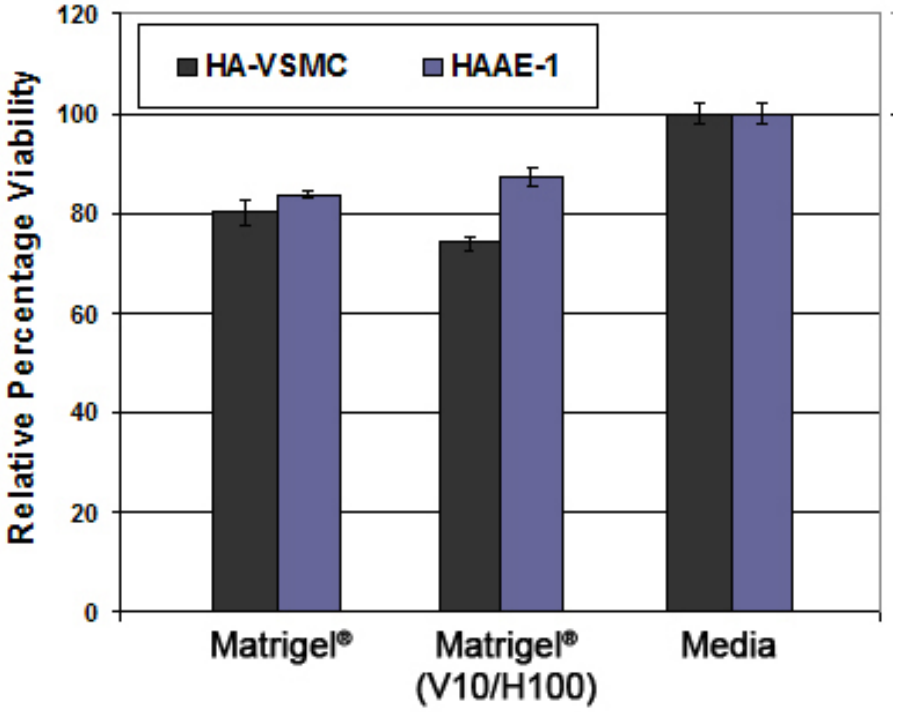

Figure 92. MTT cell viability of HA-VSMC and HAAE-1 for Matrigel®, Matrigel® (with 10 ng/ml VEGF and 100 units/ml heparin) normalized with media. *Data represented as mean ± standard deviation. ($p<0.05$)*

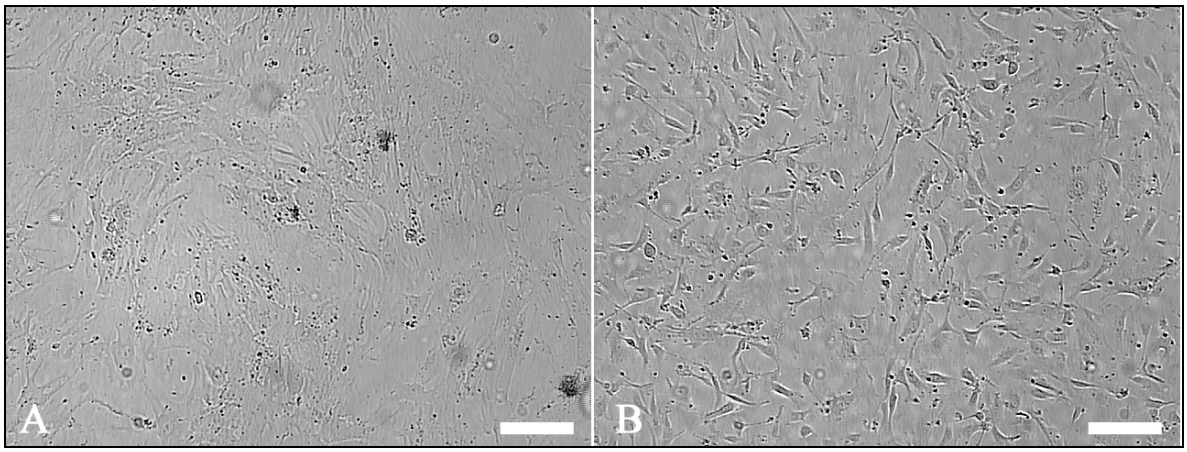

Figure 93. Optical micrograph of A) HA-VSMC and B) HAAE-1 cells (in Matrigel + 10 ng/ml VEGF + 100 units/ml heparin) at 24 hours post seeding. *Scale bar equals 100 μm.*

Matrigel® containing V10/H100 was used to promote proliferation of HAAE-1 endothelial cells and inhibit growth of HA-VSMC smooth muscle cells in selective layers. HAAE-1 and HA-VSMC were seeded in microfabricated agarose channels and single-ring designs to observe growth and proliferation. The cells were then seeded on three-circular ring designs with *human elastin* in the centre layer. Figure 94 contains an optical micrograph of an elastin-stained agarose channel. The middle-ring layer containing *HA587 human elastin* was stained dark purple.

As observed previously with with B35 neuroblast-like cells, within 6–9 h, the cells stayed well-adhered to the Matrigel® filled microfabricated regions and did not adhere to the remainder of the agarose area. The HAAE-1 human aortic endothelial cells and HA-VSMC human aortic smooth muscle cells showed signs of differentiation with distinctive change in morphology. Between 12-24 h, the cells continued to proliferate within the micromachined region with increased coverage. By 48 hours, the cells became confluent and past 72 hours they delaminated from the gel into a free-standing tissue-like network. Figure 95A contains an optical micrograph of HA-VSMC-Matrigel® network in a confluent state. These full grown cellular networks start to delaminate from the agarose gel interface at 72 hours. Figure 95B contains an image of a 200μm partially delaminated HA-VSMC-Matrigel® network. The micromachined channel is clearly visible.

The cells were also studied in co-culture (50:50 media) to develop vascular tissue-like networks. Figure 96A contains an optical micrograph of multi-layered HAAE-1/HA-VSMC-humanelastin-Matrigel® network containing 10 ng/ml VEGF and 100 units/ml heparin. The entire network was delaminated without much change from the original design. Figure 96B contains *live/dead* stained image of a HAAE-1 network at 48 hours. Figure 97 contains

additional *live/dead* images of HA-VSMC network, HAAE-1 network, and multi-cellular networks. The multi-cellular network in Figure 97C was comprised of HA-VSMC/HAAE-1-Matrigel®-human elastin network. The endothelial layer on the inner ring became confluent in a Matrigel®+10 ng/ml VEGF+100 units/ml heparin environment. Human elastin was present in the middle layer, and smooth muscle cells proliferated on the outer layer. Green fluorescing nuclei in these live-dead stained cells indicated viability of the cell with no damage to the nucleus. In some cases during co-culture, few red fluorescing dead cells indicating apoptosis were also observed. *Live/dead* analysis of the multi-cellular networks showed (>99%) viability at 72 hours without any loss in structural integrity. Post 72 hours all networks delaminated into a free-standing network. This aspect ratio was preserved after delamination and the free-standing multi-cellular structure was sustained in media for 96 more hours. These results follow similar patterns to previously observed delamination with B35-neuroblast-like cell networks.

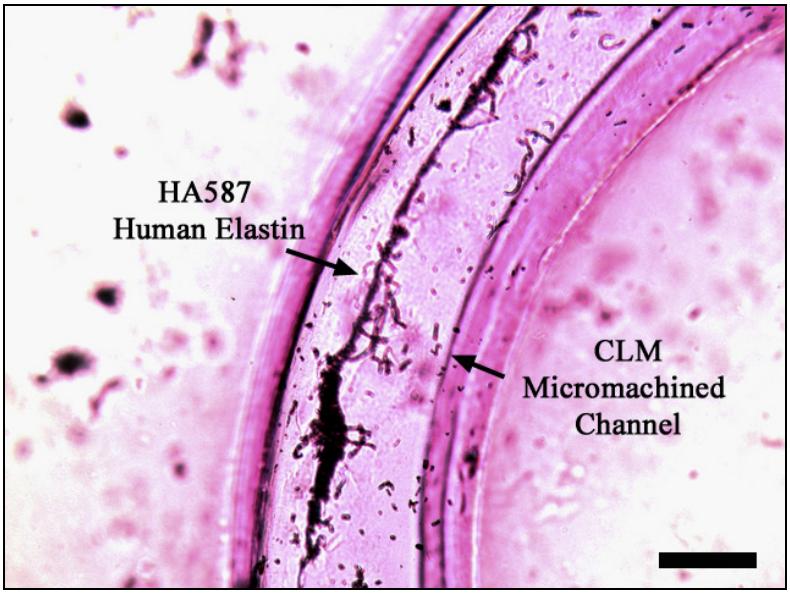

Figure 94. Optical micrograph of an elastin-stained agarose channel containing HA587 human elastin in the middle layer. *Scale bar equals 250 μm.*

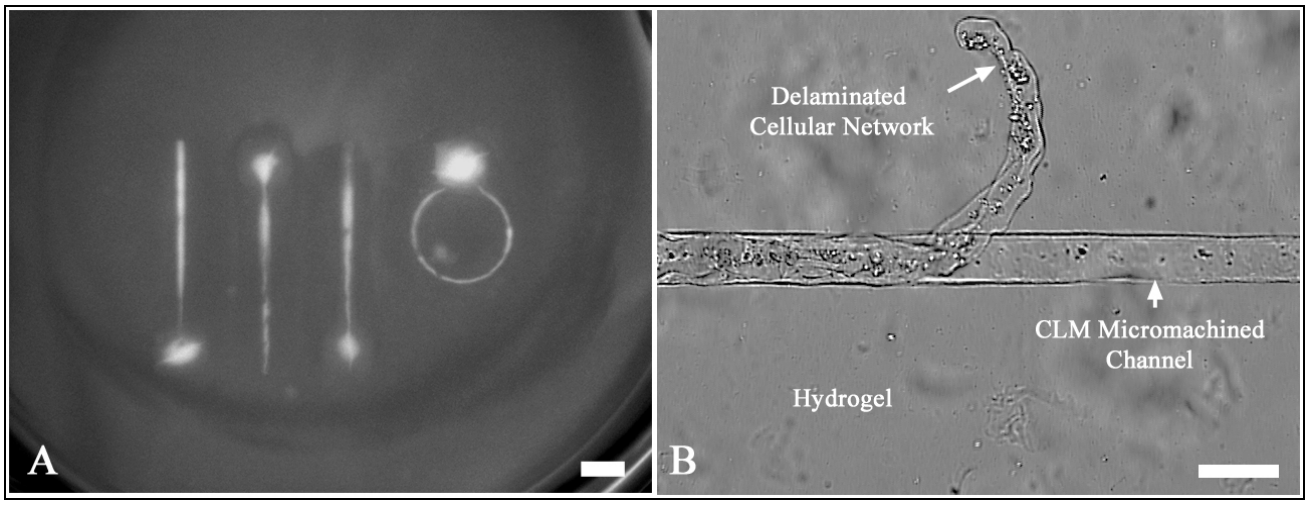

Figure 95. A) Optical micrograph of a full-grown HA-VSMC-Matrigel® network at 72 hours. *Scale bar equals ~ 2 mm.* **B)** Optical micrograph of a 200 μm delaminated HA-VSMC-Matrigel® network, post 72 hours. *Scale bar equals ~ 250 μm.*

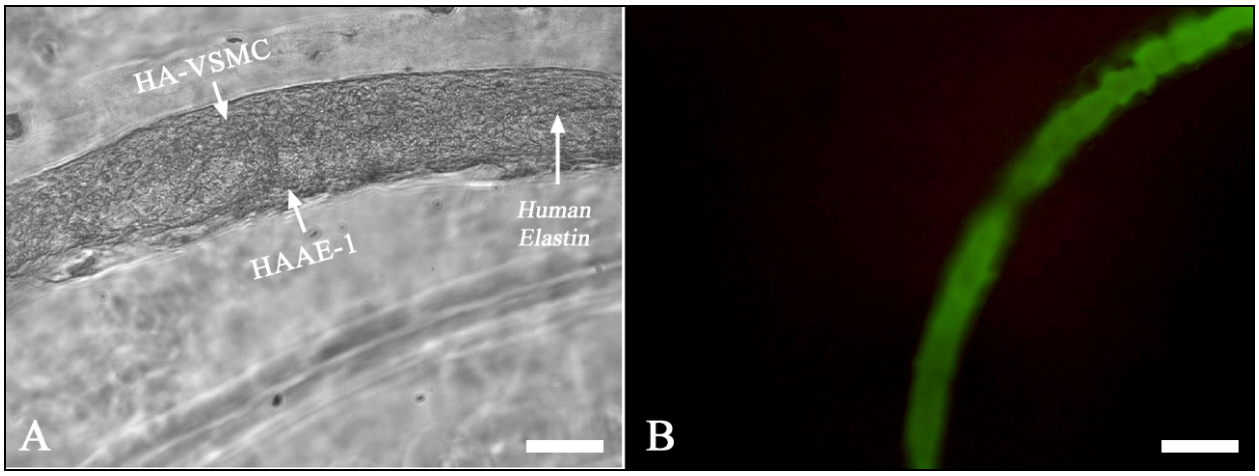

Figure 96. Optical micrograph of **A)** multi-layered HAAE-1/HA-VSMC-humanelastin-Matrigel® (V10/H100) network at 72 hours and **B)** *live/dead* stained HAAE-1 network at 48 hours. *Scale bar equals ~ 250 μm.*

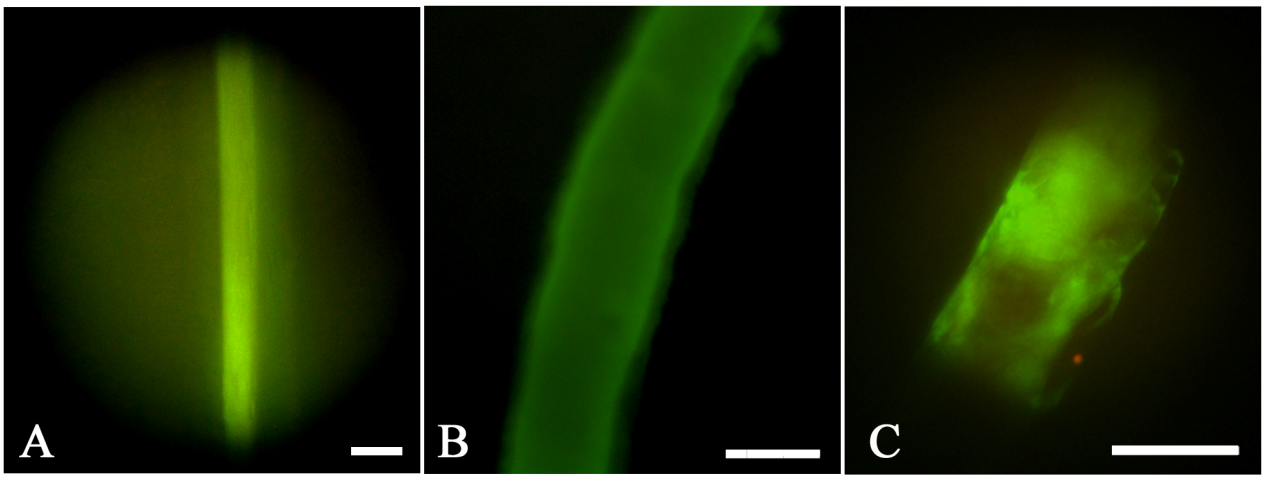

Figure 97. *Live/dead* stained fluorescent micrographs of **A)** HA-VSMC-Matrigel® network, **B)** HAAE-1-Matrigel® network, and **C)** HA-VSMC/HAAE-1-Matrigel®-human elastin network. *Images were recorded at 48 hours. Scale bar equals ~ 200 μm.*

Most conventional techniques have employed cell-seeding on a pre-formed polymeric conduit to facilitate growth of vascular networks, which may not entirely allow control over the various cellular and extracellular layers. CLM provides a unique direct-write approach to microfabricate complex geometries that may be used to develop vascular networks including small diameter blood vessels for bypass surgery and repair of heart components. Further, microscale integration and computer-aided controlled alignment of multi-cellular components may allow development of unique tissue-constructs for next-generation patient-specific care.

3.4 PIT - Piezoelectric Ink-jet Technology

Synthetic adhesives have largely displaced natural adhesives in the automotive, biomedical, and electronic equipment industries over the past century. However, rising concerns over the environmental and health effects of solvents, monomers, and additives used in synthetic adhesives have recently led the scientific community to seek natural alternatives. Marine mussel adhesive protein is a formaldehyde-free natural adhesive that demonstrates excellent adhesion to several classes of materials, including pure metals, metal oxides, polymers, and glasses.

In this section, piezoelectric ink-jet technology was developed for CAD/CAM administration of naturally derived and synthetic biological adhesives. A MEMS based piezoelectric actuator was used to control the flow of the adhesive solution through the ink jet nozzles. Various characterization techniques were employed to determine the extent of chelation caused by Fe(III) on mussel proteins. Piezoelectric ink-jet printing of naturally derived biological adhesives may overcome several problems associated with conventional tissue bonding materials, and may be employed for future clinical applications.

As a first step, PIT process was validated using biological proteins. Various aspects including feasibility of ink-jetting, resolution of the micropatterns, biological activity of proteins after processing, were analyzed. Similar steps were also taken for administration of adhesives.

3.4.1 Validation with Streptavidin/Biotin

The piezoelectric print-head utilizes a voltage waveform input that allows control over volume of solution dispensed. The print head moves the ink solution from the cartridge to the channel. The impedance matching unit allows the solution to move through the descender where it is ejected through a 21 μm nozzle. Sixteen such nozzles are employed.

3.4.1.1 Microscopy

Figure 98 contains images of the streptavidin ink drops generated at 13 V using a high speed camera. Images a, b, c, and d were recorded at 20, 50, 100 and 200 μs time delays, respectively. At constant voltage and firing frequency, the drop traveled approximately 90 μm after 20 μs, 290 μm after 50 μs, 600 μm after 100 μs, and 1170 μm after 200 μs. The mass-velocity remained constant after the initial period of 25-30 μs. A graph showing drop travel at various time intervals is also shown. Figure 99 contains fluorescent micrographs of the streptavidin microarray. The streptavidin protein was labeled with rhodamine for detection using fluorescence microscopy. Distinct microscale protein structures with feature sizes of ~20 μm were observed. Owing to control over front-velocity of the droplet, piezoelectric ink-jet printing may allow proteins to be embedded into gel-like substrates. Figure 100 contains optical fluorescence micrographs of streptavidin microarrays embedded into a methylcellulose gel at various resolutions. The embedding depth was varied by changing the fluid velocity. Figure 101 contains a microarray pattern of fluorescein-labeled biotin drops (~20 μm diameter) on a silicon substrate.

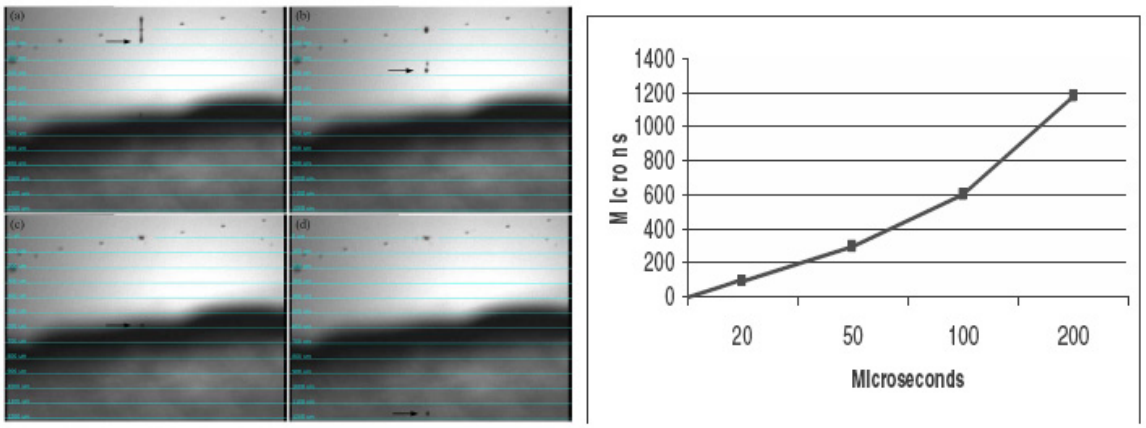

Figure 98. Optical micrograph of streptavidin drop generated at 13 V and captured at t=20, 50, 100 and 200 μs, and corresponding graph of drop travel (microns) vs. time (microseconds).

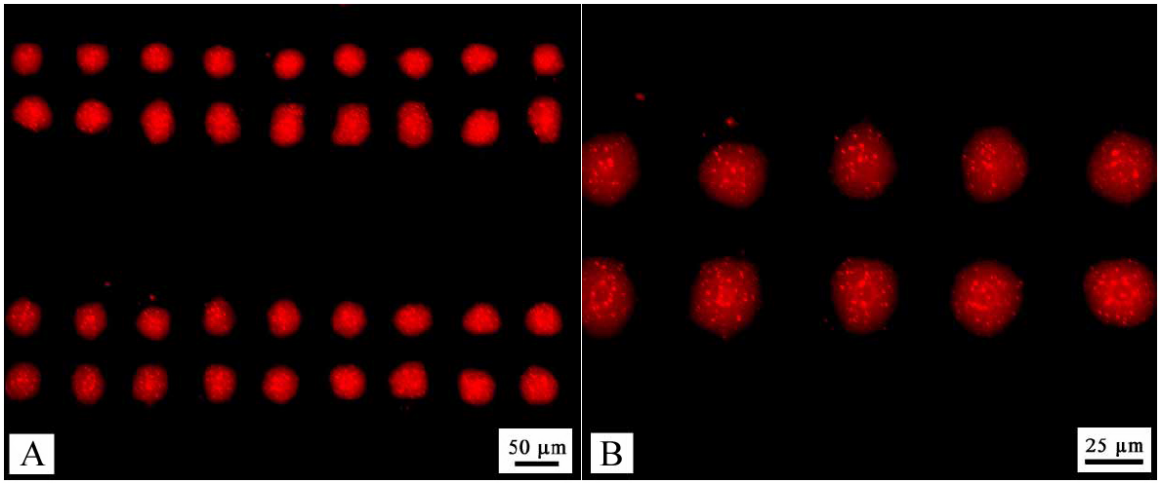

Figure 99. Fluorescent micrographs of rhodamine-labeled streptavidin microarray deposited on a silicon substrate. *Shown at different magnifications.*

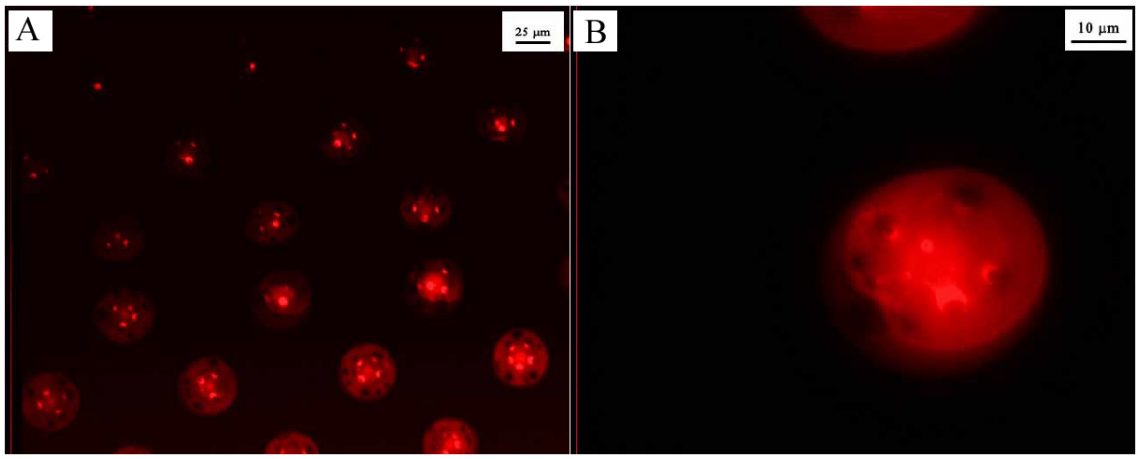

Figure 100. Fluorescent micrographs of rhodamine-labeled streptavidin microarray patterned on a methyl cellulose gel (embedding matrix). *Shown at different magnifications.*

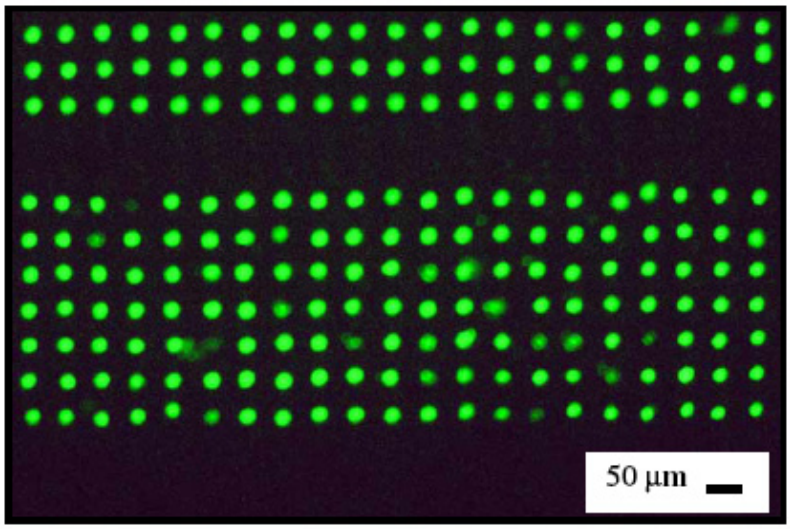

Figure 101. Fluorescent micrograph of fluorescein- labeled biotin microarray deposited on a silicon substrate. *Scale bar equals 50 µm.*

3.4.1.2 Atomic Force Microscopy

Figure 102 contains low and high resolution atomic force micrograph (*topographic scan in contact mode*) of the protein micropattern. Within the ink -jetted protein pattern, the microstructural arrangement appears to be randomly oriented. Three-dimensional topographic images are shown in Figure 103. The microstructures varied between 3 and 8 μm in length and were ~2 μm in height. These structures demonstrate spacing of 8-10 μm. Over a 0.67 mm scan size, the ink-jetted protein microstructures showed randomly oriented peaks and troughs, with distance (peak to peak) of 0.68 μm and average surface roughness of approximately 0.09 μm.

3.4.1.3 Spectroscopy

Fluorescence spectroscopy analysis for *rhodamine-streptavidin* and *fluorescein-biotin* demonstrate control over fluorescent signal output. This was achieved by an increase in deposited amount generated by increasing jetting voltages (10-40 V). Graphs are shown in Figure 104 and 105. Fourier-transform infrared absorption spectra overlay (Figure 106) of *ink-jetted* and *drop-cast* rhodamine-streptavidin demonstrate presence of relevant peaks (listed in Table 3). A strong match of all structurally relevant peaks suggested no damage to the protein during piezoelectric ink-jetting. These preliminary findings were used to validate the piezoelectric ink-jetting process for efficacy, accuracy, and repeatability, which were used in the next stages of developing this technology for next-generation bioadhesives.

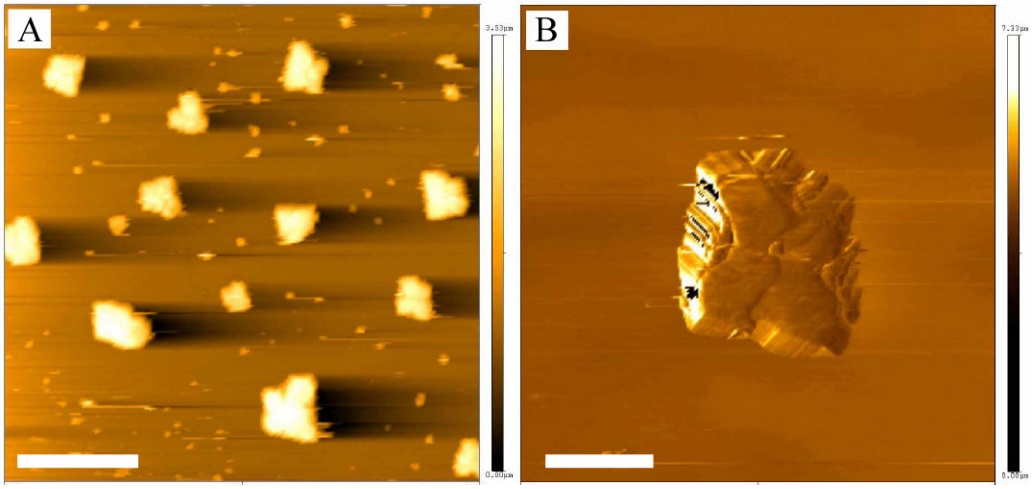

Figure 102. Atomic force micrograph topographic scan of ink-jet-deposited rhodamine-streptavidin micropattern at different resolutions.

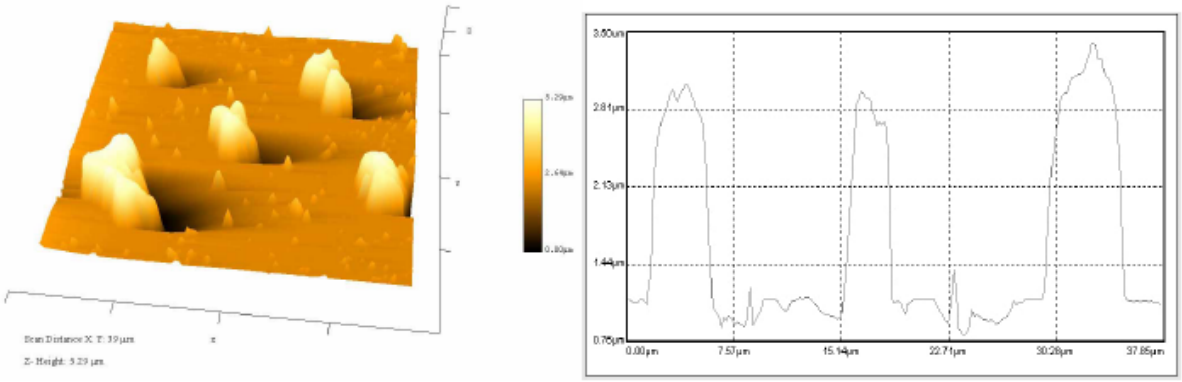

Figure 103. (Left): Three-dimensional topography of ink-jetted *rhodamine-streptavidin* micropatterns. *Scan size = 39 μm. Z-height = 5.29 μm.* (Right): Height profile of the micropatterns.

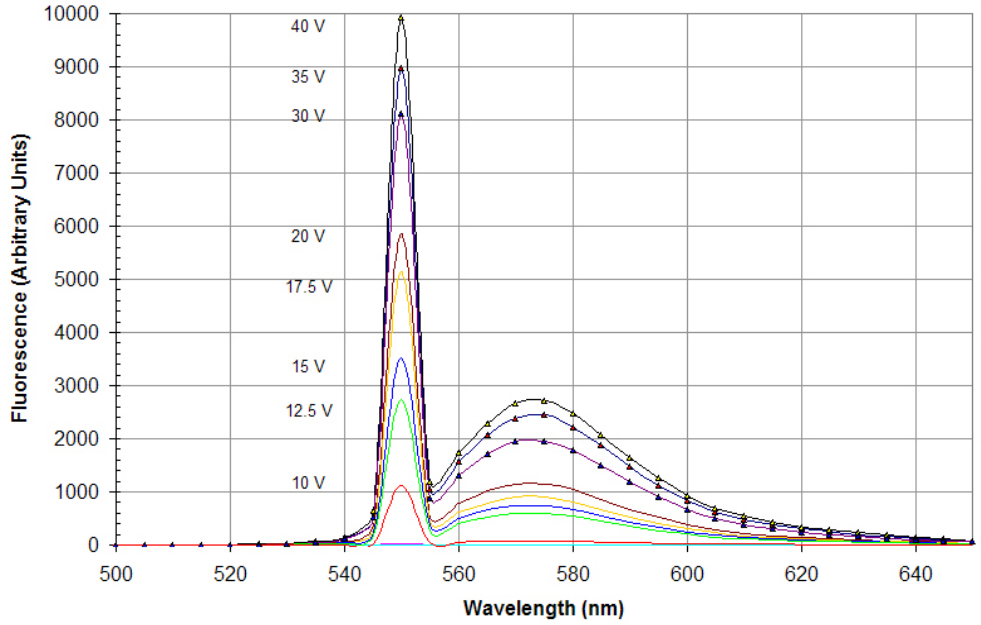

Figure 104. Fluorescence spectroscopy reading for ink-jetted *rhodamine-streptavidin* at various jetting voltages.

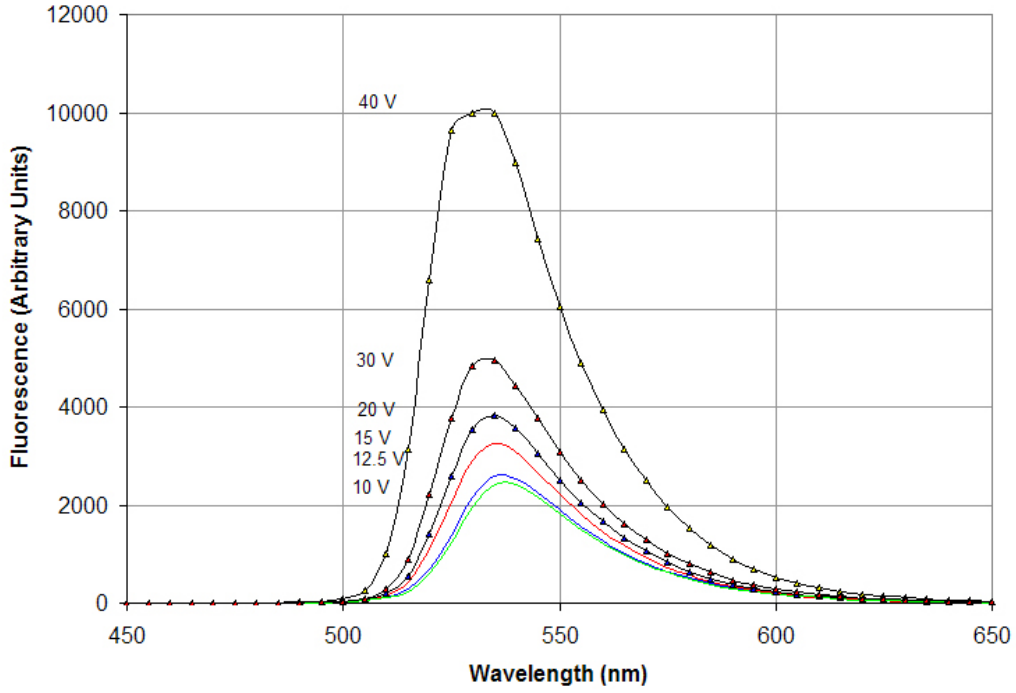

Figure 105. Fluorescence spectroscopy reading for ink-jetted *fluorescein-biotin* at various jetting voltages.

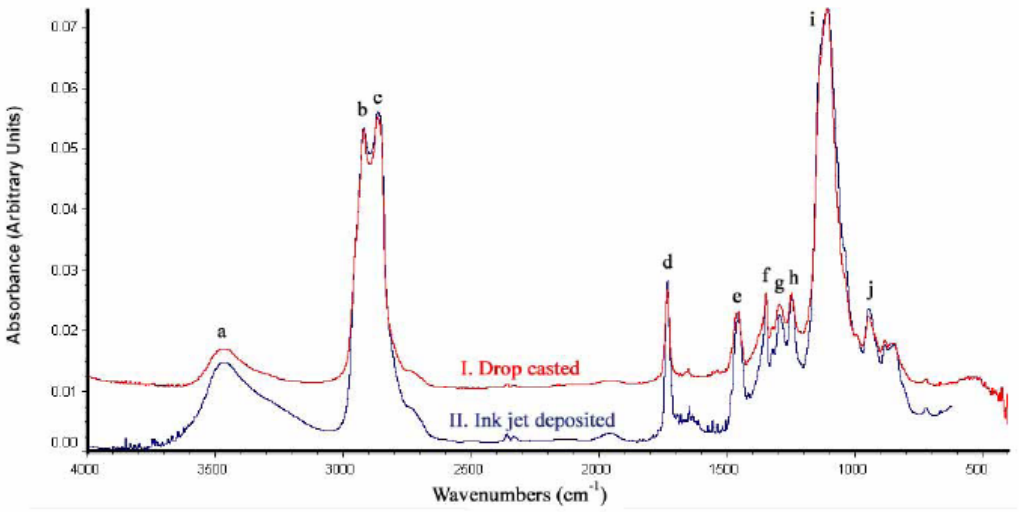

Figure 106. FTIR absorption spectra overlay of ink-jetted and drop-cast *rhoadmine-streptavidin.*

Table 3. FTIR absorption peaks of ink-jetted *rhodamine-streptavidin.*

Notation	Peak wavenumber (cm^{-1})	Peak Assignment
a	3476.0	Monosubstituted amide (O=C-NH)
b	2923.3	Strong amino acid zwitterions (H_3N^+-CH-CO_2^-)
C	2868.4	Secondary amine (CH_2 – N)
D	1734.8	C=O stretching
E	1458.5	Aromatic ring stretching
f	1350.1	Weak amino acid zwitterions
g, h	1297.9, 1249.9	(Aryl – NH)
i	1110.8	(CH_2- NH-CH_2)
j	948.1	Conjugate Thiol

3.4.2 CAD/CAM Administration of Natural Bioadhesives

Next-generation bioadhesives are currently being developed to preserve the advantages of conventional cyanoacrylate adhesives, while lowering the exposure hazards and illness-associated with these materials. Marine mussel adhesive protein is a formaldehyde-free natural adhesive that has gained great interest in the scientific community.[181-185] In this section, piezoelectric ink-jet processing of natural mussel adhesive proteins and their chelation to Fe is studied. The results were analyzed with cyanoacrylate tissue adhesives as controls.

Mussel protein solutions (containing 80% Mefp-1, 20% Mefp-2 and 0.16 mM DOPA) were ink-jetted using a validated waveform. Images of the drop dispensed at various voltages (Figure 107) was used to estimate the velocity and volume dispensed (*in picoliters*) for a given CAD pattern. A 2.5 V increase in jetting voltage developed a significant effect ($p<0.05$) over the jetting velocity. Figure 108 contains a graph of drop velocity (of protein solution) plotted against various jetting voltages. A linear increase in mean velocity with increasing voltages can be observed. Such control over picoliter amount of volume dispensed may allow developments in precision administration and tooling for next-generation surgical applications.

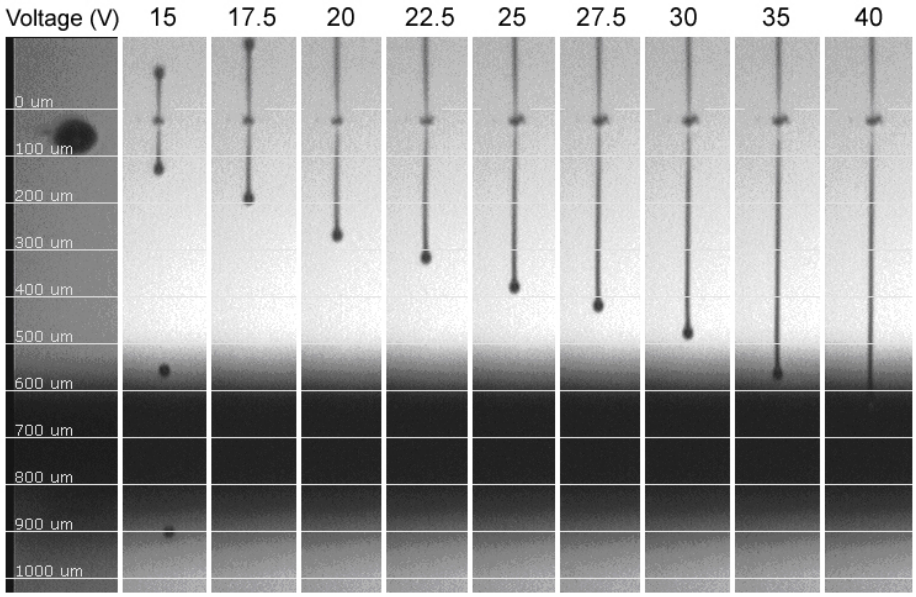

Figure 107. Optical micrograph of mussel protein solution ink-jetted at various voltages (15 - 40V). Images were captured at 30 μs time-delay.

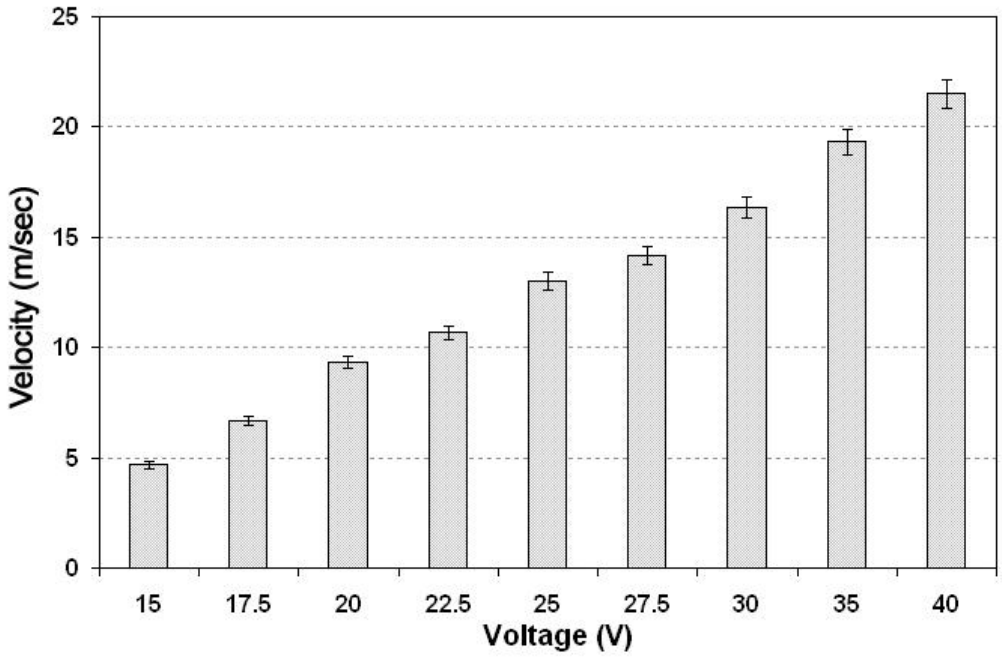

Figure 108. Graphical representation of drop velocity of protein solution vs. jetting voltage. *Values expressed as mean velocity ± standard deviation. (*P<0.05)

3.4.2.1 Microscopy

Mussel protein solution, $FeCl_3$ solutions and synthetic cyanoacrylate tissue adhesive resins were successfully deposited into CAD patterns. Ink-jetting of mussel protein solution in microarray patterns showed resolution up to 50 μm and in line-patterns showed approximate widths of 60 μm, 90 μm, 180 μm, and 300 μm (Figure 109). Ink-jetting of cyanoacrylate adhesives showed development of micropatterns with control over 2D space (Figure 110). An average human cell-size is approximately 20 μm. Thus, bonding line-widths of approximately 60 μm as demonstrated here may be sufficient for microsurgery and delicate wound-closure procedures.

3.4.2.2 Contact Angle Measurements

Contact angle study (Figure 111) performed on mussel protein solutions with varying Fe(III) content showed hydrophilic characteristic values (Table 4). Addition of $FeCl_3$ to DOPA (in mussel protein solution) in ratios of 1:1, 10:1, and 100:1 showed no significant change in contact angle values ($p<0.05$).

3.4.2.3 Spectroscopy

Fourier-transform infra-red absorption (FTIR) spectra overlay of *ink-jetted* (at voltages 10, 20, 30 and 40 V) and *drop-cast* mussel protein solution (*Mefp*) (as control) revealed the presence of all relevant structural peaks (Figure 112A). However, an increasing

shift in absorption peaks was observed, which was consistent with increasing jetting voltage. This result may be attributed to the increase in jetting volume that results from an increase in voltage, as seen previously. FTIR spectra overlay of ink-jetted mussel protein solution (*Mefp*) and *Mefp* with varying concentrations of iron (in Fe:DOPA ratios of 1:1, 10:1, and 100:1) revealed match of all relevant structural peaks with no significant change in absorption intensity between the materials (Figure 112B). The FTIR spectroscopy data demonstrated that unlike thermal based prototyping systems, piezoelectric ink-jet printing does not significantly alter the structure (and thus the functionality) of mussel adhesive proteins (*Mefp*) and DOPA. Similarly, FTIR overlay of *ink-jetted* and *drop-cast* (control) n-butyl cyanoacrylate (Figure 113A) and 2-octyl cyanoacrylate (Figure 113B) revealed match of all relevant structural peaks, indicating no significant structural damage to the adhesive during piezoelectric ink jetting.

X-ray photoelectron spectra of mussel protein solutions (Mefp) (Figure 114) revealed peaks C-C peak corresponding to 285 eV, C-N peak corresponding to 286.1 eV and N-C=O peak corresponding to 288.2 eV. The peaks may be attributed to aliphatic and aromatic carbons in the Mefp and DOPA group. Denconvolution of the C 1s peak revealed the percentage distribution of the peaks present (Table 5). Fe:DOPA in ratios 1:1 and 10:1 revealed lower C-C than Mefp (0.16 mM DOPA) in the absence of Fe. However, excess amount of Fe(III) (as 100:1 Fe:DOPA) revealed increase in C-C peak and a decrease in N-C=O peak. XPS spectra of ink-jetted protein solutions were inconclusive in determining the role of Fe(III) in complex formation. However, the distribution of peaks was similar to previously observed spectra in drop-cast mussel protein solution*s*.[186]

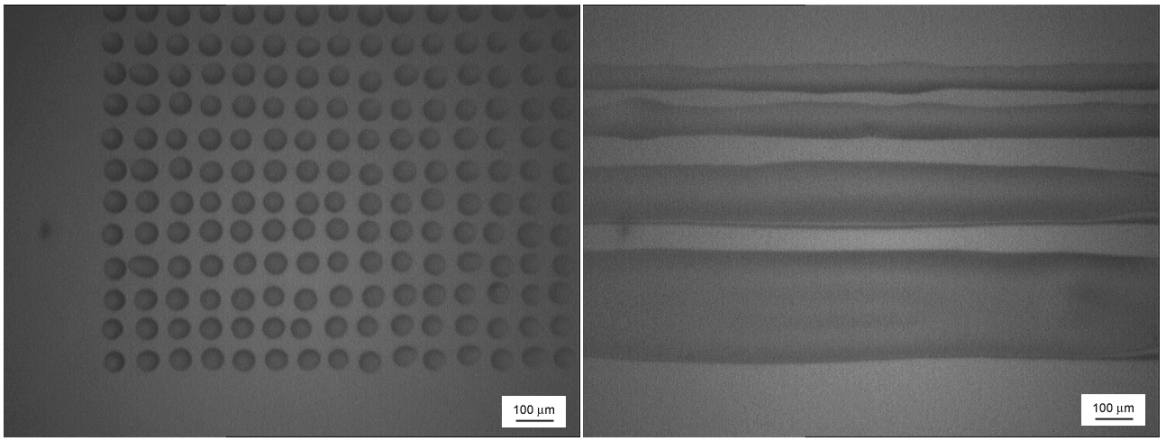

Figure 109. Optical micrographs of mussel protein (Mefp-1 and Mefp-2 containing 0.16 mM DOPA) solution ink-jetted into microarray and line patterns. *Scale bar equals 100 µm*.

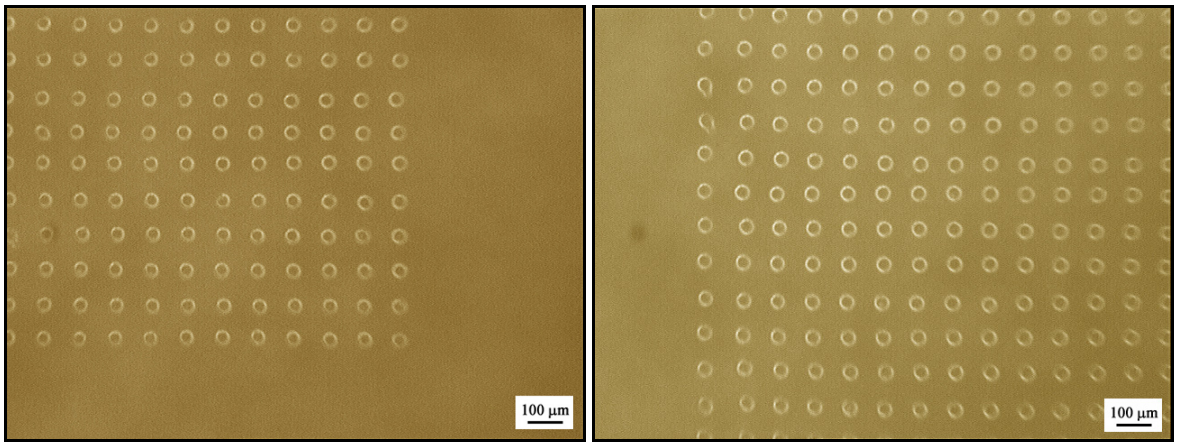

Figure 110. Optical micrographs of 2-octyl cyanoacrylate (Nexaband®) ink-jetted into microarrays. *Scale bar equals 100 µm.*

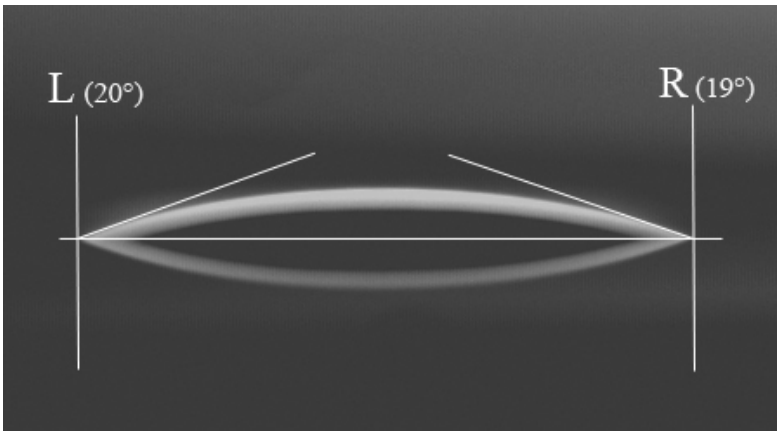

Figure 111. Contact angle measurement of an Mefp solution containing 80% Mefp-1, 20% Mefp-2 and 0.16 mM DOPA.

Table 4. Contact angle measurements for mussel protein solutions with varying Fe content tested on Si (111) substrate.

Solution on Si (111) substrate	**Contact Angle***
Mefp (0.16 mM DOPA)	20.0° ± 2.2°
1:1 Fe:DOPA	18.6° ± 2.0°
10:1 Fe:DOPA	21.3° ± 1.6°
100:1 Fe:DOPA	22.2° ± 1.9°
Control: Deionized water	13.2° ± 1.6°

**Values are expressed as mean + SD*

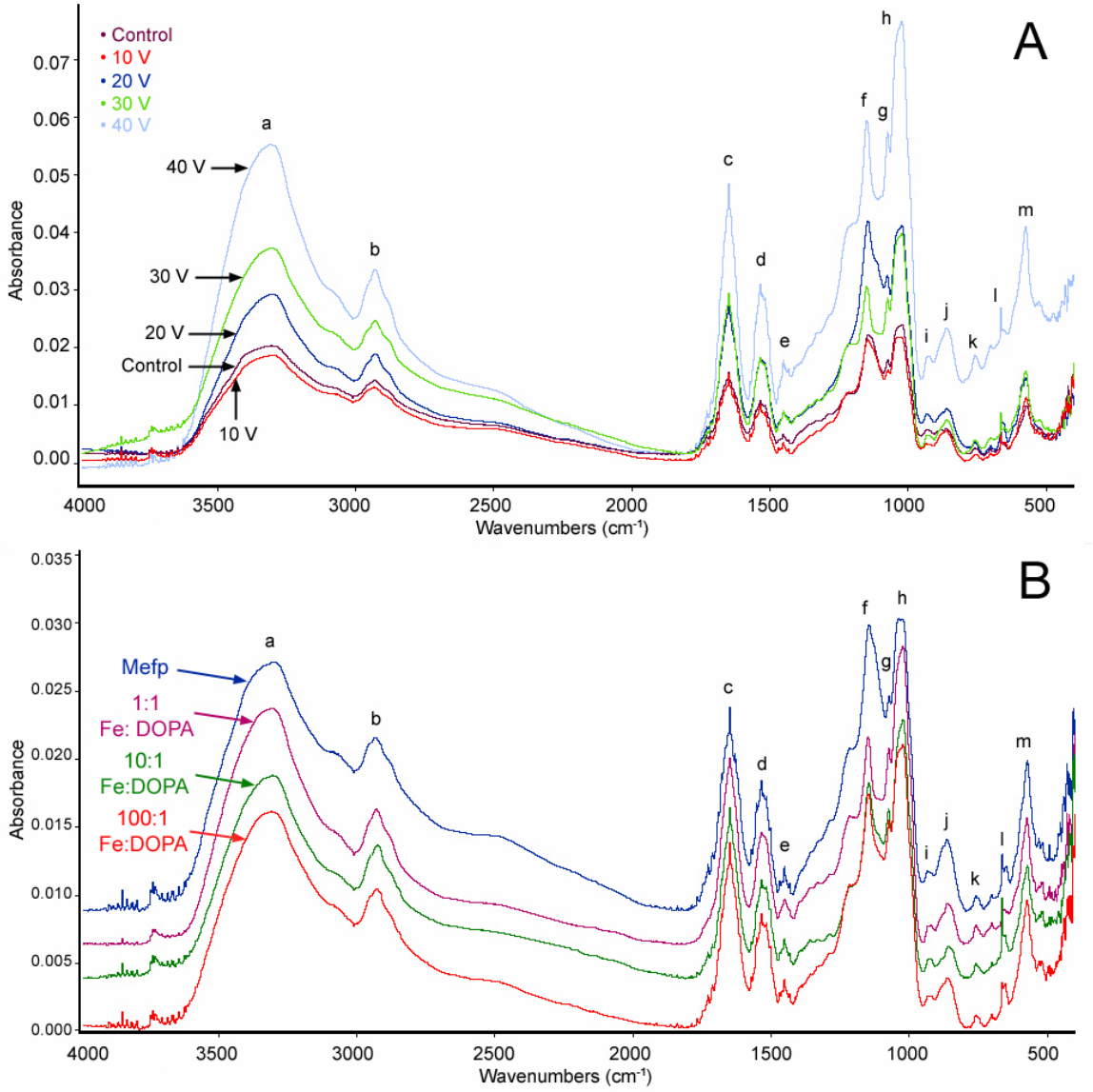

Figure 112. (A) FTIR spectroscopy overlay of ink-jetted mussel protein solution (Mefp) as a function of jetting voltage (10-40 V). Control is a *drop-cast* mussel protein solution. **(B)** FTIR spectroscopy overlay of ink-jetted mussel protein solution (Mefp) as a function of Fe(III) concentration. *Relevant structural peaks are labeled*.

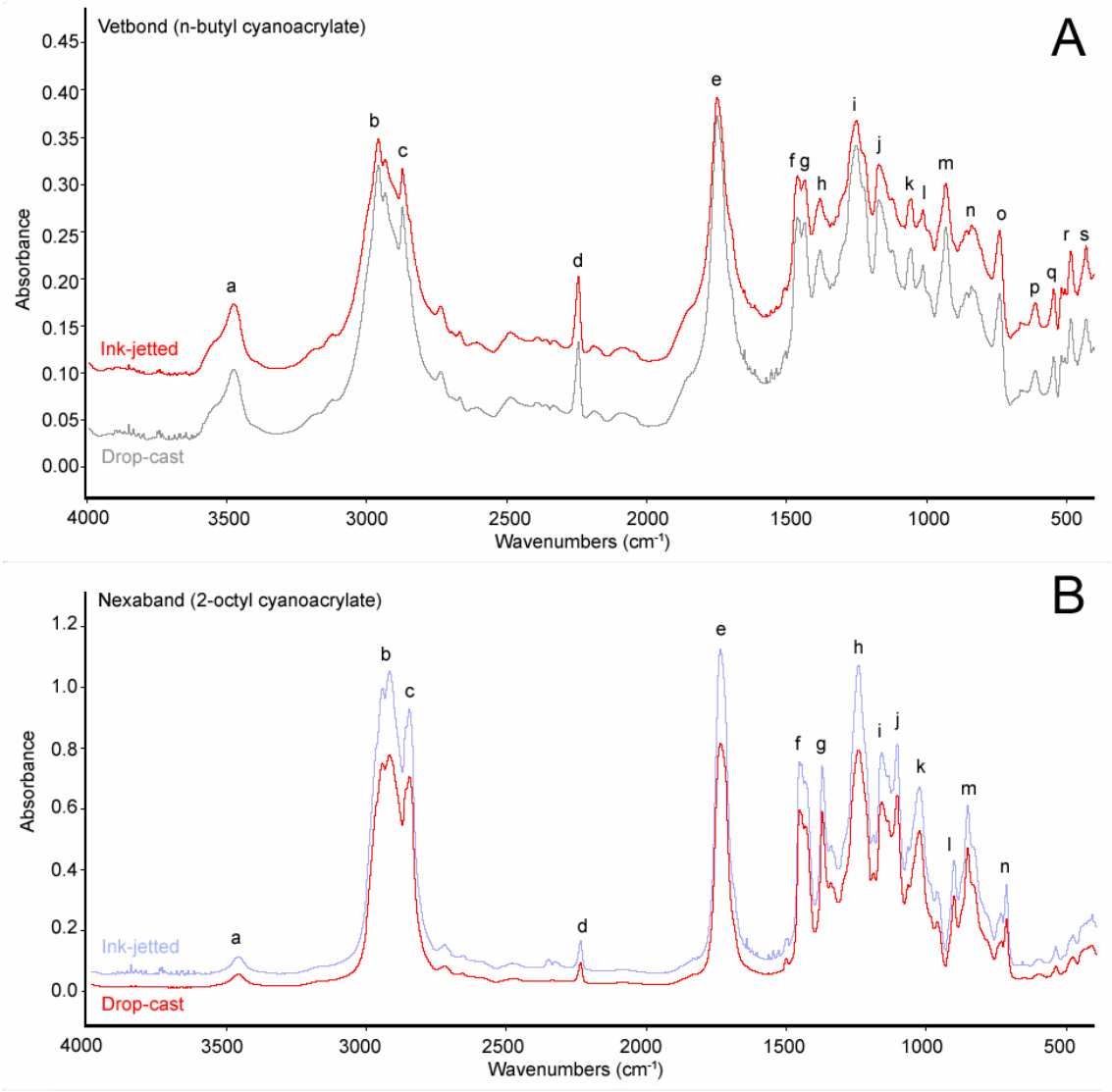

Figure 113. (A) FTIR spectroscopy overlay of *ink-jetted* and *drop-cast* (control) n-butyl cyanoacrylate (Vetbond®). **(B)** FTIR spectroscopy overlay of *ink-jetted* and *drop-cast* (control) 2-octyl cyanoacrylate (Nexaband®). Relevant structural peaks are labeled.

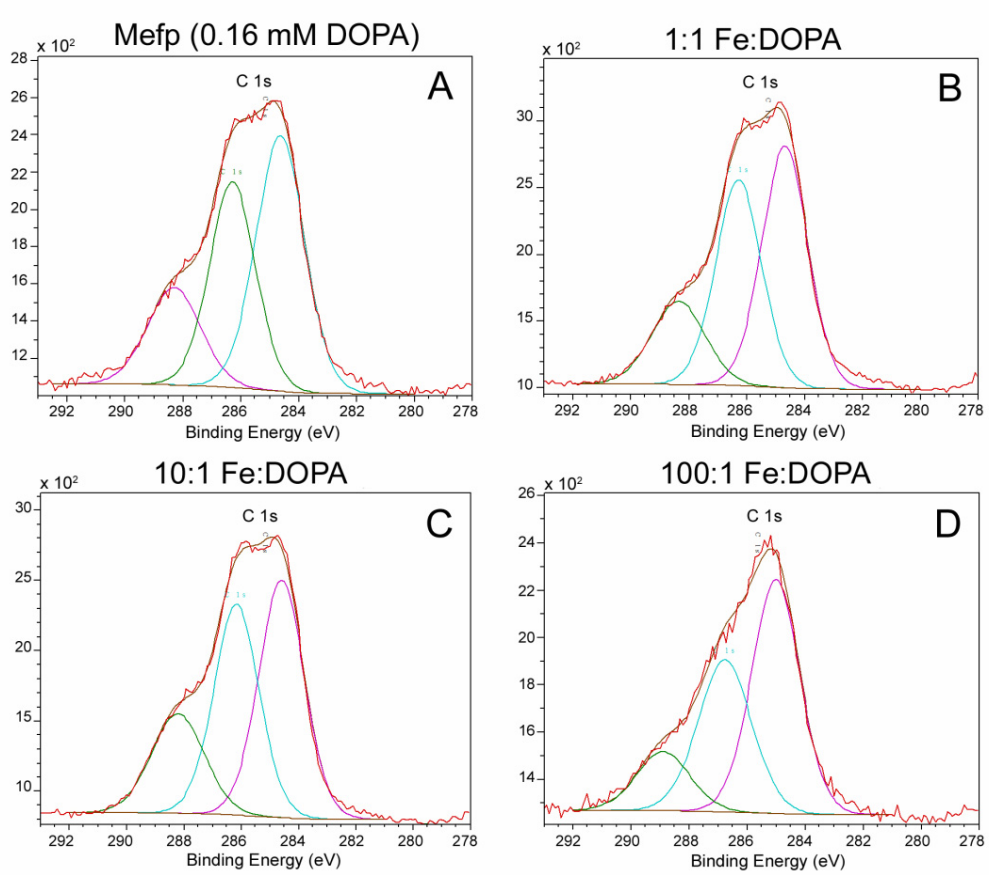

Figure 114. C 1s spectra of ink-jetted mussel protein solutions cured with varying amounts of Fe(III). X-ray photoelectron spectra shown for **A)** Mefp (0.16 mM DOPA), **B)** 1:1 Fe:DOPA, **C)** 10:1 Fe:DOPA, and **D)** 100:1 Fe: DOPA.

Table 5. Deconvolution of C1s peak from x-ray photoelectron spectra.

Assignment	C-C [a]	C-N [b]	N-C=O [c]
Mefp (0.16 mM DOPA)	46%	35%	19%
1:1 Fe:DOPA	44	38	18
10:1 Fe:DOPA	42	37	21
100:1 Fe:DOPA	50	36	14

[a] C-C peak corresponds to 285 eV, [b] C-N peak corresponds to 286.1 eV, and [c] N-C=O peak corresponds to 288.2 eV

3.4.2.4 Atomic Force Microscopy

Atomic force microscopy of ink-jetted mussel protein solution (Figure 115) revealed varying levels of precipitation/cross-linking upon addition of Fe(III). In the absence of Fe, mussel protein (Mefp) (Figure 115A) showed some cross-linking and presence of fibrous networks. The precipitation of long protein complex fibers was clear in 1:1 and 10:1 Fe:DOPA (Figures 115B and 115C), with a higher degree of precipitation in 10:1 Fe:DOPA. Three-dimensional SPM imaging (Figure 116) at the surface of 1:1 Fe:DOPA revealed high-aspect ratio fibrous structures, indicative of protein cross-linking. The height of these fibrous networks varied from approximately 400 nm to 800 nm, while the width varied from 500 nm to 5 μm. Excess amount of Fe in 100:1 Fe:DOPA revealed islands of cross-linked protein mass in most areas (Figure 115D). However, areas of fibrous networks within the printed pattern were also observed. Binding properties of DOPA has been previously studied using atomic force microscopy measurements of DOPA residues against organic and inorganic surfaces.[187] The interaction and strength is known to vary depending on the substrate.

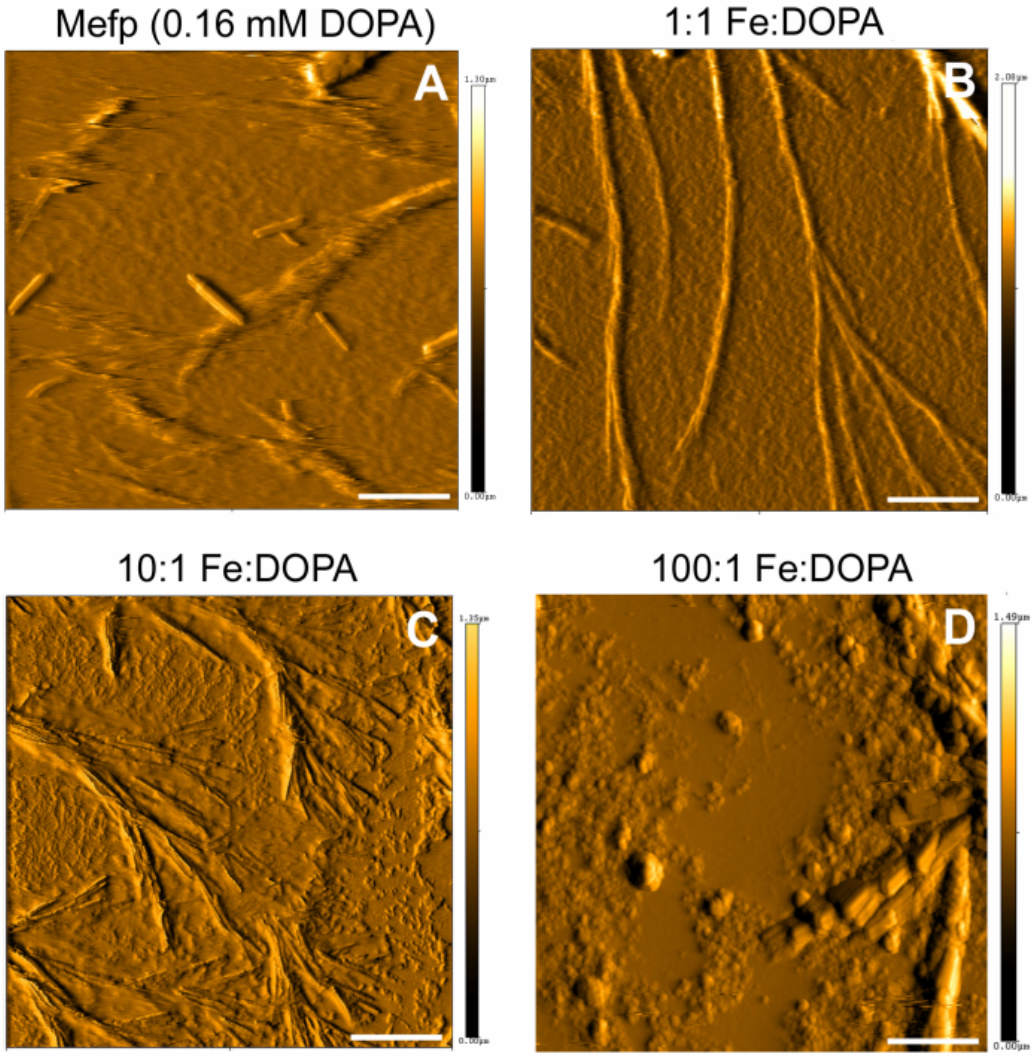

Figure 115. Atomic force micrographs of ink-jetted **A)** mussel protein (0.16 mM DOPA), **B)** 1:1 Fe:DOPA, **C)** 10:1 Fe:DOPA, and **D)** 100:1 Fe:DOPA solutions.
Scale bar equals 10 μm.

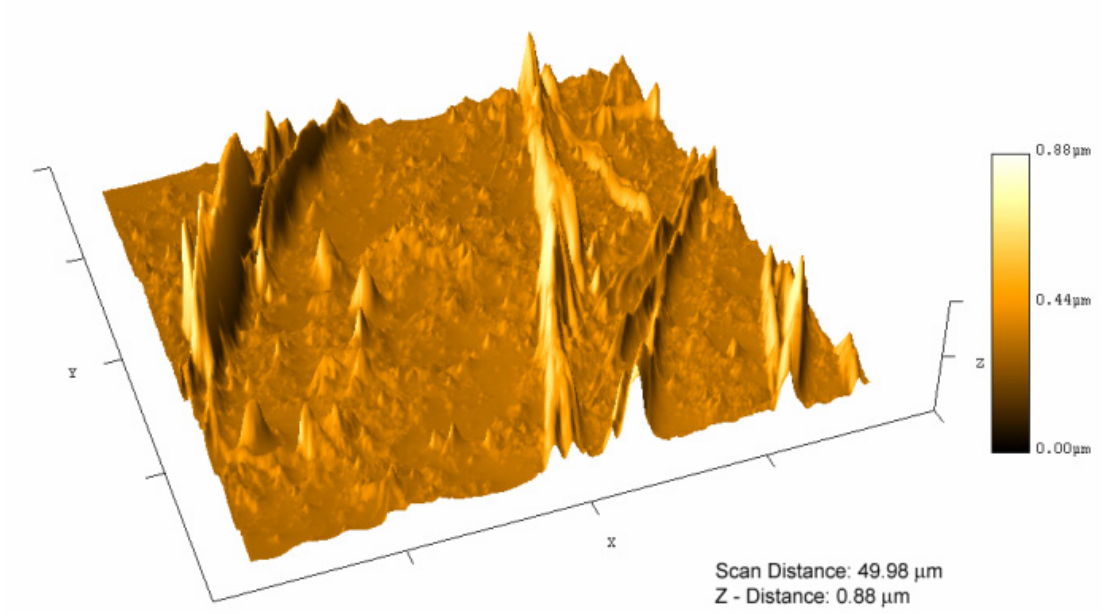

Figure 116. AFM three-dimensional representation of the surface of mussel protein solution + Fe(III) as 1:1 Fe:DOPA. *Scan recorded 24 hours after curing.*

3.4.2.5 Adhesive Properties

Adhesive characteristics of pure marine mussel extracts have been previously examined under different curing conditions.[188, 189] Low-humidity and non-oxidative conditions have been shown to be critical in obtaining strong adhesion properties in these materials. Tensile testing of ink-jetted mussel proteins (0.16 mM DOPA) on full-thickness porcine skin revealed significantly lower values than cyanoacrylate adhesives (Figure 117). Ink-jetted n-butyl cyanoacrylate (Vetbond®) and 2-octyl cyanoacrylate (Nexaband®) showed no significant difference in strength. Ink-jetted ethyl cyanoacrylate (Quick Set™ Loctite®) showed highest strength among tested adhesives. Addition of Fe(III) to Mefp (0.16 mM DOPA) in 1:1 Fe:DOPA showed improved strength of adhesion. 10:1 Fe:DOPA did not show a significant change in strength in comparison to 1:1 Fe:DOPA. However, 100:1 Fe: DOPA revealed lower strengths than 1:1 and 10:1 Fe:DOPA, and no significant change in comparison to Mefp (0.16 mM DOPA).

The extremities observed in the absence and excess of Fe content, may be correlated to the extent of cross-linking and precipitation in these ink-jetted patterns. As examined earlier, metal mediated catechol complexation is thought to responsible for the adhesion of the mussel plaque to the interface. It is also contemplated that two different ferric catecholate complexes may be formed at low and high Fe:DOPA ratios.[190] Previous EPR studies have confirmed iron-induced cross-linking in precursor proteins matching that of intact mussel plaques.[191] From the AFM images, the large area of fibrous networks observed in 1:1 and 10:1 Fe:DOPA are not immediately evident in Mefp (0.16 mM DOPA) and 100:1 Fe:DOPA. This observation may be directly correlated with the adhesion strength observed in these materials.

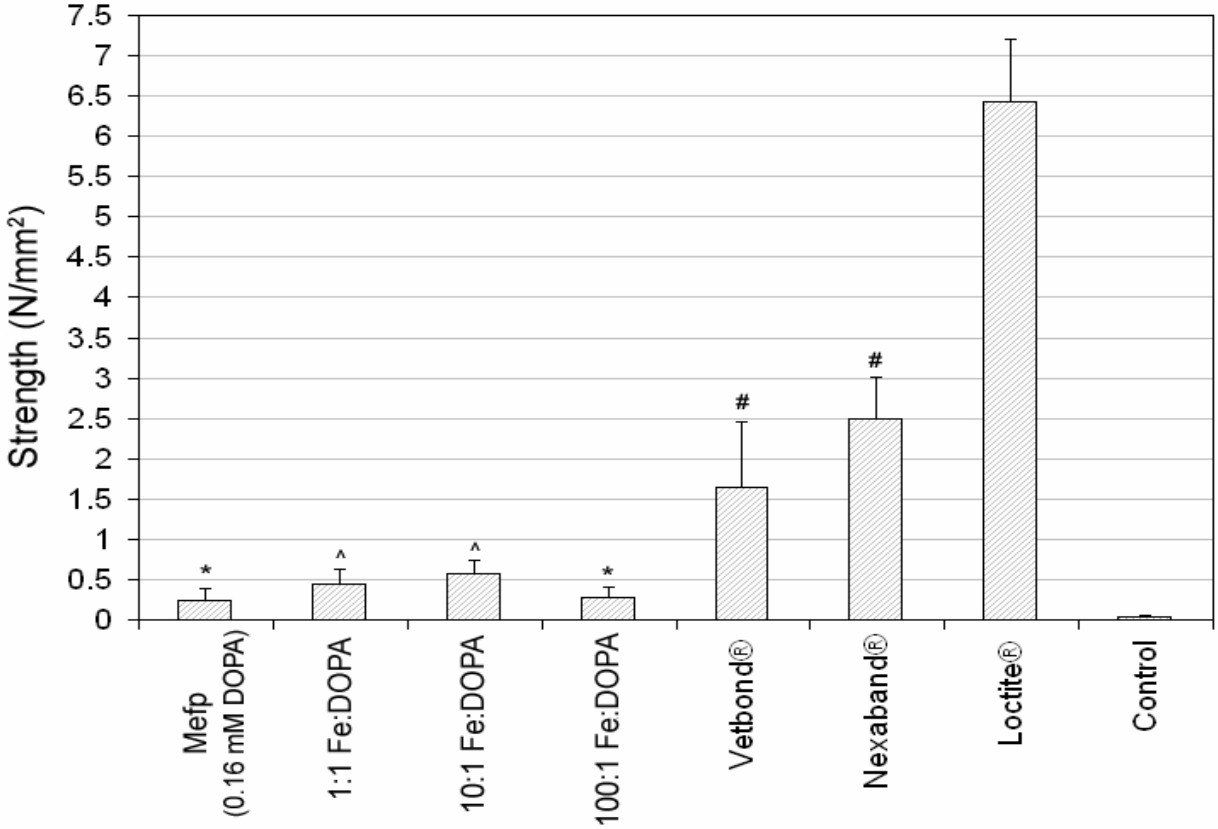

Figure 117. Comparison of mean strength of bioadhesives *ink-jetted* on full thickness porcine skin. Bioadhesives: Mussel protein (0.16 mM DOPA), mussel protein (DOPA with increasing Fe content), Vetbond®, Nexaband®, and Loctite®. All samples were cured for 24 hours. The difference in strength was statistically significant for all except those indicated by "*", "^", and "#" ($P<0.05$). *Bars indicate standard deviation of mean strengths.*

3.4.2.6 HAAE-1 Endothelial Cytotoxicity

Mussel adhesive proteins do not interact with components of the human immune system, and thus may be useful in medical and surgical applications.[192-194] Mussel species are also known to be immunogenic to erythrocytes and mouse tumor cells.[195] Hybid of mussel adhesive proteins and RGD peptides have been demonstrated for applications as cell or tissue bioadhesive.[196]

Figure 118 contains graph illustrating the MTT viability of HAAE-1 vascular entothelial cells for various bioadhesives. The data was normalized with cell-viability in media as control. Comparison of the MTT viability showed significant differences between all bioadhesives tested ($p < 0.05$). Cell-tak™ containing polyphenolic proteins derived from *Mytilus edulis* showed greatest HAAE-1 viability at approximately 12% more than control media. Nexaband® (2-octyl cyanoacrylate) showed 9% greater viability than control media. All other bioadhesives showed lower viability than control. *Mytilus edulis* mussel proteins (80% Mefp-1 and 20% Mefp-2) solvated in water with a DOPA concentration of 0.16 mM showed greater viability than Vetbond® (n-butyl cyanoacrylate) and Loctite® (ethyl cyanoacrylate). Addition of Fe(III) to the mussel protein-DOPA solution significantly lowered the relative viability of cells from approximately 73% to 30%. A comparison at ratios of 1:1 Fe:DOPA, 10:1 Fe:DOPA, and 100:1 Fe:DOPA, showed significant reduction in cytoviability with addition of Fe(III). Iron has previously been shown to induce increased cytotoxicity in endothelial cells.[197] Iron-induced toxicity to vascular endothelial cells have also been reported with implications in various vascular diseases.[198] Employment of other elements in metal-mediated chelation of mussel proteins may address elevated cytotoxicity.

Mussel adhesive proteins could serve as environmentally friendly alternatives to cyanoacrylate adhesives in biomedical, electronics and marine-equipment applications. *Mytilus edulis* foot proteins may overcome several problems associated with conventional tissue bonding materials, and greatly improve wound repair in next generation eye repair, fracture fixation, organ fixation, wound closure, tissue engineering, and drug delivery devices.

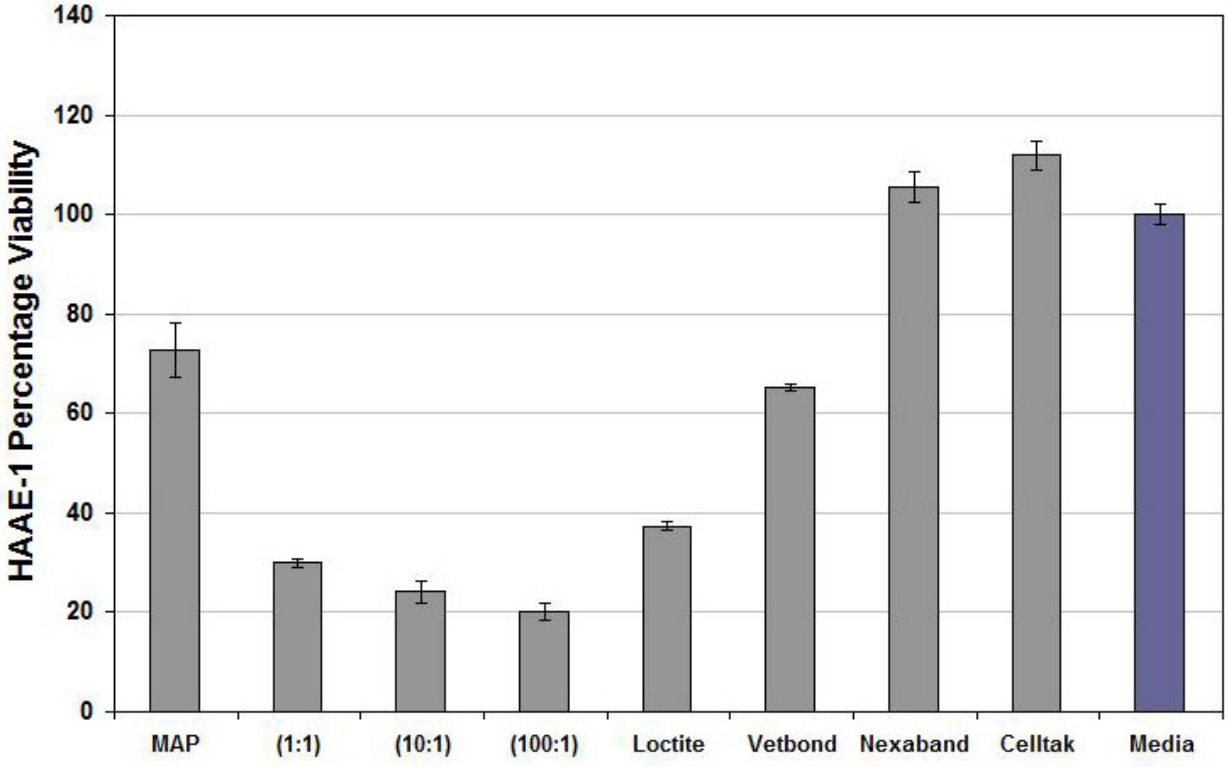

Figure 118. MTT cell viability of HAAE-1 vascular endothelial cells for various bioadhesives normalized with media. *Data represented as mean ² standard deviation. ($p<0.05$)*

3.4.3 CAD/CAM Administration of Synthetic Adhesives

As previously, a MEMS based piezoelectric actuator was controlled to jet uniform fluid flow of the adhesive solution through the ink jet nozzles. Piezoelectric ink jet deposition of biological adhesives may greatly improve wound repair in next generation eye repair, fracture fixation, organ fixation, and wound closure.

Vetbond® and CoSeal® solutions were successfully deposited into CAD patterns using the piezoelectric ink-jet printer. Ink-jetting of CoSeal® was achieved in two steps. First, the PEG powder/sodium carbonate solution (part I) was ink-jetted into a predefined pattern. This was followed by ink-jetting of the second component (HCl solution, part II) into a subsequent layer of the matching pattern. The gelation of CoSeal® was almost immediate. CAD/CAM micropatterns of CoSeal® hydrogel were more difficult to reproduce owing to the rapid setting upon mixing the two components.

3.4.3.1 Microscopy

Ink-jetting of Vetbond® tissue adhesive in microarray patterns in Silicon (111) showed good reproducibility (Figure 119) as seen in the previous section with Nexaband®. Figure 120 contains various patterns of CoSeal® hydrogel *ink-jetted* using this two-component layer-by-layer approach. Figure 100A contains a circular ring pattern and Figure 120B contains dot patterns of the two-component hydrogel. Figures 120C and 120D contain *ink-jetted* thin-film and thick-film of the hydrogel, respectively. Scanning electron micrograph performed on these patterns show additional details of the hydrogel formation

after ink-jetting the two-components separately. Figure 121A shows a 100X SEM image of the cross-linked hydrogel pattern. The width of the circular pattern varies from 300 to 400 μm with uneven shrinkage and swelling across the pattern. Figures 121B and 121C contain higher magnification micrographs that reveal randomly oriented cross-linked networks of the hydrogel components.

3.4.3.2 Spectroscopy

Fourier-transform infra-red (FTIR) absorption spectra overlay of ink-jetted and drop-cast CoSeal® PEG-powder solution (part I) of the two component system shows match of all relevant structural peaks (Figure 122A). FTIR overlay of ink-jetted and drop-cast CoSeal® solution (part II) also revealed match in all structural peaks and close similarity to the peaks in part I (Figure 122B). The structural peaks in the formation of hydrogel via ink-jetting and drop-casting was also compared (Figure 122C) and revealed presence of all relevant peaks. The spectra of the hydrogel when compared with that of Part I and II showed presence of additional and narrower/sharper peaks.

Figure 123 contains X-ray photoelectron spectra survey of ink-jetted CoSeal® components (part I and II) in Silicon (111). The spectra revealed presence of C, O, Si and Na for PEG-powder solution (part I) and presence of C, O, Si for the other solution (part II). The positions of the peak, full-width half-max (FWHM), area and atomic percentage for both components are listed in Table 6. Figure 124 contains the C 1s spectra of the two components. The C-N peak corresponds to 286.1 eV shown in the curve-fitted graph.

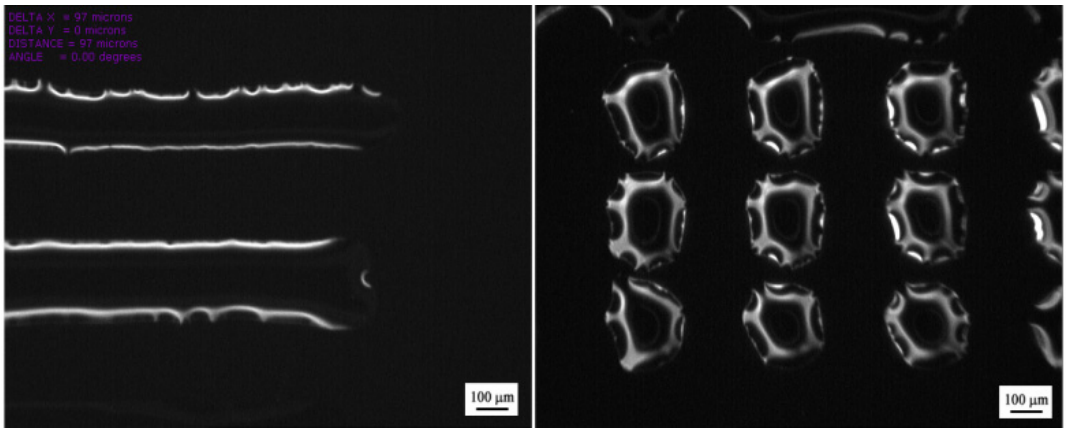

Figure 119. Optical micrographs of n-butyl cyanoacrylate (Vetbond®) *ink-jetted* into CAD patterns. *Scale bar equals 100 µm.*

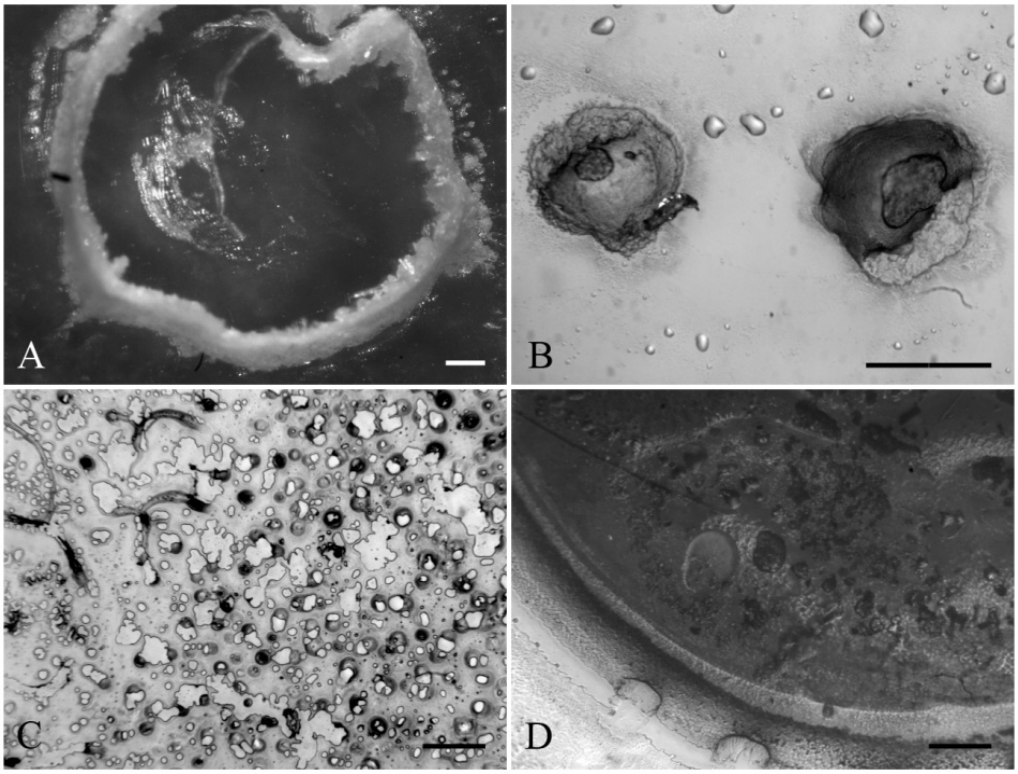

Figure 120. Optical micrograph of CoSeal® patterns ink-jetted on borosilicate glass substrates. **A:** Circular ring pattern; **B:** Dot patterns; **C:** Thin-film; and **D:** Thick-film patterns. *Scale bar equals 200 µm.*

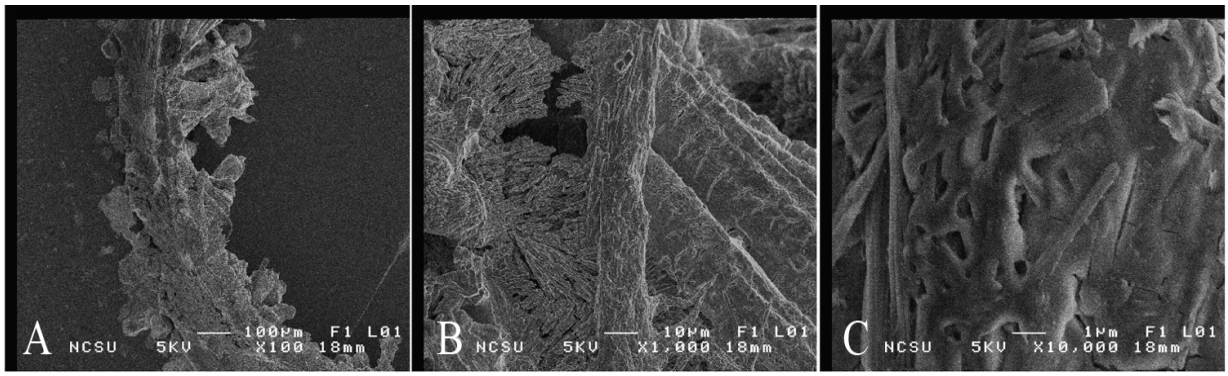

Figure 121. Scanning electron micrographs of CoSeal® circular ring pattern ink-jetted on Si (111) substrates. **A:** 100X, **B:** 1000X, and **C:** 10000X.

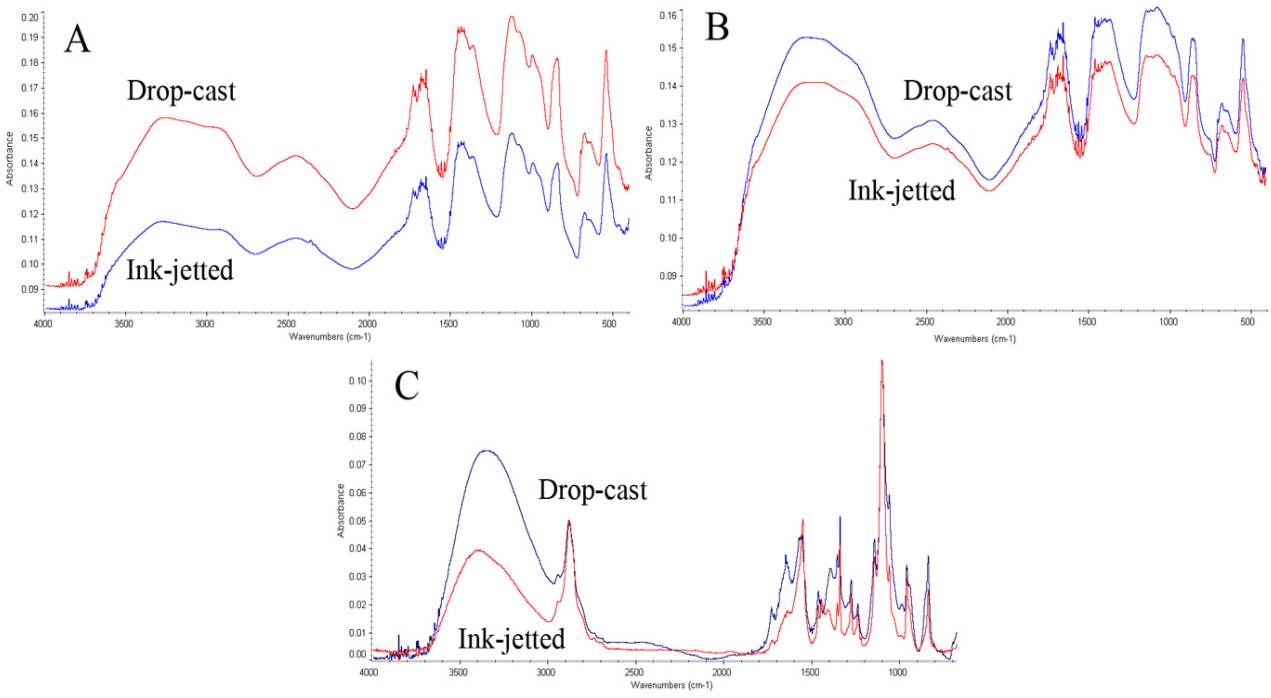

Figure 122. Fourier-transform infra-red (FTIR) absorption spectra overlay of *ink-jetted* and *drop-cast* CoSeal® solutions. **A.** Part I *(PEG-powder solution)*, **B.** Part II *(HCl solution)*, and **C.** Part I+II *(CoSeal® hydrogel formed by mixing the two-components)*.

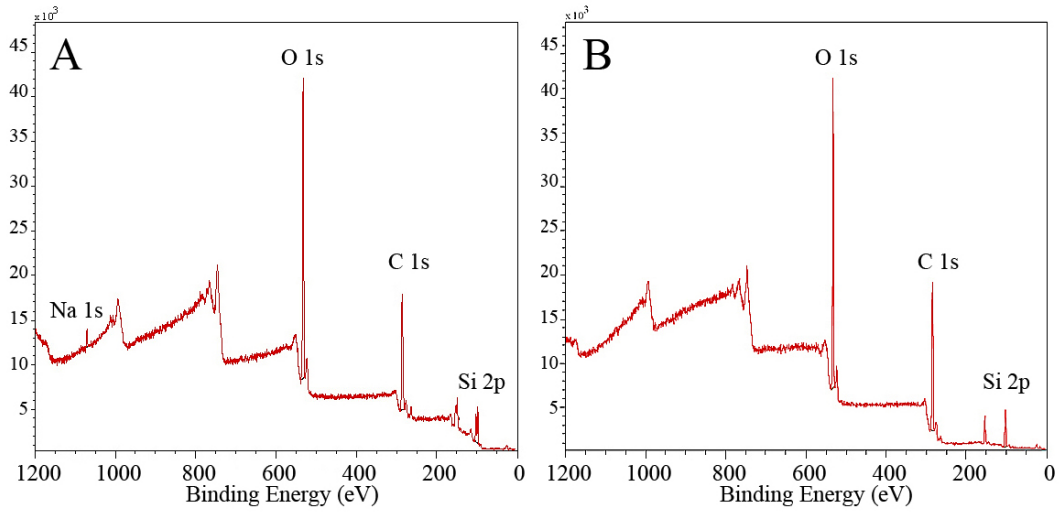

Figure 123. X-ray photoelectron spectra survey of ink-jetted CoSeal® components. A. Part I (PEG-powder solution) and B. Part II (HCl solution).

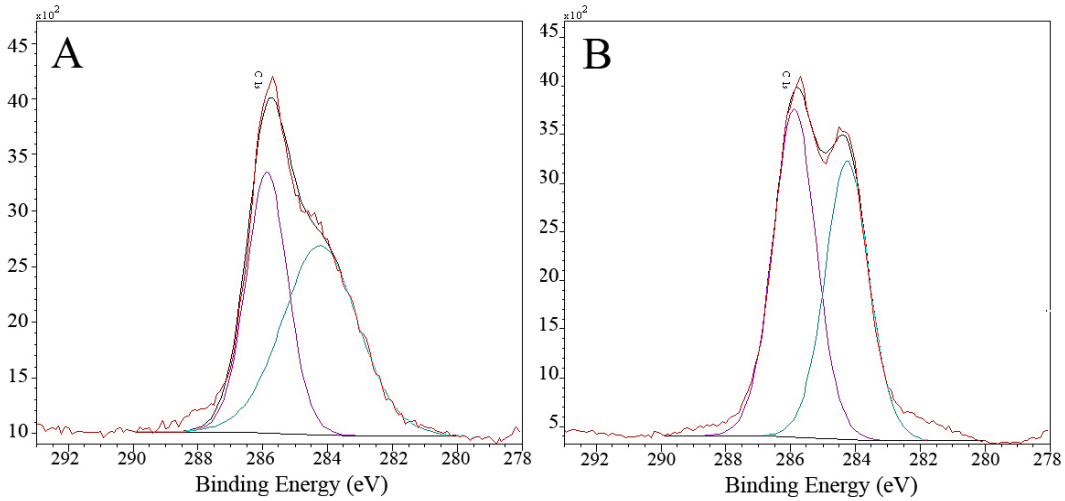

Figure 124. X-ray photoelectron C 1s spectra of ink-jetted CoSeal® components. A. Part I (PEG-powder solution) and B. Part II (HCl solution).

Table 6. X-ray photoelectron spectra survey of ink-jetted CoSeal® components.

	Name	Position	FWHM	Area	At%
CoSeal® PEG-powder solution (Part I)	O 1s	531.5	2.69	95266.20	35.00
	C 1s	285.5	3.16	43788.10	45.85
	Si 2p	97.0	1.91	15345.70	18.58
	Na 1s	1071.5	2.13	4302.20	0.56
CoSeal® component in HCl solution (Part II)	O 1s	532.0	2.21	86159.80	31.18
	C 1s	285.5	3.18	55630.50	57.38
	Si 2p	101.5	2.09	9584.80	11.43

3.4.3.3 Atomic Force Microscopy

Figure 125 contains atomic force micrographs (*deflection, topography and LFM*) of CoSeal® hydrogel *ink-jetted* with pattern size of approximately 40 μm. The micrograph also revealed several rounded cross-linked networks of the hydrogel. A three-dimensional representation of the topography micrograph (Figure 126) revealed a dome-shaped pattern with approximate peak-height of the hydrogel at 5.50 μm.

Figure 127 contains atomic force micrographs of CoSeal® hydrogel *ink-jetted* into a thin-film. The micrographs revealed 1-6 μm round-shaped interconnected islands with an uneven topology. The average surface roughness (S_a) over the 20 μm scan-range was observed to be 0.258 μm with root mean square (S_q) of 0.345 μm. Figure 128 contains atomic force micrographs of Vetbond® adhesive *ink-jetted* into a thin-film. The micrographs revealed presence of randomly oriented 2-3 μm globular structures. The size distribution of the features was narrower than that observed in the CoSeal® hydrogel. The average surface roughness (S_a) over the 20 μm scan-range was observed to be 0.117 μm with root mean square (S_q) of 0.180 μm, both lower than that observed in CoSeal® hydrogel. Figure 128 contains atomic force micrographs of Loctite® quick set adhesive *drop-cast* into a thin-film. The micrographs revealed a smooth surface and an even topology. The average surface roughness (S_a) over the 20 μm scan-range was observed to be 0.034 μm with root mean square (S_q) of 0.045 μm, both significantly lower than that observed in the other two adhesives/sealants.

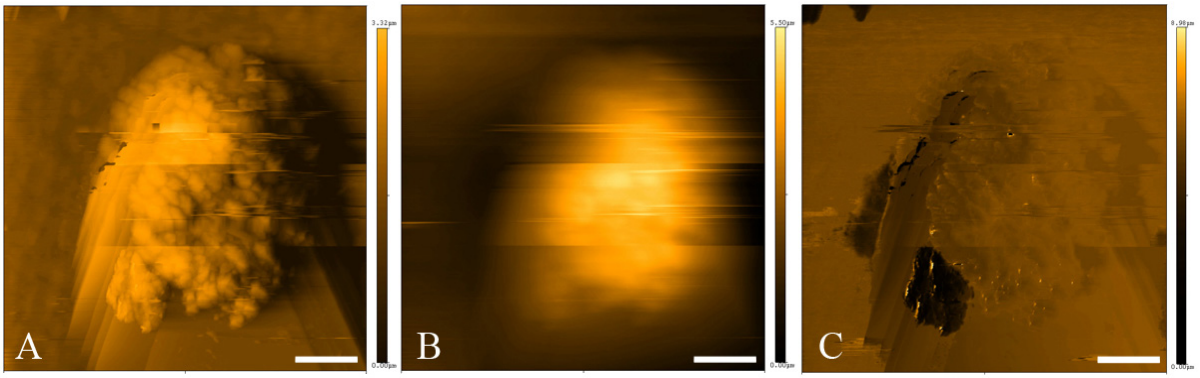

Figure 125. Atomic force micrographs of CoSeal® hydrogel *ink-jetted* in a dot-pattern. **A:** Deflection, **B:** Topography, and **C:** LFM. *Scale bar equals 10 μm.*

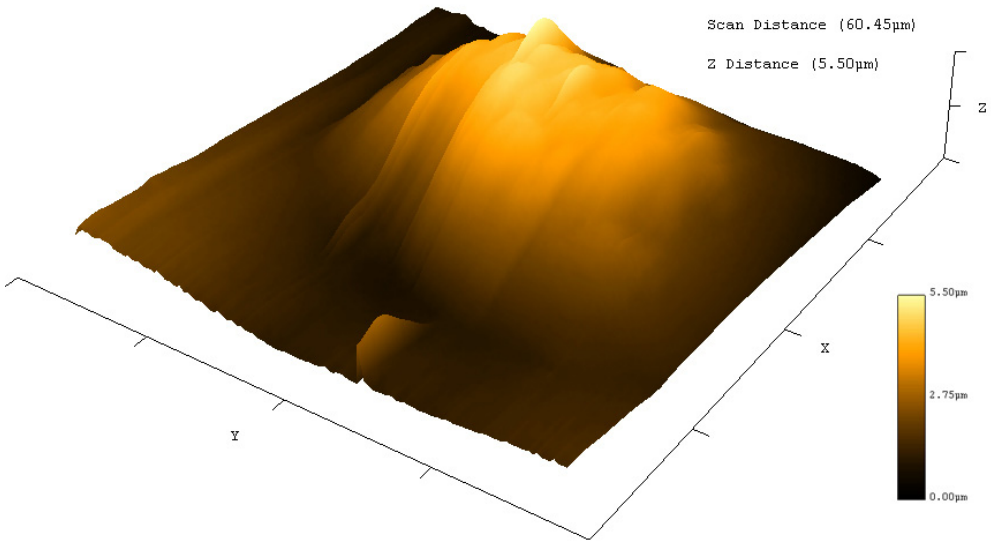

Figure 126. AFM three-dimensional topographical representation of the CoSeal® hydrogel dot-pattern. *Scan-distance = 60.45 μm, z-distace = 5.50 μm.*

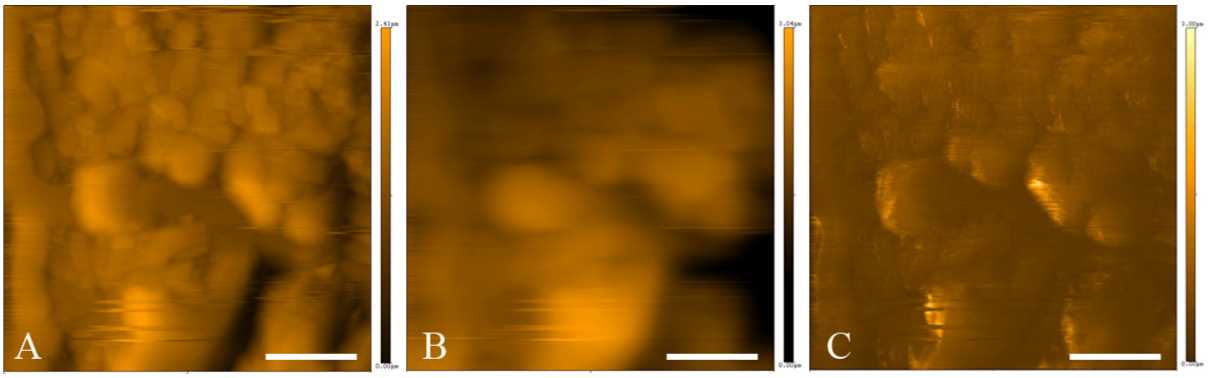

Figure 127. Atomic force micrographs of CoSeal® hydrogel *ink-jetted* into a uniform thin-film on borosilicate glass substrate. **A:** Deflection, **B:** Topography, and **C:** LFM. *Scale bar equals 5 μm.*

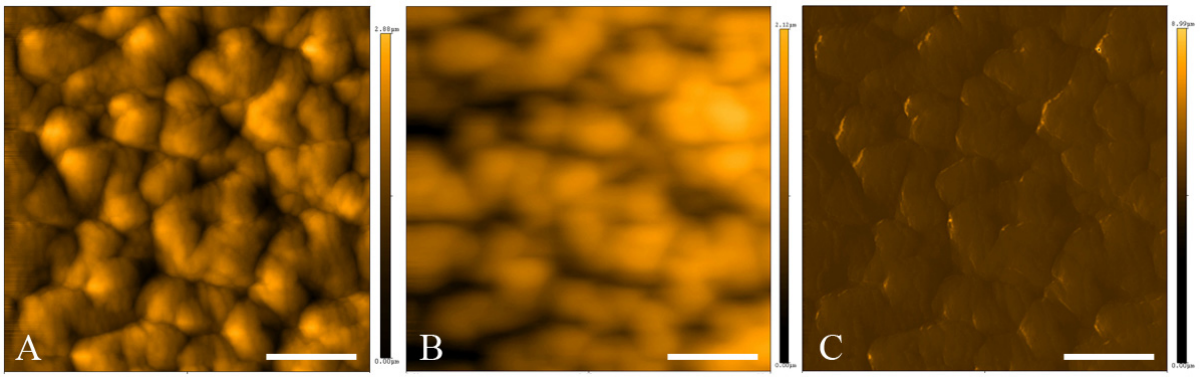

Figure 128. Atomic force micrographs of Vetbond® liquid adhesive *ink-jetted* into a uniform thin-film on borosilicate glass substrate. **A:** Deflection, **B:** Topography, and **C:** LFM. *Scale bar equals 5 μm.*

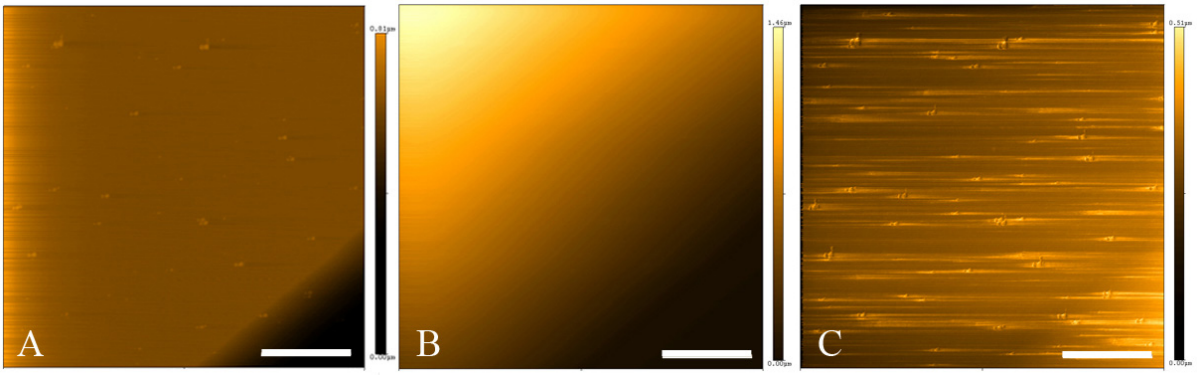

Figure 129. Atomic force micrographs of Loctite® adhesive *drop-cast* on borosilicate glass substrate. **A:** Deflection, **B:** Topography, and **C:** LFM. *Scale bar equals 5 μm.*

3.4.3.4 Mechanical Properties

Figure 130 contains the measured average hardness of CoSeal® hydrogel, Vetbond®, and Loctite® polymer adhesive thin-films. The indentation depth was up to 500 nm for Vetbond® and Loctite®, and up to 750 nm for CoSeal® hydrogel. The average hardness values were highest for Loctite® followed by Vetbond® and lowest for CoSeal® hydrogel. The error bars in the charts signify the standard deviations of the data. Figure 131 contains the measured average modulus of the three adhesives under similar indentation depths. The average modulus followed a similar trend with highest values for Loctite® followed by Vetbond® and lowest for CoSeal® hydrogel. The difference in mean hardness and modulus values between all three adhesives were significantly different ($p<0.01$). Also, delamination of CoSeal® sealant from substrates after *ink jetting*, precluded adhesion strength measurements. The various measured properties of the ink-jetted cyanoacrylate adhsives and CoSeal® hydrogel are listed in table 7.

Piezeolectric ink-jetting was revealed as a powerful, non-contact and non-destructive technique for controlled administration of surgical sealants and biological adhesives for future clinical applications. Microscopic patterning of adhesives/sealants including CoSeal® and Vetbond® enables improved bonding for a range of advanced biomedical applications. By printing such small and spatially aligned drops, bond lines between materials are reduced, ultimately resulting in increased bond strength and structural integrity. Unlike most other rapid prototyping techniques that employ heating elements or laser, piezoelectric ink-jetting is completely safe for biological adhesives.

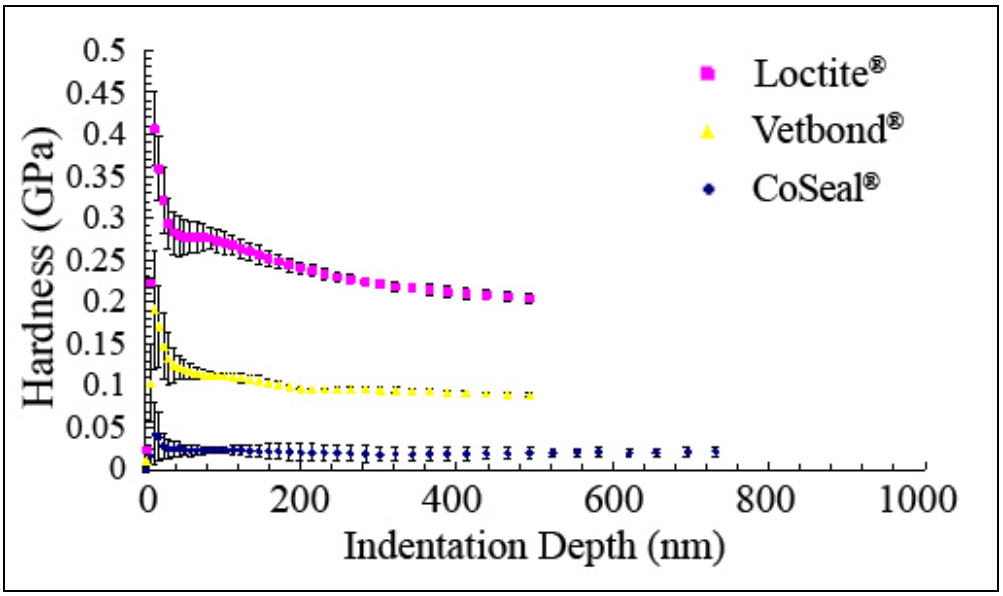

Figure 130. Graph of hardness (GPa) vs. indentation depth (nm) of the adhesive thin-films. Symbols "■" , "▲", and "●" represent values for Loctite®, Vetbond® and CoSeal® respectively. Bars indicate standard deviation of mean hardness. P<0.01

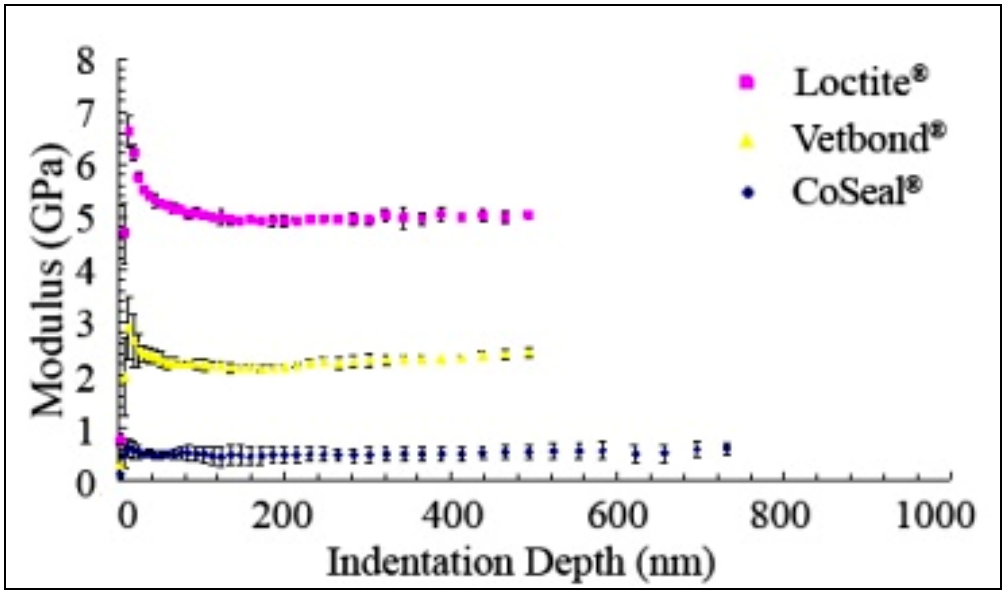

Figure 131. Graph of modulus (GPa) vs. indentation depth (nm) of the adhesive thin-films. Symbols "■" , "▲", and "●" represent values for Loctite®, Vetbond® and CoSeal®, respectively. Bars indicate standard deviation of mean modulus. P<0.01

Table 7. Measured properties of the adhesive thin-films

Adhesive	Formation/Components	Average Hardness (GPa)	Average Modulus (GPa)	Average Surface Roughness, Sa (μm)
CoSeal®	Hydrogel formed by mixing synthetic PEG powder solutions	0.022	0.522	0.258
Vetbond®	Polymerization of N-butyl cyanoacrylate	0.095	2.240	0.117
Loctite®	Polymerization of Ethyl cyanoacrylate	0.210	5.033	0.034

CHAPTER 4

CONCLUSIONS AND FUTURE DIRECTIONS

An aging population with growing healthcare needs demands multifaceted tools for diagnosis and treatment of health conditions. In the near-future, drug-administration devices, implantable devices/sensors, enhanced prosthesis, artificial and unique functional tissue constructs will become increasingly significant. Conventional rapid prototyping techniques do not sufficiently take individual patient anatomy into account and have several limitations that preclude their use for next-generation biomedical applications. Development of novel CAD/CAM rapid prototyping techniques may significantly accelerate progress of these devices for next-generation patient-care.

In this dissertation, a variety of novel rapid prototyping methods were introduced and developed for several biomedical applications. First, two-photon polymerization (2PP) a laser direct write technique was studied for several photopolymers. Among them, Ormocer® photopolymer demonstrated superior mechanical strengths, surface properties and cytocompatibility. 2PP was used to microfabricate Lego®-like scaffolds for tissue engineering applications, microneedles for drug-delivery and ossicular replacement prostheses. A variety of microneedle geometries including off-centered tips were developed. Administration of fluorescing agents into skin demonstrated localized delivery within the

dermal layers. Polymeric microneedles developed by 2PP may be integrated with MEMS devices to allow control over amount and rate of pharmacologic administration. Ormocer® ossicular replacement prosthesis developed by 2PP demonstrated good mechanical properties, cytocompatibility, ease of forming and ease of handling. These results suggest that 2PP may be employed to create medical microdevices with a larger range of sizes, shapes, and materials than conventional polymer, silicon, stainless steel, or titanium microfabrication techniques.

Laser direct-writing may also be developed to create tissue constructs and scaffolds. CAD/CAM rapid prototyping by MAPLE direct write (MDW) allowed microfabrication of a variety of materials including bioceramics, organic polymeric materials, and viable cells such neuroblasts and osteoblasts. A triazene polymer release layer was developed to demonstrate lower threshold energy levels for micropatterning. Cytotoxicity studies showed no damage to cells during the process. The MDW process was also employed to develop microstructures of bioceramics such as hydroxyapatite, zirconia, and viable mammalian osteosarcoma cells. CAD/CAM co-deposition of osteosarcoma cells and hydroxyapatite may exploit advantage of osteoconductive properties of bioactive ceramics. Integration of viable cells and biomaterials prior to tissue fabrication may allow significant advantages including adequate cell penetration and control over cell-density through the scaffold. Such a technique may allow integration of cell into the matrix while the construct is being created.

MDW was demonstrated as a versatile technique for creating multilayer, heterogeneous structures that may be developed for tissue scaffolds. The ability to microfabricate cell-ceramic composites offers structural integrity in using two-dimensional layers to build mechanically robust three dimensional heterogeneous constructs.

Reproducible control over microstructure and surface characteristics may provide unique biological functionalities at the tissue/implant interface. The interaction among several MDW process parameters, including the laser fluence, laser spot size, ceramic powder size, ribbon-substrate length, amount of solvent used to prepare the ribbon, and choice of solvent used to prepare the ribbon, may allow development of unique surface morphologies and improved tissue/implant interfaces.

Every tissue and organ in the human body has its own unique geometry which varies in size between individuals undermines the applicability of most conventional fabrication techniques. Novel tissue engineering approaches are required to address issues facing conventional techniques and permit development of three-dimensional networks to replace failed tissue.

In another laser-based approach, CAD/CAM laser micromachining (CLM) was developed to engineer biointerfaces with programmed dimensions and required functionality. CLM processing of silicon was used to understand laser interaction of material and to integrate the various process parameters. Microstructures and biointerfaces developed by CLM were utilized as surface recognition regions for differential adherence of cells to grow into tissue-like networks. The alignment and packing of cells within the microfabricated channels was dependent on the shape, growth rate, and signaling of cell. CAD/CAM generated free-standing self-sustained cellular networks of B35 rat neuroblast-like cells, A431 human epithelial carcinoma cells and C2C12 mouse myoblast-like cells were developed. Neuron bundles that match with the served nerve stumps may potentially aid in the regeneration of damaged peripheral nerves. Development of multi-cellular tissue

networks using selective growth factors may prove to be further valuable to the field of regenerative medicine.

CLM was also developed for engineering multi-cellular vascular networks. Cytotoxic evaluations and growth studies demonstrated VEGF-induced proliferation of HAAE-1 human aortic endothelial cells with inhibition of HA-VSMC human aortic smooth muscle cells. VEGF concentration at 10 ng/ml and heparin at 100 units/mL were integrated with Matrigel® polymer matrix to allow development of scaffolds within the CLM microfabricated networks. Conventional techniques for vascular networks have employed cell-seeding on a pre-formed polymeric conduits. Such techniques may not entirely allow control over cellular penetration and geometry of the various layers. CLM provides a unique direct-write approach to microfabricate complex geometries that may be used for vascular tissue engineering including small diameter blood vessels for bypass surgery and repair of heart components.

Finally, a CAD/CAM liquid dispensing technique was developed to allow high-throughput production of patterned multiplexed biological materials without the use of masks, stamps, ribbons, or other expensive processing equipment. Piezoelectric inkjet technology (PIT) was developed for controlled administration of naturally derived and synthetic biological adhesives. The PIT process was validated for feasibility, resolution, and safety using biological proteins. A MEMS based piezoelectric actuator was used to control the flow of solutions through the ink jet nozzles. Microscopic patterning of adhesives/sealants enables significant reduction of bond lines between materials, ultimately resulting in increased bond strength and structural integrity. PIT was demonstrated as a

powerful, non-contact and non-destructive technique for controlled administration of surgical sealants and biological adhesives.

Various characterization techniques were employed to understand the role of metals such as Fe(III) on the adhesive properties of mussel proteins. Metal-mediated catechol complexation was thought to be responsible for the adhesion of the mussel plaque to the interface. Piezoelectric inkjet printing of naturally derived biological adhesives may overcome several problems associated with conventional tissue bonding materials, and greatly improve wound repair in next generation eye repair, fracture fixation, organ fixation, wound closure, tissue engineering, and drug delivery devices.

REFERENCES

1. H. Kodama, *Rev. Sci. Instrum.* **1981**, 52, 1770-1773.

2. C.C. Kai, L.F. Fai, L. Chu-Sing, *Rapid Prototyping: Principles and Applications, Second Edition,* World Scientific Publishing, **2003**.

3. D.W. Hutmacher, M. Sittinger, M.V. Risbud, *Tr. Biotechnol.* **2004**, 22, 354-362.

4. http://www.stratasys.com/sys_main.html

5. http://www.me.umn.edu/info/desres/rapid/images/Figure02.html

6. F. Despa, D.P. Orgill, J. Neuwalder, R.C. Lee, *Burns.* **2005**, 31(5), 568-77.

7. C. Nishigori, *Photochem. Photobiol. Sci.* **2006**, 5, 208-14.

8. http://www.princeton.edu/~cml/assets/images/stereo02.gif

9. N.K. Vail, *Mater. Des.* **1999**, 20, 123-132.

10. http://www.emeraldinsight.com/fig/0330210401001.png

11. T. Boland, A. Ovsianikov, B.N. Chichkov, A. Doraiswamy, R.J. Narayan, W.Y. Yeong, K.F. Leong, C.K. Chua, *Adv. Mater. & Processes,* **2007**, Apr. p9.

12. D.B. Chrisey *et al.,* "Nanoscale Laser Processing and Micromachining of Biomaterials and Biological Components" in *Recent Advances in Laser Processing of Materials by J. Perriere, E. Millon, E. Fogarassy, ISBN: 0-08-044727-9,* **2006,** Elsevier**.**

13. J.C. Ion, *Laser Processing of Engineering Materials*, *Elsevier,* **2005**.

14. D.B. Chrisey, G.K. Hubler, *Pulsed Laser Deposition of Thin Films*, *Wiley,* **1994**.

15. J. Serbin, A. Egbert, A. Ostendorf, B.N. Chichkov, R. Houbertz, G. Domann, J. Shulz, C. Cronauer, L. Froehlich, I.M. Popall, *Opt. Lett.* **2003**, 28, 301-303.

16. K.D. Belfield, K.J. Schafer, Y.U. Liu, J. Liu, X.B. Ren, E.W. Van Stryland, *J Phys Org Chem.* **2000**, 13, 837-849.

17. R. Houbertz, L. Froehlich, M. Popall, U. Streppel, P. Dannberg, A. Braeuer, J. Serbin, B.N. Chichkov, *Adv. Eng. Mat.* **2003**, 5, 551-55.

18. J. Serbin, A. Ovsianikov, B.N. Chichkov, *Opt. Express.* **2004**, 12, 5221-5228.

19. K.H. Haas, *Adv Eng Mat.* **2000**, 2, 571-582.

20. A. Ovsianikov, B. Chichkov, P. Mente, N.A. Monteiro-Riviere, A. Doraiswamy, R.J. Narayan, *Int. J. Appl. Ceram. Technol.* **2007**, 4(1), 22-29.

21. M. Rosin, A.D. Urban, C. Gartner, O. Bernhardt, C. Splieth, G. Meyer, *Dent. Mater* **2002**, 18, 521-528.

22. K.H. Haas, H. Wolter, *Curr. Opin. Solid State Mater Sci*. **1999**, 4, 571-580.

23. A.J. Garcia, M.D. Vega, D. Boettiger, *Molecular Biology of the cell*, **1999**, 10, 785.

24. S. Takayama, J.C. McDonald, E. Ostuni, M.N. Liang, P.J.A. Kenis, R.F. Ismagilov, G.M. Whitesides, *Proc. Natl. Acad. Sci. U.S.A.* **1999**, 96, 5545.

25. A. Folch, B. Jo, O. Hurtado, D.J. Beebe, M. Toner, *J. Biomed. Mater. Res.* **2000**, 52, 346.

26. R.S. Kane, S. Takayama, E. Ostuni, D.E. Ingber, G.M. Whitesides, *Biomater.* **1999**, 20, 2363.

27. N. Patel, R. Bhandari, K.M. Shakersheff, S.M. Cannizzaro, M C. Davies, R. Langer, C.J. Roberts, S.J.B. Tendler, and P.M. Williamsm, *J. Biomater. Sci. Polym. Ed.* **2000**, 11/2, 319.

28. T. Matsue, N. Matsumoto, I. Uchida, *Electrochim. Acta.* **1997**, 42/20-22, 3251.

29. D.B. Chrisey, A. Pique, R.A. McGill, J.S Horwitz, B.R. Ringeisen, D.M. Bubb. P.K. Wu, *Chem. Rev.* **2003**, 103, 553.

30. M.L. Harris, A. Doraiswamy, R.J. Narayan, T. Patz, D.B. Chrisey, *Mater. Sci. Eng. C.* **2007**, In press.

31. B.R. Ringeisen, D.B. Chrisey, A. Pique, H.D. Young, R. Modi, M. Bucaro, J. Jones-Meehan, B.J. Spargo, *Biomater.* **2002**, 23, 161.

32. D.S. Zhao, B. Roy, M.T. McCormick, W.G. Kuhr, S.A. Brazill, *Lab Chip,* **2003**, 3, 93.

33. S.T. Retterer, K.L. Smith, C.S. Bjornsson, K.B. Neeves, A.J.H. Spence, J.N. Turner, W. Shain, M.S. Isaacson, *IEEE Trans. Biomed. Eng.* **2004,** 51, 2063.

34. E. Mutapcic, P. Iovenitti, J.P. Hayes, *Int J Adv Manuf Technol*. **2006**, 30, 1076–1083

35. K. Sugioka, K. Obata, K. Midorikawa, M.H. Hong, D.J. Wu, L.L. Wong, Y.F. Lu, T.C. Chong, *J Photochem Photobiol A: Chemistry*. **2003**, 158, 171–178

36. P. Holgerson, D.S. Sutherland, B. Kasemo, D. Chakarov, *Appl. Phys. A* **2005**, 81, 51–56.

37. S. Kaihara, J. Borenstein, R. Koka, S. Lalan, E.R. Ochoa, M. Ravens, H. Pien, B. Cunningham, J.P. Vacanti, *Tissue Eng.* **2000**, 6, 2.

38. A.V. Lemmo, D.J. Rose, T.C. Tisone, *Curr. Opin. Biotechnol.* **1998**, 9, 615

39. E.A. Roth, T. Xu, M. Das, C. Gregory, J.J Hickman, T. Boland, *Biomaterials.* **2004**, 25(17), 3707

40. F.J. Kampfhoefner, *IEEE Trans. Elec. Devices ED-19.* **1972**, 584.

41. L. Kuhn, A. Myers, *Sci. Am.* **1979**, 240, 162.

42. W.C. Wilson, T. Boland, *Anat. Rec. Part A*, **2003**, 272, 491.

43. V. Mironov, T. Boland, T. Trusk, G. Forgacs, R.R. Markwald, *Trends Biotechnol*. **2003**, 51 (4), 157.

44. J.A. Barron, B.J. Spargo, B.R. Ringeisen, *Appl. Phys. A*, **2004**, 79, 1027.

45. A. Doraiswamy *et al. In preparation to J. Adhesion Sci. Technol.* **2007**.

46. P. Calvert, *Chem. Mater.* **2001**, 13, 3299.

47. J. Brünahl, A.M. Grishij, *Sens. Act. A*. **2002**, 101, 371.

48. M.R. Prausnitz, *Adv Drug Deliver Rev*. **2004**, 56, 581–7.

49. S. Kaushik, A.H. Hord, D.D. Denson, D.V. McAllister, S. Smitra, M.G. Allen, *Anesth Analg*. **2001,** 92, 502–4.

50. M.R. Prausnitz, S. Mitragotri, R. Langer, *Nature Rev Drug Discov.***2004,** 3, 115–24.

51. S.P. Davis, W. Martanto, M.G. Allen, M.R. Prausnitz, *IEEE Trans Biomed Eng*. **2005**, 52, 909–15.

52. W.H. Smart, K. Subramanian, *Diabetes Technol.Ther*. **2000**, 2, 549–59.

53. R.K. Sivamani, B. Stoeber, G.C. Wu, H.B. Zhai, D. Liepmann, H. Maibach, *Skin Res Technol*. **2005,** 11(2), 152–6.

54. S.P. Davis, B.J. Landis, Z.H. Adams, M.G. Allen, M.R. Prausnitz, *J. Biomech*. **2004**, 37, 1155–63.

55. H.J. Gardeniers, R. Luttge, E.J.W. Berenschot, M.J. de Boer, S.Y. Yeshurun, M. Hefetz, *J Microelectromech Syst*. **2003**, 12, 855–62.

56. P. Griss, G. Stemme, *J Microelectromech Syst.* **2003**, 12, 296–301.

57. J.H. Park, M.G. Allen, M.R. Prausnitz, *J Control Release*. **2005**, 104, 51–66.

58. B. Stoeber, D. Liepmann, *J Microelectromech Syst*. **2005**, 14, 472–9.

59. M. Yang, J.D. Zahn, *Biomed Microdev*. **2004,** 6, 177–82.

60. S.J. Moon, S.S. Lee, H.S. Lee, T.H. Kwon, *Microsyst Technol.* **2005**, 11, 311–8.

61. S. Henry, D.V. McAllister, M.G. Allen, M.R. Prausnitz, *J Pharm Sci*. **1998**, 87, 922–5.

62. R.L. Daniels, F.M. Rizer, A.G. Schuring, W.L. Lippy, *Laryngoscope*. **1998**, 108, 1674.

63. A. de la Cruz, K.J. Doyle, Otolaryngol. Clin. *North Am*. **1994**, 27, 799.

64. S. Albu, G. Babighian, F. Trabalzini, *Am. J. Otolaryngol.* **1994**, 19, 136.

65. A.Y. Bayazit, *Laryngoscope.* **1997**, 107, 1193.

66. R.L. Goode, Otolaryngol. *Clin. North Am.* **1994**, 28, 141.

67. V. Colletti, F.G. Fiorino, *Otolaryngol. -Head Neck Surg.* **1999**, 120, 437.

68. D.E. Brackmann, *Ann. Otol., Rhinol. Laryngol.* **1986**, 95, 76.

69. K. Jahnke, D. Plester, G. Heimke, *Biomaterials*. **1983**, 4, 137.

70. K. Schwager, *Eur. Arch. Otorhinolaryngol.* **1998**, 255, 396.

71. C.H. Stupp, C. Dalchow, D. Gru¨n, H.F. Stupp, J. Wustrow, *Laryngorhinootologie*. **1999**, 78, 299.

72. S. Schmerber, J. Troussier, G. Dumas, J.P. Lavieille, D.Q. Nguyen, *Eur. Arch. Otorhinolaryngol.* **2006**, 263, 347.

73. X. Wang, J. Song, H. Wang, *Otolaryngol. -Head Neck Surg.* **1999**, 121, 606.

74. T. Zahnert, K.B. Hu¨ttenbrink, D. Mu¨rbe, M. Bornitz, *Am. J. Otol.* **2000**, 21, 322.

75. J.J. Grote, *Ann. Otol., Rhinol. Laryngol.* **1990**, 144, 12.

76. J.J. Grote, *Am. J. Otol.* **1998**, 19, 565.

77. C.A. van Blitterswijk, J.J. Grote, H.K. Koerten, W. Kuijpers, *J. Biomed. Mater. Res.* **1986**, 20, 1197.

78. R.E. Wehrs, *Otolaryngol. Clin. North Am.* **1994**, 27, 677.

79. C.A. Mangham, R.C. Lindeman, *Ann. Otol., Rhinol., Laryngol.* **1990**, 99, 112.

80. R.A. Goldenberg, M. Driver, *Otolaryngol. -Head Neck Surg.* **2000**, 122, 635.

81. S.N. Merchant, M.E. Ravicz, S. Puria, S.E. Voss, K.R. Whittemore, W.T. Peake, J.J. Rosowski, *Am. J. Otol.* **1997**, 18, 139.

82. E. Murugasu, S. Puria, J.B. Robertson, *Otol. Neurotol.* **2005**, 26, 572.

83. C.T. Laurencin, A.M.A. Ambrosio, M.D. Borden, J.A. Cooper, *Annu Rev Biomed Eng*. **1999**, 1, 19-46.

84. A.J. Salgado, O.P. Coutinho, R.L. Reis, *Macromol Biosci*. **2004**, 4, 743-765.

85. D. Josefson, *Brit Med J*. **2002**, 324, 1541.

86. B. Charlton, H. Auchincloss, C.G. Fathman, *Annu Rev Immunol*. **1994**, 12, 707-734.

87. T. Boyce, J. Edwards, N. Scarborough, *Orthop Clin North Am*. **1999**, 30, 571-581.

88. A. Lumelsky, *J Law Med Ethics*. **2002**, 30, 474-476.

89. R. Langer, J. Vacanti, *Science*. **1993**, 260, 920.

90. R.P. Lanza, R. Langer, J.P. Vacanti, *Principles of Tissue Engineering, 2nd edition, Academic Press,* **2000**.

91. L. Pramatarova, E. Pecheva, R. Presker, M.T. Pham, M.F. Maitz, M. Stutzmann, *Europ Cells Mater*. **2005,** 9, 9-12.

92. A.L. Rosa, M.M. Beloti, V.N. Van Noort, *Dent Mater*. **2003**, 19, 768-772.

93. B.D. Ratner, A.S. Hoffman, F.J. Schoen, J.E. Lemons, *Biomaterials Science, 2nd edition, Academic Press* **2004.**

94. L.E. Weiss, *Science & Medicine.* **2002**, 8, 1.

95. R. Forough, *New Frontiers in Angiogenesis, Springer,* **2006**, 111-124.

96. A.T. Shin'oka, Y. Imai, Y. Ikada, *New Engl J Med*., **2001**, 344, 532-3.

97. A.T. Shinoka, D. Shum-Tim, P.X. Ma, R.E. Tanel, N. Isogai, R. Langer, J.P. Vacanti, J.E. Mayer, *J Thorac Cardiovasc Surg.* **1998**, 115, 536-545.

98. L.E. Niklason, J. Gao, W.M. Abbott, K.K. Hirschi, S. Houser, R. Marini, R. Langer, *Science* **1999**, 284, 489-493.

99. F. Opitz, K. Schenke-Layland, W. Ritcher, D.P. Martin, I. Degenkolbe, T. Wahlers, U.A. Stock, *Annals of Biomedical Eng*. **2004**, 32, 212-22.

100. M. Remy-Zolghadri, J. Laganiere, J.F. Oligny, L. Germain, F.A. Auger, *J.Vasc.Surg*. **2004**, 39, 613-620.

101. F.I. Stuart, *Human Physiology, 4th Edition*, *Brown Publishers,* **2000**.

102. R.D. Madison, C. da Silva, P. Dikkes, R.L. Sidman, T.H. Chiu, *Exp. Neurol.* **1987**, 95, 378-390.

103. J.M. Rosen, J.A. Padilla, K.D. Nguyen, M.A. Padilla, E.E. Sabelman, H.N. Pham, *Ann. Plast. Surg.* **1990**, 25, 375-387.

104. J.S. Applebaum, T. Zalut, D. Applebaum, *Ann. Emerg. Med.***1993**, 22 1190.

105. R. Vanholder, A. Misotten, H. Roels, G. Matton, *Biomaterials.***1993**, 14, 737.

106. E.L. Herod, J. Can. *Dent. Assoc.* **1990**, 56, 331.

107. M. Hauptmann, J.H. Lubin, P.A. Stewart, R.B. Hayes, A. Blair, *J. Nat. Cancer Inst.* **2003**, 95, 1615

108. L. Pinkerton, M. Hein, L. Stayner, L.T. Stayner, *Occup. Environ. Med.* **2004**, 61, 193.

109. P.A. Leggat, D.R. Smith, U. Kedjarune, *Anz. Journal of Surgery*, **2007**, 77(4), 209.

110. C.J. Dunn, K.L. Goa, *Drugs.* **1999**, 58(5), 863.

111. J.H. Waite, T.J. Housley, M.L. Tanzer, *Biochem.***1985**, 24, 5010.

112. J.H. Waite, *Int. J. Adhes. Adhes.***1987**, 7, 9.

113. M. Wiegemann, *Aquat. Sci.* **2005**, 67, 166.

114. A. Doraiswamy, R.J. Narayan, R. Cristescu, I.N. Mihailescu, D.B. Chrisey, *Mater. Sci. Eng. C.* **2007**, 27, 409.

115. X.X. Qin, K.J. Coyne, J.H. Waite, *J. Biol. Chem.* **1997***,* 272, 32623.

116. J.H. Waite, *Integr. Comp. Biol.* **2002**, 42, 1172.

117. J.H. Waite, M.L. Tanzer, *Biochem. Biophys. Res. Commun.* **1980**, 96, 1554.

118. S.W. Taylor, J.H. Waite, M.M. Ross, J. Shabanowitz, D. F. Hunt, *J. Am. Chem. Soc.* **1994**, 116, 10803.

119. M. Yu, T.J. Deming, *Macromolecules*, **1998**, 31, 4739.

120. S.W. Taylor, D.B. Chase, M.H. Emptage, M.J. Nelson, and J.H. Waite, *Inorg. Chem.* **1996**, 35, 7572.

121. J. Monahan, J.J. Wilker, *Chem. Commun.* **2003**, 1672.

122. M.J. Sever, J.T. Weisser, J. Monahan, S. Srinivasan, J.J. Wilker, *Angew. Chem. Int. Ed.* **2004**, 43, 448.

123. J.H. Waite, N.H. Andersen, S. Jewhurst, C. Sun, *J. Adhesion.* **2005**, 81, 297.

124. M.P. Olivieri, R.E. Baier, R.E. Loomis, *Biomaterials.* **1992**, 13, 1000.

125. D.C. Hansen, G.W. Luther III, J.H. Waite, *J. Colloid Interface Sci.* **1994**, 168, 206.

126. D.S. Hwang, Y. Gim, D.G. Kang, Y.K. Kim, H.J. Cha, *J. Biotechnol.* **2007**, 127, 4, 727-735.

127. J .L. Dalsin, B.-H. Hu, B.P. Lee, P.B. Messersmith, *J. Amer. Chem. Soc.* **2003,** 125, 4253-8.

128. H. Lee, S.M. Dellatore, W.M. Miller, and P.B. Messersmith, *Science*. **2007**, 318, 426-430.

129. Fraunhofergesellschaft, Germany http://www.microresist.de/ormocomp_de.htm, **2006.**

130. Sartomer Technical Data Sheet, **2006.**

131. S.K. Chang, and J.E. Riviere, *Fundam. Appl. Toxicol.***1991**, 17, 494–504.

132. T. Lippert, M. Hauer, C.R. Phipps and A. Wokaun, *Appl. Phys. A.* **2003**, 77, 259.

133. J.H. Waite, *Methods Enzymol.* **1995**, 258, 1.

134. M.T. Gale, C. Gimkiewicz, S. Obi, M. Schnieper, J. Sochtig, H. Thiele, S. Westenhofer, *Opt Laser Eng.* **2005**, 43, 373-386.

135. S. Obi, M.T. Gale, C. Gimkiewicz, S. Westenhofer, *IEEE J Sel Top Quant Elect.* **2004**, 10, 440-444.

136. J. Manhart, K.H. Kunzelmann, H.Y. Chen, R. Hickel, *J Biomed Mater Res.* **2000**, 53, 353-361.

137. A.U.J. Yap, X.Y. Wang, X.W. Wu, S.M. Chung, *Biomaterials*, **2004**, 25, 2179-2185.

138. G. Hasshoff, H. Schneider, K. Merle, *J Biomed Mater Res*. **2004**, 71B, 38-45.

139. A.U.J. Yap, L.Y. Lim, T.Y. Yang, A. Ali, S.M. Chung, *Oper. Dent.* **2005**, 30, 129-133.

140. A.S. Al-Hiyasat, H. Darmani, M.M. Milhem, *Clin Oral Invest*. **2005**, 9, 21-25.

141. R. Janda, J.F. Roulet, M. Kaminsky, G. Steffin, M. Latta, *Eur. J Oral Sci.* **2004**, 112, 280-285.

142. A. Doraiswamy, C. Jin, R. J. Narayan, P. Mageswaran, P. Mente, R. Modi, R. Auyeung, D. B. Chrisey, A. Ovsianikov, and B. Chichkov, *Acta Biomateri.*, **2006**, 2 (3), 267–275.

143. J.R. Rasmussen, J.E. Riviere, N.A. Monteiro-Riviere, *Toxiocol. Sci.* **2006**, 91 (1), 159-165.

144. J.H. Park, M.G. Allen, M.R. Prausnitz, *J Control Release*. **2005**, 104, 51–66.

145. B. Stoeber, D. Liepmann, *J Microelectromech Syst*. **2005**, 14, 472–9.

146. M. Yang, J.D. Zahn, *Biomed Microdev*. **2004,** 6, 177–82.

147. S.J. Moon, S.S. Lee, H.S. Lee, T.H. Kwon, *Microsyst Technol.* **2005**, 11, 311–8.

148. S. Henry, D.V. McAllister, M.G. Allen, M.R. Prausnitz, *J Pharm Sci*. **1998**, 87, 922–5.

149. D.J. Kelly, P.J. Prendergast, A.W. Blayney, *Otol. Neurotol.***2003,** 24.

150. A. Ovsianikov, B. Chichkov, O. Adunka, H. Pillsbury, A. Doraiswamy, R.J. Narayan, *App. Surf. Sci.* **2007**, 253, 6603.

151. D.B. Chrisey, A. Pique, R. Modi, H.D. Wu, R.C.Y. Auyeung, H.D. Young, *App. Surf. Sci.* **2000**, 168 (1-4) 345.

152. T. Lippert, M. Hauer, C. R. Phipps, A. Wokaun, *App. Phys. A*. **2003**, 77, 259.

153. T. Lippert, L.S. Bennett, T. Nakamura, H. Niino, A. Yabe, *Appl. Surf. Sci.* **1996**, 96-98, 601-604.

154. A.S. Posner, A. Perloff, A.D. Diorio, *Acta Crystallogr.* **1958**, 11, 308-309.

155. C.M. Cotell, D.B. Chrisey, K.S. Grabowski, J.A. Sprague, C.R. Gossett, *J Appl Biomater.* **1992**, 3, 87-93.

156. M. Okumura, H. Ohgushi, Y. Dohi, T. Katuda, S. Tamai, H.K. Koerten, S. Tabata, *J Biomed Mater Res*. **1997**, 37, 122-129.

157. A. Bigi, B. Bracci, F. Cuisinier, R. Elkaim, M. Fini, I. Mayer, I.N. Mihailescu, G. Socol, L. Sturba, P. Torricelli. *Biomaterials*. **2005**, 26, 2381-2389.

158. C.L. Camire, U. Gbureck, W. Hirsiger, M. Bohner, *Biomaterials* **2005**, 26, 2787-2794.

159. W.L. Suchanek,, K. Byrappa, P. Shuk, R.E. Riman, V.F. Janas, K.S. TenHuisen, *Biomaterials.* **2004**; 25:4647-4657.

160. G. Willmann, *Adv Eng Mater,* **2001,** 3, 135-141.

161. A.L. Rosa, M.M. Beloti, V.R. Noort. *Dent Mater*. **2003**, 19, 768-772.

162. Z. Schwartz, C.H. Lohmann, J. Oefinger, L.F. Bonewald, D.D. Dean, B.D. Boyan, *Adv Dent Res*. **1999**, 13, 38-48.

163. J.H. Brauker, V.E. Carrbrendel, L.A. Martinson, J. Crudele, W.D. Johnston, R.C. Johnson, *J Biomed Mater Res*. **1995**, 29, 1517-1524.

164. A. Doraiswamy, R.J. Narayan, M.L. Harris, S.B. Qadri, R. Modi, D.B. Chrisey, *J. Biomed. Mater. Res.* **2007**, 80A, 635-643.

165. T.M. Patz, A. Doraiswamy, R.J. Narayan, W. He, Y. Zhong, R. Bellamkonda, R. Modi, D.B. Chrisey, *J. Biomed. Mater. Res. Part B,* **2006**, 78B 124-130.

166. A. Doraiswamy, R. Narayan , T. Lippert, L. Urech, A. Wokaun, M. Nagel, B. Hopp, M. Dinescu, R. Modi, R. Auyeung, D. Chrisey, *Appl. Surf. Sci.* **2006**, 252**,** 4743.

167. B.R. Ringeisen, D.B. Chrisey, A. Pique, H.D. Young, R. Modi, M. Bucaro, J.J. Meehan, B.J. Spargo, *Biomater*. **2002**, 23, 161-166.

168. D.B. Chrisey, A. Pique, R.A. McGill, J.S. Horwitz, B.R. Ringeisen, D.M. Bubb, P.K. Wu, *Chem Rev*. **2003**, 103, 553-576.

169. P.K. Wu, B.R. Ringeisen, J. Callahan, M. Brooks, D.M. Bubb, W.D. Wu, A. Pique, B. Spargo, R.A. McGill, D.B. Chrisey, *Thin Solid Films.* **2001,** 398-399, 607-614.

170. M. Maley, M.J. Davies, M.D. Grounds, *Exp Cell Res*. **1995**, 219, 169-179.

171. C.D.W. Wilkinson, M. Riehle, M. Wood, J. Gallagher, A.S.G. Curtis, *Mat Sci Eng C-Bio S*. **2002**, 19 (1-2), 263-269.

172. T.M. Patz, A. Doraiswamy, R.J. Narayan, R. Modi, D.B. Chrisey, *Mat Sci Eng B-Solid,* **2005**, 123 (3), 242-247.

173. F.I. Stuart, Human Physiology, 4th Edition, Brown Publishers, **2000**.

174. A.E. Koch, L.A. Harlow, G.K. Haines, E.P. Amento, E.N. Unemori, W.L. Wong, R.M. Pope, N. Ferrara, *J. Immunology*. **1994**, 152, 4149.

175. T. Asahara, C. Bauters, C. Pastore, *Circulation.* **1995**, 91, 2793--801.

176. S.S. Kang, C. Gosselin, D. Ren, H.P. Greisler, *Surgery.***1995**, 118, 280-7.

177. T.M. Yau, G. Li, R.D. Weisel, A. Reheman, Z.Q. Jia, D.A.G. Mickle, R.K. Li, *J. Thorac Cardiovasc Surg*. **2004**, 127, 1180-7.

178. V. Linder, R.A. Majack, M.A. Reidy, *J. Clin. Invest.* **1990**, 85, 2004-8.

179. A.W. Clowes, M.J. Karnovsky, *Nature*. **1977**, 265, 625-6.

180. D.A. Weatherford, J.E. Sackman, T.T. Reddick, M.B. Freeman, S.L. Stevens, M.H. Goldman, Surgery, **1996**, 120, 433-9.

181. J.H. Waite, T.J. Housley, M.L. Tanzer, *Biochem.***1985**, 24, 5010.

182. J.H. Waite, *Int. J. Adhes. Adhes.***1987**, 7, 9.

183. M. Wiegemann, *Aquat. Sci.* **2005**, 67, 166.

184. A. Doraiswamy, R.J. Narayan, R. Cristescu, I.N. Mihailescu, D.B. Chrisey, *Mater. Sci. Eng. C.* **2007**, 27, 409.

185. X.X. Qin, K.J. Coyne, J.H. Waite, *J. Biol. Chem.* **1997***,* 272, 32623.

186. A.M. Baty, P.A. Suci, B.J. Tyler, and G.G. Geesey, *J. Colloid Interf. Sci.* **1996**, 177, 307.

187. H. Lee, N.F. Scherer, P.B. Messersmith, *P. Natl. Acad. Sci. USA*. **2006**, 103(35), 12999.

188. L. Ninan, J. Monahan, R.L. Stroshine, J.J. Wilker, R. Shi, *Biomaterials.* **2003,** *24,* 4091.

189. J. Schnurrer, C.M. Lehr, *Int. J. Pharm*. **1996**, *141,* 251.

190. S.W. Taylor, D.B. Chase, M.H. Emptage, M.J. Nelson, and J.H. Waite, *Inorg. Chem.* **1996**, *35*, 7572.

191. J. Monahan, J.J. Wilker, *Chem. Commun.* **2003**, 1672.

192. R. L. Strausberg, R. P. Link, *Trends Biotechnol.* **1990,** 8, 53.

193. J. B. Robin, P. Picciano, R. S. Kusleika, J. Salazar and C. Benedict, *Arch. Ophthalmol.* **1988**, 106, 973.

194. J. B. Robin, C. F. Lee, J. M. Riley, *Refract. Corneal Surg.***1989**, 5, 302.

195. F. Hubert, W. vanderKnaap, T. Noel, P. Roch, *Aquatic Living Resources.* **1996** 9 (2): 115-124.

196. D.S. Hwang, S.B. Sim, H.J. Cha, *Biomaterials.* **2007**, 28 (28) 4039-4046.

197. M.L. Bassett, J.E. Dahlstrom, M.C. Taylor, M.E. Koina, L. Maxwell, D. Francis, S. Jain, A.J. McLean, *Exp. Toxicol. Pathol.* **2003**, 55 (1) 11-6.

198. J. Balla, G.M. Vercellotti, V. Jeney, A. Yachie, Z. Varga, J.W. Eaton, G. Balla, *Mol. Nutrition & Food Res.* **2005,** 49 (11), 1030-1043.